TARGETING MICROGLIAL FUNCTION IN POST-STROKE REGENERATION

Kelsey Pinkham

Graduate School of
Systemic Neurosciences
LMU Munich

Dissertation at the
Graduate School of Systemic Neurosciences
Ludwig-Maximilians-Universität München

June, 2025

Supervisor
Prof. Dr. med. Arthur Liesz
Institute for Stroke and Dementia Research (ISD),
LMU University Hospital

First Reviewer: Prof. Dr. med. Arthur Liesz
Second Reviewer: Prof. Dr. Dr. Anna-Sophia Wahl-Ommer
External Reviewer: Prof. Dr. med. Christoph Harms
Date of Submission: 13, June, 2025
Date of Defense: 14, October, 2025

TABLE OF CONTENTS

ABSTRACT

Neuroinflammation following ischemic stroke is characterized by the activation of resident microglia and the infiltration of circulating leukocytes, including a relatively small number of lymphocytes. Despite their low numbers, lymphocytes, particularly T cells, have been consistently shown to be among the most potent leukocyte subpopulations contributing to secondary brain injury. However, the mechanisms by which this minimal number of T cells profoundly affects stroke outcomes remain largely elusive. It is also well described that microglia interact with T cells through cell-to-cell contact, cytokine signaling, and antigen presentation, which in turn leads to the polarization of adaptive immune cells that infiltrate into the brain.

Notably, neuroinflammation is now recognized to persist even months to years after stroke. Although microglia are key components of acute neuroinflammation, their functional states in the chronic phase after stroke remain poorly understood. Therefore, we aimed to investigate how immunomodulatory and metabolic interventions can be employed to influence microglial response across both acute and chronic phases after stroke to promote brain repair and enhance functional recovery.

In the acute phase after stroke, we explore how distinct T cell subsets differentially regulate early microglial activation. Using an experimental stroke mouse model, we demonstrate that T_{H1} cells promote a pro-inflammatory microglial phenotype through the induction of type I interferon signaling, while regulatory T cells (T_{REG}) induce a microglial transcriptional profile associated with chemotaxis and a more reparative profile. Importantly, we show that acute administration of engineered T cells overexpressing the anti-inflammatory cytokine IL-10 (eTcIL10) into the cisterna magna following stroke leads to a shift in microglial gene expression toward pro-regenerative functions, including reduced expression of damage-associated microglia (DAM) markers and downregulation of processes such as spine pruning, phagocytosis, and complement activation. Although T cell–mediated microglial polarization did not significantly alter acute infarct volume, it significantly improved post-stroke functional recovery, highlighting the therapeutic potential of targeting T cell-microglia interactions.

In the chronic phase after stroke, we address the long-term consequences of sustained neuroinflammation driven by microglial dysfunction using an experimental stroke mouse model. Utilizing PET imaging, single-cell RNA sequencing, and analysis of morphological and

functional changes, we reveal that microglia chronically accumulate lipid droplets and cholesterol crystals, hallmarks of impaired lipid metabolism that drive persistent inflammasome activation and IL-1β production. This lipid-driven dysfunction contributes to impaired phagocytic capacity, neurodegeneration, and persistent behavioral deficits. Targeting lipid dysregulation through administration of the liver X receptor agonist GW3965 promotes cholesterol efflux from microglia, reduces lipid overload and cholesterol crystal formation. Thus, microglia are able to cope with a lipid burdened environment, ultimately supporting microglial-to-oligodendrocyte lipid transport that supports the enhancement of post-stroke recovery.

Collectively, our studies position microglial modulation as a robust and versatile therapeutic intervention strategy across multiple stages of stroke recovery. By employing T cell-mediated microglial polarization to an anti-inflammatory state and targeting microglia metabolism to mitigate chronic lipid dysregulation, we advance the understanding of microglia plasticity as a central determinant of stroke recovery. Our work provides a framework for developing immune and metabolism-based interventions to alleviate neuroinflammation, promote tissue repair, and improve long-term outcomes after stroke.

LIST OF ABBREVIATIONS

24S-OHC	24S-hydroxycholesterol
ABCA1	ATP-binding cassette transporter
ABCG1	ATP-binding cassette transporter
ApoE	Apolipoprotein E
ASC	Apoptosis-associated Speck-like protein containing a CARD
BBB	Blood-Brain Barrier
BDNF	Brain Derived Neurotrophic Factor
CE	Cholesterol Esters
ChC	Cholesterol Crystals
CNS	Central Nervous System
CR3	Complement Receptor-3
CV	Cresyl Violet
DAMPs	Damage-Associated Molecular Patterns
DAPI	4’,6-Diamidino-2-Phenylindole
DEG	Differentially Expressed Gene
dMCAo	Distal Middle Cerebral Artery Occlusion
EVs	Extracellular Vesicles
eTc-IL10	T cells to overexpress IL-10
fMCAo	Filament Middle Cerebral Artery Occlusion
FFAs	Free Fatty Acids
FOXP3	Forkhead Box Protein P3
GFAP	Glial Fibrillary Acidic Protein
GSDMD	Gasdermin D
HDL	High-Density Lipoprotein
Iba1	Ionized calcium-Binding Adaptor molecule 1
IFN-γ	Interferon Gamma

IL-1	Interleukin-1 Beta
IL-10	Interleukin-10
IL-4	Interleukin-4
IL-5	Interleukin-5
IL-13	Interleukin-13
IVT	Intravenous Thrombolysis
KO	Knock Out
LD	Lipid Droplet
LXR	Liver-X-Receptor
MRI	Magnetic Resonance Imaging
MS	Multiple Sclerosis
MT	Mechanical Thrombectomy
NG2	Nerve/Glial Antigen 2
NLRP3	NOD-like receptor family pyrin domain containing 3
NRF2	Nuclear Factor Erythroid 2-related Factor 2
Oligos	Oligodendrocytes
OPCs	Oligodendrocyte Progenitor/Precursor Cells
oxLDL	Oxidized Low-Density Lipoprotein
P2Y12	Purinergic Receptor P2Y, G-Protein-coupled Receptor
PET	Positron Emission Topography
PLINs	Perilipins
PT	Photothrombosis
Rag1	Recombination Activating Gene 1
RAM	Repair-Associated Microglia
RNA	Ribonucleic Acids
ROS	Reactive Oxygen Species
RXR	Retinoid X Receptor
scSeq	Single-Cell mRNA Sequencing

SCAP	SREBP cleavage-activating protein
SFAs	Saturated Fatty Acids
SREBP	Sterol Regulatory Element Binding Protein
TBI	Traumatic Brain Injury
Tc	Cytotoxic T cell
Tγδ	Gamma Delta T cell
TGFb	Transforming Growth Factor Beta
TGFa	Transforming Growth Factor Alpha
T_{H1}	Helper 1 T cell
T_{H17}	Helper 17 T cell
TGs	Triglycerides
TNF	Tumor Necrosis Factor-Alpha
Treg	Regulatory T cell
UFAs	Unsaturated Fatty Acids
Vglut1	Vesicular Glutamate Transporter 1

1 INTRODUCTION

1.1 Comprehensive overview of stroke

1.1.1 The global burden of stroke

Stroke is the third leading cause of mortality and a major cause of disability worldwide [40]. Stroke patients have an alarming annual death rate of 7 million and it's estimated that 50% of all stroke survivors are chronically disabled [63]. Thus, a substantial global burden of economic costs of post-stroke treatment and care that is predicted to increase from the billions to trillions by 2025 in the USA alone [63].

1.1.2 Limitations of current stroke treatments

Despite the staggering health and socioeconomic impact of stroke, there are limited therapeutic options for ischemic stroke patients. The primary treatment is intravenous thrombolysis (IVT), which promote vessel recanalization using plasminogen activators to break down fibrin in thrombi [92]. However, IVT is only effective within 4.5 hours of stroke onset [22].. Mechanical thrombectomy (MT) extends the treatment window but is applicable to only 5-10% of patients [82]. Even with these available treatments, many patients do not regain full functional independence [57], highlighting the urgent need for treatments feasible weeks or months post-stroke.

1.1.3 Classification and pathophysiology of stroke

The brain relies on continuous oxygen and nutrient supply to maintain its function [87]. When blood flow is disrupted, brain cells begin to die within minutes, leading to functional impairments such as speech, mobility and memory deficits depending on the brain region [22].

Stroke can be classified in two major subtypes: Hemorrhagic stroke is caused by the rupture of a blood vessel, resulting in bleeding and pressure buildup in brain tissue. Though less common, accounting for about 10-15%, it does carry significantly higher mortality risks than the ischemic subtype [4]. The focus of this thesis, ischemic stroke, accounts for over 80% of all cases globally and results from an arterial blockage, for example, by a blood clot or atherosclerotic plaque, reducing oxygen and energy flow to the brain [93].

Ischemia prevents neurons from maintaining ionic homeostasis, leading to a cascade of events: excitotoxicity, oxidative stress, neuroinflammation and ultimately, cell death [117]. This creates a necrotic core of irreversibly damaged tissue and surrounding this core is the penumbra, a zone of impaired but potentially salvageable tissue [79]. Over time, inflammation and degradation of the blood-brain barrier exacerbate damage, leading to edema and increased injury damage [35].

1.2 Immunological landscape of ischemic stroke

1.2.1 Neuroinflammation in stroke

Neuroinflammation, a central pathomechanism of stroke defined as an inflammatory response in the brain or spinal cord [21]. It is a protective response triggered by the activation of the innate immune system, involving complex mechanisms and the production of chemokines, cytokines, reactive oxygen species (ROS) and secondary messengers. Immunoactive molecules known as damage-associated molecular patterns (DAMPs) activate resident central nervous system (CNS) glial cells such as microglia and astrocytes [72]. They also promote recruitment of peripherally derived immune cells to the brain by their release into the blood circulation [40].

1.2.2 Temporal dynamics of immune response after stroke

Immediately following ischemic injury, DAMPs released from injured tissue activate resident brain macrophage-like cells, termed microglia [67]. During this acute phase, microglia proliferate and secrete chemokines and cytokines, which recruit early responder leukocytes such as neutrophils and monocytes [20] (Fig.1). As the response progresses into the subacute and chronic phases (from one week to several months), there is continued expansion of other leukocyte populations, including T and B cells [28] (Fig.1). This robust pro-inflammatory response is critical for coordinating cellular activation and initiating reparative processes aimed at preserving the vulnerable penumbra and preventing further brain damage.

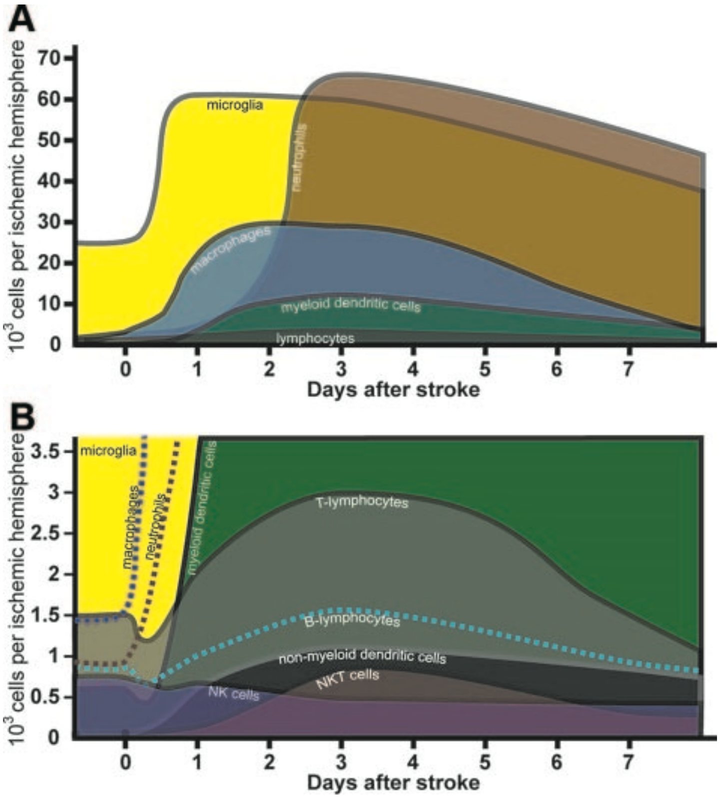

Figure 1. Schematics of temporal dynamics of immune cell infiltration post-stroke. A. Number of cells per hemisphere found ipsi-lesional to the infarct. Microglia activate immediately after ischemic stroke and this activation persists weeks after insult. Monocyte derived macrophages and neutrophils infiltrate within hours following microglia activation. Lymphocytes experience a delayed infiltration kinetic and begin entering the brain days to weeks after ischemic attack. B, Magnification of lower part A. Reproduced with publisher approval [28].

1.2.3 Persistence of neuroinflammation after stroke

Contrary to earlier views that neuroinflammation resolves within weeks [105], emerging evidence shows it can persist for months or even years, contributing to prolonged neuronal damage and impaired recovery (Fig. 2). While acute inflammation is characterized by microglial activation and infiltration of peripheral immune cells, studies have shown that these responses do not fully resolve in the subacute phase (weeks) and may extend into the chronic phase (months to years) [77]. Persistent microglial activation and sustained expression of proinflammatory cytokines such as TNF-α and IL-1β have been detected in both animal models and human patients up to a year after stroke [28]. Chronic inflammation has been linked to secondary neurodegenerative changes in areas remote from the primary infarct, contributing to delayed neuronal loss and cognitive decline [43]. These findings highlight the need to consider chronic neuroinflammation not as a resolved event but as a sustained pathological process and a therapeutic target for long-term recovery in stroke patients.

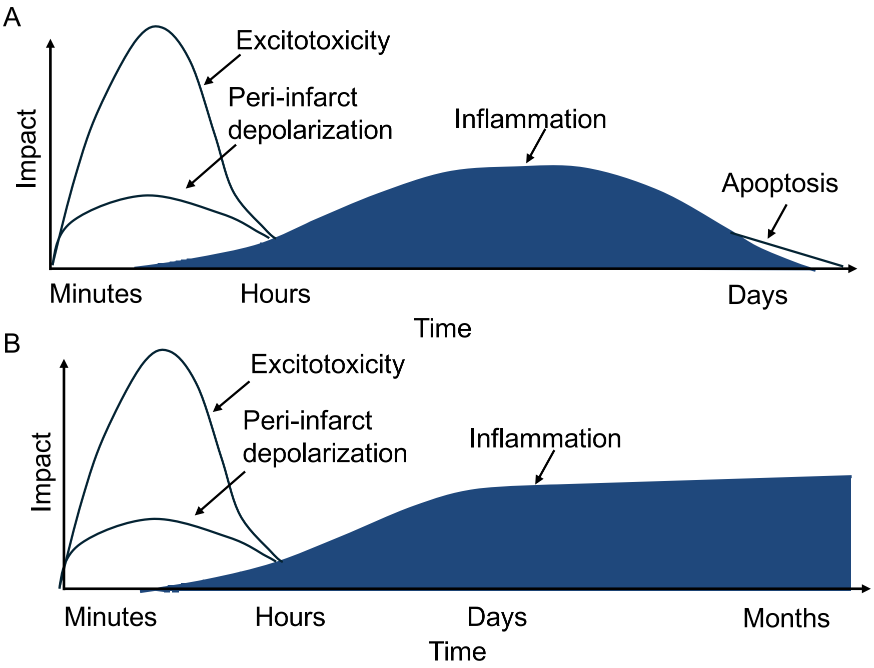

Figure 2. Cascade of damaging events following cerebral ischemia. A. Original model of neuroinflammation dynamics. Very early after onset of the focal perfusion deficit, excitotoxic mechanisms can damage neurons and glia and induce cell death. Excitotoxicity also triggers several events that can further contribute to the demise of the tissue. Such events include peri-infarct depolarizations and the more-delayed mechanisms of inflammation and programmed cell death. This neuroinflammation mechanism was originally believed to resolves within days or weeks after the ischemic event. The x-axis reflects the evolution of the cascade over time, while the y-axis aims to illustrate the impact of each element of the cascade on the outcome. B. Illustrates the revised model of neuroinflammation, which remains unresolved extending from months to years after the ischemic insult.
Reproduced with publisher approval [104].

1.2.4 The evolving role of microglia in post-stroke pathophysiology

Microglia are the resident myeloid cells of the brain, playing a central role in maintaining homeostasis. Under physiological conditions, these “resting” microglia constantly survey the brain microenvironment with their highly motile processes [78]. They are extremely sensitive to disturbances and rapidly shift into an activated state in response to injury. Depending on the specific signaling molecules they encounter, microglia exhibit a diverse range of activation phenotypes [78].

In the context of ischemic stroke, microglia are among the first responders to cerebral injury, as they are among the earliest cells exposed to DAMPs released from injured tissue [20]. Upon activation, microglia undergo marked morphological changes, transitioning from a ramified, branched structure to an amoeboid shape, a shift associated with increased phagocytic activity and pro-inflammatory signaling (Fig.3) [59]. Also depending upon their activation state, microglia may exert neuroprotective or neurotoxic effects [26]. Microglia were initially studied in stroke due to the observation that they secrete neurotrophic factors, such as brain-derived neurotrophic factor (BDNF), along with other growth factors supporting neuronal survival and repair [65, 49]. They also engage in homeostatic functions such as synapse pruning and regulation of neuronal circuit plasticity through direct contact with neurons (Fig.3) [2].

While microglia were once considered primarily relevant to the acute phase of stroke, it is now well established that their activation persists into the chronic phase, lasting months after insult [108]. Chronic microglia activation is increasingly associated with maladaptive responses, including sustained release of pro-inflammatory cytokines, ROS and aberrant synaptic remodeling [110]. These processes can disrupt neural connectivity, impair cognitive recovery and contribute to secondary neurodegeneration [48]. Therefore, understanding the phenotypic shifts of microglia in the post-stroke brain is crucial for identifying therapeutic windows in which modulation of their activity could promote recovery rather than injury exacerbation.

Another hallmark function of microglia that may have significant implications in the chronic phase after stroke is their role in myelin repair and maintenance. This complex process encompasses multiple, coordinated microglial functions. Microglia continuously survey the CNS environment, using dynamic processes to monitor axons and myelin sheaths to detect myelin disruption [54]. Upon damage identification, they clear apoptotic oligodendrocytes and myelin debris, a task that requires the coordination of several phagocytic receptors [54]. This clearance step is essential for creating a permissive environment for oligodendrocyte progenitor cell (OPC) differentiation and remyelination [54].

In addition to debris clearance, microglia shape the inflammatory milieu after injury. The cytokines they secrete play a decisive role in determining whether the environment supports or impedes remyelination. Pro-inflammatory microglia, for example, can hinder repair by releasing cytokines such as IL-1β and IL-18, while pro-regenerative microglia promote OPC maturation and remyelination by secreting anti-inflammatory cytokines like IL-10 and TGF-b, as well as trophic factors [6, 53].

Microglia also provide metabolic support to oligodendrocytes, particularly through regulating lipid metabolism within the lesion environment. Studies show that cholesterol efflux and ApoE-dependent lipid transfer by microglia facilitate the recycling of cholesterol from myelin debris, making it available for remyelinating oligodendrocytes [8].

While microglial roles in myelin repair are increasingly well characterized in the context demyelinating diseases, such as multiple sclerosis, these functions are not yet well understood after stroke. Therefore, further research is needed to clarify how microglia influence myelin dynamics in the post-stroke brain.

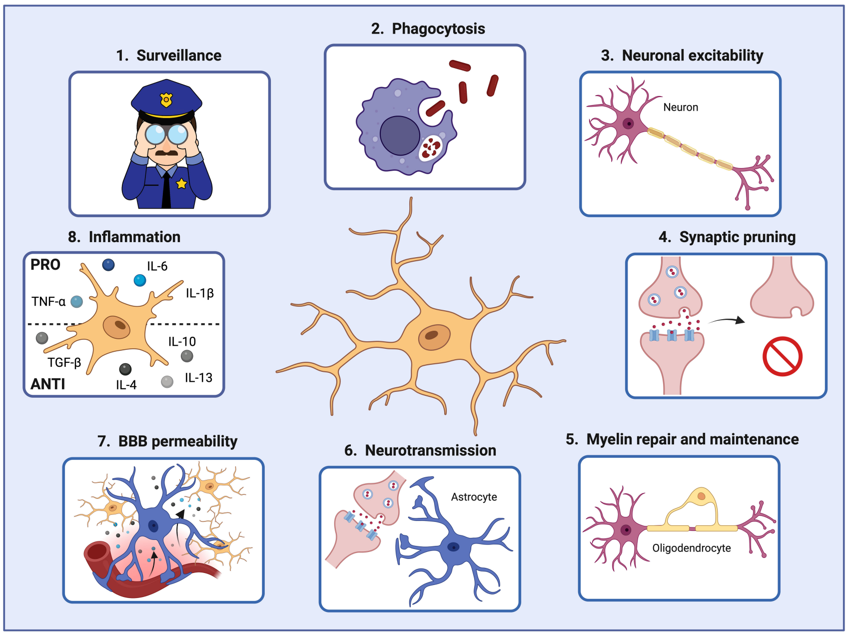

Figure 3. Microglial cells play crucial roles in the brain during development and adulthood. In order to maintain brain homeostasis, microglial cells 1) act as sentinels constantly surveilling the brain environment and adapting their functions to specific triggers, 2) phagocytose pathogens and damaged cells that may threaten the brain homeostasis and function, 3) regulate neuronal excitability, 4) prune defective synapses, 5) interact with oligodendrocytes for myelin repair and maintenance, 6) assist astrocytes in controlling neurotransmitter levels, 7) modify the blood-brain barrier permeability by secreting factors that increase the expression of cell adhesion molecules in endothelial cells, and 8) secrete pro- and anti-inflammatory factors controlling the inflammatory response. Created by Biorender. Reproduced with publisher approval [75].

1.2.5 Dual role of T cells in stroke: pathogenic and protective

Following stroke, lymphocytes start to infiltrate the brain beginning within hours after the ischemic event [28]. This is driven by the release of pro-inflammatory cytokines from activated microglia and continues into the chronic phase after stroke (weeks to months) [28]. Neutrophils are among the earliest responders and enter the brain within hours after an ischemic event. Monocytes follow shortly after, particularly CCR2$^+$ Ly6C^{high}, which peak around 2-4 days post stroke and differentiate into macrophages [28]. While B cells and natural killer cells typically arrive later [28].

Lymphocytes, including T cells, infiltrate the brain several days after stroke onset [28] and extends into the chronic phase (weeks to months) (Fig. 4) [52]. While T cells enter in lower numbers compared to other immune cells, they have been shown to have disproportionately strong effects on stroke outcome, influencing both injury progression and repair mechanisms

T cells exhibit significant functional and phenotypic heterogeneity, and their influence on stroke pathology varies by subtype. Acute infiltration of T cells has been associated with exacerbation of brain injury, largely due to the release of pro-inflammatory cytokines such as IL-17 [114]. In particular, pro-inflammatory subsets of CD4+ T_{HELPER} cells (T_{H1} and T_{H17}), along with γδ T cells, have been shown to worsen stroke outcomes by promoting secondary neurotoxicity and expansion of infarct volume [28].

In contrast, regulatory T cells (T_{REG}) play a neuroprotective role, promoting resolution of inflammation through the secretion of anti-inflammatory cytokines. Depletion of T_{REG} have been associated with larger infarcts and worsened stroke outcomes in experimental stroke models [60]. T_{REG} reduce the number of infiltrating neutrophils, which are key producers of inflammatory mediators such as TNF-a, IFN-γ and IL-1β, thereby dampening the inflammatory response. Among the cytokines secreted by T_{REG}, IL-10 has been identified as particularly beneficial in improving stroke outcome [60]. A recent study has also demonstrated that by delivering IL2:IL-2 antibody complexes after stroke to enhance T_{REG} levels in mouse models, leads to an increase in OPC cell survival, promotes white matter integrity and enhances long-term functional recovery through T_{REG}-derived osteopontin [99]. Interestingly, this study also highlighted that osteopontin interacts with microglial integrin receptors and reprograms them into a reparative phenotype [99].

Furthermore, it has been well described that T cells interact with microglia cells through cytokine production, antigen presentation and cell-to-cell contact, collectively influencing the polarization or activation of immune cells that infiltrate the post-stroke brain [31]. However, the exact mechanisms by which T cells regulate microglial function remain incomplete and require further investigation. Uncovering these interactions could provide therapeautic insights into how lymphocyte modulation might improve microglial responses, reduce inflammation and ultimately enhance stroke recovery.

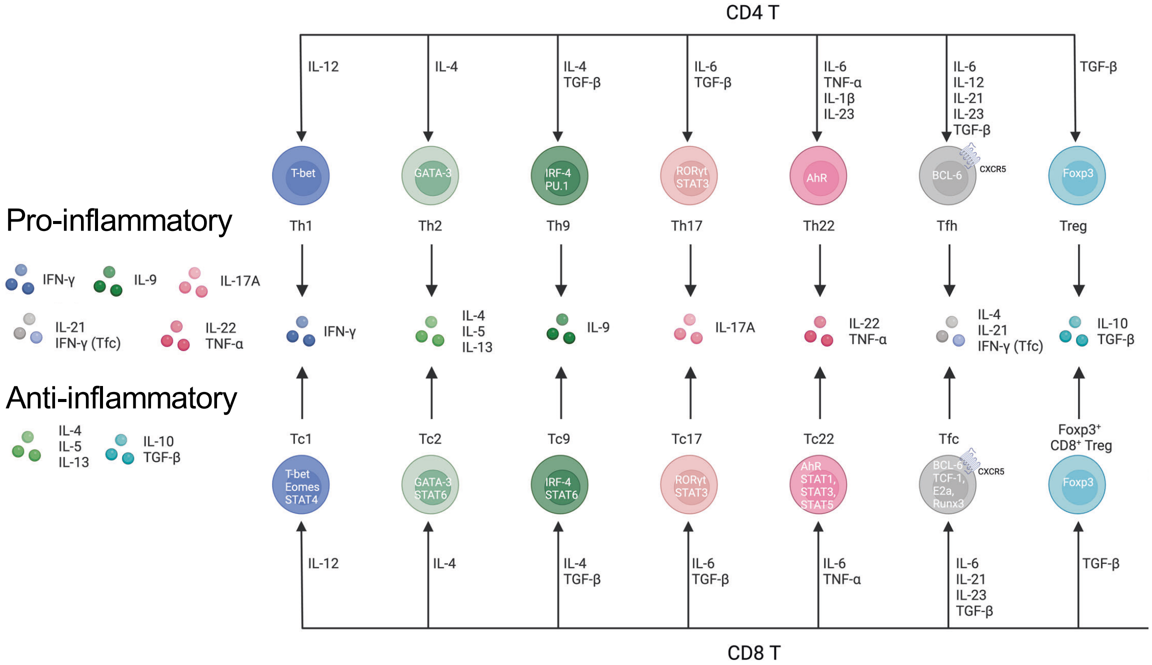

Figure 4. Comparison of Th cell and Tc subsets. Th cell subsets and Tc subsets share signal 3 cytokines, lineage-determining transcription factors, and effector cytokine profiles. Depending upon the Tc or Th subtype a CD4 or CD8 T cell differentiates into dictates the cytokines that they release. In general, these cytokines can be categorized as either pro-inflammatory or anti-inflammatory. Some cells can produce both pro and anti-inflammatory cytokines, such as Th cells. Most T cell subsets correlate with anti-inflammatory properties. However, Tc9, Th2, Foxp3$^+$ CD8 and CD4 Treg are known to express anti-inflammatory cytokines. Those anti-inflammatory cytokines being IL-4, IL-5, IL-13, TGF-b and IL-10. Reproduced with publisher approval [52].

1.2.6 Inflammasomes and their role in neuroinflammation

Neuroinflammation is a key contributor in the pathogenesis of central nervous system disease (CNS) [66]. It serves not only as a consequence of disease progression, but as a catalyst for its continuation [102]. One major contributor to neuroinflammation are inflammasomes, which are multiprotein complexes activated by damage- or pathogen-associated molecular patterns, acting as critical components of the innate immune response [85]. NOD-like receptor family pyrin domain containing 3 (NLRP3) is one pattern recognition receptor that when primed upon sensing stress or damage, forms an inflammasome consisting of a sensor (NLRP3), an adaptor apoptosis-associated-speck-like protein containing a CARD (ASC), and effector caspase-1 [110]. This inflammasome complex then mediates an inflammatory response through the activation of caspase-1, which promotes the maturation of inflammatory cytokines such as IL-1β and stimulates the removal of damaged cells and ultimately supporting repair [110].

While inflammasome activation is essential to support repair, if it becomes excessive or prolonged, it has the capability of contributing to increased tissue damage, which has been shown to be the case in many CNS related diseases [114]. Interestingly, previous studies have shown that microglia express high levels of NLRP3, positioning them as key contributors to inflammasome-mediated responses in CNS pathology [114]. Given their rapid activation after brain injury, inflammasomes have been well studied in the acute phase. Therefore, exploration of their role in long-term outcomes still requires further investigation.

Studies have found that lipids are major regulators of NLRP3 inflammasome activity (Fig. 5) [58]. It has been demonstrated that inhibiting fatty acid synthase (FASN) significantly dampens NLRP3 activation in mouse and human macrophages and that inflammasome activation relies on FASN-dependent NLRP3 Cyss898 palmitoylation [56]. Cholesterol crystals have also been linked to NLRP3 activation through lysosomal damage [74]. Other lipids including oxidized LDL and ceramides have been demonstrated to prime and activate the NLRP3 inflammasome [58], while arachidonic acid has been shown to inhibit NLRP3 [76]. These findings highlight that both pro- and anti-inflammatory lipids modulate NLRP3 activity. Given that microglia have been shown to express high levels of NLRP3 and phagocytose lipid-rich myelin debris, investigating lipid signaling as a key regulator of chronic neuroinflammation could offer a potential target for modulating neuroinflammation in the post-stroke brain.

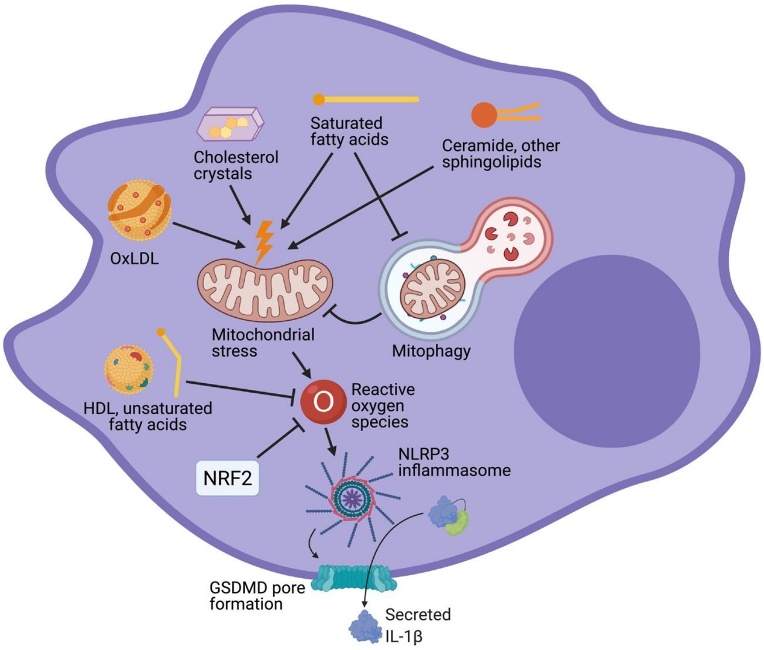

Figure 5. Lipids activate the NLRP3 inflammasome through mitochondrial stress and reactive oxygen species (ROS). Oxidized low-density lipoprotein (oxLDL), cholesterol crystals, saturated fatty acids (SFAs), and sphingolipids all cause mitochondrial stress, as measured by mitochondrial (figure legend continued on next page)

depolarization and/or ROS production, and ROS is an important mediator of NLRP3 activation by these lipids. Reduction of ROS, either through cell intrinsic mechanisms like NRF2, or exogenous stimuli like high-density lipoprotein (HDL) and unsaturated fatty acids (UFAs), can decrease NLRP3 activation. Mitophagy, which removes stressed mitochondria, can also blunt NLRP3 activation by lipids, and inhibition of autophagy contributes to the ability of saturated fatty acids to activate NLRP3. Reproduced with publisher approval [58].

1.2.7 Timing and regulation of IL-1β expression in neuroinflammation

A controlled acute inflammatory response following stroke is essential to initiate repair mechanisms, such as neurogenesis and tissue remodeling. IL-1β is a key pro-inflammatory cytokine acting as an immediate responder in the immune response [68]. The primary producers of this cytokine are activated glial cells, such as microglia, which are rapid responders to environmental stimuli [68]. Upon activation, microglia release IL-1β to promote the production of chemokines and additional cytokines, facilitating the recruitment of peripheral immune cells to the site of injury and orchestrating the broader neuroinflammatory response [68].

While the acute secretion of IL-1β is necessary for initiating repair, many studies have demonstrated its detrimental effects, particularly when its release persists past the early stages of injury. For example, IL-1β has been shown to enhance brain edema and contribute to the breakdown of the blood-brain barrier [61]. Furthermore, if left unchecked, IL-1β can drive secondary neuronal death, exacerbating the damage. Experimental studies have shown that blocking IL-1β can reduce infarct size and improve neurological function [61].

Thus, although the early release of IL-1β is critical for mounting an immune response and promoting repair after brain injury, its prolonged or excessive expression have been proven to be harmful. Hence, the timing and regulation of IL-1β expression is critical. Therefore, continued investigation into IL-1β dynamics, particularly during the chronic phase after stroke, is essential for developing strategies to mitigate the detrimental effects of neuroinflammation and improve post-stroke recovery.

1.3 The role of lipid metabolism in the central nervous system

1.3.1 Lipid metabolism in the brain

The brain has the second-highest lipid content in the human body, accounting for 50% of its dry weight [64]. The predominant lipid species found in the brain are cholesterol, phospholipids and sphingolipids [112]. These lipids serve three primary functions: maintaining cell membrane integrity and function, acting as energy reservoirs and participating in critical inter- and intracellular signaling pathways [112].

Importantly, lipids are not uniformly distributed, but highly enriched in specific cell types and structures, particularly in myelin [90]. Cholesterol, for example, is a critical component of myelin sheath and is indispensable for its formation and maintenance [90]. Neurons, oligodendrocytes, astrocytes and microglia each play specialized roles in lipid synthesis, transport and recycling, reflecting a tightly regulated and cell-type-specific lipid metabolism essential for CNS homeostasis [104].

Disruptions in lipid metabolism are increasingly recognized as central features of several neurological diseases, including Alzheimer’s, multiple sclerosis and stroke. In these disease contexts, abnormal lipid accumulation or impaired clearance can lead to inflammation, cell stress and impaired repair mechanisms [111]. Therefore, understanding the role of lipids in brain physiology is essential for revealing molecular drivers of neurodegeneration and regeneration.

1.3.2 The role of cholesterol in the CNS

Cholesterol constitutes approximately 25% of the brain’s total lipid content [111]. It plays a vital role in regulating membrane fluidity, permeability and serve as essential platforms for signaling molecules and receptors in neurotransmission [73]. As one of the most abundant lipid classes involved in myelination, and being the rate limiting factor in the process, cholesterol is crucial for maintaining structural integrity and stability of the myelin sheath [39]. Moreover, it is a critical component that ensures the insulation of axons, which in turn facilitates the rapid conduction of nerve impulses in the CNS [89].

During development, oligodendrocytes are responsible for synthesizing their own cholesterol to build myelin [115]. In the adult brain, however, whether in healthy or pathological conditions, astrocytes become the primary source of cholesterol [104]. They transport cholesterol to neurons and other glial cells via lipoprotein particles containing apolipoprotein E (ApoE) [80]. This shift in cholesterol sourcing highlights its importance in sustaining myelin maintenance and regeneration across the lifespan.

Oligodendrocytes, the cell type responsible for myelination, must first differentiate from progenitor to mature myelinating cells, and cell signaling pathways responsible for this maturation, such as PI3K/Akt/mTOR, are heavily influenced by cholesterol [119]. Mature oligodendrocytes must rapidly expand their membrane surface during myelination, in which cholesterol is key. It is also essential for forming the multilamellar structure of myelin and provides membrane stability within the myelin membrane [120]. Formation of lipid rafts, which are essential for organizing membrane proteins, such as myelin basic protein (MBP) and proteolipid protein (PLP), are made by cholesterol [121]. It has been shown that mice with disrupted cholesterol biosynthesis in oligodendrocytes show severely impaired CNS myelination [90].

Studies have shown that local cholesterol availability is necessary for efficient remyelination following CNS injury [8]. Due to the restrictive nature of the blood-brain barrier (BBB), cholesterol from peripheral circulation cannot enter the brain; instead, it must be synthesized *de novo* or recycled from lipids by glial cells [46]. After CNS injury, when myelin is degraded and cleared primarily by microglia, cholesterol can be recycled or exported and subsequently reused by OPCs to support remyelination [8]. This lipid trafficking process is regulated by the Liver X receptor (LXR) and ApoE pathways [8]. From maintaining membrane integrity to serving as a critical component of myelin synthesis, cholesterol is indispensable for sustaining brain structure, function and homeostasis.

1.3.3 Myelin debris clearance following neural injury

Phagocytosis is a hallmark function of microglia supported by several classes of receptors. Microglia use pattern recognition receptors (PRRs) to detect pathogen associated molecular patterns (PAMPs) and damage-associated molecular patterns (DAMPs) [26]. Scavenger receptors come into play to uptake oxidized lipids, apoptotic cells and lipoproteins [12]. The TAM receptor family, Tyro3, Axl, and MerTK, is essential for the clearance of apoptotic cells, a process known as efferocytosis [33]. Fc receptors are responsible for the binding of antibodies to enable antibody-dependent phagocytosis, while complement receptors recognize complement opsonized targets, such as synapses [10]. Additionally, triggering receptor expressed on myeloid cells (TREM receptors), such as TREM2, are involved in lipid sensing, phagocytosis and immune regulation [16]. While lipoprotein receptors do directly mediate phagocytosis, they are essential in cholesterol and lipid transport following debris uptake [64].

Following an ischemic stroke, neuronal death and axonal degeneration generate abundant myelin debris in the surrounding tissue [14], and microglia are central to its clearance [104]. Microglial scavenger receptors, TAMs and TREM2 directly bind or interact with bridging ligands like Gas6 and Protein S on myelin and apoptotic cell membranes to initiate debris recognition and engulfment [33]. TAM receptors and TREM2 aid in suppressing excessive inflammation, while promoting clearance [33]. TREM2 and lipoprotein receptors, including those for ApoE, are essential for cholesterol-rich myelin debris, supporting the lipid metabolism needed for phagocytic function and microglial homeostasis [64].

This coordinated activity across receptor classes ensures efficient, non-inflammatory clearance of myelin debris after stroke. Proper debris removal and processing not only facilitates a healthy milieu, but facilitates oligodendrocyte maturation and remyelination, which are critical for functional recovery after stroke.

1.3.4 Intracellular lipid metabolism and cholesterol efflux

Once internalized, myelin debris is enclosed within phagosomes that subsequently fuse with lysosomes, forming phagolysosomes that harbor enzymes for degradation [11]. Some lipid components, such as fatty acids, are oxidized within microglia to serve as energy sources or signaling molecules [106]. However, excess cholesterol that cannot be metabolized is exported out of the cell via lipid transporters like ATP-binding cassette transporters ABCA1 and ABCG1 [115]. These transporters load cholesterol onto ApoE-containing lipoproteins, which can then be taken up and recycled by neighboring glial cells or neurons [104] (Fig.6). The liver X receptor (LXR), a key transcription factor, regulates this reverse cholesterol transport by controlling the expression of genes involved in lipid transport, including ABCA1, ABCG1 and ApoE [1] (Fig. 6).

1.3.5 Lipid imbalance and disease progression

When lipid efflux pathways become overwhelmed, as described in certain disease states, free fatty acids (FFAs) and unesterified cholesterol need to be processed and stored into lipid droplets (LDs) (Wie et al., 2023). Once considered inert lipid reservoirs, LDs are now recognized as dynamic organelles involved in multiple metabolic processes [29]. Structurally, LDs consist of a phospholipid monolayer coated with regulatory proteins such as perilipins (PLINs), which provide stability and coordinate metabolic activities like lipolysis and lipophagy [15]. Their hydrophobic core primarily contains neutral lipids such as cholesterol esters (CEs) and triglycerides (TGs).

Although LDs serve essential roles in energy storage, metabolic regulation and protection against lipotoxicity, their excessive accumulation, as seen under disease conditions, can disrupt lipid homeostasis [45]. In glial cells, an imbalance between lipid uptake, synthesis and mobilization can result in pathological LD buildup ([117]. This accumulation can drive phagocytic cells, such as microglia, to adopt a foam cell-like phenotype, characterized by chronic activation, impaired phagocytic capacity and the release of pro-inflammatory cytokines (Fig.6) [117].

When lipid influx overwhelms the cell's metabolic capacity, the ability to esterify and sequester cholesterol into lipid droplets becomes compromised [5]. As a result, excess free cholesterol can crystallize, forming cytotoxic cholesterol crystals [32]. This phenomenon has been most notably described in the context of atherosclerosis, where lipid laden foam cells accumulate cholesterol crystals and further contribute to plaque formation and vascular inflammation [34]. Similarly, in a model of multiple sclerosis (MS), phagocytes overloaded with myelin debris showed defective cholesterol clearance, which triggered cholesterol crystal formation that drove NLRP3 inflammasome activation and overall inhibited remyelination [13].
These findings underscore the importance of lipid metabolism not only in maintaining CNS homeostasis but also in supporting regeneration and recovery following injury. Targeting lipid handling pathways, including cholesterol synthesis, efflux and storage, may offer promising therapeutic strategies for a range of neurodegenerative diseases and conditions such as stroke.

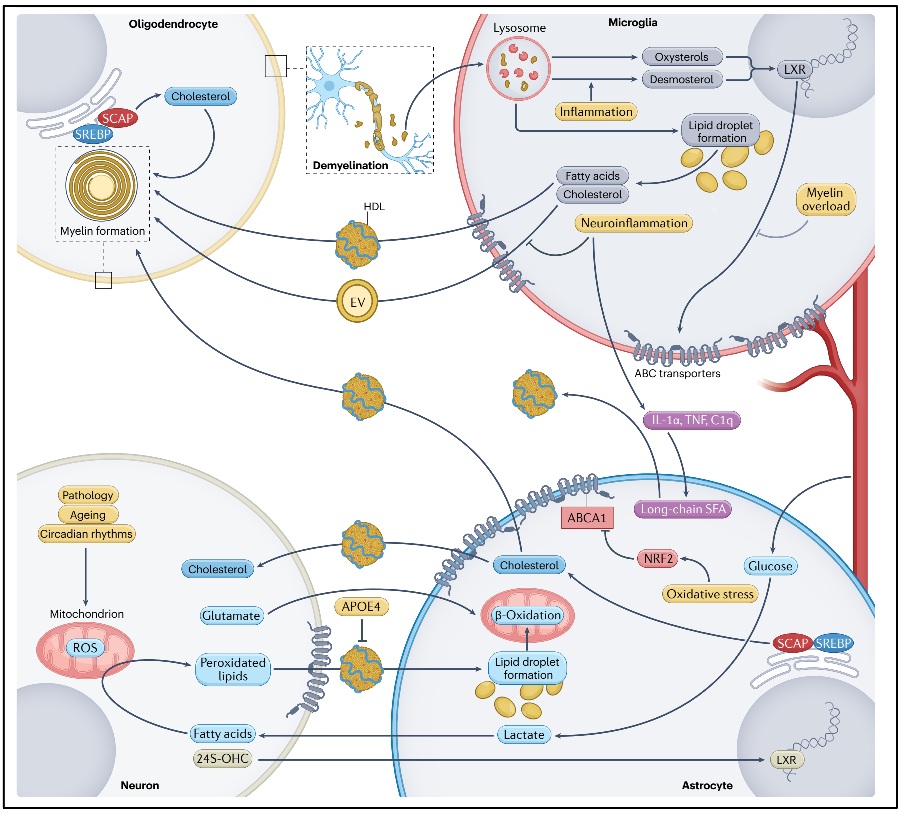

Figure 6. Intercellular lipid transfer in the CNS. Although all CNS-resident cells can synthesize lipids through pathways mediated by sterol regulatory element-binding proteins (SREBPs) and SREBP cleavage-activating protein (SCAP), intercellular lipid transfer is thought to be key in maintaining lipid homeostasis in the CNS. In pathological conditions, astrocytes convert blood glucose to lactate, which (figure legend continued on next page)

is then transported to neurons and converted to FAs. Reciprocally, neurons expel peroxidated lipids, formed through peroxidation by ROS, which are taken up by astrocytes and stored in lipid droplets. This intercellular lipid transfer, along with astrocytic lipid droplet formation and β-oxidation, depends on APOE-containing HDLs and glutamate, and protects against neurodegeneration. Neurons transfer 24S-hydroxycholesterol (24S-OHC) to astrocytes, likely under both homeostatic and diseased conditions, resulting in the activation of nuclear LXRs, which control the expression of genes involved in lipid homeostasis. Astrocytes have been reported to transfer de novo cholesterol to neurons via HDLs, to support their function and to promote remyelination. During remyelination, enhanced cholesterol biosynthesis occurs in astrocytes. Astrocytic lipid transfer is also closely associated with CNS pathology, with inflammatory mediators released by microglia, enhancing the astrocytic loading of APOE HDLs with toxic long-chain saturated fatty acids (SFAs). Microglia also drive intercellular lipid transfer in the CNS. Following demyelination, they process myelin debris and generate lipid droplets, oxysterols and desmosterol, with the latter two activating LXRs. LXR activation drives ABC transporter expression, facilitating APOE lipidation and HDL formation that can be taken up by oligodendrocytes to aid myelin formation. Microglia release lipid-containing extracellular vesicles (EVs) to oligodendrocytes for the genesis of new myelin sheaths. Diverse pathological and environmental factors, such as neuroinflammation, ageing, APOE4, oxidative stress, lipid droplet overload, can impair cell-cell lipid fluxes, thereby driving CNS pathologies. Reproduced with publisher approval [105].

2 AIM OF THE STUDY

Neuroinflammation following ischemic stroke is driven by activation of resident microglia and infiltration of circulating leukocytes, including a small but influential subset of T lymphocytes. Despite their relatively low numbers, T cells have been consistently implicated as key modulators of secondary brain injury; however, the mechanisms by which they impact microglial responses and stroke outcomes remain poorly understood. Furthermore, while acute microglial activation has been extensively studied, the chronic alterations in microglial function, and their contribution to persistent neuroinflammation and impaired recovery long after the initial insult, remain largely unexplored.

The central aim of this study is to investigate how immunomodulatory and metabolic strategies can be employed to influence microglial behavior during both the acute and chronic phases following ischemic stroke, with the goal of promoting brain repair and enhancing functional recovery.

To address the acute phase, we utilized an experimental mouse model of ischemic stroke to investigate how distinct T cell subsets regulate early microglial activation. We engineered T cells to overexpress the anti-inflammatory cytokine IL-10 (eTc-IL10) via viral transduction and administered these cells directly into the cisterna magna during the acute post-stroke phase to locally modulate the immune environment. Through this approach, we aimed to delineate the differential effects of pro-inflammatory (T_{H1}) versus anti-inflammatory (T_{REG} and Il-10 expressing) T cell subsets on microglial gene expression profiles and functional polarization.

To investigate the chronic phase of neuroinflammation, we also used an experimental stroke model to longitudinally track microglial activation and dysfunction over time. We employed positron emission tomography (PET) imaging to monitor persistent microglial activation up to several months after stroke and performed single-cell RNA sequencing (scRNA-seq) to characterize transcriptional changes in microglia over time. Morphological analysis, phagocytosis assays, and lipid staining were used to assess functional and lipid alterations in microglial populations. To target chronic microglial lipid dysfunction, we administered GW3965, a liver X receptor (LXR) agonist known to promote cholesterol efflux, and assessed its impact on microglial lipid accumulation, inflammasome activation, and neuroinflammatory signaling.

Through these complementary approaches, we sought to define how microglial responses are shaped by early adaptive immune interactions and late-stage metabolic dysfunction, and to evaluate the therapeutic potential of targeting these processes to improve brain repair and long-term functional outcomes after stroke.

3 RESEARCH ARTICLES

3.1 T cells Modulate the Microglial Response to Brain Ischemia

3.1.1 Summary

The immune response following ischemic stroke is well characterized, notably involving microglial activation and the release of pro-inflammatory cytokines that promote leukocyte infiltration into the brain. However, the influence of infiltrating leukocytes, particularly T cells, on resident innate immune cells like microglia remains poorly understood. Although T cells are present in relatively low numbers compared to other immune cells, they have been shown to exert disproportionately strong effects on post-stroke neuroinflammation. The mechanisms by which T cells modulate microglial response and contribute to neuroinflammation are still not fully elucidated.

In this study, using an experimental ischemic stroke mouse model, we demonstrate that during the acute post-stroke phase, when microglia activation is at its peak, this activation is differentially modulated by distinct T cell subsets. Specifically, we show T_{H1} cells induce a type I interferon signaling in microglia, linked to a pro-inflammatory response, whereas T_{REG} cells elicit microglial transcriptional changes associated with chemotaxis and an anti-inflammatory response. To further investigate the effect of T_{REG} cells on microglia, we engineered T cells to overexpress anti-inflammatory cytokine IL-10 (eTc-IL10) through viral transfection and administered them into the cisterna magna 4 hours after stroke induction. Mice receiving eTcIL10 cells exhibited significantly improved functional recovery. Bulk RNA sequencing of the ischemic hemisphere revealed downregulation of damage-associated microglia (DAM)-related genes and a shift toward gene expression profiles linked to chemokine signaling. In addition, decreased expression of effector functions such as spine pruning, phagocytosis and complement activation. Overall, eTc-IL10 treatment promoted a pro-regenerative microglial phenotype, suggesting a promising immunomodulatory approach to enhance post-stroke recovery.

3.1.2 Reference

The paper was published in the journal “eLife” under the following reference:

Corinne Benakis, Alba Simats, Sophie Tritschler, Steffanie Heindl, Simon Besson-Girard, Gemma Llovera, **Kelsey Pinkham**, Anna Kolz, Alessio Ricci, Fabian J Theis, Stefan Bittner, Özgün Gökce, Anneli Peters, Arthur Liesz (2022) **T cells modulate the microglial response to brain ischemia** eLife 11:e82031

RESEARCH ARTICLE

T cells modulate the microglial response to brain ischemia

Corinne Benakis[1]*, **Alba Simats**[1], **Sophie Tritschler**[2], **Steffanie Heindl**[1], **Simon Besson- Girard**[1], **Gemma Llovera**[1], **Kelsey Pinkham**[1], **Anna Kolz**[3], **Alessio Ricci**[1], **Fabian J Theis**[2], **Stefan Bittner**[4], **Özgün Gökce**[1,5], **Anneli Peters**[3,6], **Arthur Liesz**[1,5]*

[1]Institute for Stroke and Dementia Research, University Hospital, LMU Munich, Munich, Germany; [2]Institute of Diabetes and Regeneration Research, Institute of Computational Biology, Helmholtz Zentrum München, Neuherberg, Germany; [3]Institute of Clinical Neuroimmunology, University Hospital, LMU Munich, Munich, Germany; [4]Department of Neurology, Focus Program Translational Neuroscience (FTN) and Immunotherapy (FZI), RhineMain Neuroscience Network (rmn(2)), University Medical Center of the Johannes Gutenberg University Mainz, Mainz, Germany; [5]Munich Cluster for Systems Neurology (SyNergy), Munich, Germany; [6]Biomedical Center (BMC), Faculty of Medicine, LMU Munich, Munich, Germany

***For correspondence:**
Corinne.Benakis@med.uni-muenchen.de (CB);
Arthur.Liesz@med.uni-muenchen. de (AL)

Competing interest: See page 17

Funding: See page 17

Preprinted: 26 September 2021
Received: 20 July 2022
Accepted: 23 November 2022
Published: 13 December 2022

Reviewing Editor: Carla V Rothlin, Yale University, United States

Abstract Neuroinflammation after stroke is characterized by the activation of resident microglia and the invasion of circulating leukocytes into the brain. Although lymphocytes infiltrate the brain in small number, they have been consistently demonstrated to be the most potent leukocyte subpopulation contributing to secondary inflammatory brain injury. However, the exact mechanism of how this minimal number of lymphocytes can profoundly affect stroke outcome is still largely elusive. Here, using a mouse model for ischemic stroke, we demonstrated that early activation of microglia in response to stroke is differentially regulated by distinct T cell subpopulations – with T_{H1} cells inducing a type I INF signaling in microglia and regulatory T cells (T_{REG}) cells promoting microglial genes associated with chemotaxis. Acute treatment with engineered T cells overexpressing IL- 10 administered into the cisterna magna after stroke induces a switch of microglial gene expression to a profile associated with pro- regenerative functions. Whereas microglia polarization by T cell subsets did not affect the acute development of the infarct volume, these findings substantiate the role of T cells in stroke by polarizing the microglial phenotype. Targeting T cell- microglia interactions can have direct translational relevance for further development of immune- targeted therapies for stroke and other neuroinflammatory conditions.

Editor's evaluation

This manuscript should be of interest to neuroimmunologists investigating how microglia may be manipulated to improve neuroinflammation in stroke and beyond. The data support the hypothesis that manipulation of lymphocytes and the cytokines they secrete may be an effective therapeutic strategy to modulate inflammation and improve the outcome after stroke.

Introduction

Among peripheral leukocytes invading the injured brain, T cells have been consistently identified as the invading leukocyte subpopulation with the largest impact on secondary neurodegeneration and modulation of the ischemic brain damage (***Kleinschnitz et al., 2010***; ***Liesz et al., 2011***). T cell subpopulations have the potential to play either a neuroprotective or a deleterious role in post- stroke neuroinflammation. In particular, the pro- inflammatory T_{H1}, T_{H17} subsets of T_{HELPER} cells, and IL- 17- producing γδ T cells have been shown to induce secondary neurotoxicity, leading to infarct expansion with worse functional outcome (***Gelderblom et al., 2012***; ***Shichita et al., 2009***), whereas regulatory T cells (T_{REG}) exert anti- inflammatory and neuroprotective function suppressing an excessive inflammatory reaction to the brain infarct. Recruitment of peripheral immune cells is not limited to the brain parenchyma since an accumulation of T cells is observed in the choroid plexus and the meninges after stroke (***Benakis et al., 2016***; ***Llovera et al., 2017***). Attempt in blocking the recruitment of peripheral effector T cells diminished neuronal damage in different cerebral ischemic models, resulting in improvement of stroke outcome and suggesting a possible therapeutic target (***Liesz et al., 2011***; ***Llovera et al., 2015***). Considering the relatively low number of only a few thousand lymphocytes invading the brain after stroke compared to more than 50 times higher cell count of innate immune cells (invading and resident) in the post-stroke brain (***Gelderblom et al., 2009***), it is surprising to observe such a dramatic effect of a small number of T cells on the neuroinflammatory response to stroke.

Therefore, we hypothesized that T cells have a polarizing effect on microglial function. In turn, microglia – as the most abundant immune cell population in the ischemic brain – could amplify the T cells' impact on the cerebral immune milieu. Indeed, microglia interact with T cells via either cell- to-cell contact, cytokine- mediated communication, or antigen presentation, leading to activation/ polarization of adaptive immune cells entering the brain (***Goldmann and Prinz, 2013***). T cell-microglia interaction can further influence the neuroinflammatory response in experimental models of multiple sclerosis (***Dong and Yong, 2019***) and possibly in stroke (***Wang et al., 2016***). In fact, recent evidence suggests a crosstalk between microglia and T cells as a key determinant of neuronal plasticity during recovery from brain injury (***Shi et al., 2021***). However, while the influence of microglia/macrophages on T cells has been well studied, it is still unclear how in reverse the T cells influence microglial function, and whether early interaction of T cells with microglia in the acute response to stroke can have an immediate impact on microglia and further change the course of disease progression.

Using morphological analysis, single- cell sequencing and adoptive transfer models of ex vivo differentiated T_{HELPER} cell subpopulations, we performed an in-depth analysis of the immunomodulatory effects of T cells on microglial polarization. Better understanding of the T cell-microglia crosstalk holds the potential to use polarized T cells as a therapeutic approach with large impact on the cerebral inflammatory milieu potentiated by resident microglia.

Results

Lymphocytes modulate the activation state of microglia in response to stroke

First, we investigated the effect of lymphocytes on microglial morphology and transcriptome in male *Rag1*$^{-/-}$ mice deficient in T and B lymphocytes after experimental stroke using the distal occlusion of the middle cerebral artery (dMCAO; ***Llovera et al., 2014***; ***Figure 1A***). Microglia were analyzed 5 days after stroke at the lesion border because this region and this acute time point were identified as the maximal cerebral leukocyte infiltration as previously published (***Llovera et al., 2017***) and exemplified in (***Figure 1B***). CD3+ T cells were localized at the infarct border as quantified on immunohistochemistry coronal sections and represented in the cumulative topographic maps 5 days after stroke (***Figure 1C***). Using an automated morphological analysis of IBA1 positive cells (***Heindl et al., 2018***) located at the perilesional (ipsilateral) cortex, where CD3+ T cells accumulated (***Figure 1B***), we identified that microglia of *Rag1*$^{-/-}$ mice displayed extended ramifications and a lower sphericity compared to microglia of wild- type (WT) mice, indicating a less reactive phenotype of microglia in the absence of lymphocytes (***Figure 1C, D***). In contrast, microglial morphology remained relatively unchanged between *Rag1*$^{-/-}$ and WT mice in the contralateral (unaffected) hemisphere which does not show recruitment of lymphocyte in considerable amounts, supporting the role of local lymphocyte infiltration for changing microglial morphology. Because the absence of lymphocytes prevents microglial morphological changes toward a reactive state, we asked whether the ischemic lesion is decreased in lymphocyte-deficient mice lacking microglia. We depleted microglia using PLX5622 incorporated in the mouse diet for 2 weeks prior inducing dMCAO (***Figure 1E, F***). Surprisingly, we

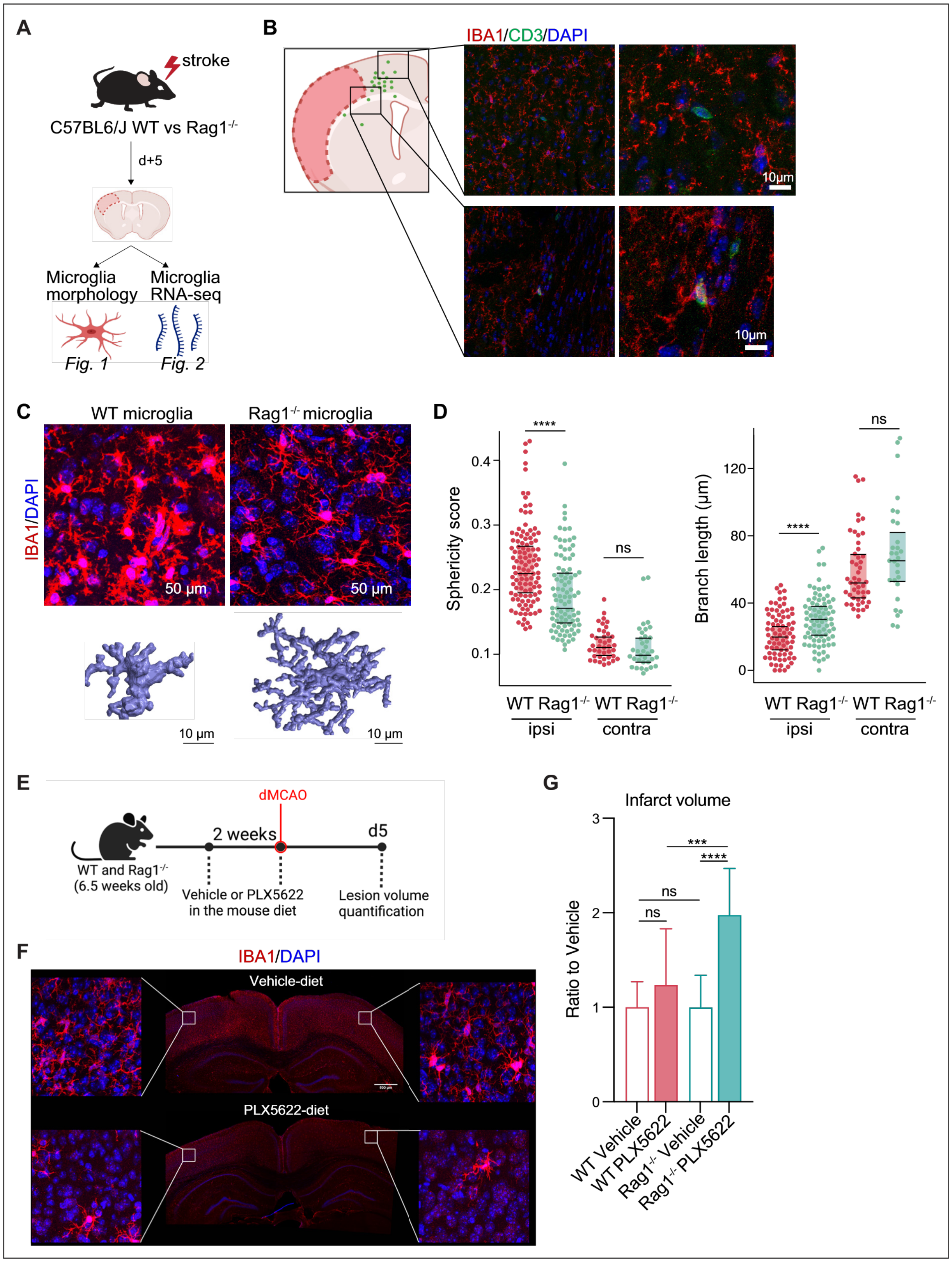

Figure 1. Lymphocytes influence microglia morphology after stroke. (**A**) Schematic of the experimental design: morphological analysis of microglia and transcriptomic profile of sorted microglia were performed in naïve mice or 5 days after stroke in wild-type (WT) and *Rag1*$^{-/-}$ mice. (**B**) Top left, cumulative topographic maps of CD3+ T cells 5 days after stroke. Cells were accumulated from one section at bregma level of five animals each. Each cell is represented as a single dot. The infarct is depicted in pink. Right, representative immunohistochemistry images of microglia (IBA1, red) and T cells (CD3,

Figure 1 continued on next page

Figure 1 continued green) in the perilesional area 5 days after stroke in WT mice. 4’,6- Diamidin- 2- phenylindol (DAPI; blue) was used as nuclear dye. Bar scale indicates 10 µm. (**C**) Top, representative images of IBA1+ microglial cells in the perilesional region (900 µm distal to the infarct border, cortical layer 4). Bottom, three-dimensional (3D) reconstruction of microglia in WT and *Rag1*$^{-/-}$ mice. (**D**) Morphological analysis of microglia in the peri- infarct area (ipsi) and in the contralateral hemisphere (contra) for two representative features: sphericity and branch length (µm) in WT (red) and *Rag1*$^{-/-}$ (green) mice. Each dot corresponds to one microglial cell; n=3mice per condition; ns, non significant; ****, p<0.0001. Wilcoxon rank sum test with continuity correction and Bonferroni post- hoc correction for multiple testing. (**E**) WT and *Rag1*$^{-/-}$ mice were fed a chow diet containing the CSF1 receptor antagonist, PLX5622 (1200 ppm in mouse chow) for 2 weeks and until 5 days post-stroke to eliminate microglia from the brain, and another group of mice were fed with a control chow diet (vehicle). Infarct volumetry was quantified on cresyl violet staining 5 days after distal occlusion of the middle cerebral artery (dMCAO). (**F**) Images show that 2 weeks of PLX5622- diet almost completely depleted microglia from the brain (IBA1, red; 4’,6- Diamidin- 2- phenylindol [DAPI], blue), scale bar: 500 µm. (**G**) Infarct volumes of PLX5622- treated mice as a ratio to vehicle-treated mice 5 days after stroke; One- way ANOVA and Tukey’s multiple comparison test; n=13–15 mice per condition; bar graphs show the mean and the standard deviation (SD); ns, non significant; ***, p<0.001; ****, p<0.0001.

found a significant increase of the infarct volume in *Rag1*$^{-/-}$ mice depleted of microglia in comparison to vehicle-treated *Rag1*$^{-/-}$ mice, whereas depletion of microglia in WT mice has no significant effect (***Figure 1G***), showing that depletion of microglia in WT mice does not have the same effect on stroke as in the lymphocyte deficient mice. These data suggest that microglia- T cell interaction is required to influence the development of the infarct. To better understand this interaction, we investigated the functional implications of cerebral lymphocyte invasion for microglia by single-cell sequencing (10 × Genomics pipeline) of sorted CD45^{+}CD11b^{+} cells.

CD45^{+}CD11b^{+} myeloid cells were sorted by flow cytometry from naïve mice or 5 days after stroke (pool of 3 mice per condition; ***Figure 1A*** and ***Figure 2A***). To better discriminate the transcriptional signature of microglial cells from other CD45^{+}CD11b^{+} myeloid cells, we performed an unsupervised clustering analysis and identified 15 distinct clusters across conditions (***Figure 2—figure supplement 1A***). Based on the expression of previously defined markers of homeostatic and reactive microglia per cell cluster (high gene expression of *Fcrls*, *P2ry12*, and *Trem2;* low expression of *Itgax*, *Ccr2*, and *Lyz2*; ***Keren- Shaul et al., 2017***; ***Miron and Priller, 2020***; ***Prinz and Priller, 2014****),* five clusters were annotated as microglial cells (***Figure 2B***). We then performed a subclustering analysis on only the microglia cells (***Figure 2—figure supplement 1B***) and identified subpopulations showing either a transcriptomic profile preferentially associated with homeostatic microglial function (clusters 0, 1, 4, and 6) or a profile of reactive microglia (clusters 2, 3, 5, and 7; ***Figure 2C***, left plot and ***Figure 2—figure supplement 1C***). The cell distribution across condition highlighted that stroke is the main driver of the microglial transcriptomic changes, both in WT and *Rag1*$^{-/-}$ mice (***Figure 2C***, right plot). Volcano plots of the differentially expressed genes revealed that *Apoe* and *Cd74* were down- regulated in naïve *Rag1*$^{-/-}$ mice, indicating that the transcriptional profile of microglia is affected by the absence of lymphocytes in homeostatic condition (***Figure 2D***, left plot). Interestingly, several genes, known to define the signature of the disease- associated microglia (DAMs, Keren- Shaul et al., 2017), were up- regulated in *Rag1*$^{-/-}$ mice after stroke (*Apoe*, *Cd74*, *Cstb*, *Lgals3*, and *Lyz2*; ***Figure 2D***, right plot). When we compared the stroke-associated microglial genes between WT and *Rag1*$^{-/-}$ mice, we found that 67 genes – including the majority of the DAM signature (*Apoe*, *B2m*, *Cstb*, *Lgals3*, *Lyz2*, and *Spp1)* – were not specific to the lymphocyte deficiency (***Figure 2E***), whereas 120 stroke-associated microglial genes were only present in mice lacking lymphocytes, such as genes involved in cytokine signaling and chemotaxis (i.e. *Cd74*, *Ccl2*, *Ccl7*, *H2- Ab1*, *Infgr1*, *Mif*, *Pf4*, and *Tnf*).

The microglial reaction to stroke causes a gradual shift from the homeostatic transcriptomic profile to a reactive state. In order to capture differences in the microglia transcriptome along its transition phase, we performed single-cell trajectory inference analysis (***Figure 2—figure supplement 2***). Partition-based graph abstraction (PAGA) revealed two distinct paths with high connectivity from the homeostatic (naïve) microglia cluster (root cluster) to the reactive (stroke) microglia cluster (end cluster; ***Figure 2—figure supplement 2A***). Interestingly, the number of microglial cells in stroke *Rag1*$^{-/-}$ increased in the end cluster and was decreased along the trajectory path 2 in comparison to stroke WT (***Figure 2—figure supplement 2B***), suggesting that lymphocytes influence the transition of a microglia subpopulation from the homoeostatic to the reactive state. Differential gene expression analysis between the root and end clusters of the trajectory path 2 in WT and *Rag1*$^{-/-}$ mice (***Figure 2— figure supplement 2C***) revealed that genes associated with ribosomal metabolic processes and mitochondrial ribosomal proteins were specifically enriched, whereas genes associated with phagocytosis

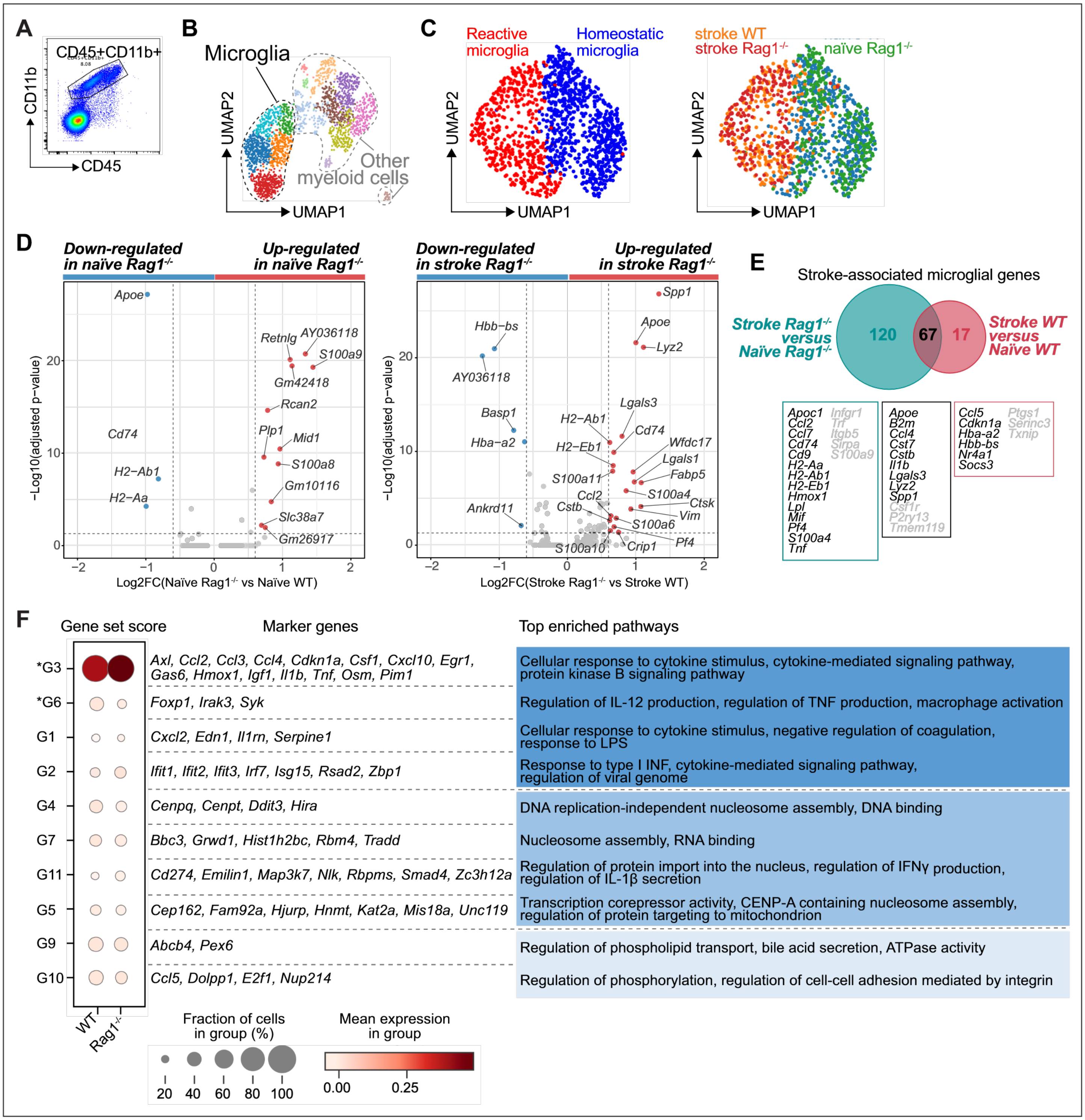

Figure 2. Lymphocytes influence microglia transcriptional signature. (**A**) CD45^{+}CD11b^{+} cells were sorted from the ipsilateral hemisphere in naïve mice or 5 days after stroke in wild- type (WT) and *Rag1*$^{-/-}$ (3 mice per condition), and RNA was isolated for single cell RNA sequencing (10× Genomics). (**B**) Uniform manifold approximation and projection 2D space (UMAP) plots of 2345 CD45^{+}CD11b^{+} cells colored by 15 distinct transcriptional clusters (***Figure 2—figure supplement 1A***). (**C**) Clustering of the microglia subset color-coded by homeostatic and reactive microglia (right) and by conditions (left). (**D**) Volcano plots of the differentially expressed genes in microglia in naïve and stroke condition. Dotted lines indicate an adjusted p- value≤0.05 and FC = 1.5. (**E**) Number of microglial genes regulated after stroke in comparison to naïve condition in *Rag1*$^{-/-}$ and WT mice. 67 genes were common to both genotypes, 17 genes were specifically regulated in WT mice and 120 genes only in *Rag1*$^{-/-}$ mice. Boxes indicate key microglial genes in each condition (genes indicated in gray were down- regulated after stroke). (**F**) Selected gene sets of highly correlated and anti- correlated genes *Figure 2 continued on next page*

Figure 2 continued

based on trajectory inference analysis in stroke condition (***Figure 2—figure supplement 2E–G***). Mean gene set activation score in WT and *Rag1*$^{-/-}$ cells, selected marker genes, and top enriched gene ontology pathways associated to each gene set. Gene sets were classified by p-value (the lowest p-value at the top, asterisks [*] indicate significant difference between genotype in stroke condition) and by similar pathways, such as: pathways related to inflammation (dark blue), pathways related to DNA/RNA regulation (blue), and lipid pathways (light blue).

The online version of this article includes the following figure supplement(s) for figure 2:

Figure supplement 1. Transcriptomic analysis of microglia isolated from wild-type (WT) and *Rag1*$^{-/-}$ mice in naïve and stroke conditions.

Figure supplement 2. Microglia single cell trajectory inference in wild- type (WT) and *Rag1*$^{-/-}$ mice in naïve and stroke conditions.

Figure supplement 3. Immune cell infiltration in wild- type (WT) and *Rag1*$^{-/-}$ mice after stroke.

were down- regulated in microglia of *Rag1*$^{-/-}$ mice (***Figure 2—figure supplement 2D***). We then clustered genes into groups of correlating and anti-correlating genes and investigated the activation of these gene sets along the identified trajectory path 2 in stroke condition only (***Figure 2—figure supplement 2E–G***). Gene sets which were significantly different between WT and *Rag1*$^{-/-}$ mice after stroke revealed that the absence of lymphocytes significantly reduces microglial genes associated with macrophage activation state (G6: *Foxp1*, *Syk* ***Shi et al., 2008***; ***Tabata et al., 2020***), whereas genes associated with cytokine/chemokine stimulus were enriched (G3: *Il1b*, *Tnf*, *Csf1*, and *Ccl2*) in *Rag1*$^{-/-}$ in comparison to WT microglia (***Figure 2F***). These results revealed that stroke is the primary driver of transcriptomic changes in microglia at this acute time point and that lymphocytes modulate the activation status of a subset of stroke-associated microglial cells associated with cytokine/chemokine regulation in the post-ischemic brain.

Because *Rag1*$^{-/-}$ mice lack mature T cells and B cells, it is possible that the observed morphological and transcriptional changes of microglia may be due to B cells or other myeloid cell types. We performed flow cytometry analysis of the ipsilesional hemisphere 5 days after dMCAO in WT and *Rag1*$^{-/-}$ mice. First, we demonstrate that T cells are 14 times more abundant than B cells in the ipsilesional hemisphere in WT mice (***Figure 2—figure supplement 3A***). In addition, the abundance of myeloid cell subsets is not affected by the Rag1 gene deletion (***Figure 2—figure supplement 3B***). These data support the hypothesis that lymphocytes and most likely T cells are the main contributor to the observed microglial phenotype at this time point after stroke. Because previous findings showed the CD4+ T cell subpopulations exert distinct effects during the post-stroke immune response (***Liesz et al., 2009***; ***Iliff et al., 2012***), we next determined whether functionally different T cell subsets induce or suppress genes in microglia related to cytokine production or cell migration as observed in ***Figure 2E, F***.

T$_{\mathrm{HELPER}}$ cell subpopulations drive the distinct polarization of microglia

To test whether microglial phenotypes can be specifically skewed by the CD4+ T cell subsets of functionally opposing T$_{\mathrm{HELPER}}$ cell subpopulations, we differentiated T$_{\mathrm{H1}}$ and T$_{\mathrm{REG}}$ in vitro (***Figure 3—figure supplement 1A***) and tested whether these T$_{\mathrm{HELPER}}$ cells can reprogram the stroke-associated microglia. Differentiated T cells or vehicle were injected into the cisterna magna (CM) of lymphocyte- deficient *Rag1*$^{-/-}$ mice 24 hr after stroke. Microglia cells CD45+CD11b+ were sorted from the ipsilesional hemisphere 24 hr after polarized T$_{\mathrm{HELPER}}$ cell (T$_{\mathrm{H1}}$ or T$_{\mathrm{REG}}$ cells) or vehicle administration (***Figure 3A***). The transcriptional profile of microglia induced by T$_{\mathrm{REG}}$ cells was more similar to vehicle treated *Rag1*$^{-/-}$ mice (named control [CT]) than microglial gene expression induced by T$_{\mathrm{H1}}$, as shown in the heatmap and volcano plots of the differentially expressed genes ($p<0.05$ and |fold change|>1.5) with 34 and 12 microglial genes regulated in T$_{\mathrm{H1}}$ or T$_{\mathrm{REG}}$ conditions compared to control injection, respectively (***Figure 3B, C***). Gene ontology analysis of the differentially up-regulated genes revealed T$_{\mathrm{H1}}$- dependent pathways associated with antigen presentation, response to cytokines, and regulation of type I INF, whereas T$_{\mathrm{REG}}$-dependent microglial genes were associated with chemotaxis (***Figure 3D***). These results demonstrate the potency of T cell subpopulations to differentially skew the microglial transcriptome toward distinct phenotypes previously associated with different cellular functions. In particular, we found that T$_{\mathrm{H1}}$ polarized microglia toward an antigen-immunocompetent phenotype (*Cd74* and *Lag3*) and expression of INF response- related genes (*Irf7* and *Stat1*). This profile of microglial response was previously associated with a pronounced immune response during the later stages of neurodegeneration (***Mathys et al., 2017***). In addition, after experimental stroke, the T$_{\mathrm{H1}}$- mediated effects on the

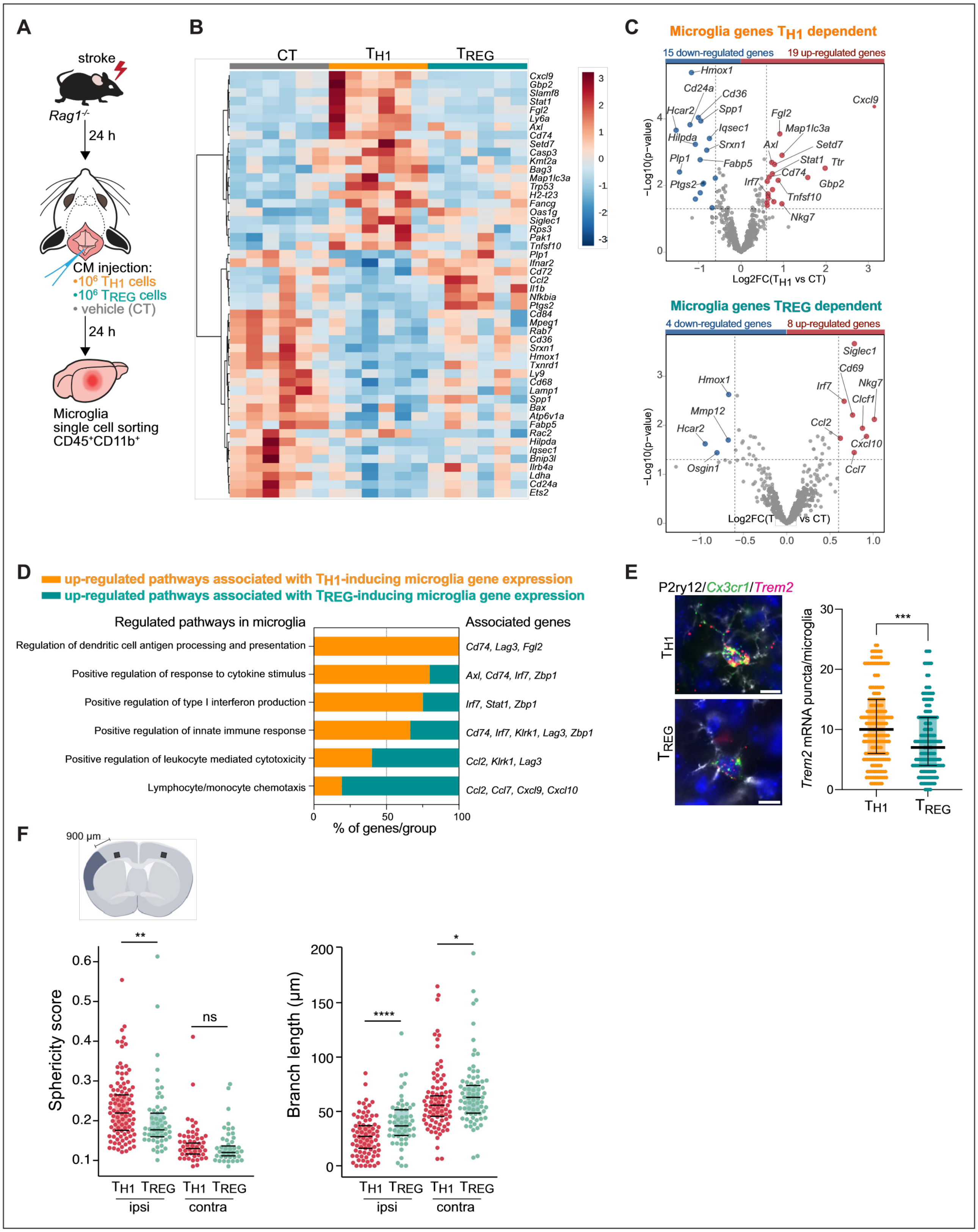

Figure 3. T_{H1} and regulatory T cells (T_{REG}) cells influence microglia gene expression after stroke. (**A**) Naïve CD4 cells were polarized in vitro to T_{H1} or T_{REG} phenotype (*Figure 3—figure supplement 1A*). One million cells (T_{H1} or T_{REG} cells) or vehicle (control, CT) were injected into the cisterna magna (CM) in *Rag1*$^{-/-}$ mice 24 hr after stroke induction (n=6 mice per condition). Microglia cells CD45+CD11b+ were sorted from the ipsilesional hemisphere, and RNA was extracted. Gene expression analysis was performed using the Neuroinflammation Panel profiling kit on the Nanostring platform. In a second

Figure 3 continued on next page

Figure 3 continued set of experiment, 100 µm coronal sections were proceeded for single- molecule fluorescence in situ hybridization (smFISH) or microglia morphology. (**B**) Heatmap representation of microglia gene expression between conditions: control (CT; vehicle administration of PBS), T_{H1} or T_{REG}. (**C**) Up- and down-regulated differentially expressed genes between either isolated microglia from T_{H1}- (top) and T_{REG}- (bottom) treated *Rag1*$^{-/-}$ mice relative to control condition (microglia isolated from *Rag1*$^{-/-}$ mice treated with vehicle, genes are color- coded accordingly to a p- value<0.05 and |fold change|>1.5). (**D**) Pathway analysis was performed for the up-regulated genes in each condition using the ClueGO package from Cytoscape. (**E**) Higher amount of *Trem2* mRNA puncta (red) per *Cx3cr1*-positive (green) in P2ry12- labeled microglia (white) in T_{H1}- treated mice in comparison the T_{REG}-treated mice. 4',6-Diamidin- 2- phenylindol (DAPI; blue) was used as nuclear dye. Scale bar = 10 µm. Each dot corresponds to one P2ry12-microglial cell; n=3 mice per condition; graphs show the median with interquartile range . (**F**) Morphological analysis of IBA1+ microglia in the ipsilateral (900 µm distal to the infarct border, cortical layer 4) and contralateral hemisphere, as shown in the representative coronal section. Sphericity score and branch length (µm) of microglia treated with T_{H1} (orange) or T_{REG} cells (green). Each dot corresponds to one microglial cells; ns, non significant; n=3 mice per condition. *, p<0.05; **, p<0.01; ****, p<0.0001. Wilcoxon rank sum test with continuity correction and Bonferroni post-hoc correction for multiple testing.

The online version of this article includes the following figure supplement(s) for figure 3:

Figure supplement 1. T cell polarization in vitro and infarct volumetry in *Rag1*$^{-/-}$.

microglial transcriptomic profile were associated with an increase of *Trem2* expression, a key marker of DAM in various brain disorders, in comparison to microglia primed by T_{REG} cells (***Figure 3E***). In contrast, T_{REG} cells promoted the expression of chemokines/cytokines in microglia (*Ccl2*, *Ccl7*, and *Cxcl10*), which can have either pro-regenerative or detrimental effects such as the regulation of leukocyte chemotaxis to the injured brain (***Llovera et al., 2017***), mechanisms of protective preconditioning (***Garcia- Bonilla et al., 2014***) or promoting neuronal stem cell recruitment and angiogenesis (***Andres et al., 2011***; ***Lee et al., 2012***; ***Liu et al., 2007***). Interestingly, this set of chemotactic genes induced by T_{REG} cells were also differentially expressed in microglia isolated from *Rag1*$^{-/-}$ mice in comparison to WT mice (***Figure 2E, F***), suggesting that the stroke associated microglia may lose their chemotactic properties in a T cell- dependent manner and especially a T_{REG} cell dependent (***Chen and Bromberg, 2006***). Because T_{REG} cells induce beneficial functions in cerebral ischemia (***Liesz et al., 2009***), it could be speculated that restoring microglial chemotactic behavior by T_{REG} cells could contribute to recovery. These transcriptomic differences in microglia related to the in vivo T_{H1} or T_{REG} cell exposure were also reflected by the difference in the morphology of microglia between these conditions. Microglia displayed a reactive state as shown by a more spherical and less branched morphology in T_{H1} cell- injected compared to T_{REG}- injected mice (***Figure 3F***) similarly to microglia in *Rag1*$^{-/-}$ mice (***Figure 1C, D***). Interestingly, these morphological changes were not only restricted to the ipsilesional hemisphere as seen in *Rag1*$^{-/-}$ not reconstituted with T cell subsets (***Figure 1D***) but were also observed in the contralateral hemisphere, suggesting possible brain- wide effects of differentiated T_{HELPER} cells injected to the CSF compartment. In accordance, we found that intra- CM injection of eGFP- labeled T_{H1} cells to *Rag1*$^{-/-}$ mice after stroke was primarily recruited to the ischemic brain parenchyma but was additionally localized in border tissues including the meninges, and some CM- injected cells even circulated and could be detected in the spleen (***Figure 4A, B*** and ***Figure 4—figure supplement 1***). Importantly, no difference in infarct volumes was observed between WT and *Rag1*$^{-/-}$ mice (***Figure 3— figure supplement 1B***) and in T_{H1} or T_{REG}- supplemented *Rag1*$^{-/-}$ mice (***Figure 3—figure supplement 1C***), suggesting the transcriptional changes observed in microglia are primarily due to T cell subsets and not biased by differences in stroke severity. Together, these findings support that polarized T cells are recruited to the infarction site and may modify in situ the inflammatory micromilieu.

Engineered T cells overexpressing IL-10 induce a pro-regenerative transcriptomic profile in microglia

In order to further explore the implication of T_{REG}- microglia interactions to modulate the post- stroke inflammatory environment, we tested the therapeutic potential of the known anti- inflammatory properties of T_{REG} via IL10 on the local microglial immune milieu. We engineered T cells by viral transfection to overexpress the anti-inflammatory cytokine IL- 10 (eTc- IL10; ***Figure 4—figure supplement 1B, C***). In a therapeutic approach, we injected eTc- IL10 cells into the CM of WT mice 4 hr after stroke – a translationally relevant time window considering a similar time window for acute therapy with thrombolytics in stroke patients (***Figure 4C***). We investigated whether eTc-IL10 treatment affected stroke outcome but did not find any difference in infarct volumes between conditions (***Figure 4D***). This is in accordance with the concept of early ischemic lesion formation in stroke which is not being affected

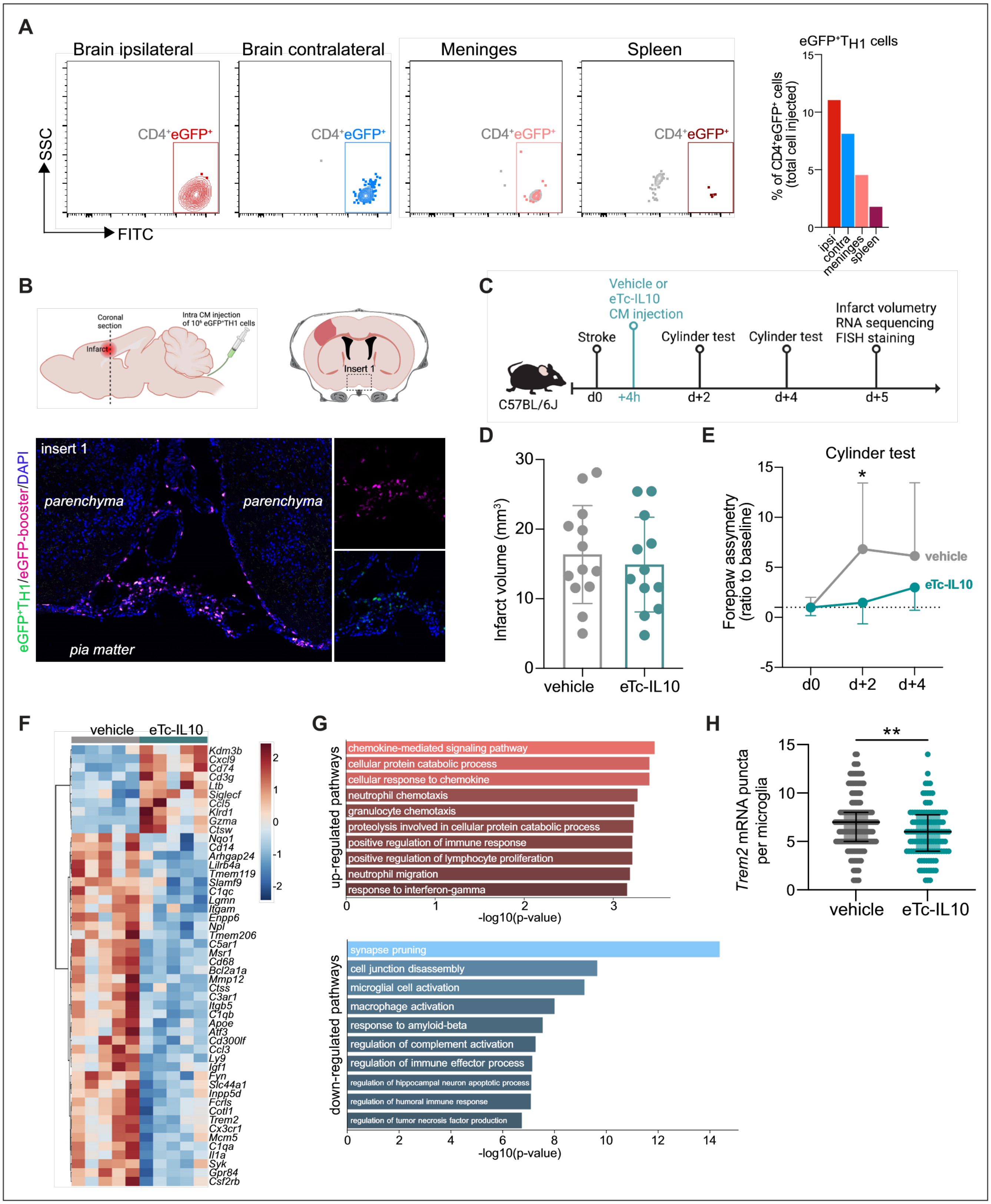

Figure 4. Acute post- stroke treatment with engineered T cells overexpressing IL- 10 modulates microglial activation and ameliorates functional deficit. (**A and B**) Flow cytometry analysis and whole skull- brain coronal sections of 10^6 eGFP+T$_{H1}$ cells injected into the cisterna magna (CM) of *Rag1*$^{-/-}$ mice 24 hr after stroke. Samples were collected 4 hr after CM injection for further analysis. (**A**) Flow cytometry plots showing CD4+eGFP+ cells isolated from the brain (ipsilateral and contralateral hemispheres), meninges, and spleen (the detailed gating strategy is shown in ***Figure 4—figure supplement 1A***).

Figure 4 continued on next page

Figure 4 continued

The graph represents the percentage of eGFP+T_{H1} cells relative to the total number of cells injected in the CM (10^6 eGFP+T_{H1} cells). (**B**) Coronal section showing eGFP+T_{H1} cells in the meninges. Insert 1 indicates a representative photomicrograph of eGFP+T_{H1} cells counterstained with an eGFP- booster (magenta), and cell nuclei are stained with 4',6- Diamidin-2- phenylindol (DAPI; blue). The magnified images of white boxed area show eGFP+T_{H1} cells injected into the CM are located in the meninges. (**C**) Timeline of the experimental design. (**D**) Infarct volumes at 5 days after stroke in wild-type (WT) C57BL/6 J mice treated by CM administration of either T cells secreting IL- 10 (eTc- IL10, 10^6 naïve CD4+) cells transfected with a plasmid overexpressing IL- 10, ***Figure 4—figure supplement 1B, C***, **d** or vehicle (aCSF) 4 hr after stroke induction. (**E**) Percentage of assymetry in independent forepaw use ('0%' indicates symmetry) in mice treated with vehicle or eTc- IL10; *, $p<0.05$, ANOVA with Šídák's multiple comparisons test; n=12–13 mice per condition. (**F**) Heatmap representation of ipsilateral brain gene expression between vehicle and eTc- IL10 treated mice 5 days after stroke; n=5 mice per condition; one sample per condition was excluded due to unsatisfactory quality control check. (**G**) Selected gene ontology annotations for the 50 genes that were up- (top) and down- regulated (bottom) in the whole ipsilateral brain tissue of eTc- IL10 treated mice in comparison to vehicle treated mice. (**H**) Single- molecule fluorescence in situ hybridization (smFISH) analysis of brains from eTc- IL10 treated mice showed a reduction of *Trem2* mRNA puncta per *Cx3cr1*-positive microglia in the peri- infarct region in comparison to vehicle treated mice; **, $p<0.01$, Mann- Whitney U test; each dot corresponds to one microglial cell; n=3 mice per condition; graphs show the median with interquartile range.

The online version of this article includes the following figure supplement(s) for figure 4:

Figure supplement 1. Localization of polarized T cell and IL-10 plasmid construct.

by the delayed immunological mechanisms (***Dirnagl et al., 1999***). In contrast, mice receiving eTc- IL10 injection in the CM had a significant improvement of functional outcome at 48 hr after stroke as shown by a reduced forelimb asymmetry in comparison to vehicle-treated mice (***Figure 4E***). This might reflect the implication of inflammatory pathways and specifically cytokine secretion on functional deficits and delayed recovery after stroke in contrast to the early primary lesion development (***Filiano et al., 2017***; ***Roth et al., 2020***). We then evaluated whether gene expression was altered after stroke upon eTc-IL10 treatment. RNA was isolated from the whole ischemic hemisphere, and neuroinflammatory genes were quantified using the Nanostring platform. Interestingly, we found that several genes associated with a DAM profile were down-regulated in mice treated with eTc-IL10 such as *Cd68*, *Apoe*, *Trem2*, *Tyrobp*, and *Cst7* (***Figure 4F*** and ***Figure 4—figure supplement 1D***). Gene ontology analysis revealed that T cell-derived IL-10 overexpression increased pathways associated with chemokine responses – similarly to *Rag1*$^{-/-}$ mice reconstituted with T_{REG} cells – and the down- regulation of several microglial effector functions such as spine pruning, phagocytosis, and complement activation (***Figure 4G***). Although the observed regulated genes are well known to be associated with microglial function, it is conceivable that in this analysis, other cell types than microglia, including various brain- invading myeloid cell subsets, could account for this effect since the whole ischemic brain tissue was processed for Nanostring analysis. This anti-inflammatory effect of eTc-IL10 treatment on microglia was confirmed by a reduction of *Trem2* mRNA in *Cx3cr1*+microglia from eTc-IL10 compared to vehicle- treated mice (***Figure 4H***). Since we observed a down regulation of genes associated with synapse pruning (*C1qa*, *C1qb*, and *C1qc*), microglia activation, and phagocytosis (*Apoe*, *Ctss*, *Trem2*, and *Cd68*) in mice treated with eTc-IL10, we postulate that acute intra- CM administration of eTc- IL10 induces a switch of the microglia gene signature possibly involved in promoting post-stroke recovery mechanisms.

Discussion

The cellular constituents of the acute neuroinflammatory response to stroke have been well characterized, including microglial activation, leukocyte invasion, and the contribution of different lymphocyte subpopulation (***Anrather and Iadecola, 2016***). However, the reciprocal interactions of these different immune cell populations remain largely under- investigated in the context of brain injury. A better understanding of the T cell- polarizing effect on microglial function has strong translational implication since T cells may act as a 'Trojan horse' with large impact on the cerebral inflammatory milieu potentiated by microglia (***Cramer et al., 2018***).

Here, we established a mechanistic link between T cells and microglial morphology and transcriptomic signature in the context of stroke. We showed the distinct role of T cell subpopulations on switching microglial polarization state in response to stroke. Our results from transcriptomic analysis suggest that the microglia-polarizing effect of different T_{HELPER} cell subpopulations is mainly mediated via their specific cytokine/chemokine secretion pattern. Microglia that were challenged with T_{H1} cells expressed an up-regulation of genes associated with type I INF signaling – the key cytokine secreted by the T_{H1} subpopulation. In contrast, T_{REG} cells modulated a gene set in microglia associated with chemotaxis- mediated mechanisms (*Ccl2*, *Ccl7*, and *Cxcl10*). Although it remains to be defined whether microglia primed by T_{REG} cells contribute to the recruitment of other immune cells, especially of T_{REG} cells inducing neuroprotective mechanisms. We also observed that T_{REG} cells mediate a down-regulation of markers associated with reactive microglia such as the expression of *Trem2*, which have previously been described to be regulated by the T_{REG}-cytokine IL- 10 (***Shemer et al., 2020***). These previous and our own results here clearly show the direct role of IL- 10 in modulating microglial function. Likewise, using adult human microglial cells co- culture with T lymphocytes, others demonstrated an enrichment of IL- 10 secretion upon direct cell- cell contact (***Chabot et al., 1999***). In addition, we previously reported using whole genome sequencing that intracerebroventricular injection of IL-10 is sufficient to modulate the neuroinflammatory response after experimental stroke (***Liesz et al., 2014***). However, we cannot exclude in this study the contribution of IL- 10 from other lymphocyte subpopulations, particularly IL- 10-producing regulatory B cells (***Bodhankar et al., 2013***; ***Ortega et al., 2020***; ***Seifert et al., 2018***), as we did not specifically deplete IL- 10 in T cells.

An important caveat and potential key reason for the so far still pending success in harnessing the therapeutic function of IL-10 are its short half-life (less than 1 hr) and limited bioactivity after in vivo administration as a recombinant protein (***Le et al., 1997***; ***Saxena et al., 2015***). Moreover, the systemic IL-10 application can have considerable and unforeseen side- effects due to the potentially divergent function of IL- 10 on inflamed and homeostatic tissue, including direct effects on neurons, astrocytes, endothelial cells, and other cellular constituents of physiological brain function (***Saraiva et al., 2019***). Therefore, we aimed to take a different approach for the localized and sustained production of IL-10 at the inflamed peri-lesional brain parenchyma. For this, we took advantage of the potent capability of T cells to be specifically recruited and accumulated to the ischemic lesion site in order to deliver IL- 10 from genetically engineered IL-10- overexpressing T cells (***Heindl et al., 2021***; ***Llovera et al., 2017***). We demonstrated that IL-10 overexpression by this approach substantially modulated microglia gene expression by down- regulation of microglial gene signature associated with phagocytosis of synapses correlating with functional recovery after stroke. Interestingly, eTc-IL10 cells did not exclusively invade the injured brain but were also located in the meningeal compartment and could additionally contribute to functional recovery by resolving inflammation at these border structures or providing IL-10 to the brain parenchyma along CSF flow. This concept is in accordance with previous observations of meningeal immune cell accumulation after stroke (***Benakis et al., 2018***) and that meningeal T cell- derived cytokines may enter the brain via CSF flow and paravascular spaces (***Iliff et al., 2012***).

An important finding in this study was the observation that IL-10 overexpression in T cells modulated microglial genes involved in the complement pathway, phagocytosis, and synaptic pruning and was associated with a better functional outcome after stroke. Complement factors are localized to developing CNS synapses during periods of active synapse elimination and are required for normal brain wiring (***Schafer et al., 2012***). Inactive synapses tagged with complement proteins such as C1q may be eliminated by microglial cells. Likewise in the mature brain, early synapse loss is a hallmark of several neurodegenerative diseases (***Stephan et al., 2012***). Indeed, complement proteins are profoundly up-regulated in many CNS diseases prior to signs of neuron loss, suggesting mechanisms of complement-mediated synapse elimination regulated by microglia potentially driving disease progression (***Stephan et al., 2012***) and stroke recovery. It is therefore conceivable that T cells overexpressing IL-10 down-regulate the complement system in microglia and prevent excessive elimination of synapse and consequently protect against neuronal dysfunction. This is particularly of interest because microglia effector function has not only been associated with inflammatory neurodegenerative processes but recently also been shown to be neuroprotective (***Szalay et al., 2016***) by tightly monitoring neuronal status through somatic junctions (***Cserép et al., 2020***). Microglia interact with the extra- neuronal space by not only regulating the elimination of existing synapses but also by modifying the extracellular matrix to enable efficient synaptic remodeling (***Zaki and Cai, 2020***). Accordingly, we found T cell- dependent regulation of several microglial genes that can mediate such extracellular matrix modifications involved in phagocytosis and proteases (*Clstn1* and *Mmp12*, cathepsins and MMPs, respectively).

Whereas at this acute time point, the transcriptomic changes in microglia are mainly attributed to their reactivity to the tissue injury itself, we have been able to demonstrate that brain- invading T cells can specifically ‘fine- tune’ the transition of the stroke- associated microglia to a distinct cell morphology and transcriptomic profile. Our data suggested that the anti-inflammatory T_{REG} cells induce a shift of microglial genes associated with a homeostatic state and immune cell recruitment. However, the specific functional change of microglia induced by T cell subsets and biological significance for stroke remain to be further investigated. We postulate that the development of engineered T cells could have important translational implication by targeting a specific effector function of microglia with a relevant impact on the chronic progression of stroke pathobiology.

Materials and methods

Animal experiments

All animal procedures were performed in accordance with the guidelines for the use of experimental animals and were approved by the respective governmental committees (Licenses: 02- 21- 46 and 02- 21- 95; Regierungspraesidium Oberbayern, the Rhineland Palatinate Landesuntersuchungsamt Koblenz). Male WT C57BL6/J mice were purchased from Charles River, *Rag1*$^{-/-}$ mice (NOD.129S7[B6]Rag-1 tm1Mom/J) and eGFP-reporter mice (C57BL/6- Tg[CAG- EGFP]131Osb/LeySopJ) were bred and housed at the animal core facility of the Center for Stroke and Dementia Research (Munich, Germany). All mice were housed with free access to food and water at a 12 hr dark- light cycle. Data were excluded from all mice that died during surgery. Animals were randomly assigned to treatment groups, and all analyses were performed by investigators blinded to group allocation. All animal experiments were performed and reported in accordance with the ARRIVE guidelines (***Kilkenny et al., 2011***).

Permanent distal middle cerebral artery occlusion model

Permanent coagulation of the middle cerebral artery (MCA) was performed as previously described (***Llovera et al., 2014***). Briefly, animals (male; age = 8–12 weeks) were anesthetized with volatile anesthesia (isoflurane in 30%O_2/70%N_2O) and placed in lateral position. After a skin incision between eye and ear, the temporal muscle was removed, and the MCA was identified. Then, a burr hole was drilled over the MCA, and the dura mater was removed. The MCA was permanently occluded using bipolar electrocoagulation forceps. Permanent occlusion of the MCA was visually verified before suturing the wound. During the surgery, body temperature was maintained using a feedback-controlled heating pad. Mice that developed a subarachnoid hemorrhage during surgery were excluded from the analysis.

Cylinder test

To evaluate forepaw use and asymmetry, the cylinder test was performed 2 days prior to stroke (baseline) and day 2 and day 4 post stroke. Mice were placed in a transparent acrylic glass cylinder (diameter 8 cm; height: 25 cm) in front of two mirrors and videotaped. To assess independent forelimb use, contact with one forelimb (left and right forelimbs) during full rearing and landing performance of mice was scored by frame-to- frame analysis of recorded videos. Mice with forepaw preference at baseline (absolute value difference between right and left forepaws >10) were excluded from the analysis. All rearing movements during the trial were counted and used as indication of the animal's overall activity.

Intra-CM injection

Mice were anesthetized with isoflurane in 30%O_2/70%N_2O and fixed in a stereotaxic frame by the zygomatic arch, with the head slightly tilted to form an angle of 120° in relation to the body. A small incision was made at the nape of the neck between the ears to expose the neck muscles, which were bluntly dissected to expose the CM. Cannulas composed of a glass capillary (ID, inner diameter 0.67 mm; OD, outside diameter, 1.20 mm) attached to a polyethylene tubing (ID 0.86 mm and OD 1.52 mm; Fisher Scientific UK Ltd.) were used to perform the CM injections. Glass capillaries were sharpened using a flaming micropipette puller (P- 1000, Sutter Instrument GmbH), filled with 10 µL of the cell suspension diluted in artificial CSF (aCSF: 126 mM NaCl, 2.5 mM KCl, 1.25 mM NaH_2PO_4, 2 mM Mg_2SO_4, 2 mM $CaCl_2$, 10 mM glucose, and 26 mM $NaHCO_3$; pH 7.4 when gassed with 95% O_2 and 5% CO_2), and fixed to the micromanipulator arm of the stereotaxic. Cell suspension was injected into the CM at a rate of 2 µL/min. At the end of the injection, mice are sutured and allowed to recover in a preheated awake cage for 1 hr, after which they are returned to the animal husbandry.

In vivo depletion of microglia

For microglia depletion, WT and *Rag1*$^{-/-}$ mice were fed a chow diet containing the CSF1 receptor antagonist, PLX5622 (1200 ppm PLX5622 in mouse chow, Brogaarden Research Diets) for 2 weeks to induce microglia apoptosis. Mice of the control group were fed control chow diet without the antagonist.

Infarct volume quantification

Mice were deeply anesthetized 5 days after stroke induction and transcardially perfused with 20 mL saline. Brains were removed, frozen immediately on powdered dry ice, and stored at −20°C until use. For infarct volumetry, brains were serially sectioned (400 #m intervals, 20 #m thick) and stained for cresyl violet (CV) as previously described (***Llovera et al., 2014***). CV-stained sections were scanned at 600 dpi on a fatbed scanner (Canon). Direct infarct measurement was used after validating the absence of edema at the investigated time point. The total infarct volume was measured with ImageJ and determined by integrating measured areas and distances between sections.

Immunohistochemistry and confocal microscopy

Microglia morphology analysis was performed on brain coronal sections as previously described (***Heindl et al., 2018***). Briefly, mice were perfused with 4% paraformaldehyde (PFA), and brains were post- fixed overnight and placed in sucrose for dehydration. Then, free floating 100 µm coronal sections were stained for microglia with 1:200 anti- Iba1 (rabbit, Wako, #019–19741). Nuclei were stained using 4′,6- Diamidin- 2- phenylindol (DAPI, Invitrogen, #D1306), and images were acquired at a distance of 900 #m from the border of the lesion in layer 4 (ipsilateral) and the homotypic contralateral region using a Zeiss confocal microscope with 40× magnification (objective: EC Plan-Neofluar 40 ×/1.30 Oil DIC M27) with an image size of 1024×1024 pixel, a pixel scaling of 0.2×0.2 #m, and a depth of 8 bit. Confocal images were collected in Z-stacks with a slice- distance of 0.4 #m. Morphological features of microglia were acquired using a fully automated analysis as previously described (***Heindl et al., 2018***).

Fluorescent in situ hybridization

Single-molecule fluorescence in situ hybridization (smFISH) was performed using the RNAscope Multiplex Fluorescent Reagent Kit v2 (Advanced Cell Diagnostics) by the manufacturer's protocols. Briefly, free floating 100 µm coronal brain sections (***Figure 3e***) or 20 µm cryo-sections (***Figure 4g***) were first dried, washed, and then incubated in RNAscope hydrogen peroxide. Antigen retrieval and protease treatment were performed as per protocol. Sections were then incubated with the probe mix (C2-*Trem2* and C1-*Cx3cr1*) for 2 hr at 40°C and then immediately washed with wash buffer. Next, sections were incubated with RNAscope Multiplex FL v2 AMP1, AMP2, and AMP3 and then probes were counterstained with TSA Plus Cy3 for C1-*Cx3cr1* and TSA Plus Cy5 for C2-*Trem2*. For microglia identification (***Figure 3e***), slides were incubated in blocking at room temperature for 1 hr before overnight incubation at 4°C with the primary rabbit anti-P2Y12 receptor antibody (1:200, AnaSpec #AS-55043A) and labeling for 1 hr with the secondary antibody AF488 goat anti-rabbit, (1:200, Invit rogen #A11034). Finally, sections were stained with DAPI (Invitrogen) and mounted with fluoromount medium (Sigma). smFISH-stained RNA molecules were counted only within the DAPI staining of the cell; a cell was considered *Cx3cr1*-positive when more than four *Cx3cr1* puncta were present.

Whole skull immunofluorescence

Rag- $1^{-/-}$ mice were anesthetized with isoflurane and perfused transcardially with ice-cold PBS followed by 4% PFA. After removing the mandibles, skin and muscles were carefully detached from the skull (http://www.nature.com/protocolexchange/protocols/3389). The skull decalcification was performed as previously described (***Benakis et al., 2016***). Coronal skull sections (20 #m) were stained with GFP- booster Atto647N (1:500, ChromoTek GmbH) to visualize eGFP-labeled T cells. Sections were counterstained with DAPI (Invitrogen) to visualize cell nuclei and observed by confocal laser microscopy (Leica SP5).

In vitro T cell polarization

Single- cell suspensions were generated from spleen, inguinal, axial, brachial, and mandibular lymph nodes of C57BL/6 or b-actin- EGFP mice by passing the tissue through a 70 cm cell strainer. Naive CD4+ T cells were obtained by pre- enrichment using an 'untouched' CD4+ T Cell Isolation Kit (Miltenyi Biotec) with subsequent flow cytometric analysis (CD4+ [clone RM4-5, 0.5 ng/µL], CD44low [clone IM7, 2 ng/µL], and CD62Lhigh [MEL-14, 0.8 ng/µL]). Cells were seeded at a density of 300,000 or 400,000 cells/well in a flat-bottom 96- well plate and stimulated with plate- bound anti- CD3 and anti- CD28 Abs 0.5 µg/mL or 2 µg/mL anti- CD3 (clone 145–2 C11) for T_{REG} and T_{H1}, respectively and 2 µg/mL anti-CD28 (clone 37.51). Different mixtures of cytokines and mAbs were added to RPMI (supplemented with 10% fetal calf serum (FCS), 50 µM β-mercaptoethanol, 50 U/mL penicillin, 50 µg/ mL streptomycin, 1% GlutaMAX, and 1% N-2- hydroxyethylpiperazine- N-2- ethane sulfonic acid [Gibco HEPES]) and used as follow: T_{H1} conditions with anti-IL- 4 (10 µg/mL, BioXCell, #BE0045) and IL-12 (10 ng/mL, BioLegend, #577002); T_{REG} conditions: anti–IL-4 (10 µg/mL, BioXCell, #BE0045), anti-IFN- γ (10 µg/mL, BioXCell, #BE0055), and TGFβ (3 ng/mL, BioLegend, #580702). After 2 days in culture, cells were split into two new 96-well plates and incubated with freshly prepared supplemented RPMI media with IL- 2 (10 ng/mL, BioLegend, #575402). Cells were cultured for a total of 5 days before injection. Quality control was performed on day 4 to assess the percentage of T cell expressing Tbet (clone 4B10, 2 ng/µL; T_{H1}) or FoxP3 (clone FJK- 16s, 2 ng/µL; T_{REG}; ***Figure 3—figure supplement 1A***). One million differentiated T cells were resuspended in sterile aCSF and injected into the CM in *Rag1*$^{-/-}$ recipient mice 24 hr after dMCAO induction.

IL-10 overexpression in naïve T cells

Engineered T cells overexpressing IL- 10 (eTc- IL10) were generated by transfection of naïve T cells with an IL- 10 plasmid (pRP[Exp]-TagBFP2-CMV>mIl10[NM_010548.2]) designed and prepared by Vector Builder (***Figure 4—figure supplement 1B***). First, splenocytes were isolated from C57BL/6 mice (male, 6–12 weeks old) and enriched using a CD4+ T Cell Isolation Kit (Miltenyi Biotec, No:130-104- 453). Quality control was performed by flow cytometry (CD4+ [clone RM4- 5, 1:25], CD44low [clone IM7, 1:25], and CD62Lhigh [clone MEL- 14, 1:25]). Cells were resuspended in RPMI (supplemented with 10% fetal bovine serum (FBS), 50 µM β-mercaptoethanol, 50 U/mL penicillin, 50 µg/mL streptomycin, 1% GlutaMAX, and 1% HEPES and 10 ng/mL IL-2) . To induce CD4+ cells to enter the cell cycle for efficient DNA uptake, 4#10^{5} cells/well were seeded in a flat- bottom 96-well plate containing bound anti-CD3 (2µg/mL, clone 145–2 C11) and anti-CD28 (2 µg/mL, clone 37.51) for 48 hr. After 48 hr stimulation, 1.5#10^{6} cells multiplied by the number of mice to be injected were transfected with the pIL-10 vector (1#10^{6} cells/1.5 µg pIL- 10 DNA per cuvette) using the Mouse T Cell Nucleofector Kit (Lonza, No: VPA- 1006) with Nucleofector II Device (program X- 100). Once electroporated, cells were diluted with conditioned RPMI from the 48 hr stimulation and fresh supplemented RPMI (1:1) and seeded in a 12- well plate (1 cuvette of cells/ well). 24 hr post transfection, cells and supernatant were collected. Supernatant was used to confirm IL-10 secretion by ELISA (***Figure 4—figure supplement 1C***), and cells were collected for intra- CM injection (1#10^{6}/mouse).

ELISA

Secreted IL- 10 was determined by ELISA as per the manufacturer’s protocol (Mouse IL- 10, Invitrogen, No: 88- 7105- 88). The color reaction was measured as OD450 units on a Bio-Rad iMark microplate reader. The concentration of supernatant IL-10 was determined using the manufacturer’s standard curve over the range of 32–4000 pg/mL.

Flow cytometry

For differentiation of live and dead cells, we stained cells with the Zombie Violet Fixable Viability Kit according to the manufacturer’s instructions (BioLegend). For surface marker analysis, cell suspensions were adjusted to a density of 0.5#10^{6} cells in 50 µL FACS buffer (2% FBS, 0.05% NaN_3 in PBS). Nonspecific binding was blocked by incubation for 10 min at 4°C with anti- CD16/CD32 antibody (Biolegend, clone 93, 5 ng/ µL) antibody and stained with the appropriate antibodies for 15 min at 4°C. The following antibodies were used for extracellular staining: CD45 (clone 30 F- 11, 0.5 ng/µL), CD4 (clone RM4- 5, 0.5 ng/µL), CD11b (clone M1/70, 0.6 ng/µL), CD19 (eBio1D3, 0.6 ng/µL), B220 (clone RA3- 6B2, 0.32 ng/µL), CD3ε (clone 145–2 C11, 2 ng/µL), CD8a (clone 53–6.7, 2 ng/µL), and CD62L (clone MEL- 14, 0.8 ng/µL) from Thermofisher. For intracellular cytokine staining, cells were restimulated for 4 hr with PMA (50 ng/mL, Sigma), ionomycin (1 µM, Sigma), and brefeldin A (1 µL for ~10^{6} cells/mL). Cells were then stained for surface markers as detailed below, fixed, and permeabilized using Fixation and Permeabilization Buffers from eBiosciences following the manufacturer’s instructions. Briefly, cells were fixed for 30 min at 4°C (or RT for FoxP3), washed with permeabilization buffer, and incubated for 30 min with the appropriate antibodies in permeabilization buffer at 4°C (or RT for FoxP3). The cells were stained with the transcription factors FoxP3 (clone FJK-16 s, 2 ng/µL) and T- bet (clone 4B10, 2 ng/µL) or IFN-γ (clone 4 S.B3, 2 ng/µL). Cells were washed with FACS buffer, resuspended in 200 µL of FACS buffer and acquired using a BD FACSverse flow cytometer (BD Biosciences, Germany), and analyzed using FlowJo software (Treestar, USA). Isotype controls were used to establish compensation and gating parameters.

Nanostring analysis

The ipsilateral hemispheres were lysed in Qiazol Lysis Reagent, and total RNA was extracted using the MaXtract High Density kit with further purification using the RNeasy Mini Kit (all Qiagen). 70 ng of total RNA per sample was then hybridized with reporter and capture probes for nCounter Gene Expression code sets (Mouse Neuroinflammation codeset) according to the manufacturer's instructions (NanoString Technologies). Samples (6/condition) were injected into NanoString cartridge, and measurement run was performed according to nCounter SPRINT protocol. Background (negative control) was quantified by code set intrinsic molecular color-coded barcodes lacking the RNA linkage. As a positive control code set, intrinsic control RNAs were used at increasing concentrations. Genes below the maximal values of the negative controls were excluded from the analysis. All gene counts were normalized (by median) and scaled (mean- centered and divided by SD of each variable). Heatmaps were performed using the MetaboAnalystR package on normalized expression values. The regulated genes in microglia treated with T_{H1} or T_{REG} in comparison to vehicle treated microglia (CT) are represented in the volcano plots; genes with a p<0.05 were color-coded. The significantly up- reg ulated genes in microglia (FC>1.5 and p<0.05) were further used for pathway analysis using Cytoscape ClueGO (***Bindea et al., 2009***): T_{H1}/CT, 19 up-regulated genes (*Axl*, *Cd74*, *Cryba4*, *Cxcl9*, *Ezh1*, *Fgl2*, *Gbp2*, *Klrk1*, *Irf7*, *Klrk1*, *Lag3*, *Map1lc3a*, *Nkg7*, *Pld2*, *Setd7*, *Siglec1*, *Stat1*, *Tnfsf10*, *Ttr*, and *Zbp1*) and T_{REG}/CT, 8 up- regulated genes (*Ccl2*, *Ccl7*, *Cd69*, *Clcf1*, *Cxcl10*, *Irf7*, *Nkg7*, and *Siglec1*).

Microglia cell isolation for RNA sequencing

Mice were perfused transcardially with ice- cold saline containing Heparin (2 U/mL). Brains were placed in HBSS (w/ divalent cations Ca^{2+} and Mg^{2+}) supplemented with actinomycin D (1:1000, 1 mg/mL, Sigma, #A1410), and microglia was isolated with the Papain- based Neural Tissue Dissociation Kit (P) (# 130-092- 628, Miltenyi Biotec B.V. & Co. KG) according to the manufacturer's instructions. Cell suspension was enriched using 30% isotonic Percoll gradient. 1#10^3–1.5#10^3 live microglia cells from 3 mice per condition were sorted according to their surface marker CD45+CD11b+7-AAD negative (SH800S Cell Sorter, Sony Biotechnology) and proceed for 10# Genomics according to the manufacturer's instructions (ChromiumTM Single Cell 3' Reagent kits v2).

Single-cell data analysis

The CellRanger software (v2.0.0, 10# Genomics) was used for demultiplexing of binary base call files, read alignment, and filtering and counting of barcodes and unique molecular identifiers (UMIs). Reads were mapped to the mouse genome assembly reference from Ensembl (mm10/GRCm38). Downstream data analyses were performed using the Scanpy API (scanpy v ≥ 1.4 with python3 v ≥ 3.5; ***Wolf et al., 2018***). Details on analyses, selected thresholds, and package versions are provided in available source scripts (See Code and Data availability). Outlier and low-quality cells were filtered if the fraction of mitochondria- encoded counts was greater than 10%, or the total number of counts was greater than 48,000. Thresholds were selected upon visual inspection of distributions as recommended (***Luecken and Theis, 2019***). Genes expressed in less than 10 cells were excluded. Furthermore, doublet cells as identified by the Scrublet algorithm (v0.2.1; ***Wolock et al., 2019***) were excluded. Doublet scores and thresholds were determined for each sample separately. Raw counts of a cell were normalized by total counts neglecting highly expressed genes which constitute more than 5% of total counts in that cell. Then, counts were log-transformed (log[count+1]). These processed and normalized count matrices were used as input for all further analyses.

For the full data set and the microglia subset, first a single- cell nearest- neighbor graph was computed on the first 50 independent principal components. Principle components were calculated using the 3000 most variable genes of the full data set as input. The UMAP algorithm (***Becht et al., 2019***) as used to obtain a two- dimensional embedding for visualization. Iterative clustering was performed with the Louvain algorithm (***Blondel et al., 2008***) as implemented in louvain-igraph (v0.6.1, Traag et al., https://github.com/vtraag/louvain-igraph) with a varying resolution parameter. Clusters were annotated using previously described marker genes and merged if expressing the same set of marker genes. For ***Figure 2d and e***, data were converted into a Seurat object and further analyzed in R to identify differentially expressed genes between WT and *Rag1*$^{-/-}$ samples in stroke and naïve conditions (Seurat package, version 4.2.0 ***Hao et al., 2021***). Gene dataset associated with microglia subsets was submitted to log- normalization, identification of high- variable genes using the mean- variance plot (MVP) method, scaling, and regression against the number of UMIs and mitochondrial RNA content per cell. Data was further subjected to unsupervised clustering and embedded using UMAP. Differentially expressed genes between WT and *Rag1*$^{-/-}$ samples in stroke and naïve conditions were calculated using the FindMarkers function. Volcano plots were created using EnhancedVolcano in R (***Blighe et al., 2022***). To obtain the Venn diagram, the significantly regulated genes (adjusted p- value<0.05) with a fold change of 1.5 (Log2FC = 0.6) – excluding Gm genes, mitochondrial and ribosomal genes (*Mrpl*, *Mrps*, *Rpl*, and *Rps*) – were included in the analysis. The differentially expressed genes that were regulated after stroke in comparison to naïve condition WT or *Rag1*$^{-/-}$ included 84 genes and 187 genes, respectively.

Trajectories from homeostatic to reactive microglia were inferred with PAGA (***Wolf et al., 2018***) and diffusion pseudotime (DPT; ***Haghverdi et al., 2016***) algorithms. First, clusters were grouped into two paths connecting the root and end cell cluster based on the computed cluster connectivities (PAGA), then cells were ordered along these paths based on the random- walk- based cell- to- cell distance (DPT). To capture processes specific to the path 2 trajectory in stroke-associated microglia, data was first subset to cells of path 2 and end cells clusters of stroke samples and gene expressed in less than 20 cells of the subset excluded. Then, gene sets were computed by clustering the 500 most varying genes using their pairwise- Pearson correlation values as input and Ward's hierarchical clustering method with Euclidean distance (scipy python package v.1.5.4; ***Virtanen et al., 2020***). One gene set with average correlation <0.05 was excluded. Finally, to obtain an activation score per cell for a given gene set, cell scores were computed as described by ***Satija et al., 2015*** and implemented in Scanpy in the *tl.score_genes* functionality. Differential activation of gene sets between WT and *Rag1*$^{-/-}$ samples was determined by a Wilcoxon rank sum test. To identify genes differentially regulated along the inferred cellular trajectory, a differential gene expression test (Welch t- test with overestimated variance) between the root and end cell cluster was performed for WT and *Rag1*$^{-/-}$ samples separately. Non- overlapping, significantly changing genes (p- value<0.05 corrected for multiple testing with the Benjamin-Hochberg method) were considered as regulated specifically in WT and *Rag1*$^{-/-}$ samples, respectively. Pathway enrichment of gene sets and differentially regulated genes was performed with the gseapy package (https://github.com/zqfang/GSEApy/) functionality of EnrichR (***Xie et al., 2021***).

Code availability

Jupyter notebooks with custom python scripts for scRNA- seq analysis is available in a github repository (https://github.com/Lieszlab/Benakis-et-al.-2022-eLife.git), copy archived at swh:1:rev:04f5dead312f071a4c760607d68f94047444bbaa (***Benakis et al., 2022***).

Statistical analysis

Data are expressed as mean ± SD or median with interquartile range and were analyzed by unpaired Student's t- test (two- tailed) or one- or two-way ANOVA and post- hoc tests as indicated in the figure legends. Exclusion criteria are described in the individual method sections. The data for microglia morphology are shown as median ± interquartile range, and statistical significance was tested using the Wilcoxon rank sum test with continuity correction and Bonferroni post- hoc correction for multiple testing in R (version 4.0.3).

Acknowledgements

The authors thank Kerstin Thuβ-Silczak and Dr. Monica Weiler for technical support and Michael Heide and Oliver Weigert for support at the DKTK Nanostring core facility. Some of the graphical schemes were created with BioRender. com. The study was supported by the European Research Council (ERC- StG 802305) and the German Research Foundation (DFG) under Germany's Excellence Strategy (EXC 2145 SyNergy – ID 390857198), through SFB TRR 274, FOR2879 and under the DFG projects 405358801 (to A.L.), 418128679 (to C.B.) and PE- 2681/1–1 (to A.P.).

Additional information

Competing interests

Fabian J Theis: reports receiving consulting fees from ImmunAI and ownership interest in Dermagnostix. The other authors declare that no competing interests exist.

Funding

Funder	Grant reference number	Author
European Research Council	ERC-StG 802305	Arthur Liesz
Deutsche Forschungsgemeinschaft	EXC 2145 SyNergy - ID 390857198	Arthur Liesz
Deutsche Forschungsgemeinschaft	SFB TRR 274	Arthur Liesz
Deutsche Forschungsgemeinschaft	FOR2879	Arthur Liesz
Deutsche Forschungsgemeinschaft	405358801	Arthur Liesz
Deutsche Forschungsgemeinschaft	418128679	Corinne Benakis
Deutsche Forschungsgemeinschaft	PE-2681/1-1	Anneli Peters
Deutsche Forschungsgemeinschaft	CRC TRR 355 (ID 490846870)	Arthur Liesz Stefan Bittner Corinne Benakis

The funders had no role in study design, data collection and interpretation, or the decision to submit the work for publication.

Author contributions

Corinne Benakis, Conceptualization, Formal analysis, Supervision, Funding acquisition, Investigation, Visualization, Methodology, Writing - original draft, Writing - review and editing; Alba Simats, Supervision, Validation, Investigation, Methodology; Sophie Tritschler, Simon Besson- Girard, Data curation, Formal analysis, Visualization; Steffanie Heindl, Data curation, Formal analysis, Investigation; Gemma Llovera, Kelsey Pinkham, Formal analysis, Investigation, Methodology; Anna Kolz, Alessio Ricci, Investigation, Methodology; Fabian J Theis, Data curation, Supervision; Stefan Bittner, Writing - review and editing; Özgün Gökce, Data curation, Formal analysis, Writing - review and editing; Anneli Peters, Investigation, Methodology, Writing - review and editing; Arthur Liesz, Conceptualization, Supervision, Funding acquisition, Writing - original draft, Project administration, Writing - review and editing

Author ORCIDs

Corinne Benakis http://orcid.org/0000-0001-6463-7949
Steffanie Heindl http://orcid.org/0000-0003-3576-2702
Simon Besson- Girard http://orcid.org/0000-0003-1194-5256
Anna Kolz http://orcid.org/0000-0002-6020-7746 Alessio Ricci
http://orcid.org/0000-0002-3051-8113
Arthur Liesz http://orcid.org/0000-0002-9069-2594

Ethics

All animal procedures were performed in accordance with the guidelines for the use of experimental animals and were approved by the respective governmental committees (Licenses: 02- 21- 46 and 02- 21- 95; Regierungspraesidium Oberbayern, the Rhineland Palatinate Landesuntersuchungsamt Koblenz). All animal experiments were performed and reported in accordance with the ARRIVE guidelines (Kilkenny et al., 2011).

Decision letter and Author response

Decision letter https://doi.org/10.7554/eLife.82031.sa1
Author response https://doi.org/10.7554/eLife.82031.sa2

Additional files

Supplementary files

- MDAR checklist

Data availability

Data is available in github repository (https://github.com/Lieszlab/Benakis-et-al.-2022-eLife, copy archived at swh:1:rev:04f5dead312f071a4c760607d68f94047444bbaa).

References

Andres RH, Choi R, Pendharkar AV, Gaeta X, Wang N, Nathan JK, Chua JY, Lee SW, Palmer TD, Steinberg GK, Guzman R. 2011. The CCR2/CCL2 interaction mediates the transendothelial recruitment of intravascularly delivered neural stem cells to the ischemic brain. *Stroke* **42**:2923–2931. DOI: https://doi.org/10.1161/ STROKEAHA.110.606368, PMID: 21836091

Anrather J, Iadecola C. 2016. Inflammation and stroke: an overview. *Neurotherapeutics* **13**:661–670. DOI: https://doi.org/10.1007/s13311-016-0483-x, PMID: 27730544

Becht E, McInnes L, Healy J, Dutertre CA, Kwok IWH, Ng LG, Ginhoux F, Newell EW. 2019. Dimensionality reduction for visualizing single- cell data using UMAP. *Nature Biotechnology* **37**:38–44. DOI: https://doi.org/10. 1038/nbt.4314, PMID: 30531897

Benakis C, Brea D, Caballero S, Faraco G, Moore J, Murphy M, Sita G, Racchumi G, Ling L, Pamer EG, Iadecola C, Anrather J. 2016. Commensal microbiota affects ischemic stroke outcome by regulating intestinal γδ T cells. *Nature Medicine* **22**:516–523. DOI: https://doi.org/10.1038/nm.4068, PMID: 27019327

Benakis C, Llovera G, Liesz A. 2018. The meningeal and choroidal infiltration routes for leukocytes in stroke. *Therapeutic Advances in Neurological Disorders* **11**:1756286418783708. DOI: https://doi.org/10.1177/ 1756286418783708, PMID: 29977343

Benakis C, Simats A, Tritschler S, Heindl S, Besson- Girard S, Llovera G, Pinkham K, Kolz A, Ricci A, Theis F, Bittner S, Gökce Ö, Peters A, Liesz A. 2022. Benakis- et- al.-2022- elife. swh:1:rev:04f5dead312f071a4c760607d68f94047444bbaa. Software Heritage. https://archive.softwareheritage.org/swh:1:dir:00e7ac02dddbcc499e48fd6b915724d186ac8859;origin=https://github.com/Lieszlab/Benakis-et- al.-2022-eLife;visit=swh:1:snp:2f1c3f9976421f4b4b87a85b70228ff82a21dce2;anchor=swh:1:rev:04f5dead312f071a4c760607d68f94047444bbaa

Bindea G, Mlecnik B, Hackl H, Charoentong P, Tosolini M, Kirilovsky A, Fridman WH, Pagès F, Trajanoski Z, Galon J. 2009. ClueGO: a cytoscape plug- in to decipher functionally grouped gene ontology and pathway annotation networks. *Bioinformatics***25**:1091–1093. DOI: https://doi.org/10.1093/bioinformatics/btp101, PMID: 19237447

Blighe K, Rana S, Lewis M. 2022. EnhancedVolcano: publication- ready volcano plots with enhanced colouring and labeling. 1.16.0. R package version. https://github.com/kevinblighe/EnhancedVolcano

Blondel VD, Guillaume JL, Lambiotte R, Lefebvre E. 2008. Fast unfolding of communities in large networks. *Journal of Statistical Mechanics* **2008**:P10008. DOI: https://doi.org/10.1088/1742-5468/2008/10/P10008

Bodhankar S, Chen Y, Vandenbark AA, Murphy SJ, Offner H. 2013. Il- 10- Producing B- cells limit CNS inflammation and infarct volume in experimental stroke. *Metabolic Brain Disease* **28**:375–386. DOI: https://doi. org/10.1007/s11011-013-9413-3, PMID: 23640015

Chabot S, Williams G, Hamilton M, Sutherland G, Yong VW. 1999. Mechanisms of IL- 10 production in human microglia- T cell interaction. *Journal of Immunology***162**:6819–6828 PMID: 10352303.

Chen D, Bromberg JS. 2006. T regulatory cells and migration. *American Journal of Transplantation* **6**:1518–1523. DOI: https://doi.org/10.1111/j.1600-6143.2006.01372.x, PMID: 16827851

Cramer JV, Benakis C, Liesz A. 2018. T cells in the post- ischemic brain: troopers or paramedics? *Journal of Neuroimmunology* **326**:33–37. DOI: https://doi.org/10.1016/j.jneuroim.2018.11.006, PMID: 30468953

Cserép C, Pósfai B, Lénárt N, Fekete R, László ZI, Lele Z, Orsolits B, Molnár G, Heindl S, Schwarcz AD, Ujvári K, Környei Z, Tóth K, Szabadits E, Sperlágh B, Baranyi M, Csiba L, Hortobágyi T, Maglóczky Z, Martinecz B, et al. 2020. Microglia monitor and protect neuronal function through specialized somatic purinergic junctions. Science **367**:528–537. DOI: https://doi.org/10.1126/science.aax6752, PMID: 31831638

Dirnagl U, Iadecola C, Moskowitz MA, Dirnagl U, Iadecola C, Moskowitz MA. 1999. Pathobiology of ischaemic stroke: an integrated view. *Trends in Neurosciences* **22**:391–397. DOI: https://doi.org/10.1016/s0166-2236(99) 01401-0, PMID: 10441299

Dong Y, Yong VW. 2019. When encephalitogenic T cells collaborate with microglia in multiple sclerosis. *Nature Reviews. Neurology* **15**:704–717. DOI: https://doi.org/10.1038/s41582-019-0253-6, PMID: 31527807

Filiano AJ, Gadani SP, Kipnis J. 2017. How and why do T cells and their derived cytokines affect the injured and healthy brain? *Nature Reviews. Neuroscience* **18**:375–384. DOI: https://doi.org/10.1038/nrn.2017.39, PMID: 28446786

Garcia- Bonilla L, Benakis C, Moore J, Iadecola C, Anrather J. 2014. Immune mechanisms in cerebral ischemic tolerance. *Frontiers in Neuroscience* **8**:44. DOI: https://doi.org/10.3389/fnins.2014.00044, PMID: 24624056

Gelderblom M, Leypoldt F, Steinbach K, Behrens D, Choe CU, Siler DA, Arumugam TV, Orthey E, Gerloff C, Tolosa E, Magnus T. 2009. Temporal and spatial dynamics of cerebral immune cell accumulation in stroke. *Stroke* **40**:1849–1857. DOI: https://doi.org/10.1161/STROKEAHA.108.534503, PMID: 19265055

Gelderblom M, Weymar A, Bernreuther C, Velden J, Arunachalam P, Steinbach K, Orthey E, Arumugam TV, Leypoldt F, Simova O, Thom V, Friese MA, Prinz I, Hölscher C, Glatzel M, Korn T, Gerloff C, Tolosa E, Magnus T. 2012. Neutralization of the IL- 17 axis diminishes neutrophil invasion and protects from ischemic stroke. *Blood* **120**:3793–3802. DOI: https://doi.org/10.1182/blood-2012-02-412726, PMID: 22976954

Goldmann T, Prinz M. 2013. Role of microglia in CNS autoimmunity. *Clinical & Developmental Immunology*

2013:208093. DOI: https://doi.org/10.1155/2013/208093, PMID: 23840238

Haghverdi L, Büttner M, Wolf FA, Buettner F, Theis FJ. 2016. Diffusion pseudotime robustly reconstructs lineage branching. *Nature Methods* **13**:845–848. DOI: https://doi.org/10.1038/nmeth.3971, PMID: 27571553

Hao Y, Hao S, Andersen- Nissen E, Mauck WM, Zheng S, Butler A, Lee MJ, Wilk AJ, Darby C, Zager M, Hoffman P, Stoeckius M, Papalexi E, Mimitou EP, Jain J, Srivastava A, Stuart T, Fleming LM, Yeung B, Rogers AJ, et al. 2021. Integrated analysis of multimodal single- cell data. *Cell* **184**:3573–3587. DOI: https://doi.org/10. 1016/j.cell.2021.04.048, PMID: 34062119

Heindl S, Gesierich B, Benakis C, Llovera G, Duering M, Liesz A. 2018. Automated morphological analysis of microglia after stroke. *Frontiers in Cellular Neuroscience* **12**:106. DOI: https://doi.org/10.3389/fncel.2018. 00106, PMID: 29725290

Heindl S, Ricci A, Carofiglio O, Zhou Q, Arzberger T, Lenart N, Franzmeier N, Hortobagyi T, Nelson PT, Stowe AM, Denes A, Edbauer D, Liesz A. 2021. Chronic T cell proliferation in brains after stroke could interfere with the efficacy of immunotherapies. *The Journal of Experimental Medicine* **218**:e20202411. DOI: https://doi. org/10.1084/jem.20202411, PMID: 34037669

Iliff JJ, Wang M, Liao Y, Plogg BA, Peng W, Gundersen GA, Benveniste H, Vates GE, Deane R, Goldman SA, Nagelhus EA, Nedergaard M. 2012. A paravascular pathway facilitates CSF flow through the brain parenchyma and the clearance of interstitial solutes, including amyloid β. *Science Translational Medicine* **4**:147ra111. DOI: https://doi.org/10.1126/scitranslmed.3003748, PMID: 22896675

Keren- Shaul H, Spinrad A, Weiner A, Matcovitch- Natan O, Dvir- Szternfeld R, Ulland TK, David E, Baruch K, Lara- Astaiso D, Toth B, Itzkovitz S, Colonna M, Schwartz M, Amit I. 2017. A unique microglia type associated with restricting development of Alzheimer's disease. *Cell* **169**:1276–1290.. DOI: https://doi.org/10.1016/j.cell. 2017.05.018, PMID: 28602351

Kilkenny C, Browne W, Cuthill IC, Emerson M, Altman DG, National Centre for the Replacement, Refinement and Reduction of Amimals in Research. 2011. Animal research: reporting in vivo experiments--the ARRIVE guidelines. *Journal of Cerebral Blood Flow and Metabolism* **31**:991–993. DOI: https://doi.org/10.1038/jcbfm. 2010.220, PMID: 21206507

Kleinschnitz C, Schwab N, Kraft P, Hagedorn I, Dreykluft A, Schwarz T, Austinat M, Nieswandt B, Wiendl H, Stoll G. 2010. Early detrimental T- cell effects in experimental cerebral ischemia are neither related to adaptive immunity nor thrombus formation. *Blood* **115**:3835–3842. DOI: https://doi.org/10.1182/blood-2009-10- 249078, PMID: 20215643

Le T, Leung L, Carroll WL, Schibler KR. 1997. Regulation of interleukin- 10 gene expression: possible mechanisms accounting for its upregulation and for maturational differences in its expression by blood mononuclear cells. *Blood* **89**:4112–4119 PMID: 9166853.

Lee Y, Awasthi A, Yosef N, Quintana FJ, Xiao S, Peters A, Wu C, Kleinewietfeld M, Kunder S, Hafler DA, Sobel RA, Regev A, Kuchroo VK. 2012. Induction and molecular signature of pathogenic Th17 cells. *Nature Immunology* **13**:991–999. DOI: https://doi.org/10.1038/ni.2416, PMID: 22961052

Liesz A, Suri- Payer E, Veltkamp C, Doerr H, Sommer C, Rivest S, Giese T, Veltkamp R. 2009. Regulatory T cells are key cerebroprotective immunomodulators in acute experimental stroke. *Nature Medicine* **15**:192–199. DOI: https://doi.org/10.1038/nm.1927, PMID: 19169263

Liesz A, Zhou W, Mracskó É, Karcher S, Bauer H, Schwarting S, Sun L, Bruder D, Stegemann S, Cerwenka A, Sommer C, Dalpke AH, Veltkamp R. 2011. Inhibition of lymphocyte trafficking shields the brain against deleterious neuroinflammation after stroke. *Brain* **134**:704–720. DOI: https://doi.org/10.1093/brain/awr008, PMID: 21354973

Liesz A, Bauer A, Hoheisel JD, Veltkamp R. 2014. Intracerebral interleukin- 10 injection modulates post- ischemic neuroinflammation: an experimental microarray study. *Neuroscience Letters* **579**:18–23. DOI: https://doi.org/ 10.1016/j.neulet.2014.07.003, PMID: 25019688

Liu XS, Zhang ZG, Zhang RL, Gregg SR, Wang L, Yier T, Chopp M. 2007. Chemokine ligand 2 (CCL2) induces migration and differentiation of subventricular zone cells after stroke. *Journal of Neuroscience Research* **85**:2120–2125. DOI: https://doi.org/10.1002/jnr.21359, PMID: 17510981

Llovera G, Roth S, Plesnila N, Veltkamp R, Liesz A. 2014. Modeling stroke in mice: permanent coagulation of the distal middle cerebral artery. *Journal of Visualized Experiments* **01**:e51729. DOI: https://doi.org/10.3791/ 51729, PMID: 25145316

Llovera G, Hofmann K, Roth S, Salas- Pérdomo A, Ferrer- Ferrer M, Perego C, Zanier ER, Mamrak U, Rex A, Party H, Agin V, Fauchon C, Orset C, Haelewyn B, De Simoni M- G, Dirnagl U, Grittner U, Planas AM, Plesnila N, Vivien D, et al. 2015. Results of a preclinical randomized controlled multicenter trial (prct): anti-cd49d treatment for acute brain ischemia. *Science Translational Medicine* **7**:299ra121. DOI: https://doi.org/10.1126/ scitranslmed.aaa9853, PMID: 26246166

Llovera G, Benakis C, Enzmann G, Cai R, Arzberger T, Ghasemigharagoz A, Mao X, Malik R, Lazarevic I, Liebscher S, Ertürk A, Meissner L, Vivien D, Haffner C, Plesnila N, Montaner J, Engelhardt B, Liesz A. 2017. The choroid plexus is a key cerebral invasion route for T cells after stroke. *Acta Neuropathologica* **134**:851–868. DOI: https://doi.org/10.1007/s00401-017-1758-y, PMID: 28762187

Luecken MD, Theis FJ. 2019. Current best practices in single- cell RNA- seq analysis: a tutorial. *Molecular Systems Biology* **15**:e8746. DOI: https://doi.org/10.15252/msb.20188746, PMID: 31217225

Mathys H, Adaikkan C, Gao F, Young JZ, Manet E, Hemberg M, De Jager PL, Ransohoff RM, Regev A, Tsai L- H. 2017. Temporal tracking of microglia activation in neurodegeneration at single- cell resolution. *Cell Reports* **21**:366–380. DOI: https://doi.org/10.1016/j.celrep.2017.09.039, PMID: 29020624

Miron VE, Priller J. 2020. Investigating microglia in health and disease: challenges and opportunities. *Trends in Immunology* **41**:785–793. DOI: https://doi.org/10.1016/j.it.2020.07.002, PMID: 32736967

Ortega SB, Torres VO, Latchney SE, Whoolery CW, Noorbhai IZ, Poinsatte K, Selvaraj UM, Benson MA, Meeuwissen AJM, Plautz EJ, Kong X, Ramirez DM, Ajay AD, Meeks JP, Goldberg MP, Monson NL, Eisch AJ, Stowe AM. 2020. B cells migrate into remote brain areas and support neurogenesis and functional recovery after focal stroke in mice. *PNAS* **117**:4983–4993. DOI: https://doi.org/10.1073/pnas.1913292117, PMID: 32051245

Prinz M, Priller J. 2014. Microglia and brain macrophages in the molecular age: from origin to neuropsychiatric disease. *Nature Reviews. Neuroscience* **15**:300–312. DOI: https://doi.org/10.1038/nrn3722, PMID: 24713688

Roth S, Yang J, Cramer JV, Malik R, Liesz A. 2020. Detection of cytokine- induced sickness behavior after ischemic stroke by an optimized behavioral assessment battery. *Brain, Behavior, and Immunity* **91**:668–672. DOI: https://doi.org/10.1016/j.bbi.2020.11.016, PMID: 33197540

Saraiva M, Vieira P, O'Garra A. 2019. Biology and therapeutic potential of interleukin- 10. *The Journal of Experimental Medicine* **217**:e20190418. DOI: https://doi.org/10.1084/jem.20190418, PMID: 31611251

Satija R, Farrell JA, Gennert D, Schier AF, Regev A. 2015. Spatial reconstruction of single- cell gene expression data. *Nature Biotechnology* **33**:495–502. DOI: https://doi.org/10.1038/nbt.3192, PMID: 25867923

Saxena A, Khosraviani S, Noel S, Mohan D, Donner T, Hamad ARA. 2015. Interleukin- 10 paradox: A potent immunoregulatory cytokine that has been difficult to harness for immunotherapy. *Cytokine* **74**:27–34. DOI: https://doi.org/10.1016/j.cyto.2014.10.031, PMID: 25481648

Schafer DP, Lehrman EK, Kautzman AG, Koyama R, Mardinly AR, Yamasaki R, Ransohoff RM, Greenberg ME, Barres BA, Stevens B. 2012. Microglia sculpt postnatal neural circuits in an activity and complement- dependent manner. *Neuron* **74**:691–705. DOI: https://doi.org/10.1016/j.neuron.2012.03.026, PMID: 22632727

Seifert HA, Vandenbark AA, Offner H. 2018. Regulatory B cells in experimental stroke. *Immunology* **154**:169– 177. DOI: https://doi.org/10.1111/imm.12887, PMID: 29313944

Shemer A, Scheyltjens I, Frumer GR, Kim J- S, Grozovski J, Ayanaw S, Dassa B, Van Hove H, Chappell- Maor L, Boura- Halfon S, Leshkowitz D, Mueller W, Maggio N, Movahedi K, Jung S. 2020. Interleukin- 10 prevents pathological microglia hyperactivation following peripheral endotoxin challenge. *Immunity* **53**:1033–1049. DOI: https://doi.org/10.1016/j.immuni.2020.09.018, PMID: 33049219

Shi C, Sakuma M, Mooroka T, Liscoe A, Gao H, Croce KJ, Sharma A, Kaplan D, Greaves DR, Wang Y, Simon DI. 2008. Down-regulation of the forkhead transcription factor foxp1 is required for monocyte differentiation and macrophage function. *Blood* **112**:4699–4711. DOI: https://doi.org/10.1182/blood-2008-01-137018, PMID: 18799727

Shi L, Sun Z, Su W, Xu F, Xie D, Zhang Q, Dai X, Iyer K, Hitchens TK, Foley LM, Li S, Stolz DB, Chen K, Ding Y, Thomson AW, Leak RK, Chen J, Hu X. 2021. Treg cell- derived osteopontin promotes microglia- mediated white matter repair after ischemic stroke. *Immunity* **54**:1527–1542. DOI: https://doi.org/10.1016/j.immuni.2021.04. 022, PMID: 34015256

Shichita T, Sugiyama Y, Ooboshi H, Sugimori H, Nakagawa R, Takada I, Iwaki T, Okada Y, Iida M, Cua DJ, Iwakura Y, Yoshimura A. 2009. Pivotal role of cerebral interleukin- 17- producing gammadeltat cells in the delayed phase of ischemic brain injury. *Nature Medicine* **15**:946–950. DOI: https://doi.org/10.1038/nm.1999, PMID: 19648929

Stephan AH, Barres BA, Stevens B. 2012. The complement system: an unexpected role in synaptic pruning during development and disease. *Annual Review of Neuroscience* **35**:369–389. DOI: https://doi.org/10.1146/ annurev-neuro-061010-113810, PMID: 22715882

Szalay G, Martinecz B, Lénárt N, Környei Z, Orsolits B, Judák L, Császár E, Fekete R, West BL, Katona G, Rózsa B, Dénes Á. 2016. Microglia protect against brain injury and their selective elimination dysregulates neuronal network activity after stroke. *Nature Communications* **7**:11499. DOI: https://doi.org/10.1038/ncomms11499, PMID: 27139776

Tabata H, Morita H, Kaji H, Tohyama K, Tohyama Y. 2020. Syk facilitates phagosome- lysosome fusion by regulating actin-remodeling in complement- mediated phagocytosis. *Scientific Reports* **10**:22086. DOI: https:// doi.org/10.1038/s41598-020-79156-7, PMID: 33328565

Virtanen P, Gommers R, Oliphant TE, Haberland M, Reddy T, Cournapeau D, Burovski E, Peterson P, Weckesser W, Bright J, van der Walt SJ, Brett M, Wilson J, Millman KJ, Mayorov N, Nelson ARJ, Jones E, Kern R, Larson E, Carey CJ, et al. 2020. Author correction: scipy 1.0: fundamental algorithms for scientific computing in python. *Nature Methods* **17**:352. DOI: https://doi.org/10.1038/s41592-020-0772-5, PMID: 32094914

Wang S, Zhang H, Xu Y. 2016. Crosstalk between microglia and T cells contributes to brain damage and recovery after ischemic stroke. *Neurological Research* **38**:495–503. DOI: https://doi.org/10.1080/01616412.2016. 1188473, PMID: 27244271

Wolf FA, Angerer P, Theis FJ. 2018. SCANPY: large- scale single- cell gene expression data analysis. *Genome Biology* **19**:15. DOI: https://doi.org/10.1186/s13059-017-1382-0, PMID: 29409532

Wolock SL, Lopez R, Klein AM. 2019. Scrublet: computational identification of cell doublets in single- cell transcriptomic data. *Cell Systems* **8**:281–291.. DOI: https://doi.org/10.1016/j.cels.2018.11.005, PMID: 30954476

Xie Z, Bailey A, Kuleshov MV, Clarke DJB, Evangelista JE, Jenkins SL, Lachmann A, Wojciechowicz ML, Kropiwnicki E, Jagodnik KM, Jeon M, Ma'ayan A. 2021. Gene set knowledge discovery with enrichr. *Current Protocols* **1**:e90. DOI: https://doi.org/10.1002/cpz1.90, PMID: 33780170

Zaki Y, Cai DJ. 2020. Creating space for synaptic formation- A new role for microglia in synaptic plasticity. *Cell* **182**:265–267. DOI: https://doi.org/10.1016/j.cell.2020.06.042, PMID: 32707091

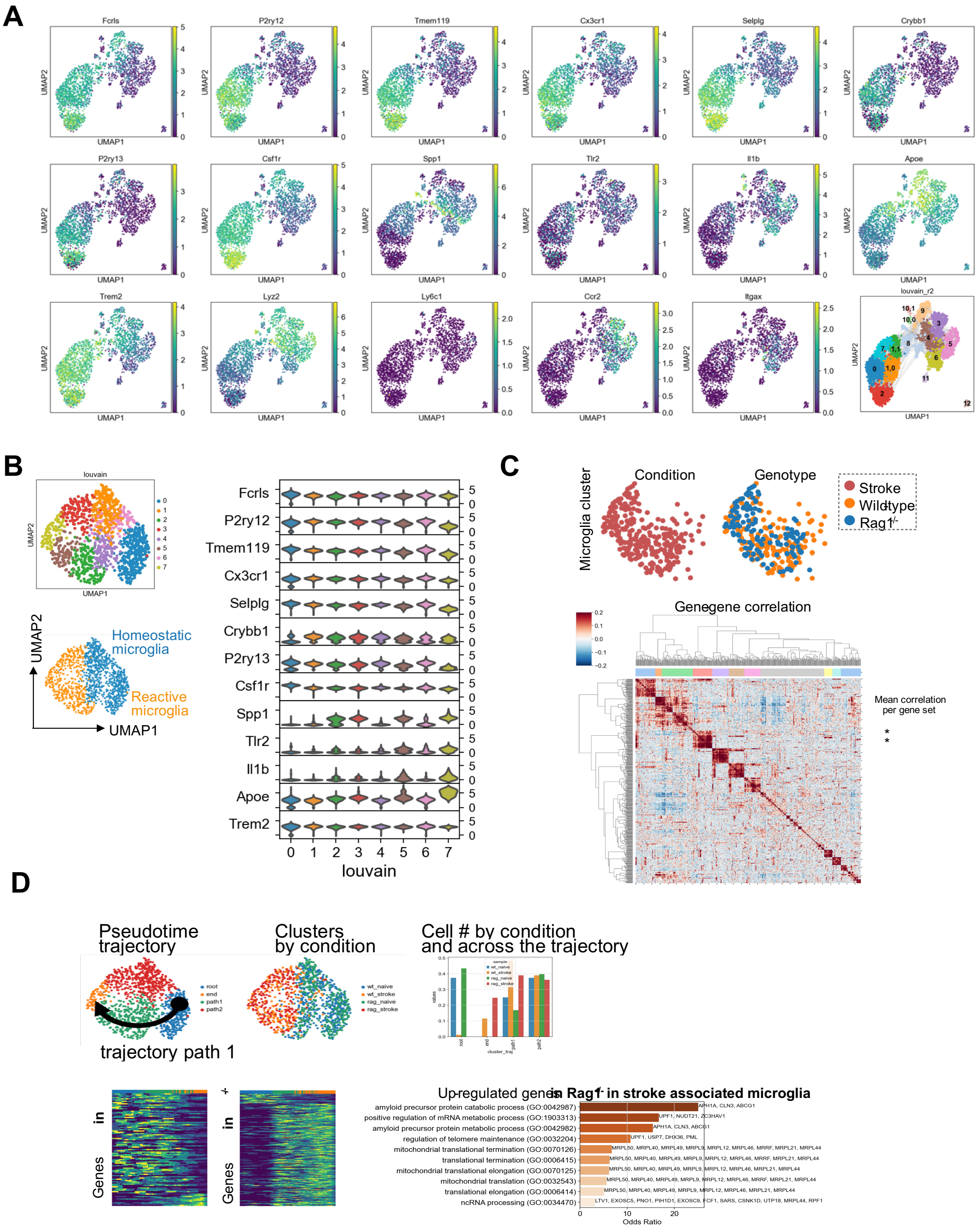

Suppl. Fig. 1: Transcritpomic analysis of microglia isolated from WT and Rag1-/- in naive and stroke conditions. (A) Clustering analysis based on known CD45+CD11b+ myeloid cell gene expression. **(B)** Sub-clustering gene expression of microglia. **(C)** Correlation matrix of microglia genes in stroke condition. Genes are ordered by hierarchical clustering to reveal 11 gene modules (G1 to G11) of highly correlated and/or anti-correlated genes. Asterics (*) indicate significant difference between genotype in stroke condition. **(B)** Microglia single cell trajectory inference analysis (pseudotime) identifies the evolution of microglia activation from naïve to stroke condition (root-to-end path). There is a higher proportion of regulated genes in ‘Rag1$^{-/-}$-microglia’ than in ‘wild-type-microglia’ in stroke mice (end path), corresponding to mitochondrial function.

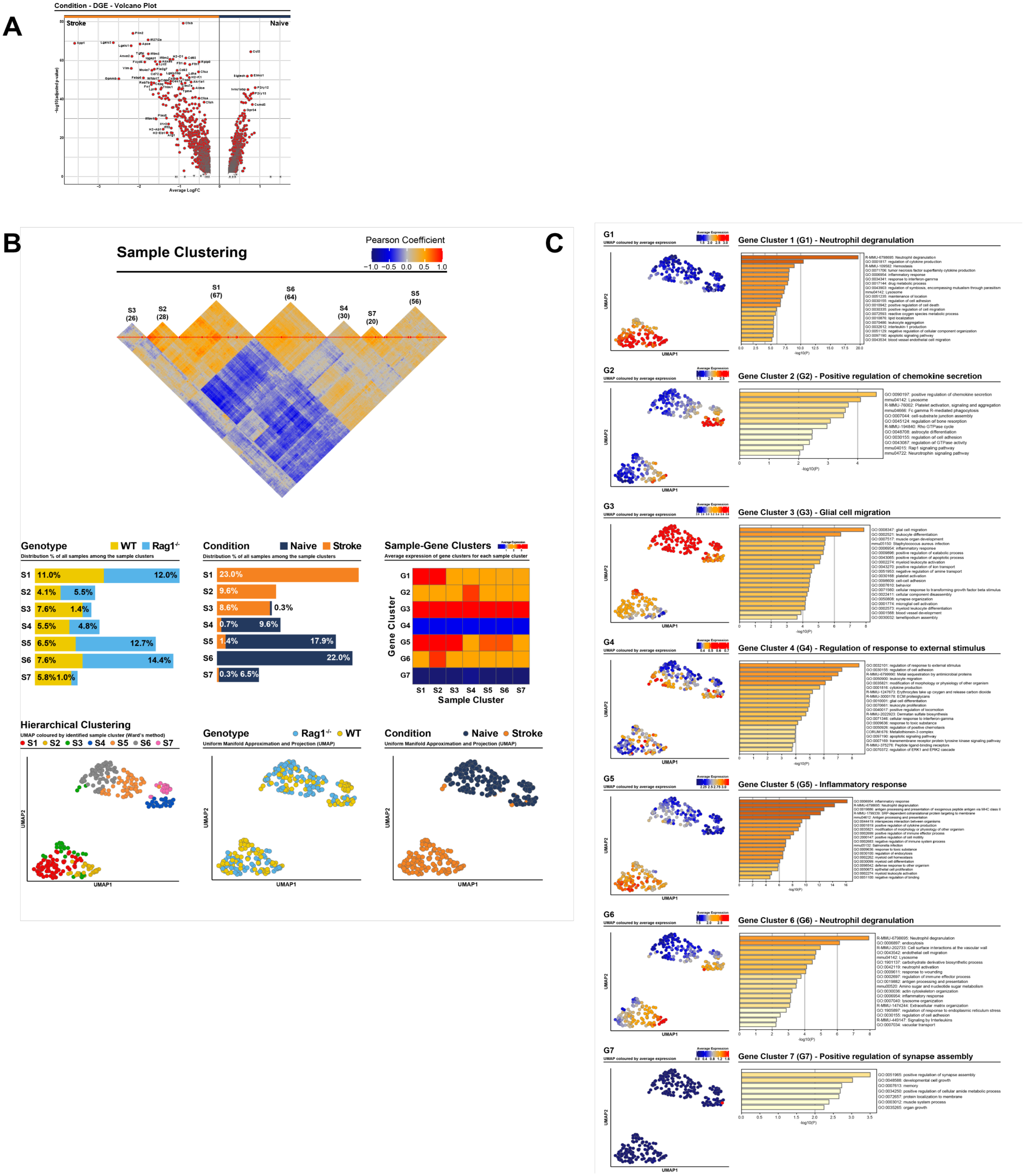

	WT	Rag1-/-
S1	11.0%	12.0%
S2	4.1%	5.5%
S3	7.6%	1.4%
S4	5.5%	4.8%
S5	6.5%	12.7%
S6	7.6%	14.4%
S7	5.8%	1.0%

	Stroke	Naive
S1	23.0%	
S2	9.6%	
S3	8.6%	0.3%
S4	0.7%	9.6%
S5	1.4%	17.9%
S6		22.0%
S7	0.3%	6.5%

Suppl. Fig. 2: Smart-seq of microglia isolated from WT and Rag1-/- in naive and stroke conditions. (A) Differentially expressed genes between condition, independently of the genotype. **(B)** Cluster analysis of microglia cells. **(C)** Pathway analysis of the gene clusters identified in B.

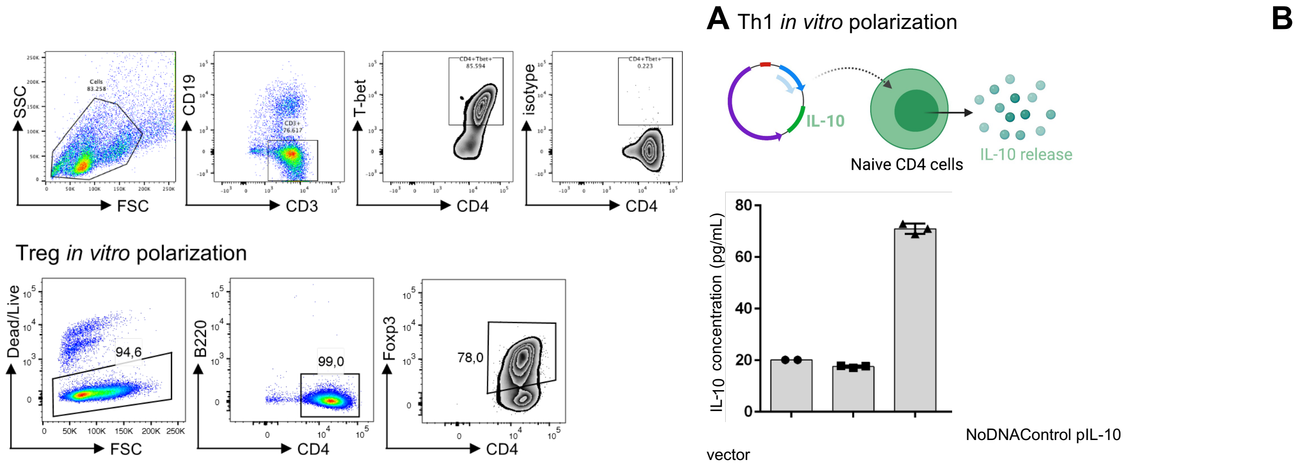

Suppl. Fig. 3: Effect of polarized T cell on microglia. (A) CD4 naive T cells were polarized in vitro towards Th1 (CD4+Tbet+) or Treg (CD4+Foxp3+). **(B)** Top row, plasmid expression vector pIL10 constructed by inserting xxxbp il10 cDNA containing antibiotic resistance cassette etc. Bottom row, IL-10 concentration measured by ELISA.

3.2 Enhancing Microglial Cholesterol Export Promotes Oligodendrocyte Regeneration and Functional Recovery After Stroke

3.2.1 Summary

Stroke induces long-lasting neuroinflammation, with microglia, the brain's primary immune cells, playing a crucial role in secondary neurodegeneration and repair. However, chronic changes in microglial function post-stroke remain poorly understood. Therefore, we aimed to characterize chronic changes in microglia to determine a potential therapeutic target of chronic neuroinflammation and assess its impact on stroke recovery. Using an experimental stroke mouse model, we identified by PET imaging, persistent microglial activation up to six months after stroke, while altered microglial morphology lasted at least three months. Phagocytic function and stroke recovery were also impaired at least one month after stroke. Interestingly, single-cell RNA sequencing revealed a unique chronic subpopulation of microglia associated with lipid metabolism and intracellular lipid accumulation. In our model and human autopsy samples, we confirmed microglia chronically accumulate lipid droplets and unexpectedly, also cholesterol crystals. Notably, cholesterol crystals are known triggers of inflammasome activation and IL-1β production, and our findings confirm that this mechanism persists chronically after stroke. To target this lipid dysregulation, we administered GW3965, a liver X receptor agonist targeting cholesterol efflux, resulting in a significant reduction in lipid and crystal buildup, a restoration of phagocytic function and mitigation of inflammasome activation. It also gave rise to a novel microglia population, which we have term repair-associated microglia (RAM). These changes were accompanied by improved behavioral deficits and neuronal functional connectivity in mice. Furthermore, oligodendrocytes showed a robust expression of Apoe receptors, suggesting a high capacity for lipid uptake. In addition, we observed an expansion and progression along the oligodendrocyte lineage. Overall, indicating that oligodendrocytes serve as key acceptors of microglial-derived cholesterol.

Collectively, these findings corroborate that lipid accumulation is an essential driver of chronic microglial dysfunction and neuroinflammation post-stroke, ultimately impairing functional recovery. Furthermore, this study highlights cholesterol efflux as a promising therapeutic target for enhancing post-stroke recovery, particularly by supporting the microglia-oligodendrocyte axis.

3.2.2 Reference

The paper is not yet accepted for publication:

Kelsey Pinkham*, Steffanie Heindl*, Daniel Varga, Alba Simats, Nicolas Snaidero, Yuxi Zhou, Sarantos Kostidis, Martina Schifferer, Gemma Llovera, Olga Carofiglio, Merle Bublitz, Elena Sanchez, Christoph Müller, Ludwig Huber, Natalija Ivljanin, Rainer Malik, Peter Androvic, Janos Groh, Stefan Berghoff, Christian Haass, Sarah Jäkel, Dominik Paquet, Rebeka Fekete, Thomas Misgeld, Martin Dichgans, Ozgün Gökce, Mikael Simons, Adam Denes, Hannah Spitzer, Peiying Li, Martin Giera, Arthur Liesz

*Contributed equally

Enhancing Microglial Cholesterol Export Promotes Oligodendrocyte Regeneration and Functional Recovery After Stroke

Authors:

Kelsey Pinkham*[1,2], Steffanie Heindl*[1,2], Daniel Varga[1,3], Alba Simats[1], Nicolas Snaidero[4], Yuxi Zhou[5], Sarantos Kostidis[5], Martina Schifferer[2,3], Gemma Llovera[1,2], Olga Carofiglio[1], Merle Bublitz[1], Elena Sanchez[7], Christoph Müller[8], Ludwig Huber[8], Natalija Ivljanin[1], Rainer Malik[1], Peter Androvic[1,3], Janos Groh[3,4], Stefan Berghoff[3,4], Christian Haass[1,3], Sarah Jäkel[1], Dominik Paquet[1,2], Rebeka Fekete[9], Thomas Misgeld[2,3,4], Martin Dichgans[1,2,3], Ozgün Gökce[1,3], Mikael Simons[1,2,3,4], Adam Denes[1,9], Hannah Spitzer[1,10], Peiying Li[5], Martin Giera[7], Arthur Liesz[1,2#]

1 Institute for Stroke and Dementia Research (ISD), University Medical Center Munich, 81377 Munich, Germany
2 Munich Cluster for Systems Neurology (SyNergy), Munich, Germany
3 DZNE, German Center for Neurodegenerative Diseases, partner sites Bonn and Munich
4 Institute of Neuronal Cell Biology, Technical University of Munich, Munich 80802, Germany
5 Department of Anesthesiology, Renji Hospital, Shanghai Jiao Tong University School of Medicine, Shanghai, China
6 Chair of Cell Biology and Anatomy, Biomedical Center (BMC), Faculty of Medicine, LMU Munich, Planegg-Martinsried
7 Center for Proteomics and Metabolomics, Leiden University Medical Center, 2300 RC Leiden, the Netherlands
8 Department of Pharmacy, Center for Drug Research, Ludwig-Maximilians University, 81377 Munich, Germany
9 "Momentum" Laboratory of Neuroimmunology, HUN-REN Institute of Experimental Medicine, Budapest, Hungary
10 Institute of Computational Biology, Helmholtz Munich, Germany

[*] contributed equally

[#] To whom correspondence should be addressed: arthur.liesz@med.uni-muenchen.de

Graphical Abstract

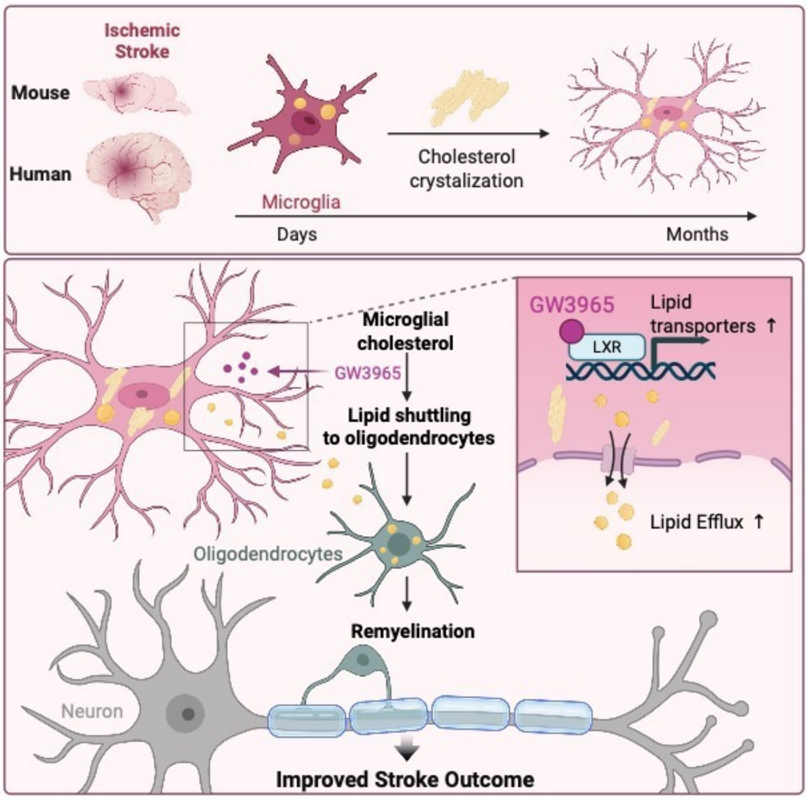

Summary

Recovery after brain injury is often incomplete, and no specific pharmacological strategies exist to enhance repair in the chronic phase. This limitation reflects an incomplete understanding of the multicellular interactions that coordinate brain regeneration, particularly the role of glial cell states and their communication. Here, we identify a distinct population of microglia that emerges during the chronic phase after stroke, defined by a unique transcriptional and metabolic profile. These microglia accumulate cholesterol crystals—a previously unrecognized phenotype associated with impaired microglial function and disrupted glial metabolic crosstalk. Using spatial transcriptomics, lipid tracing, and in vivo imaging, we show that enhancing cholesterol efflux from microglia reduces crystal burden and neuroinflammation and promotes lipid transfer to oligodendrocytes. This, in turn, supports remyelination that reestablishes long-range neuronal connectivity. Our findings define a metabolically regulated axis of glial communication and suggest a new class of therapeutic strategies with direct clinical potential to promote functional brain repair.

Introduction

Brain function relies on highly organized, compartmentalized networks of neurons and glia that operate in tight spatial and metabolic coordination[1-3]. Beyond their structural roles, glial cells—including astrocytes, oligodendrocytes, and microglia—form dynamic communication networks that maintain synaptic activity, regulate metabolic support, and shape circuit plasticity[4,5]. Disruption of these networks by acute injuries such as ischemic stroke or traumatic brain injury leads to breakdown in brain tissue homeostasis[3,6-9]. While spontaneous recovery of function after brain injury can occur, it is typically limited and incomplete, often resulting in long-term motor, cognitive, or sensory deficits. This is particularly evident in the chronic phase—weeks to months after injury—when endogenous repair processes plateau and functional gains become marginal[10,11]. Currently, no pharmacological therapies exist that specifically promote structural and functional brain repair in the chronic phase following injury[12].

Injured brain regions induce remarkable neuronal plasticity during the recovery phase, involving dendritic sprouting, remyelination, and synaptic remodeling[13-16]. These regenerative processes require equally adaptive responses from glial cells, including microglia, which orchestrate circuit rewiring through clearance of debris, modulation of synapses, and support of neurovascular remodeling[15,17]. Astrocytes and oligodendrocyte lineage cells similarly adopt region- and context-dependent phenotypes that can either promote or impede repair[18-21]. Importantly, the coordination of these regenerative functions depends on tightly regulated interactions among diverse glial subtypes. These cells form spatially organized networks that enable localized responses to injury and facilitate the re-establishment of functional tissue architecture. While previous studies have mainly focused on the (patho-)biology of single cell populations, a better understanding of these context-specific interactions within heterogenous cellular networks is critical to uncover how cellular cross-talk governs brain repair.

Among all tissue-resident macrophages, microglia stand out, exhibiting highly specialized functions shaped by the distinct environment. Unlike cardiac, hepatic, or pulmonary macrophages, microglia operate within a tightly regulated, immune-privileged environment that demands a uniquely restrained and context-sensitive response to perturbation of tissue homeostasis[22,23]. In homeostasis, microglia constantly survey the brain parenchyma, modulate synaptic connectivity, and maintain neuronal viability through the release of neurotrophic factors[23]. They also engage in dynamic, bidirectional communication with neurons, astrocytes, and oligodendrocytes, shaped by neurotransmitter and cytokine signaling unique to the CNS[8,24]. Upon injury, microglia respond rapidly but locally, balancing inflammatory activity with mechanisms that support tissue integrity[25,26]. This contrasts with the often systemically amplified and fibrosis-prone responses of macrophages in other organs such as the heart or liver[27]. Moreover, microglia also differ from peripheral macrophages in their handling of lipids: individual studies suggest that they express lower levels of cholesterol efflux transporters such as ABCA1 and ABCG1, therefore making them more prone to lipid accumulation under stress conditions[28-31]. However, systematic comparisons across tissue-resident macrophages under uniform conditions—particularly in the context of brain injury and the chronic recovery phase—are not yet available.

These distinct features equip microglia to preserve neural networks but also render the brain vulnerable to chronic dysfunction when microglial responses become dysregulated. Moreover, because neurodegeneration and peripheral organ injury pose very different pathological challenges than acute brain injury, mechanistic insights derived from those contexts are not applicable to the context of brain repair after injury. Unlike neurodegeneration, stroke and TBI induce rapid and widespread disruption of cellular networks, massive neuronal loss, and high volumes of cellular debris. How microglia respond to this environment—particularly in the chronic recovery phase—remains poorly understood and cannot be inferred from studies in other tissues or disease models. Emerging evidence suggests that chronic inflammation interferes with the reparative processes in the recovering brain by locking glia into maladaptive states that limit plasticity[32-34]. In both stroke and TBI, persistent activation of microglia and astrocytes can inhibit synapse formation, oligodendrocyte maturation, and axonal regrowth[17,34-37]. While microglia–astrocyte crosstalk has been implicated in shaping inflammatory tone, the interaction between microglia and other glial cells including oligodendrocyte lineage cells during recovery remains poorly defined; likewise, the mechanisms driving sustained inflammation after acute brain injury are also not yet defined and remains a major open question in brain research.

In this study, we identify a distinct microglial state emerging in the subacute-to-chronic phase after stroke, defined by a unique transcriptional and functional profile. We show that this regeneration-associated microglial cell populations is dysfunctional yet important for functional recovery and characterized by formation of intracellular cholesterol crystals due to impaired lipid export. Surprisingly, therapeutic induction of cholesterol export from microglia facilitated the lipid transfer to oligodendrocytes, promoting remyelination and restoring long-range network connectivity. Enhancing this glia–glia communication axis via targeted modulation of cholesterol efflux provides a potential therapeutic strategy to boost regenerative capacity in the injured brain.

Results

Microglia remain chronically reactive but are necessary to chronic post-stroke recovery.

To assess long-term microglial responses after stroke, we performed TSPO-PET/MR imaging[38,39] and morphometric of microglia for up to 12 weeks post-stroke[40]. These revealed persistently altered microglial morphology and sustained TSPO tracer uptake, indicating chronic reactivity (**Fig. 1A-G** and Suppl. Fig. 1A, B). To study the functional state of these chronically reactive microglia, we assessed phagocytosis and dynamic process motility. 28 days post-stroke, perilesional microglia exhibited a marked reduction in phagocytic uptake of zymosan particles in vivo[41] (**Fig. 1H–J**), but an increased process extension speed following laser-induced microlesions[42] (**Fig. 1K–M**; Suppl. Vid. 1), indicating a functionally divergent cell state.

To determine the relevance of microglia to post-stroke recovery, we chronically depleted microglia using CSF1R inhibition (PLX5622) starting after infarct maturation (Suppl. Fig. 1C). Despite their altered state, microglial depletion impaired sensorimotor recovery over 6 weeks (**Fig. 1N–S**) and disrupted interhemispheric cortical connectivity in perilesional sensory areas, as measured by longitudinal in vivo widefield calcium imaging[43] (**Fig. 1N-S**; Suppl. Fig. 1D). Spine density of perilesional neurons was also reduced in PLX-treated animals (Suppl. Fig. 1E), suggesting impaired structural plasticity.

These findings indicate that chronically reactive microglia are functionally altered but nonetheless essential for recovery. Given recent efforts to reprogram dysfunctional microglia in chronic neurodegeneration and demyelinating conditions using agonistic TREM2-targeting antibodies[44], we tested whether TREM2 agonism might enhance post-stroke recovery. However, unlike in models of demyelination or neurodegeneration[45,46], TREM2 stimulation failed to improve behavioral, structural, or network-level recovery after brain injury (Suppl. Fig. 1F-H). These results suggest that the role and responsiveness of microglia in post-stroke repair are fundamentally distinct from other chronic CNS pathologies, underscoring the need to define their specific function in the subacute-to-chronic phase of recovery.

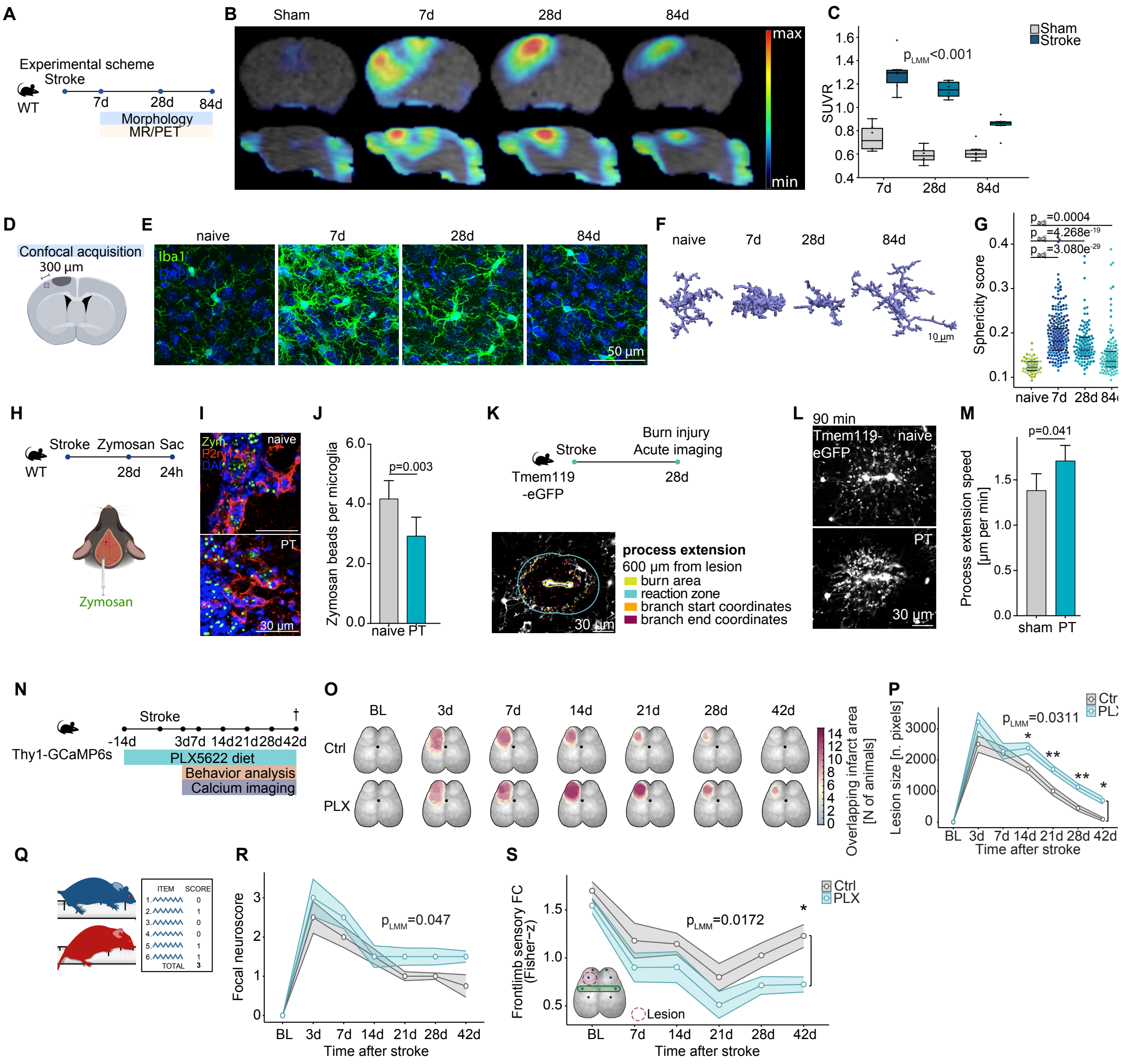

Figure 1. Microglia remain chronically reactive but necessary for chronic post-stroke recovery. (**A**) Experimental scheme for chronic assessment of microglial activation state. (**B**) Representative images of longitudinal PET/MRI after PT using GE180 tracer in lesion and perilesional area until 84 days after stroke. Upper row: coronal view, lower row: sagittal view. (**C**) SUVR of GE180 uptake normalized to cerebellum until 84 days after PT. (Linear-mixed model, group-by-time interaction, p<0.001, *n*=6 /group). (**D**) Scheme of confocal microscopy imaging positions for analysis of microglia morphology. (**E**) Representative confocal images of microglia in the perilesional area 300 µm distant to lesion border. (Scalebar = 50 µm). (**F**) 3D reconstructions of naïve microglia and at days 7, 28 and 84 after PT. (**G**) Microglia sphericity score until 84 days post stroke. Points represent individual cells, color coded for individual mice. (Pairwise Wilcoxon test and Bonferroni correction, *n*=5-6 /time point). (**H**) Experimental scheme of time point and injection area for vivo phagocytosis assay. (**I**) Representative confocal images of zymosan uptake by P2ry12$^+$ microglia in naïve mice and 28 days after PT. (**J**) Quantification of zymosan uptake in the peri-infarct area at 28 days. (Mean ± SD, T test, *n*=7 /group). (**K**) Experimental scheme for timepoint, laser-burn area, and acquisition area of microglia process reaction 28 days after PT. (**L**) Representative 2-photon images of Tmem119-eGFP labeled microglia process accumulation around laser burn injury 90 min after injury induction. (**M**) Speed of process extension at 28 days after PT within the reaction zone. (Mean ± SD, T test, *n*=4/5 /group). (**N**) Experimental scheme for widefield calcium imaging and behavioral assessment during the treatment period of 42 days with PLX5622 or Ctrl in Thy1-GCaMP6s animals. (**O**) Lesion size based on autofluorescence after PT of individual animals superimposed to depict the lesion throughout the observation period of 42 days. The color code indicates the sum of overlapping pixels in lesion area of individual mice per acquisition time point. (**P**) Quantification of lesion size as sum of autofluorescent pixels seen in calcium imaging of individual animals (Linear-mixed model, group-by-time interaction, post-hoc Kruskal-Wallis test with Benjamini-Hochberg correction for multiple comparisons, *n*=11/13 /group. (**Q**) Scheme for acquisition of multi-parameter neuroscore. (**R**) Evaluation of neurological impairment by focal neuroscore. (Median ± SE, linear-mixed model, *n*=11/13 /group). (**S**) Time course of interhemispheric functional connectivity in the sensory frontal limb cortical area in widefield calcium imaging (linear mixed models, post-hoc Kruskal-Wallis test, *n*=11/13 /group).

Repair-associated microglia (RAM) are a distinct microglial cell state that shape the chronic lesion microenvironment.

We characterized the transcriptional identity of chronically reactive microglia using scRNA-seq at multiple post-stroke time points (**Fig. 2A**). Clustering identified 16 total immune clusters, eight of which corresponded to microglia (Suppl. Fig. 2A–D). UMAP analysis of microglia revealed seven subclusters (0–6), each enriched at distinct time points (**Fig. 2B** and Suppl. Fig. 2E), indicating dynamic transcriptional changes over time. Notably, a unique cluster (cluster 5) emerged specifically at 28 days post-stroke (**Fig. 2B**, Suppl. Fig. 2E), which we termed repair-associated microglia (RAM). Other clusters matched known states: homeostatic (clusters 0,1), disease-associated (DAM; clusters 3,4,6), and an intermediate microglia state (cluster 2). Pseudotime analysis indicated a trajectory from homeostatic microglia to the RAM state (**Fig. 2C**). Notably, RAM are transcriptionally distinct from previously described DAM, interferon-responsive (IRM), and lipid-associated (LAM) microglial phenotypes (Suppl. Fig. 2F)[47-50].

To determine their spatial distribution, we derived a RAM-specific gene set score based on the top 20 cluster-specific genes and projected this onto spatial transcriptomic datasets from 10X Visium and single-cell–resolved MERFISH (**Fig. 2D-G** and Suppl. Fig. 2G, H). RAM were localized predominantly to the perilesional cortex at 28 days post-stroke, with a decreasing gradient away from the lesion and absence in uninjured areas. Gene set enrichment analysis of RAM revealed upregulation of lipid metabolism and immune signaling pathways, and downregulation of genes involved in neuronal interactions (Suppl. Fig. 2I). Indeed, cell-cell interaction analysis using CellChat identified substantial changes in the microglial interactome (**Fig. 2H**). Interestingly, we identified Tenascin as the most affected signaling axis, a pathway critical for oligodendrocyte precursor cell (OPC) maturation, which was markedly downregulated in the chronic phase relative to naïve or acutely injured tissue (**Fig. 2I–J**)—indicating a potential effect of RAM on OPC function or maturation.

We next asked whether RAM also actively contribute to the altered extracellular environment in the chronic phase or rather represent a senescent cell state. Therefore, we performed longitudinal in vivo microperfusion of the perilesional tissue[51], followed by proteomic analysis of the extracellular compartment perfusate (**Fig. 2K**). Unsupervised clustering identified a module of secreted proteins (cluster 2) that increased progressively over time(**Fig. 2L**). To assign cell-of-origin, we applied the DESP algorithm to deconvolute proteomic signatures using matched single-cell transcriptomic data (**Fig. 2M**). This analysis confirmed microglia as the principal contributors to the persistently altered secretome, particularly at the chronic recovery phase after stroke (**Fig. 2N**). These findings support a role for RAM as a previously unrecognized microglial cell state that actively modulate the chronic lesion microenvironment.

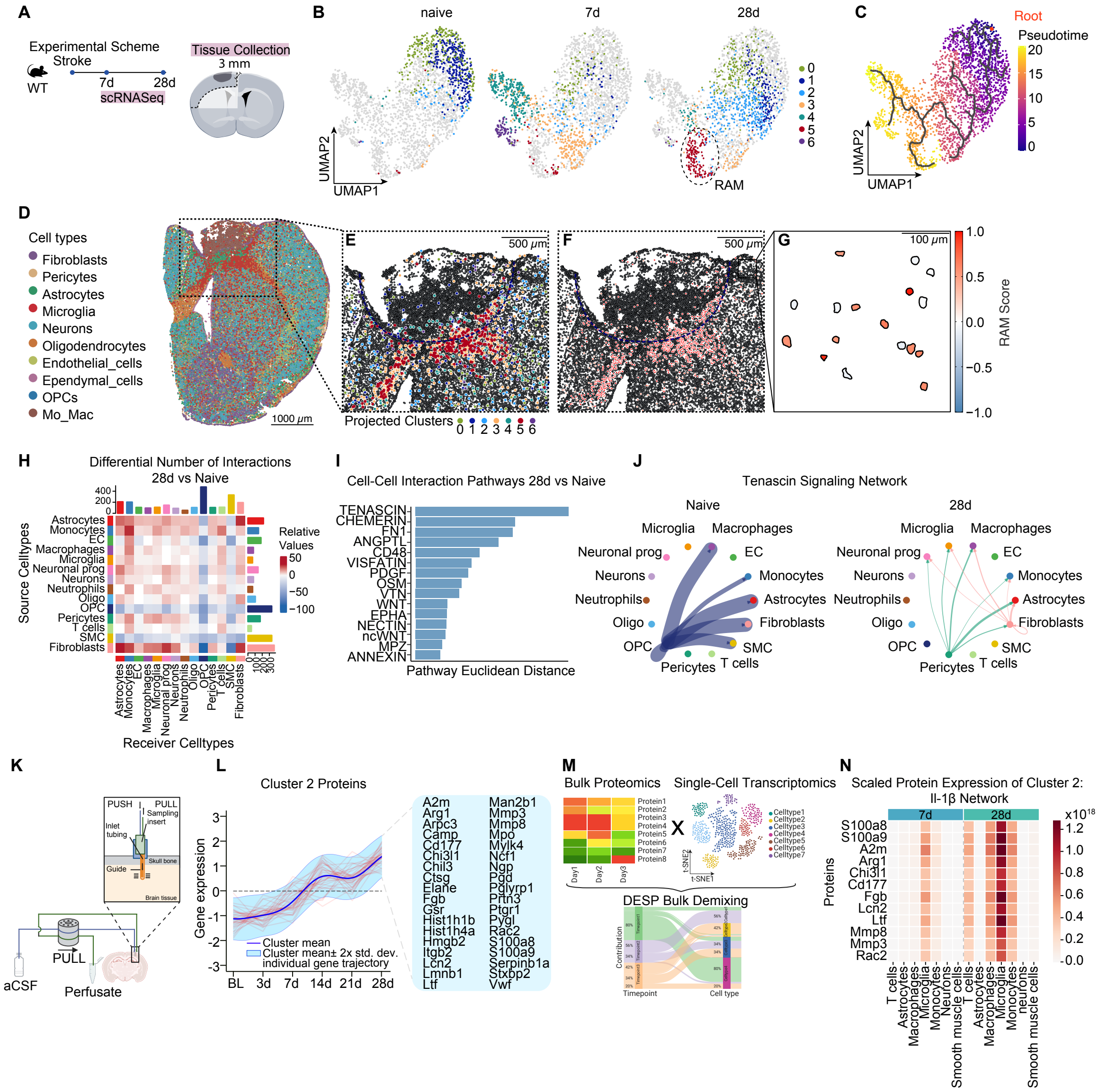

Figure 2. Repair-associated microglia (RAM) are a distinct microglial state that shapes the chronic lesion microenvironment. (**A**) Experimental scheme for timepoints and location of collected brain tissue for scRNA sequencing. (**B**) UMAP of microglia subset showing representative clusters for each individual time point. (**C**) Trajectory representing microglia states along pseudotime. (**D**) Single cell spatial transcriptomics (MerScope) of individual cell types in ipsilateral hemisphere at 28 days after stroke. (**E**) Microglia subclusters projected into spatial transcriptomic dimensions in lesion area (**F**) RAM score (cluster 5) in microglia within the lesion area and (**G**) 300 µm from lesion border. (**H**) Differential number of cell-cell interactions between 28 days after PT and naive condition. (**I**) Euclidean distance of top differentially regulated cell-cell interaction pathways between 28d after PT and naive condition. (**J**) Cell-cell interaction network for Tenascin signaling between 28 days after PT and naive. (**K**) Schematic illustration of longitudinal microperfusion sampling of ipsilateral brain until 28 days post stroke. (**L**) Unsupervised clustering of microperfusate protein expression shows consistently increasing levels of cluster 2 proteins (n=7-8 /time point). (**M**) Schematic illustration of demixing procedure from bulk protein expression to individual cell types (gene expression by scRNA-seq) using DESP algorithm. (**N**) Scaled protein expression of cluster 2 proteins per demixed cell type within the Il-1β-regulated network at baseline, 7 days and 28 days after stroke.

Microglial cholesterol crystallization impairs neuronal recovery after stroke.

Building on transcriptomic evidence of altered lipid metabolism in RAM, we examined microglial lipid storage during the chronic phase post-stroke. Histological staining with the neutral lipid dye BODIPY revealed marked lipid accumulation in microglia within the perilesional cortex at 28 days, which was absent in control brains (**Fig. 3A**). This phenotype was consistent across three different stroke models and confirmed by flow cytometry using the lipid droplet marker Perilipin-2 (Plin2), which showed progressive accumulation over time (**Fig. 3B**, Suppl. Fig. 3A, B). Given prior evidence that excess cholesterol can precipitate as cholesterol crystals in macrophages[52], we assessed for crystal formation using reflection microscopy. This revealed a progressive accumulation of birefringent structures in the perilesional cortex (**Fig. 3C**). Spatial lipidomics by MALDI-MSI further confirmed a localized enrichment of free cholesterol (m/z 339.351) specifically in the ipsilateral lesion area at 28 days (**Fig. 3D**). Enzymatic quantification of free and esterified cholesterol revealed a substantial post-stroke increase, with a predominance of esterified cholesterol, the biochemical precursor of crystalline deposits (**Fig. 3E**, Suppl. Fig. 3C). Ultrastructural analysis by electron microscopy provided definitive evidence of intracellular crystalline structures and lipid droplets within perilesional microglia at 28 days (**Fig. 3F**). Reflective microscopy on postmortem human chronic stroke tissue (124 days after stroke) confirmed the accumulation of lipid droplets as well as crystal deposits in perilesional regions compared to histologically normal cortex in humans (**Fig. 3G**). Together, these findings demonstrate chronic lipid and cholesterol crystal accumulation in RAM after stroke, with validation in human tissue supporting its clinical relevance to chronic brain injury.

To counteract cholesterol crystallization in microglia after stroke, we pharmacologically activated liver X receptors (LXRs), key nuclear regulators of cholesterol export, using the small molecule agonist GW3965[53-55]. Given their role in promoting cholesterol efflux by induction of lipoprotein transporters including ABCA1 and ABCG1[56,57], we hypothesized that LXR activation would reduce intracellular cholesterol burden and lipid droplet accumulation. Indeed, GW3965-treated mice showed significantly reduced lipid droplet and cholesterol crystal accumulation in the perilesional cortex (**Fig. 3H**) and a more ramified microglial morphology (Suppl. Fig. 3D). To assess broader transcriptional effects, we performed scRNA-seq on mixed cortical cells 28 days after stroke in GW3965- and vehicle-treated mice (Suppl. Fig. 3E, F). Microglia were the most abundantly regulated cell population in response to treatment (**Fig. 3I** and Suppl. Fig. 3F, G). GW3965 increased *Abca1* and *Abcg1* expression and upregulated genes associated to lipid handling and chromatin remodeling (e.g., *Rbfox1*, *Hist4h4d*, *Nlk*), while downregulating inflammation-associated genes (*Cd47*, *Abcg2*, *Ighm*, *Slc1a3*) (Suppl. Fig. 3H, I). UMAP projection of the microglia subset onto our previously defined microglial subclusters (see Fig. 2) with consecutive fate mapping analysis identified a shift in microglia of GW3965-treated mice towards an intermediate activation state which was associated with enhanced lipid transport and attenuated stress responses (**Fig. 3J, K** and Suppl. Fig. 3J).

To evaluate whether LXR-driven changes in microglia translated into functional recovery, we assessed large-scale cortical network dynamics using longitudinal widefield calcium imaging in Thy1-GCaMP6s mice. Functional connectivity analysis revealed that GW3965 treatment significantly enhanced interhemispheric correlations, particularly within the perilesional forelimb sensory and motor cortices (**Fig. 3L, M**; Suppl. Fig. 3L, M). These data indicate that pharmacological activation of cholesterol efflux restores long-range neuronal network integrity—a physiological correlate of behavioral recovery. To further test the therapeutic relevance of targeting microglial cholesterol crystals, we evaluated a second compound, 2-Hydroxypropyl-β-cyclodextrin (HβCD), which has been shown to enhance cholesterol solubilization and efflux in atherosclerosis models[53,58,59]. HβCD administration during the subacute phase significantly reduced microglial cholesterol crystal accumulation and improved neurological performance in the modified Neurological Severity Score (mNSS) test **Fig. 3N, O**). Together, these findings demonstrate that microglial cholesterol crystallization is a modifiable barrier to recovery and identify cholesterol efflux as a therapeutic axis to enhance repair after stroke.

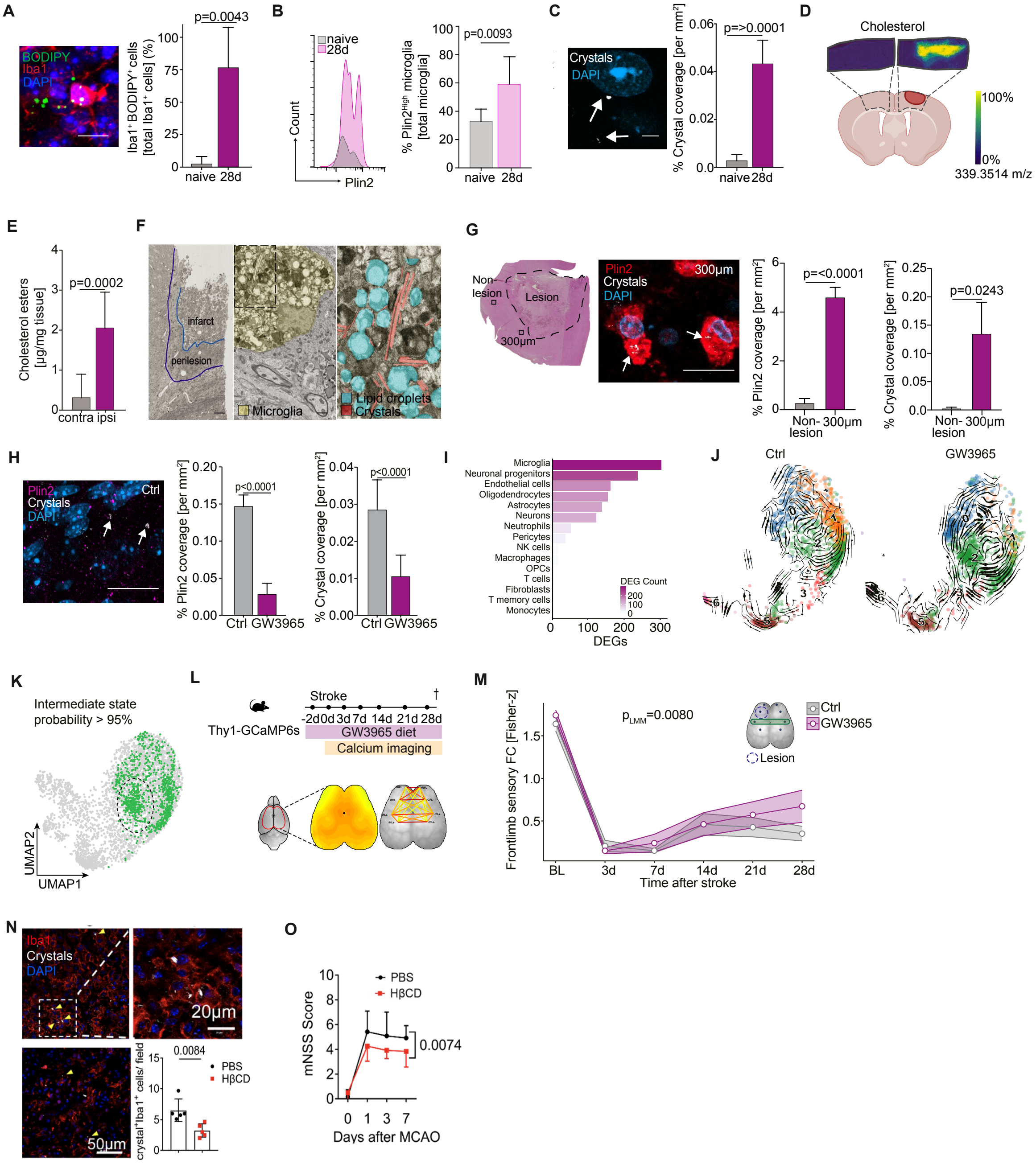

Figure 3. Microglial cholesterol crystallization impairs neuronal functional recovery after stroke. (**A**) Representative image and quantification of BODIPY$^+$(lipid particles) Iba1$^+$ (microglia) particles/ total BODIPY$^+$ particles 28 days after stroke (scale bar 10 µm; Mann-Whitney U test, n= 5-6 /group). (**B**) Microglia cells from brains of naïve mice and 28 days after stroke were analyzed by flow cytometry. Representation of Plin2 intensity graph in microglia (CD45^{int} CD11b$^+$) and quantification of Plin2^{High} (lipid droplets) microglia out of total microglia (T test, n=7/5 /group). (**C**) Representative image of crystals from the peri-infarct cortex of mouse brain tissue 28 days after stroke and quantification of crystal coverage at naive and 28 days after stroke. Arrows indicate crystals (scale bar 20 µm; Kruskal-Wallis test, n= 6 /group). (**D**) Representative image of MALDI-MSI cholesterol distribution (339.3514 m/z) in the ipsilateral and contralateral hemisphere of mouse brain tissue 28 days after stroke. (E) Quantification of cholesterol esters from contralateral and ipsilateral mouse brain cortical tissue 28 days after stroke (T test, n=6 /group). (**F**) Representative electron microscopy images of ipsilateral mouse brain tissue 28 days after stroke. Infarct and peri-lesion area outlined in blue and purple, respectively (left; scale bar 50 µm), microglia in the peri-infarct (yellow) loaded with lipids and crystals (middle; scale bar 2 µm), zoomed in image (right) of microglia loaded with lipid droplets (blue) and crystals (red). (**G**) Representative image of H&E human stroke brain tissue (left). Dashed line delineates lesion and boxes correspond to image locations of non-lesion area and 300 µm from the lesion border. Representative confocal images (center) and) quantification (right) of Plin2 immunofluorescence and reflection microscopy of crystals at non-lesion area and 300 µm from lesion border (scale bar 20 µm; T test, n= 9 /group). (**H**) Representative image in control and GW3965 peri-infarct cortex of Plin2 immunofluorescence and reflection microscopy of crystals 28 days after stroke. (Figure legend continued on next page)

White arrows indicate crystal localization (scale bar 5 µm; Mann-Whitney U test, *n*= 10/13 /group). (**I**) Number of differentially expressed genes in scRNA sequencing for mixed cell populations of the perilesional cortex 28 days after stroke in Ctrl and GW3965 treated animals. (**J**) Transition matrix from single-cell fate mapping analysis of microglia for Ctrl and GW3965 treated animals. (**K**) UMAP projection of microglia with a probability >95% to be in intermediate state. (**L**) Experimental scheme for assessment of neuronal connectivity via widefield calcium imaging in Thy1-GCaMP6s mice treated with GW3965 or Ctrl diet. (**M**) Longitudinal assessment of interhemispheric functional connectivity of frontlimb sensory cortex area in widefield calcium imaging (Median ± SE, linear-mixed model, post-hoc Kruskal-Wallis test, *n*= 10-15 /group /time). (**N**) Representative image and quantification of Iba1$^+$ crystal$^+$ cells in the cortex of control or HβCD treated mice (U test, *n*=5/5). (**O**) Evaluation of neurological function by the modified Neurological Severity Score (mNSS) (U test n=10/10).

Cholesterol crystals chronically activate the microglial inflammasome

Previous studies, particularly in atherosclerosis models, have linked intracellular cholesterol crystals to IL-1β production through activation of the NLRP3 inflammasome[52]. In the post-stroke brain, we similarly observed not only an early peak in IL-1β levels but also a previously unrecognized sustained elevation of IL-1β throughout the chronic recovery phase (Suppl. Fig. 4A). Consistently, pathway enrichment analysis of single-cell transcriptomic data at 28 days post-stroke highlighted the IL-1β signaling axis as a central inflammatory node, with multiple pathways converging on IL-1β regulation (**Fig. 4A, B**). Supporting clinical relevance, histological analysis of chronic human stroke autopsy tissue (1 month to 5 years post-stroke) revealed persistent IL-1β expression in microglia (**Fig. 4C**). We assessed the relationship between lipid droplet content (Plin2) and caspase-1 activity using the fluorescent probe FLICA660, revealing a significant correlation (**Fig. 4D**). ASC-Citrine reporter mice further demonstrated increased ASC-speck formation in perilesional microglia 28 days post-stroke, supporting chronic inflammasome activation (**Fig. 4E**). In vitro, cholesterol crystals induced ASC-speck formation in BMDMs (Suppl. Fig. 4B-D), confirming their catalytic effect. Elevated Galectin-3 levels—indicative of lysosomal damage from internalized crystals—reinforced the link between cholesterol accumulation, lysosomal stress, and inflammasome activation (Suppl. Fig. 4E).

Inflammasome activation is not the cause of impaired post-stroke recovery

Given the strong association between cholesterol crystals and IL-1β production, we tested whether pharmacologically-induced cholesterol export (GW3965 treatment – see Fig. 3) could suppress inflammasome activation. Indeed, we found reduced caspase-1 activity in perilesional microglia and significantly lower IL-1β levels in brain tissue at 28 days in GW3965-treated mice compared to controls (**Fig. 4F, G**). To directly test the role of inflammasome activity in post-stroke recovery, we assessed behavioral outcomes in caspase-1 knockout mice. Surprisingly, genetic deficiency of caspase-1 did not improve recovery across multiple domains, including coordination (rotarod test), sensorimotor integration (adhesive removal test), and general neurological function (neurological deficit score) but even further impaired neurological recovery (**Fig. 4H, I** and Suppl. Fig. 4F). These results indicate that while cholesterol crystal-induced inflammasome activation persists during the chronic phase, it is not the key mechanism limiting functional recovery, suggesting that other pathways must account for the beneficial effects of the GW3965 treatment seen in our experiments.

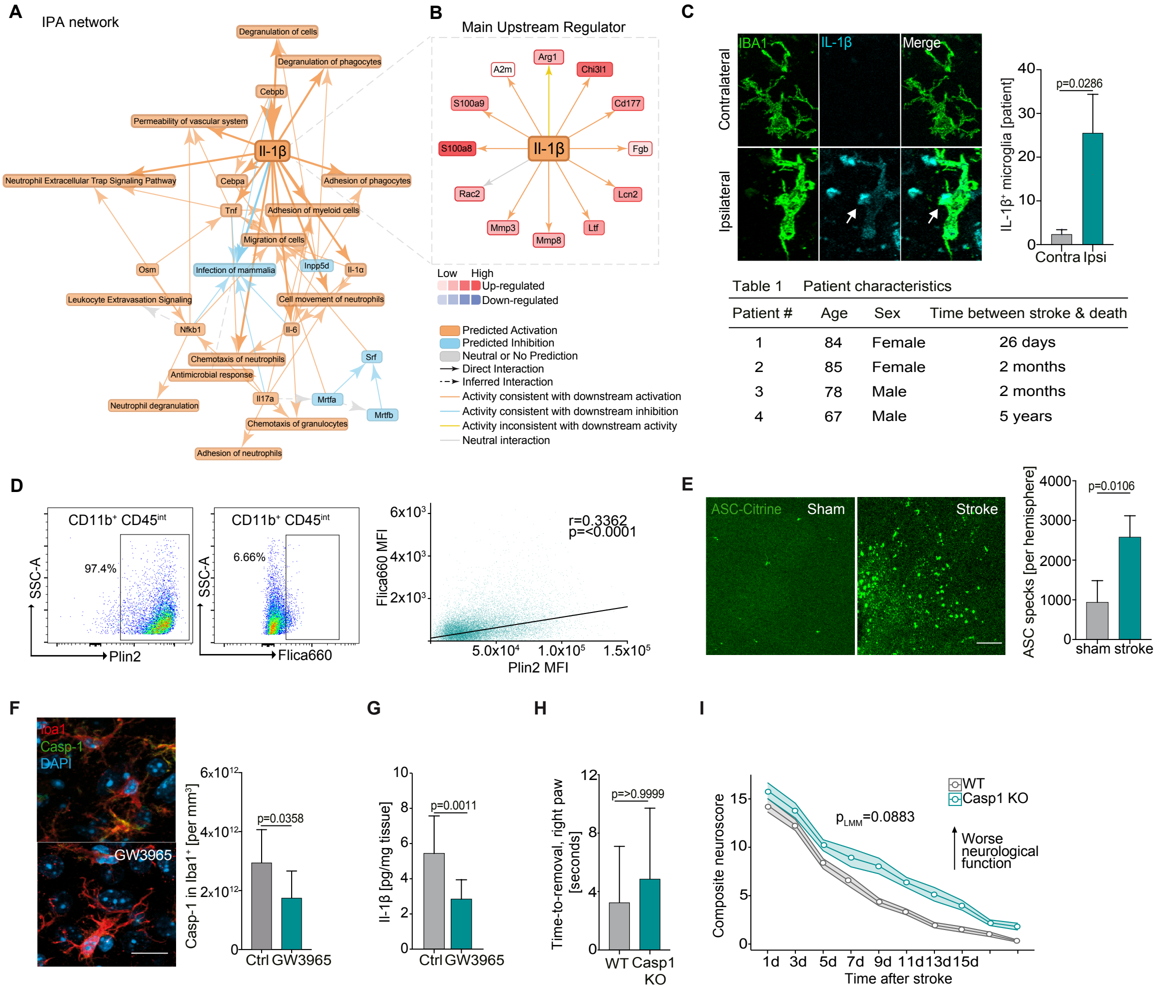

Table 1 Patient characteristics

Patient #	Age	Sex	Time between stroke & death
1	84	Female	26 days
2	85	Female	2 months
3	78	Male	2 months
4	67	Male	5 years

Figure 4. Cholesterol crystals induce chronic neuroinflammation. (**A**) Ingenuity Pathway Analysis (IPA) network of proteins in cluster 2 shows Il-1β as central regulator protein in the chronic lesion microenvironment (Fig. 2). (**B**) Protein expression regulated by main upstream regulator Il-1β. (**C**) Representative image and quantification of immunofluorescent staining of IBA1 (microglia) and IL-1β in contralateral and ipsilateral stroke human post-mortem brain tissue (test, *n=4 /group*) and patient characteristics table.(**D**) Representative flow cytometry gating strategy of microglia from ipsilateral cortical tissue of mice 28 days after stroke showing the mean fluorescent intensity and correlation of single cells between Plin2$^+$ (lipid droplets) and Flica660$^+$ microglia (active caspase enzymes) (Pearson's Correlation, *n*=8).(**E**) Representative image of ASC-Citrine speck formation in cortex from sham and 28 days after stroke with quantification (scale bar 100 µm, T test, *n=3/4* /group). (**F**) Representative images of control and GW3965 in the peri-infarct cortex of Caspase-1 (inflammasome activation) and Iba1 (microglia) immunofluorescence 28 days after stroke (scale bar 20 µm) and quantification of Caspase-1 in Iba1$^+$ cells (T test, *n*= 8 /group). (**G**) Il-1β levels in brain homogenate from peri-infarct cortical tissue of control and GW3965 mice 28 days after stroke (Mann-Whitney U test, *n*= 9/13 /group). (**H**) Chronic assessment of sensorimotor function using the adhesive removal test and quantifying time-to-remove with right front paw in WT or Caspase-1 KO mice after stroke (Two-way ANOVA, mixed effects model, Bonferroni, *n*= 10/18 /group). (**I**) Evaluation of neurological impairment by composite neuroscore in WT or Caspase-1 KO mice after stroke (Mean ± SEM, linear-mixed model, *n*= 20/14 /group).

Pharmacological cholesterol efflux promotes microglia-to-oligodendrocyte lipid transfer and restores oligodendrocyte maturation

To determine the fate of cholesterol exported by pharmacologically activated microglia, we first quantified lipid concentrations in cerebrospinal fluid (CSF) from mice treated with the LXR agonist GW3965 or vehicle for 28 days post-stroke (**Fig. 5A**). Unexpectedly, lipidomic analysis revealed no significant changes for any of the lipid species between treatment groups (**Fig. 5B**), including no detectable difference in CSF cholesterol levels (Suppl. Fig. 5A). These findings suggest that exported cholesterol is not drained via CSF but may instead be locally recycled within the brain parenchyma.

To identify potential recipient cells for microglial lipid export, we analyzed lipoprotein receptor expression across major brain cell types using our integrated single-cell transcriptomic dataset. This revealed oligodendrocytes as the predominant expressers of the ApoE receptors Sortilin-1 (*Sort1*)[60] and the very low-density lipoprotein receptor (*Vldlr*) (**Fig. 5C**), suggesting a capacity for active cholesterol uptake from the microenvironment particularly by oligodendrocyte lineage cells. We next assessed transcriptional signatures of oligodendrocytes in perilesional tissue using spatial MERFISH data (see Fig. 2). Chronic stroke induced marked transcriptional changes in oligodendrocytes, including upregulation of *C4b*, *Serpina3n*, *Klk6*, *Socs3*, and *Gfap*—genes associated with cellular stress, injury responses, and a reactive, pro-inflammatory phenotype (**Fig. 5D–E**; Suppl. Fig. 5B–C)[61,62]. In line with these findings, cell–cell interaction analysis revealed dysregulation of Tenascin C signaling (cp. Fig. 2J, a pathway critical for oligodendrocyte maturation and myelination[63,64]. Notably, GW3965 treatment attenuated these maladaptive transcriptional programs. Oligodendrocytes from treated mice exhibited significant downregulation of stress-associated genes such as *C4b*, *Serpina3n*, and *Klk6* (**Fig. 5F**), indicating a partial restoration of homeostatic function. Immunohistochemical analyses further confirmed that GW3965 significantly increased the number of mature, myelinating oligodendrocytes and oligodendrocyte precursor cells in the perilesional cortex (**Fig. 5G–H**).

To test whether LXR-induced cholesterol efflux facilitates microglia-to-oligodendrocyte lipid transfer, we developed a humanized iPSC-based transwell co-culture system (**Fig. 5K**). Human microglia were first loaded with fluorescently labeled cholesterol (TMR-cholesterol) for 2 hours and then co-cultured with human oligodendrocytes. Following treatment with GW3965 or vehicle, microglia were removed after 24 hours and TMR-cholesterol uptake by oligodendrocytes was quantified. This assay demonstrated a substantial increase in lipid transfer from GW3965-treated microglia, whereas cholesterol shuttling under control conditions was minimal (**Fig. 5L**). Importantly, this enhanced lipid transfer correlated with a significant increase in cortical myelination within the perilesional tissue at 28 days post-stroke (**Fig. 5I-J**), a key prerequisite for efficient cortical network reorganization and functional recovery after CNS injury[65-67]. Taken together, these findings identify microglia-to-oligodendrocyte lipid recycling as a critical cellular mechanism underlying the pro-regenerative effects of LXR activation. By enabling local redistribution of cholesterol from reactive microglia to oligodendrocytes, pharmacological LXR activation restores cellular homeostasis in the chronic lesion environment, thereby facilitating remyelination and network repair. This represents a mechanistically novel therapeutic strategy to enhance endogenous recovery processes in the chronic post-stroke phase.

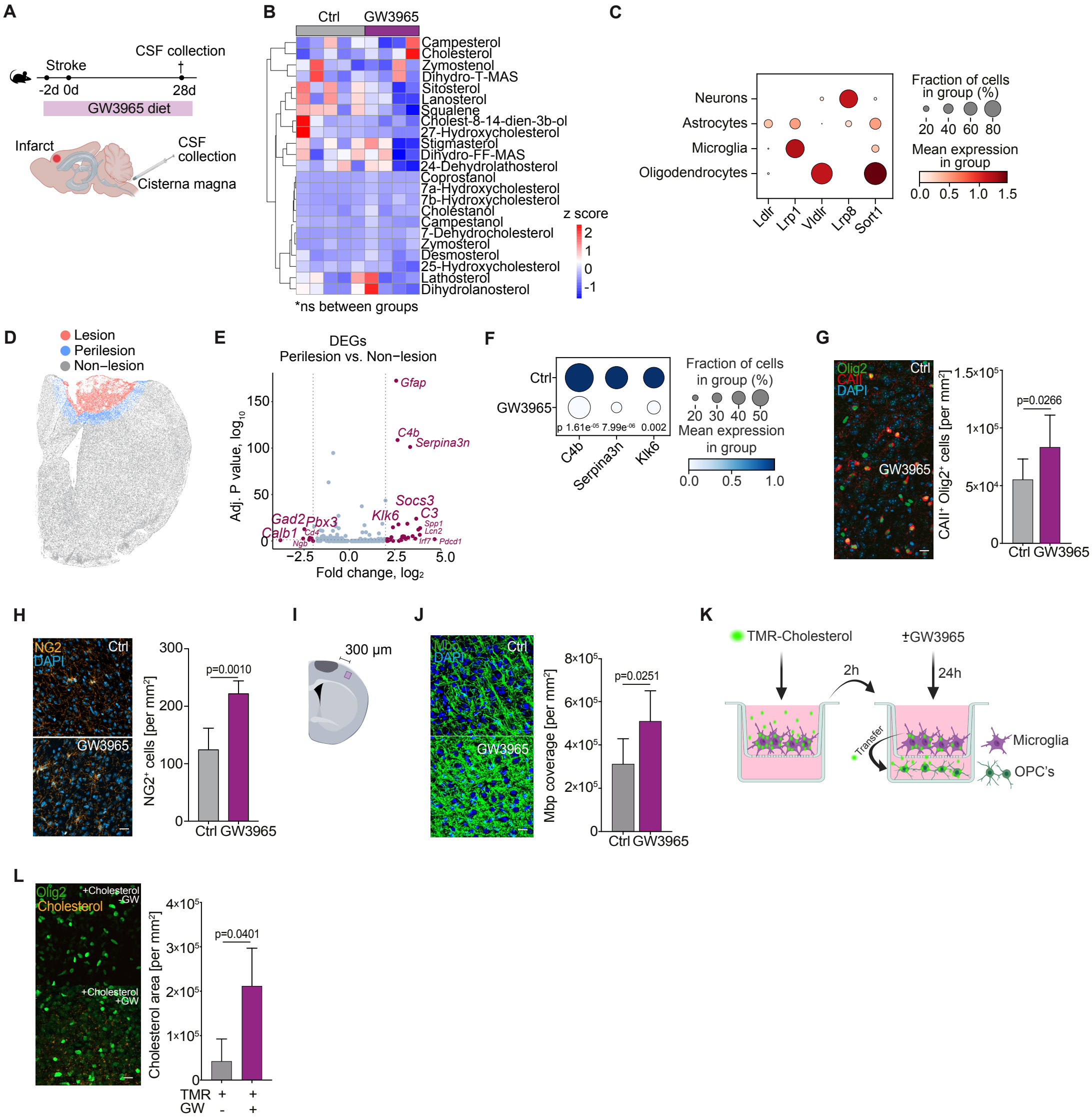

Figure 5. **Enhancing cholesterol efflux improves chronic microglia function and post-stroke recovery.**
(**A**) Experimental scheme for CSF collection 28 days after PT from GW3965 and Ctrl mice. (**B**) Heat map showing lipid species (z scores) detected in CSF collected 28 days after PT from GW3965 and Ctrl mice showing no significant different between groups (p=<0.05) (U tests with Benjamini-Hochberg correction, *n*= 5/4 /group). (**C**) Expression level of *Ldlr*, *Lrp1*, *Vldlr*, *Lrpp8*, and *Sort1* in neurons, astrocytes, microglia, and oligodendrocytes 28 days post stroke. Dot size represents fraction of cells in cell group (%), color code represents mean expression level in each cell group. (**D**) Indication of lesion area (red), peri-lesional area (blue) and non-lesioned area (grey) in representative MERFSIH spatial transcriptomics section. (**E**) Differentially expressed genes of oligodendrocytes located in the perilesional vs non-lesioned area. (**F**) Single-cell gene expression levels of *C4b*, *Serpina3n*, and *Klk6* in oligodendrocytes from Ctrl and GW3965 treated animals. Dot size represents fraction of cells in cell group (%) expressing the gene, color code represents mean expression level in each cell group. (**G**) Representative immunostaining images and quantification of Olig2 and CAII (myelinating oligodendrocytes) in the peri-infarct cortex of control and GW3965 treated mice 28 days after stroke (scale bar 20 µm; T test, *n*= 8-9 /group). (**H**) Representative images and quantification of NG2$^+$ oligodendrocyte progenitor cells (OPC's) in the peri-infarct cortex 28 days after stroke (scale bar 20 µm; T test, *n*=5 /group). (**I**) Scheme of confocal microscopy imaging positions for (**J**) analysis of myelin basic protein (Mbp) coverage in the perilesional cortex between indicated treatment groups. (**K**) Schematic representation for co-culture experiment of human iMG and iOPCs, where iMG were first loaded with TMR-cholesterol and then treated with either control or GW3965. (**L**) Quantification of cholesterol uptake (i.e.area of TMR-cholesterol) in iOPCs (scale bar 20 µm; n=3 /group, T test), indicating substantial increase in cholesterol uptake of cholesterol from GW3965-treated iMG.

Discussion

In this study, we identify a previously unrecognized mechanism by which impaired cholesterol handling in microglia limits structural and functional recovery after stroke. We show that microglia adopt a distinct RAM state during the chronic phase, characterized by intracellular cholesterol crystal accumulation due to insufficient lipid export. This crystalline burden chronically activates the inflammasome, yet unexpectedly, inflammasome signaling does not mediate the impaired recovery phenotype. Instead, we uncover a novel mechanism of microglia-to-oligodendrocyte lipid recycling that promotes remyelination and cortical network repair. By pharmacologically restoring microglial cholesterol efflux, we not only reverse maladaptive microglial states but also enhance intercellular lipid transfer and support oligodendrocyte maturation, ultimately driving functional recovery. These findings define cholesterol redistribution as a key axis in the multicellular coordination of brain repair.

Our data expand current concepts of microglial activation states by identifying RAM as a distinct population emerging in the chronic post-stroke brain. Unlike homeostatic, DAM, or LAM phenotypes described in aging and neurodegeneration[2,24,34,48,49], RAM are characterized by both persistent reactivity and impaired clearance capacity. This transcriptional and functional divergence reflects the unique demands of post-ischemic repair, where microglia must reconcile inflammatory signaling with tissue remodeling. The spatial enrichment of RAM in perilesional zones and their dominant contribution to the chronic secretome emphasize their central role in shaping the local repair milieu. Despite their dysfunctional features—such as reduced phagocytic activity and dysregulated lipid handling—RAM appear essential for recovery, as their depletion impaired functional outcomes and pharmacological reprogramming using TREM2 agonism failed to enhance repair. These findings underscore the need to study microglial heterogeneity in injury-specific contexts rather than extrapolating from neurodegenerative models.

A key mechanistic insight from our study is the link between defective cholesterol efflux and microglial dysfunction. RAM fail to resolve intracellular lipid stores, leading to the formation of cholesterol crystals. These findings align with recent reports suggesting reduced expression of ABC transporters in microglia compared to peripheral macrophages[68-71], making them particularly susceptible to lipid overload. The persistence of cholesterol crystals into the chronic phase suggests a failure of endogenous resolution mechanisms, with implications for long-term microglial impairment and synaptic dysfunction. Importantly, pharmacological activation of LXRs—nuclear receptors that regulate cholesterol efflux—restored microglial lipid homeostasis, reduced crystal formation, and shifted microglia toward a more pro-regenerative state. These effects position LXR agonism as a promising strategy to counteract microglial metabolic failure in the injured brain. Notably, the increased lipid export induced by LXR activation did not result in elevated cholesterol concentrations in the CSF, arguing against glymphatic clearance as the principal route of disposal[72]. Instead, our data support a model in which excess lipids are redistributed locally within the perilesional tissue microenvironment, emphasizing the importance of cellular lipid exchange over bulk drainage in chronic brain repair.

Although cholesterol crystals are well-established activators of the NLRP3 inflammasome[52], our data reveal that inflammasome activation, while persistently elevated, does not critically limit post-stroke recovery. Genetic deletion of caspase-1 failed to improve behavioral outcomes, indicating that chronic inflammation alone is not the primary driver of impaired repair. Instead, our findings highlight a previously underappreciated axis of glial interaction: lipid recycling from microglia to oligodendrocytes. Pharmacological enhancement of cholesterol export via LXR activation promoted oligodendrocyte maturation and increased cortical myelination—both essential for restoring network connectivity[67,73]. In vitro assays confirmed that this lipid transfer is an inducible, regulated process rather than passive diffusion. These results suggest that microglia, beyond their classical roles in surveillance and inflammation, can provide metabolic support to other glial cells in the form of lipid cargo. Strengthening this glia–glia communication axis offers a mechanistically distinct and potentially more effective strategy to promote recovery after CNS injury.

The clinical relevance of our findings is supported by multiple lines of translational validation. In human autopsy tissue from chronic stroke patients, we observed perilesional microglial accumulation of lipid droplets and cholesterol crystals, as well as sustained IL-1β expression—mirroring the murine phenotype. In vitro, the ability of human iPSC-derived microglia to transfer cholesterol to human iPSC-derived oligodendrocytes confirms the existence of this mechanism in the human system. While prospective clinical imaging studies (e.g., using MR spectroscopy) are needed to validate cholesterol accumulation or clearance non-invasively, our data offer a strong rationale to explore cholesterol handling as a biomarker and potential therapeutic target in chronic brain injury.

In contrast to existing lipid-lowering therapies such as statins, which primarily target plasma lipoproteins via HMG-CoA reductase inhibition[74], our approach targets a distinct biological process: the redistribution of cholesterol between brain-resident cells via increased expression of cholesterol transporters. This distinction is clinically relevant. Statins reduce systemic lipid levels but have shown mixed results in neurorepair, potentially due to their inability to modulate glial lipid metabolism[75-78]. By enhancing intracellular cholesterol efflux in microglia, we enable redistribution to oligodendrocytes—an effect that directly supports remyelination and network re-integration.

Limitations of the study

While our findings highlight LXR agonism as a promising strategy for brain repair, the specific compound used here, GW3965, is not currently suitable for clinical application due to previously reported adverse events in systemic administration including effects on immune function and hepatic lipogenesis[79]. However, this limitation could potentially be overcome through strategies such as brain-targeted delivery (e.g., transferrin receptor-mediated brain shuttle systems)[80] or the development of next-generation LXR modulators with improved pharmacokinetic and safety profiles. Additionally, while we demonstrate improved functional and network recovery in mice, validation of these effects in other preclinical models including large animal models and ultimately in clinical trials will be necessary.

Acknowledgments

The authors thank Christina Fürle and Kerstin Thuß-Silczak for excellent technical support. The study was supported by the Vascular Dementia Research Foundation, the European Research Council (ERC-StG 802305), the German Research Foundation (DFG) under Germany´s Excellence Strategy (EXC 2145 SyNergy – ID 390857198), through FOR 2879 (ID 405358801), TRR 274 (ID 408885537), TRR 355 (ID 490846870), SPP 2395 (ID 461101128).

Author contributions

Conceptualization, K.P., S.H., A.L.; Investigation, K.P., S.H., D.V., N.S., Y.Z, S.K., M.S., G.L., S.R., O.C., E.S., C.M., L.H., N.I., P.A., J.G., R.F., N.L., B.H.; Formal Analysis, K.P., S.H., D.V., N.S., Y.Z, S.K., M.S., G.L., E.S., C.M., L.H., N.I., P.A., J.G., R.F., O.G., P.L. H.S., B.H., M.G.; Resources, S.B., C.H., S.J., D.P., T.M., O.G., M.S., A.D., P.L., M.G; Writing – Original Draft, K.P., S.H., A.L.; Writing – Review & Editing, K.P., S.H., A.L.; Visualization, K.P., S.H., P.L., B.H., M.G, A.L.; Supervision: C.H., S.J., D.P., T.M., O.G., M.S., A.D., H.S., P.L., M.G., A.L.; Funding Acquisition: C.H., S.J., D.P., T.M., O.G., M.S., A.D., P.L., B.H., M.G., A.L.

Declaration of interests

All authors declare no competing interests.

TRANSCRIPTOMIC DATA AND CODE AVAILABILITY

Accession numbers are also listed in the key resources table. Custom written scripts for bioinformatic analysis will be made available in a github repository upon publication (https://github.com/Lieszlab). Transcriptomic data have been submitted to GEO and will be made available upon publication. Any additional information required to reanalyze the data reported in this paper is available from the lead contact upon request.

EXPERIMENTAL MODEL AND STUDY PARTICIPANTS DETAILS

Animal experiments

All experiments in this study were conducted in accordance with the national guidelines for animal experiments and approved by the German governmental committees (Regierungpräsidium Oberbayern, Munich, Germany). For single cell RNA sequencing and immunohistochemical analyses, the animals were 8 to 12 weeks old male C57BL/6J mice (Charles River Laboratories). For *in vivo* widefield calcium imaging and dendritic Golgi spine analysis the animals were 12-15 weeks old male and female C57BL/6J-Tg(Thy1-GCaMP6s)GP4.12Dkim/J (here termed: Thy1-GCamp6s) (Dana et al., 2014) heterozygous mice, bred at the Institute for Stroke and Dementia Research, Munich (> 12 generations backcrossed on C57Bl6/J WT mice). For two-photon imaging the animals were 8-10 weeks old male C57BL/6-*Tmem119*$^{em2(EGFP)Gfng}$/J animals (here termed: Tmem119-EGFP) (Stock No: 031823 | Tmem119-2A-EGFP, Jackson Laboratory). For Caspase-1 mouse experiments, 8-10 weeks old Caspase-1 cKO male animals were used that were bred at the institute for Stroke and Dementia Research, Munich (> 12 generations backcrossed on C57Bl6/J WT mice). For inflammasome activation experiments through ASC-speck formation, 8-10 weeks old ASC-Citrine animals were used that were bred at the institute for Stroke and Dementia Research, Munich (> 12 generations backcrossed on C57Bl6/J WT mice). The animals were housed under controlled temperature (22 ± 2 °C) with a 12-hour light-dark cycle and access to food and water ad libitum. All animal experiments were performed and reported in accordance with the ARRIVE guidelines (Kilkenny et al., 2010).

METHOD DETAILS

Photothrombotic stroke model

For photothrombotic stroke (PT) induction, mice were anaesthetized with isoflurane, delivered in a mixture of 30% O_2 and 70% N_2O. Mice were placed into a stereotactic frame, and body temperature was maintained at 37 °C with a mouse warming pad. Dexpanthenol eye ointment was applied to both eyes. Animals received 10 µl/g body weight of 1% Rose Bengal (Sigma, 198250-5g) in saline intraperitoneally (i.p.) 5 minutes prior to the induction of anesthesia (5% isoflurane). A skin incision was used to expose the skull. Bregma was located and the lesion location was marked in the left hemisphere (1.5 mm lateral and 1.0 mm rostral to bregma). For *in vivo* widefield calcium imaging experiments, PT was induced as previously described [1]. In brief, an independent vector analysis (IVA) was performed based on baseline resting state imaging, which allowed to define cortical functional regions as independent components. The independent component in the primary motor cortex was then used to individually define the lesion location for every mouse. Shielding was placed on the skull allowing a 2.0 mm diameter circular light exposure over the lesion area. Ten minutes after Rose Bengal injection the laser (25 mV output) was applied to the lesion area for 17 minutes. Cobolt Jive 50, 561 nm Power at 25 mV. Fiber Collimation Package: 543 nm f=7.66 mm, FC/APC (beam diameter d ≈ (4)(0.000561 mm)[7.86 mm / (pi * 0.004 mm)] = 1.4 mm). Sham procedure was performed analogous, but without laser illumination.

Permanent distal cerebral artery occlusion model

Permanent occlusion of the distal MCA (dMCAo) was performed as previously described [2]. Briefly, mice were anaesthetized with isoflurane delivered in 100% O_2 and placed in lateral position. After a skin incision between eye and ear, the temporal muscle was removed and the MCA identified. Then, a burr hole was drilled over the MCA and the dura mater was removed. The MCA was permanently occluded using bipolar electrocoagulation forceps. Permanent occlusion of the MCA was visually verified before suturing the wound. After recovery, the mice were kept in their home cage with facilitated access to water and food. Body temperature was maintained at 37 °C throughout surgery using a feedback-controlled heating pad. Exclusion criteria: Artery broken during surgery and/or major bleeding artery and remaining blood between the brain and skull.

Transient proximal cerebral artery occlusion model

Transient intraluminal occlusion of the middle cerebral artery (MCA) (fMCAo) was performed as previously described. Briefly, mice were anaesthetized with isoflurane delivered in 100% O_2 [3]. A midline neck incision was made and the common carotid artery and left external carotid artery were isolated and ligated; a 2 mm silicon-coated filament was introduced via a small incision in the external carotid artery and advanced towards the internal carotid artery, therefore occluding the MCA. MCA was occluded for 60 min for the transient MCAo stroke model. After occlusion, the animals were re-anesthetized, and the filament was removed. MCA occlusion and reperfusion were confirmed by the corresponding decrease or increase in the blood flow, respectively, measured by a laser Doppler probe affixed to the skull above the MCA territory (decrease in the laser Doppler flow signal > 80% of baseline value and increase in the laser Doppler flow signal > 80% of baseline value before reperfusion). After recovery, the mice were kept in their home cage with facilitated access to water and food. Body temperature was maintained at 37 °C throughout surgery using a feedback-controlled heating pad. The overall mortality rate of stroke mice was approximately 30%. Exclusion criteria: 1. Insufficient MCA occlusion (a reduction in blood flow to > 20% of the baseline value); 2. Insufficient MCA reperfusion (an increase in blood flow of > 80% of the baseline value before removing the filament); 3. Death during the surgery.

Organ and tissue collection

Mice were terminally anesthetized with ketamine (120 mg/kg) and xylazine (16 mg/kg). Immediately after cardiac puncture, mice were transcardially perfused with 0.9% NaCl containing Heparin (2U/mL) and the brain were carefully excised and processed according to the specific endpoint.

CSF Collection

Mice were anesthetized and positioned in a stereotaxic frame with the head slightly tilted to form a 120° angle relative to the body. A small incision was made in the neck region between the ears to expose the underlying muscles, which were separated along the midline to access the cisterna magna (CM). Cerebrospinal fluid (CSF) was collected using a custom-made cannula consisting of a glass capillary (inner diameter: 0.67 mm; outer diameter: 1.20 mm) attached to polyethylene tubing (inner diameter: 0.86 mm; outer diameter: 1.52 mm). The glass capillaries were sharpened using a flaming micropipette puller and mounted on the micromanipulator arm of the stereotaxic frame. Approximately 10 µL of CSF was collected per mouse.

Drug administrations

GW3965

Considering an average mouse weight of 32 g and a food consumption of 4 g/day, the dose of the treatment was 20 mg GW3965/(kg (body weight) × day). Diet containing GW3965 was supplied from 2 days prior to stroke induction and for the duration of the experiment.

4D9 antibody

Isotype and 4D9 antibody materials were produced, characterized, and assessed for quality performed at Denali Therapeutics as previously reported[4]. Mice were intraperitoneally administered a dose of 50 mg/kg (body weight) of isotype control antibody or 4D9 antibody cloned into a mouse backbone at 7, 14, 21, 28 and 35 days after stroke induction.

PLX5622

Microglia depletion was performed as previously described [5] and mice were treated with the CSF1R inhibitor, PLX5622 (1,200 mg PLX5622 in 1 kg chow; Plexxikon Inc.) supplied via the chow diet or with control diet for 2 weeks before PT induction until 42 days after stroke. Body weight was monitored throughout the treatment time.

Neuroscore

The multiparameter neuroscore was assessed as previously described [6]. Briefly, the score is composed of the assessment of several subtests of both global and focal deficits. Assessment of global deficits included grooming, status of ears and eyes, posture, spontaneous activity and epileptic behavior. Focal deficits were evaluated by gait, grip, forelimb-asymmetry during tail suspension, circling behavior of both entire body or only forelimb, body symmetry and whisker response. Total score ranges from 0 to 54 points (26 point for general and 28 for focal deficits), higher score indicating worse neurological deficits. Data was acquired once before stroke (baseline) and on day 3, 7, 14, 21, 28 and 42 after stroke.

Rotarod test

The rotarod test was performed as previously described[7]. Mice were trained daily for 3 days before baseline acquisition and surgical procedure (transient MCA occlusion or sham). Baseline performance was acquired using the following strategy: the rod accelerated continuously from 8 to 40 rpm over 240 s. Per mouse and time point three consecutive trials were acquired. The latency to fall off the rod was recorded, and postsurgical performance was calculated by dividing the mean of the postsurgical performance with the individual animal's baseline performance.

Adhesive removal test (ART)

The adhesive removal test was performed as previously described and used to evaluate sensory and motor deficits[7]. A round (4 mm-diameter) adhesive sticker (Neolab) was placed on the palmar side of the forepaw; same pressure was applied for each adhesive application. 2 days before baseline acquisition mice were habituated to the test cage and the adhesive placement. Baseline and (postsurgical time points) were acquired as three consecutive trials per mouse. The latency to first contact paw with adhesive and the latency to remove the adhesive completely were recorded. Motor performance was expressed as the difference between the latency to contact the paw and the latency to remove the adhesive.

Modified Neurologic Severity Score (mNSS)

The mNSS assessment, which consists of motor, reflex, and balance tests, to continuously evaluate the neurological deficits on days 0, 1, 3, 7 days after reperfusion. The mNSS scores range from 0 to 14 points, and higher scores indicate more neurological severe impairment [8].

In vivo positron emission tomography (PET) and magnetic resonance (MR) imaging

In vivo PET and MR imaging was performed as previously described [9]. Briefly, mice were scanned at 7, 28, and 84 days after PT induction using a 3T Mediso nanoScan PET/MR scanner (Mediso Ltd, Hungary) with a single-mouse imaging chamber. The mice received an intravenous injection of 18.0 ± 2.1 MBq [18F]GE-180 through the tail vein. For static PET imaging, the list-mode data were acquired at 60-90 min p.i.. A 15-min anatomical T1 MR scan was performed at 30 min after [18F]GE-180 injection (head receive coil, matrix size 96 × 96 × 30, voxel size 0.21 × 0.24 × 0.65 mm^3, repetition time 677 ms, echo time 28.56 ms, flip angle 90°). The T1 image was then used to create a body-air material map for the attenuation correction of the PET data. PET list-mode data were reconstructed within a 400-600 keV energy window using a 3D iterative algorithm (Tera-Tomo 3D, Mediso Ltd, Hungary) with the following parameters: matrix size 55 × 62 × 187 mm^3, voxel size 0.3 × 0.3 × 0.3 mm^3, 8 iterations, 6 subsets. Decay and random correction were applied.

PET Image Data Processing

Image processing was performed using PMOD View and Fuse It tools (version 4.005, PMOD Technologies, Zurich, Switzerland). The T1 MR images were deformably registered to a high-resolution (0.2 × 0.2 × 0.2 mm^3) built-in MRI template using the SPM5 procedure, and the Ma-Benveniste-Mirrione atlas [10,11] was applied to the image to obtain the cerebellum and the cortex volume of interest (VOI). Within the cerebellum VOI, we defined an elliptical volume that represented the cerebellar white matter (CBWM). The elastic transformation was applied to the corresponding PET image. Then, a predefined individual VOI in the PT area was manually segmented using the 7-day T1 MR image. This VOI was dilated by 1 mm at all borders, for including microglia located in the perilesional area. Finally, this VOI was cropped by the cortex VOI and defined as the PT VOI in each animal. The standardized uptake value ratios (SUVR) in the PT VOI were calculated by normalizing the PT VOI mean uptake by the CBWM VOI mean uptake.

In vivo widefield neuronal calcium imaging

To assess calcium dynamics in cortical layer 2/3 excitatory neurons, Thy1-GCaMP6s heterozygous mice (C57BL/6J-Tg(Thy1-GCaMP6s)GP4.12Dkim/J,[12]) were used as previously described[1]. A cranial imaging window was surgically prepared at least three days prior to the first imaging session. Animals were anesthetized with inhaled isoflurane (5% induction, 2% maintenance) in a gas mixture of 70% nitrous oxide (NO) and 30% oxygen (O_2) and positioned prone in a stereotaxic frame (Stoelting, Europe, #51501). The skin and underlying connective tissue covering the skull were carefully removed, and the exposed skull surface was cleaned. Transparent dental cement (Quick Base S398, L-Powder clear S399, Universal Catalyst S371, Parkell C&B metabond, USA) was gently applied to the intact skull, and a custom-sized glass coverslip (Menzel-Gläser, 24×60 mm, thickness #1.5) was secured in place. Animals remained anesthetized until the cement fully hardened and were allowed to recover at least 72 hours before imaging.

In vivo widefield imaging acquisition was performed as previously described [1]. For resting state *in vivo* imaging sessions, mice received medetomidine (0.05 mg/kg body weight, intraperitoneally) five minutes before anesthesia induction with 5% isoflurane in 70% NO and 30% O_2. Once anesthetized and fixed in the stereotaxic frame, anesthesia was gradually reduced—initially to 1.5% for 140 seconds, then to 0.75% for two additional minutes to achieve stable anesthesia. Resting state *in vivo* imaging was performed in mild anesthesia (0.5mg/kg body weight of Medetomidin with 0.75% isoflurane inhalation). For Fig. 1 and Suppl. Fig. 1D widefield calcium imaging was conducted using a previously described customized macroscopic imaging set-up [1]. Briefly, mice were placed in a stereotactic frame and mouse cortex was illuminated with 450 nm blue LED light. Resting state calcium activity was recorded for 4 minutes (6×1000 frames) with a high precision 2/3" Interline CCD camera (Adimec-1000m/D, Adimec, pixel size 7.4×7.4 µm, Netherlands, acquisition at 20-22 °C) at 25 Hz frame rate using longDaq software (Optical Imaging Ltd, Israel). For Suppl. Fig 1H and Fig. 3 the widefield imaging setup was further modified to include a custom-built mesoscale imaging system. This setup included a high-speed sCMOS camera (Andor Zyla 5.5, Oxford Instruments) and a 475 nm LED illumination source equipped with a laser line filter and collimating lens (Thorlabs). The system allowed visualization of cortical regions across both hemispheres through the intact skull, providing a 10×10 mm field of view with a resolution of 512×512 pixels. Imaging sessions lasted 4 minutes with a 50 Hz acquisition rate, capturing fluorescent and non-illuminated background control signals sequentially, under controlled conditions without ambient illumination. Each mouse underwent imaging sessions for baseline one day prior to stroke induction, followed by sessions on days 3, 7, 14, 21, 28, and 42 (Fig. 1 and Suppl. Fig 1) post-stroke. A photothrombotic stroke lesion was formed over the left motor cortex. After each imaging session, anesthesia was reversed using atipamezole (0.1 mg/kg, intraperitoneal injection). Body temperature was continuously maintained using a feedback-controlled heating system during all procedures, and mice recovered fully in a heated chamber post-imaging.

In vivo widefield calcium imaging analysis

Data preprocessing and functional connectivity analyses were performed as previously described[1,5], with additional analytical methods developed specifically for this study. All analyses were executed using custom-written MATLAB scripts (Mathworks, R2016b).

For Suppl. Fig 1H and Fig. 3, imaging data was first motion corrected by rigid geometric transformations aligning each frame to an averaged reference frame. Background subtraction was performed by subtracting the corresponding non-illuminated control frame from each fluorescent image. Fluorescence intensity was then normalized relative to the mean signal across the recording period for each pixel ($\Delta F/F$). Subsequently, a mild Gaussian 2D noise filter was applied to reduce minor imaging artifacts, followed by temporal filtering using a Chebyshev bandpass filter between 0.005 and 2 Hz, corresponding to the expected firing rates and GCaMP6s fluorescence kinetics of Thy1 cortical neurons. Seed-to-seed functional connectivity was computed by determining Pearson correlation coefficients between predefined bilateral homotopic seed regions of interest (ROIs) associated with hindlimb and forelimb sensory cortices. Correlation coefficients were Fisher's z-transformed, and connectivity changes were longitudinally assessed across imaging sessions. For sensory homotopic connectivity, the mean of the Fisher's z transformed Pearson's correlation coefficient of the connection between the seeds located in the ipsi and contralateral sensory cortex was calculated. The hindlimb sensory and frontlimb sensory connectivity was calculated as the Fisher's z transformed Pearson's correlation coefficients of the homotopic connection between the hindlimb sensory or frontlimb sensory seeds in both hemispheres, respectively. The time course of homotopic connectivity was displayed from baseline and weekly until day after stroke, ensuring the visibility of all seeds after exclusion of the PT lesion area. Fisher's z transformed Pearson's correlation was calculated using

MATLAB® (Mathworks R2016b with Optimization Toolbox, Statistics and Machine Learning Toolbox, Signal Processing Toolbox and Image Processing Toolbox).

Longitudinal lesion involution quantification

Lesion size was determined by autofluorescence of the ischemic tissue in Thy1-GCaMP6s animals used for *in vivo* widefield calcium imaging for every timepoint of imaging acquisition. The area of autofluorescent pixels was previously defined by thresholding and converted into a mask to exclude autofluorescent tissue from the connectivity analysis. The lesion was determined as the size of the exclusion mask by quantification of all pixels within the mask.

Brain processing for histology

Mouse

Mice were deeply anesthetized and euthanized as described previously. Brains were carefully excised and immersed in 4% paraformaldehyde overnight. Brains were embedded in 4% agarose (Avantor) and coronally sectioned into 100 µm thick free-floating sections by vibratome (Lieca) stored in PBS at 4 °C. For NG2 (Millipore) immunoflourescent staining, brains were coronally cut into 20 µm thick sections by cryostat (Lieca) and mounted onto slides and stored at -80 °C.

Human

Human brain tissue was obtained from adult subjects with ischemic stroke. Perfused human tissue blocks were embedded into 4% agarose and 60 µm thick free floating sections were cut by vibratome (VT1200S, Leica) and stored in PBS at 4 °C.

Immunofluorescence staining

Mouse tissue

Perfused mouse tissue sections were incubated with blocking solution containing 2% serum (Thermo Fisher/ abcam), 1% BSA (Sigma), 0.1% cold fish skin gelatin (Sigma), 0.1% Triton X-100 (Sigma), 0.05% Tween 20 (Roth) in PBS for 1 h at RT. If BODIPY or Plin2 were used, the sections were incubated with 0.1% Triton X-100 briefly prior to primary antibody incubated and Triton X-100 and Tween20 were omitted from the blocking solution. Sections were then incubated in primary solution containing 1% BSA (Sigma), 0.1% cold fish skin (Sigma) and 0.1% Triton-X 100 (Sigma) with the primary antibodies in against Iba1 (1:200, Fuiji), P2y12 (1:200; AnaSpec), NG2 (1:500), CAII (1:200, R&D), Mbp (1:200; Millipore), Olig2 (1:200), Plin2 (1:200; Novus), Gal3 (1:200), Caspase-1 (1:200) overnight at 4 °C. If BODIPY or Plin2 were used, Triton X-100 was omitted in the primary antibody solution. Next, sections were washed in PBS and incubated with Alexa Flour antibodies (1:200) in PBS and 0.05% Tween 20 in the dark for 2 h at RT. If BODIPY or Plin2 were used, Tween 20 was omitted. After washing with PBS, sections were stained with DAPI (1:4000) for 2 min (Thermo Fisher) and mounted with Fluoromount™ Aqueous Mounting medium (Sigma). If BODIPY was used, sections were incubated for 15 min at RT (1:5000) prior to DAPI staining. Sections also imaged for crystals were done in reflection mode. Images were acquired in a confocal microscope at 40× or 60× magnification (LSM 880, LSM 980; Carl Zeiss, Germany). Cholesterol crystals in the peri-infarct areas were visualized with standard polarized light microscopy using an Olympus microscope[13].

Human tissue

Perfused human tissue sections were washed in 0.1 M PB for 5 minutes. Sections for Plin2 staining were photobleached using the MERSCOPE^{TM} Photobleacher (Vizgen) overnight. Then sections were washed with Trish-buffered saline (TBS). This was followed by blocking for 1 hour in 1% HAS and 0.1% Triton X-100 dissolved in TBS. For Plin2 staining sections, Triton X-100 was omitted from blocking buffer and samples were briefly permeabilized prior to blocking with 0.1% Triton X-100 for 3 min. After this, slices were incubated in mixtures of primary antibodies against IBA1 (1:500; Synaptic Systems) and IL-1β (1:500; R&D Systems) or Plin2 (1:500; Novus) for 48 hours at 4 ºC and washed in TBS, then incubated in mixtures of secondary antibodies diluted in TBS at 4 °C overnight. Secondary incubation was followed by TBS washes and DAPI (1:4000, Invitrogen) was incubated for 2 min at RT and washed in TBS for the Plin2 staining. Next, sections were mounted on glass slides, and coverslipped with Aqua-Poly/Mount (Polysciences). Immunofluorescence was analyzed using a Nikon Eclipse Ti-E inverted microscope, with a CFI Plan Apochromat VC 60X oil immersion objective (numerical aperture: 1.4) and an A1R laser confocal system.

Supplementary Table 2: Patient characteristics

Patient #	Age	Sex	Time between stroke and death
1	84	Female	26 days
2	85	Female	2 months
3	78	Male	2 months
4	67	Male	5 years

Immunofluorescence staining and confocal microscopy for microglia morphology analysis

Microglia morphology analysis was performed on brain coronal sections as previously described [14]. Briefly, mice were perfused with 4% paraformaldehyde (PFA) and brains were post-fixed over-night and placed in sucrose for dehydration. Then, free floating 100 µm coronal sections were stained for microglia with 1:200 anti-Iba1 (rabbit, Wako, #019-19741) and goat anti-rabbit secondary antibody (Alexa-Fluor 594, #A11012, Invitrogen). Nuclei were stained using 4′,6-Diamidin-2-phenylindol (DAPI, Invitrogen, #D3571) and images were acquired at a distance of 300 µm from the border of the lesion in cortical layer 1/2 (ipsilateral) and the homotypic contralateral region using a Zeiss LSM 880 confocal microscope with 40x magnification (objective: EC Plan-Neofluar 40x/1.30 Oil DIC M27) with an image size of 1024 × 1024 pixel, a pixel scaling of 0.2 × 0.2 µm and a depth of 8 bit. Confocal-images were collected in Z-stacks with a slice-distance of 0.4 µm. Morphological features of microglia were acquired using a fully automated analysis as previously described.

Scanning Electron Microscopy (SEM)

Brains were perfusion fixed (4% PFA and 2.5% glutaraldehyde in 0.1 M sodium cacodylate buffer, pH 7.4; Science Services) and vibratome sections immersion fixed for 24h. We applied a standard rOTO en bloc staining protocol [15] including post-fixation in

2% osmium tetroxide (EMS), 1.5% potassium ferricyanide (Sigma) in 0.1 M sodium cacodylate (Science Services) buffer (pH 7.4). The staining was enhanced by reaction with 1% thiocarbohydrazide (Sigma) for 45 min at 40°C. The sections were washed in water and incubated in 2% aqueous osmium tetroxide, washed and then further contrasted by overnight incubation in 1% aqueous uranyl acetate at 4°C and 2h at 50°C. Samples were dehydrated in an ascending ethanol series and infiltrated with LX112 (LADD). Blocks were cured for 48 hours, trimmed (TRIM2, Leica) and sectioned at 100 nm thickness using a 35°C ultra-diamond knife (Diatome) on an ultramicrotome (UC7, Leica). Sections were collected onto ~1 x 0.5 cm carbon coated Kapton tape strips (kindly provided by Richard Schalek and Jeff Lichtman, Harvard). The samples on tape were attached to adhesive carbon tape (Science Services) on 4-inch silicon wafers (Siegert Wafer) and grounded by adhesive carbon tape strips (Science Services). Scanning EM (SEM) micrographs were acquired on a Crossbeam Gemini 340 SEM (Zeiss) with a four-quadrant backscatter detector at 8 kV using ATLAS5 Array Tomography (Fibics). Medium lateral resolution images allowed the identification of lesion areas that were in turn imaged at 4-10 nm lateral resolution. Image analysis was performed in ImageJ [16].

Flow cytometry

The primary conjugated anti-mouse antibodies (CD11b and CD45; Thermo Fisher) were used for surface marker staining of microglia. All samples were stained with Zombie NIR Fixable Viability Kit (1:1000; Biolegend) for 10 min at 4°C and then with the specific surface markers diluted in Brilliant Stain Buffer, according to the manufacturer's protocols, for 30 min at 4 °C. For the FLICA^{TM} 660 caspase-1 assay (Enzo), prior to surface antibody staining, cell suspensions were incubated with FLICA^{TM} 660 caspase-1(1:20) for 30 min at 37 °C, following manufacturer's instructions. For the Plin2 staining, after surface antibody and viability staining, cell suspensions were fixed, permeabilized and incubated with Plin2 (1:20, Novus) for 30 min at 4 °C. All flow cytometric data was acquired using a Cytek Northern lights™ flow cytometer (Cytek Biosciences) and analyzed using FlowJo software.

Single-cell RNA sequencing

For single-cell RNA-seq of microglial cells mice were perfused transcardially with ice-cold saline containing Heparin (2U/mL). Brains were placed in HBSS (w/ divalent cations Ca^{2+} and $Mg^{2+)}$ supplemented with actinomycin (1:1000, 1 mg/mL, #A1410-5MG, Sigma), and tissue was digested using the Papain-based Neural Tissue Dissociation Kit (P) (# 130-092-628, Miltenyi Biotec B.V. & Co. KG) according to the manufacturer's instructions. Cell suspension was enriched using 30% isotonic Percoll gradient, incubated with anti-CD16/CD32 antibody to block nonspecific binding, stained with CD45-eFluor450 (1:200, clone 30-F11; eBioscience), CD11b-PE/Cy7 (1:200, clone M1/70; eBioscience) and cells from individual mice were also stained with unique hashtag antibodies (1:50, TotalSeq-B0301, -B0303, and -B0304, Biolegend) for 30 min at 4 °C. Cell suspensions from 3 individual mice were then pooled and live cells (7-AAD negative) were sorted according to their surface marker CD45+CD11b+7-AAD negative (SH800S Cell Sorter, Sony Biotechnology). Sorted single live were then processed according to the respective experimental procedures.

For single-cell RNA-seq of mixed neuronal cell populations mice were perfused transcardially with ice-cold saline, brains were carefully removed and placed in EBSS. Tissue dissociation was performed using the papain dissociation system (PDS – LK003150, Worthington Biochemical Corporation). A 3 mm thick slice of the cortex containing the lesion was dissected and the tissue slice was transferred to papain solution containing DNase and actinomycin (1:1000, 1 mg/mL, #A1410-5MG, Sigma). Tissue from 3 mice per group was pooled and incubated for 15 min at 37 °C in papain solution. Dead cells were removed from the resulting single cell suspension using the dead cell removal kit (# 130-090-101, Miltenyi) and live cells were sorted as PI^- cells using a FACSAriaIII cell sorter.

Sorted cells were centrifuged and resuspended to a final concentration of 1000 cells/µl. ScRNA-seq and cell surface libraries were generated using the 10x Chromium Single Cell 3' Solution with feature barcoding technology for cell surface proteins (Chromium Next GEM Single Cell 3′ GEM, Library & Gel Bead Kit v3.1, PN-1000269, Chromium 3' Feature Barcode Kit, PN-1000262, 10x Genomics) or Next GEM Chip (PN 2000127, 10x Genomics) and Chromium Next GEM Single Cell 3' Reagent kits v3.1 (Dual Index) (PN 1000215) according to the manufacturer's protocols. Quality control and quantifying concentration of cDNA libraries was performed using the high sensitivity DNA kit (#5067-4626, Agilent Technologies) and a Bioanalyzer 2100 (Agilent Technologies). Gene expression libraries were sequenced on an Illumina NextSeq 1000 or 2000 using 20,000 reads per cell. Cell-surface protein expression libraries were sequenced aiming for 5,000 reads per cell.

Single-cell RNA-seq data analysis

Cell Ranger software (version 5.0.0 and 7.1.0, 10x Genomics) was used for sample demultiplexing, raw data processing, alignment to the mouse mm10 reference genome and summary of unique molecular identifier (UMI) counts. Barcodes with UMI counts, that did not pass the threshold for cell detection were excluded. Cell Ranger output files were used as input for further analysis using Seurat (Version 4.3.0 and 5.1.0) in R and scanpy (version 1.9.4) in python (version 3.11.4). As initial quality control for microglia single-cell RNA-seq data and mixed neuronal cell populations, cells with no or more than one hashtag oligo (doublets), cells with a number of detected genes <200 or >6000 and cells with >5 % of mitochondrial gene count were excluded from the analysis. Raw gene counts were log-normalized, scaled and regressed against the number of UMIs and mitochondrial RNA content per cell. PCA was calculated and variable features were obtained using MeanVarPlot method. Dimensionality reduction was performed using Uniform Manifold Approximation and Projection (UMAP) and clustering was generated using Louvain clustering. Non-microglial cells were excluded from downstream analysis and the data subset was pre-processed again as described above. Differentially expressed genes between conditions were calculated using the FindMarkers function in Seurat and Gene set enrichment analysis was performed using ClusterProfiler [17]. Pseudotime analysis was performed using Monocle 3 [18]. Microglia subtype scores were generated using the AddModuleScore() function in Seurat using the following gene sets as described previously [19]: Homeostatic microglia: *Lrrc3, Pmepa1, Sall1, Selplg, Grf2h2, Cx3cr1, Mfap3, P2ry13, Cd164, P2ry12, Ccr5, Tmem119, Lrba, Rab3, Med121*. Disease associated microglia (DAM): *Itgax, Mamdc2, Cst7, Fam20c, Csf1, Lpl, Ank, Cox6a2, Spp1, Axl, Igf1, Gpnmb, St14, Etl4, Capg, Lyz2, Apoe, Nceh1, Ch25h, Got1, Asb10, Cd83, Apbb2, Cadm1, St8sia6, Sulf2, Ccl6, Kcnj2, Lgals3bp, Cd34, Crlf2, Cd9, Ctsb, Serpine2, Ctsz, Tyrobp, Hif1a, Ctsl, Cd68, Soat1*. Lipid associated microglia (LAM): *Gpnmb, Lgals3, Apoe, Hpse, Ftl1, Cst7, Cybb, Spp1, Fth1, Cd63, Igf1, Ctsb, Lyz2, Crip1, Anxa5, Fabp5, Fam20c, Plin2, Capg, Atp6v0d2, Soat1, Tpi1, Pld3, Pld3, Tmem106a, Mif, Apoc1, Csf1, Anxa4, Ctsd, Rps26, P2rx4, Gpi1, Anxa2, Cd48, Nhp2, Vim, Lck, Gapdh, Tecpr1, Rtcb, Timp2, Coro1c, Ahnak2, Pla2g7, Aprt, Rftn1, Prelid1, Rrp12, Tubb5, Plbd2, Tmem205, Rab3d, Akr7a5, Xrcc1*. Interferon responsive microglia (IRM): *Usp18, Stat1, Ifit1, Iigp1, Ifitm3, Ifit2, Gm4951, Phf11a, Phf11b, Tgtp2, Ifi209, Oasl1, Ifit3b, Ifit3, Phf11d, Ifi27l2a, Rtp4, Sp100, Trim30a, Herc6, Irgm1, Ccl12, Rnf213, Ifi204, Isg20, Xaf1, Mx1, Parp12, Rsad2, Tor3a, Stat2, Slamf8, Pik3ap1, Susd6, Pml, Enkd1, Etnk1, Apobec3, Fcgr1, Grn, Igtp, Lta4h, Mgat1*. For the repair associated microglia (RAM) score, the differentially regulated genes from microglia subclusters 5 vs clusters 0 and 1 was calculated and the top 20 genes were used: *Apoe, Apoc1, Lpl, Cybb, Ccl4, Apoc4, Lyz2, Fth1, Cd52, Crip1, Cxcl16, Itgax, Cd63, Ccl3, Cd14, Axl, Id2, Ms4a7, Il1b, Cd74.*

For datasets from mixed cell populations of GW3965 and Ctrl treated mice, correction for ambient RNA was performed using SoupX (version 1.6.2), doublet prediction was performed using scvi-tools and doublets were removed from the dataset. Data were filtered for mitochondrial, ribosomal and red blood cell genes and correction of outliers was performed by percentage of mitochondrial genes (< 7%), percentage of ribosomal genes (< 15%) and cells where the number of counts was exceeding the 98th percentile. Normalization was applied to 10,000 UMIs and integration of data from GW3965 and Ctrl treated mice were integrated by modeling using scvi-tools. Clustering was performed using the leiden-method clustering with a resolution of 0.5. Cell types were annotated by specific marker expression based on the database PanglaoDB (https://panglaodb.se/). Background genes (Gm8566, Cmss1, Xist, Gm42418, Gm424181, Malat1, Ay036118 and Gm26917) were removed from downstream analysis. For quantification of differentially expressed genes per celltype, data was subsetted to the respective cell type and differentially expressed genes were calculated using the FindMarkers function in Seurat (version 5.0.1) in R version 4.3.1. For microglia, the data subset was integrated with the pre-existing clustering from the first scRNA-sequencing experiment (Fig. 2) using the FindIntegrationAnchors, IntegrateData, FindTransferAnchors, and MAPQuery function functions in Seurat (version 5.0.1). Pseudotime trajectory was generated using Monocle 3 (version 1.3.4). Single cell fate mapping analysis was performed using cellrank (version 2.0.2). Analysis of cell-cell communication was performed using CellChat (version 1.6.1).

Spatial transcriptomics (10x Genomics Visium)

Mice were perfused 28 days after stroke induction. Brains were dissected, gently frozen using isopentane and liquid nitrogen, and stored at -80 °C until further processing. Before starting the spatial transcriptomics protocol, sufficient RNA integrity (RIN>8.5) of all samples was validated using a Bioanalyzer RNA 6000 Pico Kit (Agilent, 5067-1513). Next, 10 µm cryosections in the infarct region were prepared (Thermo Scientific, CryoStar NX70) and positioned on a Visium spatial gene expression slide (10x Genomics, Visium Spatial Gene Expression Reagent Kit,4 rxns PN-1000189). Brain sections were fixed with for 30 minutes in ice-cold methanol followed by H&E staining. In short, sections were incubated in isopropanol for 1 minute and afterwards dried at room temperature. Next, Haematoxylin solution (Dako, S3309) was added, and samples were incubated for 7 minutes, followed by washing in water and 2 minutes incubation in blueing buffer (Dako, CS702). Sections were washed and EosinY solution (10% EosinY Sigma-Aldrich, HT110216 in Tris Acetic Acid Buffer (pH 6.0, 0.45 M)) was added for 1 minute followed by another washing step and drying at 37 °C. Mosaic scans (Zeiss, Axio Imager.M2) of all brain sections were prepared for spatial alignment of the sequencing data. Next, brain tissues were permeabilized for 20 minutes followed by reverse transcription into cDNA and second strand synthesis on the slide following the manufacturer's instructions (10x Genomics, PN-1000189). Afterwards, the cDNA product was eluted from the slide, amplified and cleaned using SPRIselect reagent (Beckman Coulter, B23318) cleanup. For library preparation the Library Construction Kit (10x Genomics, PN-1000196) was used. cDNA samples were first fragmented followed by end repair and double-sided size selection using SPRIselect reagent (Beckman Coulter, B23318). Next, adapter oligos were ligated, the products were cleaned (SPRIselect Beckman Coulter, B23318) and samples were indexed using Dual Index Plate TT Set A (10x Genomics, PN-1000215). Finally, a last double-sided cleanup was performed, and product quality was checked with a Bioanalyzer High Sensitivity chip (Agilent, 5067-4626). Sequencing was performed using a P2 flowcell (~65000 reads per spot) on an Illumina NextSeq2000 machine. Fastq sequencing files were processed using SpaceRanger count (v2.0.0, 10x Genomics). The function aligned sequencing reads to the mouse reference transcriptome (GENCODE vM23/Ensembl98/mm10-2020-A) using STAR [23], extracted and filtered spatial barcodes and unique molecular identifiers (UMIs), and quantified gene expression per spatial barcode to generate a gene expression matrix. H&E-stained tissue images were registered to the spatial barcode spots using manually curated alignment .json files generated in Loupe Browser (10x Genomics). Data pre-processing was performed for each sample individually using Seurat (version 5.1.0) using default settings. Briefly, data was normalized using SCTransform, linear dimensionality was reduced using RunPCA, clustering was performed using FindClusters (Louvain algorithm), and non-linear dimensionality reduction was performed using RunUMAP. The RAM score was calculated using the function AddModuleScore and the top ranked genes for scRNAseq microglia subcluster 5: *Apoe, Apoc1, Lpl, Cybb, Ccl4, Apoc4, Lyz2, Fth1, Cd52, Crip1, Cxcl16, Itgax, Cd63, Ccl3, Cd14, Axl, Id2, Ms4a7, Il1b, Cd74.*

MERFISH workflow and data analysis

Brain hemispheres were sectioned into 10-µm-thick coronal slices and mounted onto glass slides provided by Vizgen (MERSCOPE Standard FF Slide Box, Cat no. 10500125). The gene panel (Vizgen, MERSCOPE 500 Gene Panel, Cat no. 10400003) employed in this study comprised 500 protein-coding genes, supplemented by 50 blank probes (see Supplementary Table 3). This panel included a diverse set of transcripts representing established markers for neural, glial, and immune cell types, selected based on prior literature. Post-sectioning, tissues were fixed with 4% paraformaldehyde (PFA) in PBS for 15 minutes at room temperature, followed by three washes with PBS. Sections were then incubated in an autofluorescence photobleacher (Vizgen) for 3 hours. To facilitate hybridization, the samples were permeabilized overnight at 4 °C with 70% ethanol. For hybridization, tissues were washed with a sample preparation buffer (Vizgen, MERSCOPE Sample Prep Kit, Cat no. 10400012) and incubated in hybridization buffer containing formamide (Vizgen, MERSCOPE Sample Prep Kit, Cat no. 10400012) at 37 °C for 30 minutes. Subsequently, 50 µL of the gene panel mixture was applied onto the tissue, which was then hybridized at 37 °C for 36–48 hours. The sections were washed, embedded into a polyacrylamide gel, and cleared with a Proteinase K-containing premix (Vizgen, MERSCOPE Sample Prep Kit, Cat no. 10400012), followed by washing and staining with DAPI and polyT reagent (Vizgen, MERSCOPE 500 Gene Imaging Kit, Cat no. 10400006) for 15 minutes at room temperature. After additional washing, hybridization and imaging buffers (Vizgen, MERSCOPE 500 Gene Imaging Kit, Cat no. 10400006) were loaded onto the MERSCOPE system (Vizgen). Initial low-resolution mosaic images were captured using a 10× objective, from which regions of interest were selected for high-resolution imaging with a 60× lens. During high-resolution imaging, the focus was stabilized using fiducial fluorescent beads on the coverslip. Seven z-planes, each 1.5 µm thick, were imaged for each field of view.

Raw images were decoded into RNA spot locations and gene identities using Merlin software (Vizgen). Cell segmentation was performed with Cellpose, utilizing DAPI nuclear and polyT RNA staining channels. The resulting single-cell gene expression matrices were further analyzed with the Seurat v5.0 package in R. Quality control steps involved excluding cells with fewer than 20 detected genes, more than 400 transcripts, or cell volumes smaller than 90 µm^3. Data normalization was conducted using SCTransform, and PCA was performed across all 500 genes. UMAP embedding was computed from the top 30 principal components with the RunUMAP function. A shared nearest neighbor graph was constructed based on these PCs (FindNeighbors), and clustering was performed using the Louvain algorithm across various resolution parameters. Cell identities were annotated into major classes based on canonical marker genes and regional expression patterns. RAM score was calculated using the function AddModuleScore and the top ranked genes for scRNAseq microglia subcluster 5: *Apoe, Apoc1, Lpl, Cybb, Ccl4, Apoc4, Lyz2, Fth1, Cd52, Crip1, Cxcl16, Itgax, Cd63, Ccl3, Cd14, Axl, Id2, Ms4a7, Il1b, Cd74.* Projection of microglia subclusters from scRNAseq data (Fig. 1) was projected using the Seurat functions FindTransferAnchors and TransferData. Differential gene expression analysis was performed using the function FindMarkers to compare gene expression of oligodendrocytes within the peri-lesional and non-lesioned area after sub-sampling for equal oligodendrocyte number in these regions, or between 28 days post stroke to control in the same cells.

In vivo phagocytosis assay

Mice were anaesthetized with isoflurane, delivered in a mixture of 30% O_2 and 70% N_2O. Mice were placed into a stereotactic frame and body temperature was maintained at 37°C with a mouse warming pad. Dexpanthenol eye ointment was applied to both eyes. The skin covering the skull was opened and a small craniotomy was made using a dental drill 0.5 mm rostral and caudal from the photothrombotic lesion border as well as the contralateral hemisphere. Per position 1 µl of zymosan solution (pHrodo™ Green zymosan Bioparticles™, Thermo Fisher, #P35365, 2.5 µg/µL in saline) was injected in a cortical depth of 600 µm. For naïve control animals zymosan was injected in the same cortical areas. The animals were perfused 24 h after the zymosan injection with 4°C cold saline and 4% PFA. Brains were removed from the skull and post-fixed over night at 4 °C and cut into 50 µm thick free-floating sections using a vibratome. Microglia were stained using 1:200 anti-P2Y12 (rabbit, #AS-55043A, AnaSpec) and goat anti-rabbit secondary antibody (Alexa-Fluor 594, #A11012, Invitrogen). Confocal-images were acquired as Z-stacks with a slice-distance of 0.4 µm. Zymosan uptake per microglial cells was counted and calculated in FIJI ImageJ (Version: 2.0.0-rc-69/1.52p).

In vivo 2-photon imaging and analysis of microglial process motility

For *in vivo* 2-photon imaging Tmem119-EGFP animals received a photothrombotic lesion in the right somatosensory cortex (2.0 mm right, 1.0 mm caudal) with the above-described procedure. To image the microglial process outgrowth upon laser lesion in controlled conditions, cranial windows were implanted 28 days after photothrombotic lesion induction above the somatosensory cortex according to the methods described previously [24,25]. Briefly, mice were placed on a heating blanket and the head was stabilized in a stereotaxic frame and eye ointment was applied to protect the eyes from dehydration. The fur washed with three alternating swabs of 70% ethanol and betadine, and ~1 cm^2 of skin covering the skull of both hemispheres was removed using surgical scissors. 1% xylocaine was applied to the periosteum of the skull and exposed muscles at the lateral and caudal sides of the wound. The periosteum was gently removed, and the skull was thinned forming a circular groove using a dental drill. Next, the thinned skull bone was gently removed using fine forceps. The unblemished dura was covered with a circular coverglass (#1 thickness). The optical window was sealed with dental cement and a clean, and a metal bar was attached to stabilize the mouse head for imaging. Imaging and laser lesion induction was performed acutely after successful cranial window implantation. For *in vivo* imaging, mice were anaesthetized using a mixture of medetomidine, midazolam and fentanyl (MMF; 150-200 µL/kg) 30 min prior to the start of the experiment. Laser lesions of ~150 µm length were performed 30 µm below the cortical surface 600 µm distant to the lesion border, and the microglial response was recorded every 5 min for 90 min over an area of 250,000 μm^2 from the cortical surface to 70 µm depth. Microglial process motility was manually analyzed using FIJI ImageJ (Version: 2.0.0-rc-69/1.52p) using the plugin Simple Neurite Tracer and StackReg. Calculation of process extension speed and statistical analysis was performed using R (Version R 4.0.3) and R Studio (Version 1.3.1073). Briefly, the center slice of each 2-photon Z-stack was identified and the 2 slices before and after the center were combined in a maximum intensity projection of the resulting 5 sections. Afterwards, maximum intensity projection images were automatically registered for maximum overlap using the plugin StackReg. Microglia processes were labeled slice-by-slice in every 2-photon time-lapse image using Simple Neurite Tracer. The resulting coordinates were collected and the distance from first to last coordinate for each microglia process was calculated and divided by the time duration to calculate the speed of process extension.

Cerebral open flow microperfusion (cOFM)

Cortical interstitial fluid was repeatedly collected *in vivo* from mouse brains before and at multiple time points following photothrombotic stroke induction using cerebral Open Flow Microperfusion (cOFM; Joanneum Research, Austria) as previously described.

For implantation of the cOFM guide cannula, mice were anesthetized and securely fixed in a stereotaxic frame (51615T, Stoelting Europe, Ireland). Body temperature was maintained at 37 °C using a feedback-controlled heating pad, and dexpanthenol eye ointment (Bepanthen®) was applied bilaterally to prevent irritation or dryness. A skin incision (~15 mm) was made to expose the skull surface, followed by careful drilling of a 1.0 mm diameter hole at coordinates -0.5 mm caudal and 3.0 mm lateral relative to Bregma, exposing the underlying dura mater. Under sterile artificial cerebrospinal fluid (aCSF), the dura mater was gently removed to reveal the cortical surface. Subsequently, the guide cannula equipped with a healing dummy (cOFM-P-1-1, Joanneum Research, Austria) was inserted into the cortex at a controlled speed of 10 µm/s using an ultraprecise manipulator arm (51604U, Stoelting Europe, Ireland), until reaching a depth of 1 mm. Any bleeding was managed carefully, and backflow was monitored closely. The animal was allowed a brief resting period to ensure stability before the cannula was sealed. The probe was securely fixed onto the skull using biocompatible dental cement (Quick Base S398, L-Powder clear S399, Universal Catalyst S371; Parkell C&B Metabond, USA), with special care taken under an operating microscope to avoid the formation of air bubbles. Following surgery, mice recovered in a heated chamber for approximately 30 minutes and were closely monitored daily, with the healing dummy kept in place within the cannula for 14 days post-surgery. The use of transparent dental cement enabled direct laser illumination through the intact skull for photothrombotic stroke induction. Prior to stroke induction, the skull surface and dental cement were darkened with a black marker, leaving only a 2 mm diameter circular area immediately adjacent to the cOFM probe transparent for precise stroke targeting. Photothrombotic stroke was then induced following the previously described protocol.

Microperfusion sampling was prepared following the cOFM protocol guidelines (Joanneum Research, Austria). Briefly, the OFM perfusate bag (10 mL, OFM-BAG, Joanneum Research, Austria) was loaded with freshly prepared and sterile-filtered aCSF, composed of NaCl (148.18 mM), $MgCl_2$ (0.8 mM, $CaCl_2$ (1.4 mM), KCl (3 mM), NaH_2PO_4 (0.19 mM), Na_2HPO_4 (1.2 mM), glucose (3.7 mM), and urea (Carbamide, 6.7 mM), as detailed by Alzet (https://www.alzet.com/guide-to-use/preparation-of-artificial-csf/). The microperfusion pump (MPP102 PC, Joanneum Research, Austria) equipped with push-pull tubing (OFM-PP2-100-LB, Joanneum Research, Austria) was then connected to the perfusate bag with µD-Connectors (MD-1510, Joanneum Research, Austria), and the system was flushed thoroughly at a flow rate of 10 µL/min for 15 minutes prior to sample collection.

For sample collection, mice were briefly anesthetized with isoflurane (1.5%) administered in a gas mixture of 30% O_2 and 70% N_2O. During this brief anesthesia, the healing dummy within the guide cannula was replaced with the sampling insert (cOFM-P-1-1, Joanneum Research, Austria) connected to the inlet and outlet push-pull tubes. To assist awake sampling, mice were fitted with a small mouse collar (MD-1365, BASi Research, USA) and gently attached to a self-rotating Raturn sampling cage system (MD-1409, BASi Research, USA). This cage system counter-rotated to prevent tube entanglement. Following attachment, mice were allowed to fully awaken and freely move within the cage, with ad libitum access to food and water. Once mice regained consciousness, interstitial fluid samples were collected at a flow rate of 0.8 µL/min for 1 hour, and samples were immediately placed on ice and stored in -80 °C until further process.

After collection, mice were briefly anesthetized again with isoflurane to remove the sampling probe, replace the healing dummy insert, and were then placed in a recovery chamber before returning to their home cage. Perfusates were collected at baseline (14 days after probe insertion) and subsequently on days 3, 7, 14, 21, and 28 post-photothrombotic stroke induction.

Proteomics analysis of cOFM

The collected cOFM samples were carefully selected following a quality control by a multiplex bead assay (ProcartaPlex Mouse Immunoassay, Cat#: PPX-29, Assay ID: MX323KH). Around 20 µL of perfusate was collected with an estimated range of protein content of 0.1-1.5 µg per sample. 40 µL of mouse brain microperfusates were prepared according to the single-pot solid-phase-enhanced sample preparation (SP3) protocol with some adaptations. In brief, samples were mixed 1:1 with lysis buffer containing 10% SDS (Roth, #CN30.3) in PBS (Thermo Fisher Scientific, # 14190250) pH 8.5, 100mM Tris (2-carboxyethyl) phosphine (Thermo Fisher Scientific, #77720), and 30 mM 2-chloroacetamide (Thermo Fisher Scientific, #A15238.30). Proteins were denatured, reduced, and alkylated by incubating samples at 70 °C, 800 rpm on a shaker (Eppendorf, #5382000015) for 10 min. We added 2 µl of prepared magnetic bead mixtures (Sera-Mag Magnetic carboxylate modified particles, Merck, #GE44152105050250 & # GE24152105050250) to each sample and mixed them 1:1 with 100% acetonitrile (ACN, Honeywell, #34967-1L). Samples were incubated for 8 min at RT and 800 rpm on a shaker. Following, samples were transferred on a magnet (Thermo Fisher Scientific, #12321D) and magnetic beads with bound proteins were washed two times with 200 µl 70% ethanol (VWR, #153385E) and once with 100% ACN while keeping the samples the whole time on the magnet. For enzymatic digestion, the magnetic beads were resuspended in 10 µl digestion buffer containing 0.1 µg trypsin /Lys-C mixture (Promega, #V5072) in 50 mM ammonium bicarbonate buffer pH 8.0 and digestion at 37 °C, 400 rpm overnight. On the next day, samples were mixed with 380 µL 100% ACN and incubated for 8 min at room temperature. After transfer on a magnet, beads were washed with 200 µL 100% ACN and beads air-dried. Peptides were eluted from magnetic beads by resuspending the same in 9µl of 5% ACN in LC-MS-grade water (Thermo Fisher Scientific, #85189). We determined peptide concentrations (NanoDrop One, Thermo Fisher Scientific, #ND-ONE-W) and used 250 ng peptides per sample for each LC-MS run.

LC-MS/MS analysis

Samples were measured by liquid chromatography-tandem mass spectrometry using an EASY-nLC 1200 chromatographic system (Thermo Fisher Scientific, #LC140) and the Exploris 480 mass spectrometer (Thermo Fisher Scientific, #BRE725533). Peptides were separated by 90 min chromatographic gradients using a binary buffer system with buffer A (0.1% formic acid in LC-MS-grade water, VWR, #B2832-84867.290) and buffer B (80% ACN, 0.1% formic acid in LC-MS-grade water, VWR, #B2832-1.59002.4000). We used an in-house packed analytical column with a length of 50 cm and filled with 1.9 µm ReproSil-Pur 120 C18-AQ material (Dr. Maisch, #r119.aq.0005). To separate peptides the amount of buffer B was linearly increased from 4% to 25% over 70 min with a constant flow rate of 300 nL /min. Following, buffer B was increased to 55% over 8 min and a sharp increase to 95% buffer B over 2 min. The analytical column was washed at 95% for 10 min.

Eluting peptides were ionized by nano-electrospray ionization at a constant spray voltage of 2.5 kV. We measured the samples in data-independent acquisition (DIA) mode. In brief, full MS were recorded at a resolution of 60,000 with an AGC target of 300% and a maximum injection time of 55 ms. The scan range was set to *m/z* 340 – 1,080. DIA MS/MS scans were recorded at a resolution of 15,000, an AGC target of 1,000%, and a maximum injection time of 22 ms. The DIA window m/z range was set from *m/z* 400 – 1,000 separated into 50 isolation windows with a size of *m/z* 12 per window. We used a staggered window approach with isolation windows shifted by *m/z* 6 every second scan cycle. Fragment ions were generated with an HCD collision energy of 27%. We measured pooled samples for the generation of a gas phase fractioned (GPF) spectral library. Similar LC-MS methods were applied, only the DIA scan ranges were limited to *m/z* 100, covering the overall *m/z* range from *m/z* 400 – 1,000 in six consecutive runs and staggered DIA windows with a size of *m/z* 4.

Statistical analysis of proteomics data

Staggered windows were deconvoluted with the MSConvert tool of the ProteoWizard software suit (v. 3.0.21321, https://www.nature.com/articles/nbt.2377). Spectral library generation and peptide identification/quantification from LC-MS raw data was performed with the DIA-NN software suit (v. 1.8,[28]). We used the SWISS-PROT Mus musculus fasta database downloaded from UniProt (v. 2021-11-18) to make a spectral library using the six GPF measurements from pooled samples. Trypsin was set as the digestion enzyme with a maximum of one miss-cleavage and cysteine carbamidomethylation was set as a fixed modification. The scan window radius was set to 10, mass accuracies were fixed to 2e-05 (MS2) and 7.5e-06 (MS1), respectively. Precursor peptides were filtered at an FDR <1%. Label-free normalization of protein groups was performed in R using the MaxLFQ algorithm and proteotypic peptides only.

Statistical analysis of the data was performed with the Perseus software suite (v. 1.6.15, [30]). In brief, we log2 transformed protein LFQ intensities and filtered proteins for data completeness in at least one time point. Missing values were replaced sample-wise by random drawing of numbers from 1.8 standard deviations downshifted, and 0.3 standard deviations broad normal distributions. Quantile normalization was performed with an R Perseus-plugin as well as a batch correction with ComBat R Perseus-plugin (batch = animal). Significantly regulated proteins were identified by ANOVA multiple sample testing (S0 = 0.1, permutation-based FDR = 0.05, 250 randomizations). ANOVA-significant proteins were further Z-score normalized and used for hierarchical clustering using Euclidean distances. We searched systematically for enriched processes in identified clusters using Fisher‘s exact testing (Benjamini-Hochberg FDR = 0.02). Data output was filtered for ANOVA-significant proteins for downstream clustering analysis.

Clustering analysis of Proteomics data analysis

Time-series clustering was performed using an unsupervised, nonparametric model-based method, the Dirichlet process Gaussian process mixture model (DPGP) [31]. In brief, two important considerations in this problem are (1) selecting the "correct" or "optimal" number of clusters and (2) modeling the trajectory and time-dependency of protein expression. A Dirichlet process can determine the number of clusters in a nonparametric manner, while a Gaussian process can model the trajectory and time-dependency of protein expression in a nonparametric manner. Optimal clustering was selected using the '*maximum a posteriori'* (MAP) criterion.

Detected clusters were analyzed with the use of QIAGEN IPA (QIAGEN Inc., https://digitalinsights.qiagen.com/IPA) and their network and upstream regulator modules with standard parameters [32].

Proteomics demultiplexing DESP algorithm

For demixing cOFM bulk proteomics data into underlying cell state omic's profiles, we combined the output from the proteomics clustering analysis ("cluster 2") and IPA analysis ("Il-1β network") with single-cell RNA sequencing data from mixed cell populations derived from mouse brains in naïve state, 7 days and 28 days after stroke (see above). Proteomics raw data were filtered by sample and protein names using Python (version 3.13.2) using the packages pandas (version 2.2.3), anndata (version

0.11.3, scanpy (version 1.10.4), numpy (version 2.1.3), and seaborn (version 0.13.2). Single-cell RNA seq data were imported using R (version 4.3.1) and imported to python using rpy2 (version 3.5.17). To demix the bulk secretome profiles into individual cell types we used DESP (v1.0) [33]. Briefly, the DESP algorithm models bulk omics data as a product of cell proportions and cell state / type omics profiles. Using cell state proportions estimated via single-cell RNAseq data, this model enables the estimation of cell state / type specific profiles. Here, we leverage scRNAseq data at baseline (naïve state), 7 days, and 28 days after stroke to estimate expected cell type proportions using leiden clustering and manual annotation of clusters into 14 cell types (see above). Although the scRNAseq data was acquired in different specimen than the cOFM bulk proteomics data, both data measure cells in and around the lesion, to match the previously defined area of interest, and we expect that cell type proportions are representative of the underlying cell type proportions in the cOFM bulk proteomics data. Cell type proportions were calculated for each timepoint for input to DESP. As additional input to DESP, cell type similarities were calculated from the scRNAseq data by Pearson correlation of the mean expression profile per cell type. DESP was run for each timepoint, using un-logged data as input, and the resulting cell type specific secretome predictions were re-logged before further analysis. Outputs included deconvolved protein expression matrices per cell type and time point visualized as heatmap.

Golgi-Cox staining and dendritic spine analysis

Following saline perfusion, mice were perfused 42 days after PT with aldehyde fixative solution (003780, Bioenno). Brains were then carefully removed and placed in fixative solution at 4 °C overnight. Brains were then sliced at 100 µm using a vibratome and collected in 0.1 M PBS. Slices were placed in impregnation solution using the sliceGolgi Kit (003760, Bioenno) for 5 days in the dark. Staining and post-staining was performed as described by the manufacturer (Bioenno). Images of dendrites were obtained within 500 µm around the lesion area in cortical layer 2/3. In total, per animal 25 dendrites (5 dendrites from 5 neurons) in both hemispheres were recorded using an Axio Imager.M2 and a 100× objective (EC Plan-Neofluar, NA=1.3, immersion: oil, acquisition at 18-20 °C) using the AxioCam MRc and AxioVision 4.8.2 software. Dendrites from the images were then 3D-reconstructed and the spine density evaluated on the reconstructed 3D surface using Imaris x64 (8.4.0, Bitplane).

MALDI-MSI targeted for cholesterol

Sections of 10-µm thickness were sectioned on a cryostat (Leica) and mounted on ITO slides (Bruker). The ITO slides were then vacuum freeze-dried for 15 min. First, 18 layers of a 500 µg/mL solution of cholesterol-d_6 (Avanti) internal standard in 100% ethanol were applied using a SunCollect sprayer (SunChrom) with the following settings: 20 µL/min flow rate for all layers, speed x: medium 1, speed y: medium 1, z position: 30. Lastly, 48 mg of 2,5-dihydroxybenzoic acid (DHB) matrix (Sigma) in 4 mL of 100% acetone was sublimated onto the ITO slide. MALDI-2-MSI measurements were performed on a MALDI2-timsTOF flex instrument (Bruker). Positive ion mode spectra were acquired in a mass range of m/z 150–500 with a pixel size of 8 × 8 µm. Spectra were obtained with 20 shots per pixel, at a speed of 1 kHz, and with a trigger delay of 5 µs. Prior to data acquisition, the instrument was calibrated using red phosphorus. Data acquisition was performed using timsControl (Version 5.0.9, Bruker Daltonics) and flexImaging 7.3 (Bruker Daltonics). The samples were measured in random order.

MALDI-MSI untargeted negative mode

Sample Preparation

Sections of 10-µm thickness were sectioned on a cryostat (Lieca) and mounted on glass ITO slides (Bruker). The ITO slides were then vacuum freeze-dried for 15 min. Finally, 20 layers of a 7 mg/mL solution of N-(1-naphthyl) ethylenediamine dihydrochloride

(Sigma-Aldrich) (NEDC) matrix in a mixture of methanol/acetonitrile/water (70:25:5, %v/v/v) were applied using an HTX M3+ sprayer (HTX Technologies, LLC) with the following parameters: 60°C nozzle temperature, 80 µL/min flow rate, 2000 mm/min velocity, 3-mm track spacing, CC pattern, and 30-sec drying time.

MALDI-MSI Measurement

For high spatial resolution, MALDI-TOF-MSI measurements were performed on a RapifleX MALDI-TOF/TOF system (Bruker Daltonics). Negative ion mode spectra were acquired in a mass range of *m/z* 60–1000 in reflector mode, with a pixel size of 5 × 5 µm. Spectra were obtained with 90% laser power, 25 shots per pixel, at a speed of 10 kHz. Prior to data acquisition, the instrument was calibrated using red phosphorus. Data acquisition was performed using flexControl (Version 4.0, Bruker Daltonics) and flexImaging 5.0 (Bruker Daltonics). The samples were measured in random order.

For high mass resolution, MSI analysis was performed on a 12T solariX FTICR mass spectrometer (Bruker Daltonics, Germany). Negative ion mode spectra were acquired in a mass range of *m/z* 300–1050 with a pixel size of 30 × 30 µm. Spectra were obtained with 35% laser power, 15 shots per pixel, at a speed of 60 kHz. The spectra were recorded with a 1M data point transient. Prior to data acquisition, the instrument was calibrated using red phosphorus. Data acquisition was performed using ftmsControl (Version 2.1.0, Bruker Daltonics, Germany) and flexImaging 5.0 (Bruker Daltonics, Germany).

CSF-Sample Preparation

Twenty microliters of CSF were diluted with 200 µL of a BHT solution (butylated hydroxytoluene, 5 mg/mL in ethanol) and 800 µL internal standard solution (each 1.25 µg/mL of cholesterol-d_7 and desmosterol-d_6 in ethyl acetate). Next, the samples were homogenized for 10 minutes on a tube shaker at 3200 rpm. Afterwards, 400 µL of 25% aqueous potassium chloride (solved in 0.2 M hydrochloric acid) and 400 µL ethyl acetate were added. After homogenization for approximately one minute the samples were centrifuged at 12,000 g for 5 minutes at room temperature. Subsequently, the organic phase was transferred to a GC-Vial and evaporated to dryness under a gentle stream of nitrogen. Then, 1000 µL ethyl acetate were added to the aqueous phase, shaken and again centrifuged for12,000 g for 5 minutes at room temperature. The second organic phase was also transferred to the same GC-Vial and evaporated again to dryness. The extraction was performed a third time with another 1000 µL ethyl acetate. All neutral sterols were measured as trimethylsilyl ethers (TMS ethers) by adding 50 µL of MSTFA (*N*-methyl-*N*-trimethylsilyl-trifluoroacetamide):TSIM (*N*-trimethylsilyl-imidazole; 10:1) and the samples were kept for 30 minutes at room temperature. Finally, 150 µL of 1.33 µg/mL cholestane in methyl *tert*-butyl ether (M*t*BE) were added and transferred into a micro insert and were ready for GC-MS/MS analysis.

GC-MS/MS Analysis

The analysis by gas chromatography triple quadrupole MS (GC-MS/MS) was performed on an Agilent Technologies 7890B gas chromatograph with an Agilent Technologies multimode inlet (MMI) coupled to a 7010B triple quadruple with high efficiency source (HES) and a PAL RSI85 autosampler from CTC Analytics (Zwingen, Switzerland). Data analysis and instrument control were carried out with Agilent MassHunter Workstation Software package B.08.00 (Santa Clara, CA, USA). Two connected capillary columns (15 m Agilent J&W HP-5 ms ultra inert) with 0.250 mm inner diameter and 0.25 µm film thickness were used. Flow rate of the first column was set to 1.1 mL/min and 1.3 mL/min on the second column. Carrier gas was helium 99.9990% from Air Liquide (Düsseldorf, Germany). The triple quadrupole (MS/MS) was operated with electron ionization (EI) at 70 eV with collision gas argon 99.995% from Air Liquide (Düsseldorf, Germany) with a flow rate of 0.9 mL/min. The temperature for the MS transfer line was set to 300 °C, MS source to 230 °C, and MS quadrupole to 150 °C.

For the quantification of targeted analytes, a dynamic multiple reaction monitoring (dMRM) method was used. The cycle time of the method was 28.0 minutes, 20 minutes run time, 4.0 minutes post-run with backflush and requiring an additional 4.0 minutes to cool down to the starting conditions. The solvent delay was set to 8.0 minutes, and the temperature of the GC oven was set to 50 °C for 1.0 minute and a heat rate of 50 °C/min to 250 °C. Then, the heat rate was decreased to 5 °C/min until 310 °C, and was hold for 3.0 minutes. The injection volume was 10 µL. The injection was performed in a solvent vent mode at an injector temperature of 70 °C, which increased to 310 °C after 0.02 minutes. The multiplier operated with a gain factor of 10. The detector was only active for the respective transitions within the determined time windows of each analyte (one minute before and after the defined retention time). The transitions and collision energies were optimized using authentic standards and Agilent's MassHunter MRM optimizations software. For detailed information about the dMRM setting (see Supplementary Table 4).

Demixing of lipidomics signal using MERFISH and MALDI Data

Briefly, we first spatially integrated spatial transcriptomics (MERFISH) data with spatial lipidomics (MALDI) data, and then used this spatial integration in the second step to form batches of spatially corresponding cells and lipidomics spots which we used to demix a cell-specific lipidomics signal.

The spatial integration of MERFISH and MALDI data was done using moscot (version 0.4.2)[34]. First, uni-modal MERFISH and MALDI slides were spatially integrated by leveraging Fused Gromov-Wasserstein (FGW) optimal transport (named AlignmentProblem in moscot) with the features (genes / lipids) as shared features, and spatial coordinates as unique features. For MERFISH, gene expression was aggregated into spots with radius 30um, before using it as shared features for integrating samples dao3r2 and dao8r2 (alpha = 0.5, tau_a = 0.9999, tau_b = 1). For MALDI data lesional hemispheres for Ctrl1 and Ctrl2 were manually selected, a cluster of xxx tissue removed, and then integrated (alpha = 0.7, tau_a = 1, tau_b = 1). Then, MERFISH and MALDI data was integrated using coarse region annotations as shared features, and spatial coordinates from the uni-modal integration as unique features. Brain regions cortex, fibertract, lesion, subcortical were annotated on both modalities and used together with the distance from the lesion as shared features (1-hot-encoded) between the modalities to improve the spatial alignment. The spatial integration (alpha = 0.8, epsilon = 0.01) resulted in a common coordinate system for all MERFISH and MALDI slides.

This common coordinate system was used to bin the data into 22 rectangular bins, where each bin contained spatially corresponding cells from MERFISH and lipidomics spots from MALDI. For each bin cell type counts were estimated using the MERFISH data and an annotation done on a single cell reference as described for the scRNA-sequencing for mixed cell populations (Fig. 2), and a bulk lipidomics profile was estimated by summing the raw lipidomics signal of each spot in the bin. Cell type similarity was estimated by Pearson correlation of the mean expression profiles. This data then served as input for DESP [33], which demixed the lipidomics signal and resulted in a cell-type specific lipidomics profile.

BMDM isolation and differentiation

Bone marrow derived macrophage (BMDM) cells were generated from both mouse tibia and femur. After cells were flushed out from both femurs and tibias, bone marrow cells were filtered through 40µm cell strainers to obtain single cell suspensions. Cells were then resuspended in DMEM (Gibco), supplemented with 10% fetal bovine serum (FBS) (Gibco), 1% Gentamycin (Thermo Fisher) and 20% L929 cell-conditioned medium (LCM) to promote differentiation into macrophages. A total of $5x10^5$ cells were seeded per dish and cultured for 7 days at 37 °C with 5% CO_2.

Human iPSC-derived cell cultures

iPSC maintenance

All iPSCs experiments were performed according to all relevant local guidelines and regulations. Work with microglia was performed with the female iPSC line A18945 (ThermoFisher, Cat# A18945, hPSCreg name TMOi001-A, RRID:CVCL_RM92) and work with oligodendroglia with the male line 7889SA (NYSCF repository, NYSCFi003-A, RRID:CVCL_B5IZ). iPSCs were maintained on vitronectin-coated culture plates (ThermoFisher, Cat# A14700 diluted 1:100 in PBS, 1h at room temperature) and Essential 8 Flex Medium (E8F) (ThermoFisher Cat#A2858501) at 37ºC with 5% CO_2 until they reached 80% confluency. Cells were passaged using PBS with 500nM EDTA (ThermoFisher, Cat# 15575020) for 5min and plated again in E8F.

iPSC-derived Oligodendrocytes

iPSCs were differentiated into oligodendroglia using a slightly modified protocol as previously published [35]. Briefly, iPSC colonies from 6 wells of a 6-well plate were lifted with collagenase (2mg/mL; Life Technologies) and dispase (1mg/ml; Life Technologies), washed in PBS and resuspended in phase 1 neuralization medium. Phase 1 medium: chemically defined medium (CDM: 50% F12 (Invitrogen), 50% Iscove's modified Dulbecco's medium (Invitrogen), 1% chemically defined Lipid 100 (Invitrogen), BSA (5 mg/mL; Sigma), monothioglycerol (450 µM; Sigma), 1% Antibiotic Antimycotic Solution (Sigma), insulin (7 ng/mL, Roche), transferrin (15 ng/ml; Merck), supplemented with activin inhibitor SB 431542 (10 µM; Sigma), N-acetyl cysteine (1 mM; Sigma) and LDN193189 (0.1 µM; Absource). Resuspended colonies were transferred into a 10cm dish and placed on an orbital shaker. After 24 hours, embryoid bodies have formed, medium was changed every other day. After 7 days, the spheres were caudalized by switching the medium to CDM supplemented with N-acetyl cysteine (1 mM; Sigma), retinoic acid (0.1 µM; Sigma Aldrich), basic fibroblast growth factor (FGF-basic) (5 ng/ml; PeproTech), and heparin (5 pg/ml; Sigma) for additional 7 days. Afterwards, successful neural conversion was assessed by cell morphology, after spheres have been plated on laminin-coated plates (10 µg/ml; Sigma) overnight. Neuralized spheres were collected and transferred into advanced DMEM (Invitrogen), supplemented with 0.5% GlutaMAX (Invitrogen), 0.5% N2 (Invitrogen), 1% B27 (Invitrogen), purmorphamine (1 µM; Sigma), retinoic acid (1 µM; Sigma), FGF-basic (5 ng/ml; PeproTech), heparin (5 pg/ml; Sigma), and 1% Antibiotic Antimycotic Solution (Sigma) for 1 week. FGF-basic and heparin were then withdrawn from the medium and spheres were cultured for 2 more weeks. Spheres were then chopped with a razor blade and transferred into oligodendrocyte proliferation medium consisting of advanced DMEM/F12 (Invitrogen), supplemented with 1% GlutaMAX (Invitrogen), 1% N2 (Invitrogen), 1% B27 (Invitrogen), heparin (5 µg/ml; Sigma), purmorphamine (1 µM; Sigma), FGF-basic (10 ng/ml; PeproTech), T3 (60 ng/ml; Sigma), PDGF-AA (20 ng/ml; PeproTech), SAG (1 µM; Calbiochem), IGF-1 (10 ng/ml; PeproTech), and 1% Antibiotic Antimycotic Solution (Sigma) to promote oligodendrocyte progenitor cell proliferation. After 2 weeks, spheres were chopped and plated on coverslips coated with poly-ornithine (1:100;

Sigma) and laminin (10 µg/ml; Sigma Aldrich) in proliferation medium. After 24 hours the medium was changed to oligodendrocyte differentiating medium containing advanced DMEM (Invitrogen), supplemented with 1% GlutaMAX (Invitrogen), 1% N2 (Invitrogen), 1% B27 (Invitrogen), heparin (5 µg/ml; Sigma), 1% Antibiotic Antimycotic Solution (Sigma), IGF-1 (10 ng/ml; R&D Systems), T3 (60 ng/ml; Sigma), and Insulin-transferrin-sodium selenite (ITS) (1:100; Sigma). Cells were cultured for 7 days before they went into co-culture with microglia.

iPSC-derived Microglia

Differentiation of iPSC to microglia was performed following our recently published protocol[36]. Briefly, 80-90% confluent iPSC colonies were split 1:150-1:200 using PBS with EDTA, and hematopoiesis was induced for 12 days using the STEMDiff Hematopoietic Kit (STEMCELL Technologies, Cat#05310) following the manufacturer's instructions. Floating hematopoietic precursor cells were collected and frozen in Bambanker (FujiFilm Wako, Cat#302-14681). After thawing, hematopoietic precursor cells were differentiated into microglia for 12 days in DMEM/F12 supplemented with 2x Insulin-Transferrin-Selen (ITS-G, Thermo Fisher, Cat#41400-045), 2x B27 supplement, 0.5x N2 supplement, 1x GlutaMAX, 1x NEAA, 5 µg/ml Insulin, 1x Penicillin/Streptomycin, and 400 µM monothioglycerol (Sigma-Aldrich, Cat#M1753), 100 ng/ml IL34 (Peprotech, Cat#200-34), 50 ng/ml TGF-β1 (Peprotech, Cat#100-21), and 25 ng/ml M-CSF (Peprotech, Cat#300-25). Microglia were used for experiments on day 24 of differentiation.

Western blotting analysis

For cells, samples were suspended in lysis/extraction buffer RIPA buffer (Thermo Fisher) containing protease and phosphatase inhibitors and incubated on ice for 5 min and briefly sonicated. All samples were centrifuged at 12,000g for 7 min at 4°C and supernatant was collected. For mouse brain tissue, the lesion and perilesional cortex was isolated and placed into a lysis tube A (Innuscreen) containing lysis/extraction buffer RIPA with added protease and phosphatase inhibitors. Samples were homogenized using homogenizor (Qiagen) at 40 oscillations/s for 30 sec, then centrifuged at 12,000 g for 7 min at 4 °C and supernatant was collected. For cell supernatant were processed as previously described[37]. Total protein was quantified using the Pierce BCA protein assay kit (Thermo Fisher Scientific). Whole cell and tissue lysates were fractionated by SDS-PAGE using Bis-Tris gels (Thermo Fisher) and transferred onto a polyvinylidene difluoride membrane (PVDF) (BioRad). Membranes were blacked for 1h in TBS-T (TBS with 0.1 % Tween 20; pH 8.0; Roth) containing 5% BSA (Sigma Aldrich), the membrane was then incubated with the primary antibodies against following antibodies: mouse Casper-1/ p20 (1:1000; Cell signaling), rabbit Galectin3 (1:1,000; R&D Systems) rabbit anti-actin (1:5000; Sigma Aldrich) diluted in TBS-T with 5% BSA. Membranes were washed three times with TBS-T and incubated for 1 hour with HRP-conjugated anti-rabbit or anti-mouse secondary antibodies (1:5000; Agilent Technologies) at RT. Membranes were developed using ECL substrate (Millipore) and acquired via the Vilber Fusion Fx7 imaging system. Protein quantification was quantified using ImageJ and all antibodies were normalized to actin.

Enzyme linked immunosorbent assay

Total mouse Il-1B and human IL-1B were measured in brain and cell protein lysis and supernatant according to manufacturer's instructions (R&D Systems). Lesion and perilesional cortical tissue were isolated and placed into lysis A-tubes (Innuscreen) with cell lysis buffer (R&D) containing protease and phosphatase inhibitors. Samples were homogenized using a Tissue Lyser LT (Qiagen) with a speed of 40 oscillations/s for 30 sec. Samples were centrifuged at 12,000 g for 7 min at 4 °C and supernatant was collected. For cell supernatant, samples were collected and centrifuged at 3,000 g for 7 min at 4 °C and supernatant was collected. All samples were run in triplicate.

Assay for cholesterol uptake into human iPSC-derived cells

iPSC-derived Microglia (iMG) were plated on a 24-well transwell (Corning) (#cells/well) and treated with TMR-cholesterol (1 µM; Avanti) for 2 h. Cells were then washed wish PBS to remove excess TMR-cholesterol and fresh medium was added and iMG transwells were transferred on top of a 24-well with plated iPSC-derived oligodendrocytes (iOligos) at the bottom. Wells were subjected to GW3965 (Selleck) for 24 h and iOligos were observed for TMR-cholesterol uptake by confocal microscopy (Zeiss) after immunofluorescent staining using anti-Olig2 (Sigma Aldrich) as previously described.

BMDM Cholesterol crystal treatment

WT and ASC-Citrine BMDMs were isolated and differentiated as described previously. Then cells were cultured on 6-well plates ($3x10^6$ cells/well) and primed for 4h with LPS from E.coli (Adipogen). Cells were washed with PBS and then subjected to cholesterol crystals in serum-free culture medium ranging from 3-72 h. Cholesterol crystals were made as previously described[38]. WT cell supernatant was collected for western blot analysis and ASC-Citrine cells were collected for flow cytometry analysis of ASC-speck formation.

Cholesterol assay

Brain tissue was processed to measure total, free and esterified cholesterol according to manufacturer's instructions (abcam).

ASC-Speck analysis in mouse brain tissue

ASC-Citrine sham and stroke mice were perfused and brains were collected and processed as previously described. ASC-specks were quantified in the ipsilateral hemisphere using the particle analysis tool in (Image J Fiji).

QUANTIFICATION AND STATISTICAL ANALYSIS

Data were analyzed using GraphPad Prism version 9.0 and 10. All summary data are expressed as the mean ± standard deviation (s.d.), unless indicated otherwise. Normality was assessed in all datasets using the Shapiro-Wilk normality test. Normally-distributed data were analyzed using a two-way Student's t test (for 2 groups) or ANOVA (for > 2 groups). Non-normally distributed data were analyzed using the Mann-Whitney U test (unpaired data) or Wilcoxon rank sum test (paired data) (for 2 groups), or Kruskal-Wallis test (H test, for > 2 groups). Multiple comparison adjusted p values were computed using Bonferroni correction or Dunn's multiple comparison tests. Statistical analysis for longitudinal data was performed using linear-mixed models with group-by-time interaction in R (Version 4.3.1). For all analyses a p value < 0.05 was considered statistically significant.

MAIN REFERENCES

1. Iadecola, C. (2017). The Neurovascular Unit Coming of Age: A Journey through Neurovascular Coupling in Health and Disease. Neuron *96*, 17-42. 10.1016/j.neuron.2017.07.030.
2. Li, Q., and Barres, B.A. (2018). Microglia and macrophages in brain homeostasis and disease. Nat Rev Immunol *18*, 225-242. 10.1038/nri.2017.125.
3. Allen, N.J., and Lyons, D.A. (2018). Glia as architects of central nervous system formation and function. Science *362*, 181-185. 10.1126/science.aat0473.
4. Clarke, L.E., and Barres, B.A. (2013). Emerging roles of astrocytes in neural circuit development. Nat Rev Neurosci *14*, 311-321. 10.1038/nrn3484.
5. Biederer, T., Kaeser, P.S., and Blanpied, T.A. (2017). Transcellular Nanoalignment of Synaptic Function. Neuron *96*, 680-696. 10.1016/j.neuron.2017.10.006.
6. Shen, Q., Goderie, S.K., Jin, L., Karanth, N., Sun, Y., Abramova, N., Vincent, P., Pumiglia, K., and Temple, S. (2004). Endothelial cells stimulate self-renewal and expand neurogenesis of neural stem cells. Science *304*, 1338-1340. 10.1126/science.1095505.
7. Liu, Y., Shen, X., Zhang, Y., Zheng, X., Cepeda, C., Wang, Y., Duan, S., and Tong, X. (2023). Interactions of glial cells with neuronal synapses, from astrocytes to microglia and oligodendrocyte lineage cells. Glia *71*, 1383-1401. 10.1002/glia.24343.
8. Cserep, C., Posfai, B., and Denes, A. (2021). Shaping Neuronal Fate: Functional Heterogeneity of Direct Microglia-Neuron Interactions. Neuron *109*, 222-240. 10.1016/j.neuron.2020.11.007.
9. Cserep, C., Posfai, B., Lenart, N., Fekete, R., Laszlo, Z.I., Lele, Z., Orsolits, B., Molnar, G., Heindl, S., Schwarcz, A.D., et al. (2020). Microglia monitor and protect neuronal function through specialized somatic purinergic junctions. Science *367*, 528-537. 10.1126/science.aax6752.
10. Ballester, B.R., Maier, M., Duff, A., Cameirao, M., Bermudez, S., Duarte, E., Cuxart, A., Rodriguez, S., San Segundo Mozo, R.M., and Verschure, P. (2019). A critical time window for recovery extends beyond one-year post-stroke. J Neurophysiol *122*, 350-357. 10.1152/jn.00762.2018.
11. Grefkes, C., and Fink, G.R. (2020). Recovery from stroke: current concepts and future perspectives. Neurol Res Pract *2*, 17. 10.1186/s42466-020-00060-6.
12. Ward, N.S., and Carmichael, S.T. (2020). Blowing up Neural Repair for Stroke Recovery: Preclinical and Clinical Trial Considerations. Stroke *51*, 3169-3173. 10.1161/STROKEAHA.120.030486.
13. Joy, M.T., and Carmichael, S.T. (2021). Encouraging an excitable brain state: mechanisms of brain repair in stroke. Nat Rev Neurosci *22*, 38-53. 10.1038/s41583-020-00396-7.
14. Murphy, T.H., and Corbett, D. (2009). Plasticity during stroke recovery: from synapse to behaviour. Nat Rev Neurosci *10*, 861-872. 10.1038/nrn2735.
15. Shichita, T., Ooboshi, H., and Yoshimura, A. (2023). Neuroimmune mechanisms and therapies mediating post-ischaemic brain injury and repair. Nat Rev Neurosci *24*, 299-312. 10.1038/s41583-023-00690-0.
16. Ward, N.S. (2017). Restoring brain function after stroke - bridging the gap between animals and humans. Nat Rev Neurol *13*, 244-255. 10.1038/nrneurol.2017.34.
17. Willis, E.F., MacDonald, K.P.A., Nguyen, Q.H., Garrido, A.L., Gillespie, E.R., Harley, S.B.R., Bartlett, P.F., Schroder, W.A., Yates, A.G., Anthony, D.C., et al. (2020). Repopulating Microglia Promote Brain Repair in an IL-6-Dependent Manner. Cell *180*, 833-846 e816. 10.1016/j.cell.2020.02.013.
18. Escartin, C., Galea, E., Lakatos, A., O'Callaghan, J.P., Petzold, G.C., Serrano-Pozo, A., Steinhauser, C., Volterra, A., Carmignoto, G., Agarwal, A., et al. (2021). Reactive astrocyte nomenclature, definitions, and future directions. Nat Neurosci *24*, 312-325. 10.1038/s41593-020-00783-4.
19. Karve, I.P., Taylor, J.M., and Crack, P.J. (2016). The contribution of astrocytes and microglia to traumatic brain injury. Br J Pharmacol *173*, 692-702. 10.1111/bph.13125.
20. Lan, X., Han, X., Li, Q., Yang, Q.W., and Wang, J. (2017). Modulators of microglial activation and polarization after intracerebral haemorrhage. Nat Rev Neurol *13*, 420-433. 10.1038/nrneurol.2017.69.
21. Takase, H., Washida, K., Hayakawa, K., Arai, K., Wang, X., Lo, E.H., and Lok, J. (2018). Oligodendrogenesis after traumatic brain injury. Behav Brain Res *340*, 205-211. 10.1016/j.bbr.2016.10.042.
22. Louveau, A., Harris, T.H., and Kipnis, J. (2015). Revisiting the Mechanisms of CNS Immune Privilege. Trends Immunol *36*, 569-577. 10.1016/j.it.2015.08.006.
23. Borst, K., Dumas, A.A., and Prinz, M. (2021). Microglia: Immune and non-immune functions. Immunity *54*, 2194-2208. 10.1016/j.immuni.2021.09.014.
24. Hickman, S., Izzy, S., Sen, P., Morsett, L., and El Khoury, J. (2018). Microglia in neurodegeneration. Nat Neurosci *21*, 1359-1369. 10.1038/s41593-018-0242-x.

25. Banati, R.B. (2002). Visualising microglial activation in vivo. Glia *40*, 206-217. 10.1002/glia.10144.
26. Jin, X., and Yamashita, T. (2016). Microglia in central nervous system repair after injury. J Biochem *159*, 491-496. 10.1093/jb/mvw009.
27. Wynn, T.A., and Vannella, K.M. (2016). Macrophages in Tissue Repair, Regeneration, and Fibrosis. Immunity *44*, 450-462. 10.1016/j.immuni.2016.02.015.
28. Chistiakov, D.A., Bobryshev, Y.V., and Orekhov, A.N. (2016). Macrophage-mediated cholesterol handling in atherosclerosis. J Cell Mol Med *20*, 17-28. 10.1111/jcmm.12689.
29. Dahik, V.D., Kc, P., Materne, C., Reydellet, C., Lhomme, M., Cruciani-Guglielmacci, C., Denom, J., Bun, E., Ponnaiah, M., Deknuydt, F., et al. (2024). ABCG1 orchestrates adipose tissue macrophage plasticity and insulin resistance in obesity by rewiring saturated fatty acid pools. Sci Transl Med *16*, eadi6682. 10.1126/scitranslmed.adi6682.
30. Vanherle, S., Loix, M., Miron, V.E., Hendriks, J.J.A., and Bogie, J.F.J. (2025). Lipid metabolism, remodelling and intercellular transfer in the CNS. Nat Rev Neurosci *26*, 214-231. 10.1038/s41583-025-00908-3.
31. Chai, A.B., Ammit, A.J., and Gelissen, I.C. (2017). Examining the role of ABC lipid transporters in pulmonary lipid homeostasis and inflammation. Respir Res *18*, 41. 10.1186/s12931-017-0526-9.
32. Barker, R.A., Gotz, M., and Parmar, M. (2018). New approaches for brain repair-from rescue to reprogramming. Nature *557*, 329-334. 10.1038/s41586-018-0087-1.
33. Giaume, C., Kirchhoff, F., Matute, C., Reichenbach, A., and Verkhratsky, A. (2007). Glia: the fulcrum of brain diseases. Cell Death Differ *14*, 1324-1335. 10.1038/sj.cdd.4402144.
34. Hu, X., Leak, R.K., Shi, Y., Suenaga, J., Gao, Y., Zheng, P., and Chen, J. (2015). Microglial and macrophage polarization-new prospects for brain repair. Nat Rev Neurol *11*, 56-64. 10.1038/nrneurol.2014.207.
35. Small, S.L., Buccino, G., and Solodkin, A. (2013). Brain repair after stroke--a novel neurological model. Nat Rev Neurol *9*, 698-707. 10.1038/nrneurol.2013.222.
36. Planas, A.M. (2024). Role of microglia in stroke. Glia *72*, 1016-1053. 10.1002/glia.24501.
37. Lenart, N., Cserep, C., Csaszar, E., Posfai, B., and Denes, A. (2024). Microglia-neuron-vascular interactions in ischemia. Glia *72*, 833-856. 10.1002/glia.24487.
38. Zatcepin, A., Heindl, S., Schillinger, U., Kaiser, L., Lindner, S., Bartenstein, P., Kopczak, A., Liesz, A., Brendel, M., and Ziegler, S.I. (2022). Reduced Acquisition Time [(18)F]GE-180 PET Scanning Protocol Replaces Gold-Standard Dynamic Acquisition in a Mouse Ischemic Stroke Model. Front Med (Lausanne) *9*, 830020. 10.3389/fmed.2022.830020.
39. Owen, D.R., Narayan, N., Wells, L., Healy, L., Smyth, E., Rabiner, E.A., Galloway, D., Williams, J.B., Lehr, J., Mandhair, H., et al. (2017). Pro-inflammatory activation of primary microglia and macrophages increases 18 kDa translocator protein expression in rodents but not humans. J Cereb Blood Flow Metab *37*, 2679-2690. 10.1177/0271678x17710182.
40. Heindl, S., Gesierich, B., Benakis, C., Llovera, G., Duering, M., and Liesz, A. (2018). Automated Morphological Analysis of Microglia After Stroke. Front Cell Neurosci *12*, 106. 10.3389/fncel.2018.00106.
41. Krasemann, S., Madore, C., Cialic, R., Baufeld, C., Calcagno, N., El Fatimy, R., Beckers, L., O'Loughlin, E., Xu, Y., Fanek, Z., et al. (2017). The TREM2-APOE Pathway Drives the Transcriptional Phenotype of Dysfunctional Microglia in Neurodegenerative Diseases. Immunity *47*, 566-581.e569. 10.1016/j.immuni.2017.08.008.
42. Snaidero, N., Schifferer, M., Mezydlo, A., Zalc, B., Kerschensteiner, M., and Misgeld, T. (2020). Myelin replacement triggered by single-cell demyelination in mouse cortex. Nature Communications *11*, 4901. 10.1038/s41467-020-18632-0.
43. Cramer, J.V., Gesierich, B., Roth, S., Dichgans, M., Düring, M., and Liesz, A. (2019). In vivo widefield calcium imaging of the mouse cortex for analysis of network connectivity in health and brain disease. Neuroimage *199*, 570-584. 10.1016/j.neuroimage.2019.06.014.
44. Schlepckow, K., Morenas-Rodriguez, E., Hong, S., and Haass, C. (2023). Stimulation of TREM2 with agonistic antibodies-an emerging therapeutic option for Alzheimer's disease. Lancet Neurol *22*, 1048-1060. 10.1016/S1474-4422(23)00247-8.
45. Schlepckow, K., Monroe, K.M., Kleinberger, G., Cantuti-Castelvetri, L., Parhizkar, S., Xia, D., Willem, M., Werner, G., Pettkus, N., Brunner, B., et al. (2020). Enhancing protective microglial activities with a dual function TREM2 antibody to the stalk region. EMBO Mol Med *12*, e11227. 10.15252/emmm.201911227.
46. Cignarella, F., Filipello, F., Bollman, B., Cantoni, C., Locca, A., Mikesell, R., Manis, M., Ibrahim, A., Deng, L., Benitez, B.A., et al. (2020). TREM2 activation on microglia promotes myelin debris clearance and remyelination in a model of multiple sclerosis. Acta Neuropathol *140*, 513-534. 10.1007/s00401-020-02193-z.
47. Paolicelli, R.C., Sierra, A., Stevens, B., Tremblay, M.E., Aguzzi, A., Ajami, B., Amit, I., Audinat, E., Bechmann, I., Bennett, M., et al. (2022). Microglia states and nomenclature: A field at its crossroads. Neuron *110*, 3458-3483. 10.1016/j.neuron.2022.10.020.

48. Marschallinger, J., Iram, T., Zardeneta, M., Lee, S.E., Lehallier, B., Haney, M.S., Pluvinage, J.V., Mathur, V., Hahn, O., Morgens, D.W., et al. (2020). Lipid-droplet-accumulating microglia represent a dysfunctional and proinflammatory state in the aging brain. Nat Neurosci *23*, 194-208. 10.1038/s41593-019-0566-1.
49. Deczkowska, A., Keren-Shaul, H., Weiner, A., Colonna, M., Schwartz, M., and Amit, I. (2018). Disease-Associated Microglia: A Universal Immune Sensor of Neurodegeneration. Cell *173*, 1073-1081. 10.1016/j.cell.2018.05.003.
50. Escoubas, C.C., Dorman, L.C., Nguyen, P.T., Lagares-Linares, C., Nakajo, H., Anderson, S.R., Barron, J.J., Wade, S.D., Cuevas, B., Vainchtein, I.D., et al. (2024). Type-I-interferon-responsive microglia shape cortical development and behavior. Cell *187*, 1936-1954 e1924. 10.1016/j.cell.2024.02.020.
51. Czopka, T., von Holst, A., ffrench-Constant, C., and Faissner, A. (2010). Regulatory mechanisms that mediate tenascin C-dependent inhibition of oligodendrocyte precursor differentiation. J Neurosci *30*, 12310-12322. 10.1523/jneurosci.4957-09.2010.
52. Schäfer, I., Bauch, J., Wegrzyn, D., Roll, L., van Leeuwen, S., Jarocki, A., and Faissner, A. (2022). The guanine nucleotide exchange factor Vav3 intervenes in the migration pathway of oligodendrocyte precursor cells on tenascin-C. Front Cell Dev Biol *10*, 1042403. 10.3389/fcell.2022.1042403.
53. Birngruber, T., Ghosh, A., Perez-Yarza, V., Kroath, T., Ratzer, M., Pieber, T.R., and Sinner, F. (2013). Cerebral open flow microperfusion: a new in vivo technique for continuous measurement of substance transport across the intact blood-brain barrier. Clin Exp Pharmacol Physiol *40*, 864-871. 10.1111/1440-1681.12174.
54. Duewell, P., Kono, H., Rayner, K.J., Sirois, C.M., Vladimer, G., Bauernfeind, F.G., Abela, G.S., Franchi, L., Nunez, G., Schnurr, M., et al. (2010). NLRP3 inflammasomes are required for atherogenesis and activated by cholesterol crystals. Nature *464*, 1357-1361. 10.1038/nature08938.
55. Cantuti-Castelvetri, L., Fitzner, D., Bosch-Queralt, M., Weil, M.T., Su, M., Sen, P., Ruhwedel, T., Mitkovski, M., Trendelenburg, G., Lutjohann, D., Mobius, W., and Simons, M. (2018). Defective cholesterol clearance limits remyelination in the aged central nervous system. Science *359*, 684-688. 10.1126/science.aan4183.
56. Bosch-Queralt, M., Cantuti-Castelvetri, L., Damkou, A., Schifferer, M., Schlepckow, K., Alexopoulos, I., Lutjohann, D., Klose, C., Vaculciakova, L., Masuda, T., et al. (2021). Diet-dependent regulation of TGFbeta impairs reparative innate immune responses after demyelination. Nat Metab *3*, 211-227. 10.1038/s42255-021-00341-7.
57. Litvinchuk, A., Suh, J.H., Guo, J.L., Lin, K., Davis, S.S., Bien-Ly, N., Tycksen, E., Tabor, G.T., Remolina Serrano, J., Manis, M., et al. (2024). Amelioration of Tau and ApoE4-linked glial lipid accumulation and neurodegeneration with an LXR agonist. Neuron *112*, 384-403 e388. 10.1016/j.neuron.2023.10.023.
58. Ito, A., Hong, C., Rong, X., Zhu, X., Tarling, E.J., Hedde, P.N., Gratton, E., Parks, J., and Tontonoz, P. (2015). LXRs link metabolism to inflammation through Abca1-dependent regulation of membrane composition and TLR signaling. Elife *4*, e08009. 10.7554/eLife.08009.
59. Joseph, S.B., Castrillo, A., Laffitte, B.A., Mangelsdorf, D.J., and Tontonoz, P. (2003). Reciprocal regulation of inflammation and lipid metabolism by liver X receptors. Nat Med *9*, 213-219. 10.1038/nm820.
60. Zimmer, S., Grebe, A., Bakke, S.S., Bode, N., Halvorsen, B., Ulas, T., Skjelland, M., De Nardo, D., Labzin, L.I., Kerksiek, A., et al. (2016). Cyclodextrin promotes atherosclerosis regression via macrophage reprogramming. Sci Transl Med *8*, 333ra350. 10.1126/scitranslmed.aad6100.
61. Rezaei, A., Kocsis-Jutka, V., Gunes, Z.I., Zeng, Q., Kislinger, G., Bauernschmitt, F., Isilgan, H.B., Parisi, L.R., Kaya, T., Franzenburg, S., et al. (2025). Correction of dysregulated lipid metabolism normalizes gene expression in oligodendrocytes and prolongs lifespan in female poly-GA C9orf72 mice. Nat Commun *16*, 3442. 10.1038/s41467-025-58634-4.
62. Kenigsbuch, M., Bost, P., Halevi, S., Chang, Y., Chen, S., Ma, Q., Hajbi, R., Schwikowski, B., Bodenmiller, B., Fu, H., Schwartz, M., and Amit, I. (2022). A shared disease-associated oligodendrocyte signature among multiple CNS pathologies. Nat Neurosci *25*, 876-886. 10.1038/s41593-022-01104-7.
63. Bando, Y., Hagiwara, Y., Suzuki, Y., Yoshida, K., Aburakawa, Y., Kimura, T., Murakami, C., Ono, M., Tanaka, T., Jiang, Y.P., et al. (2018). Kallikrein 6 secreted by oligodendrocytes regulates the progression of experimental autoimmune encephalomyelitis. Glia *66*, 359-378. 10.1002/glia.23249.
64. Roll, L., and Faissner, A. (2019). Tenascins in CNS lesions. Semin Cell Dev Biol *89*, 118-124. 10.1016/j.semcdb.2018.09.012.
65. Franklin, R.J., and Ffrench-Constant, C. (2008). Remyelination in the CNS: from biology to therapy. Nat Rev Neurosci *9*, 839-855. 10.1038/nrn2480.
66. Armstrong, R.C., Mierzwa, A.J., Marion, C.M., and Sullivan, G.M. (2016). White matter involvement after TBI: Clues to axon and myelin repair capacity. Exp Neurol *275 Pt 3*, 328-333. 10.1016/j.expneurol.2015.02.011.
67. Franklin, R.J.M., and Simons, M. (2022). CNS remyelination and inflammation: From basic mechanisms to therapeutic opportunities. Neuron *110*, 3549-3565. 10.1016/j.neuron.2022.09.023.
68. Yvan-Charvet, L., Wang, N., and Tall, A.R. (2010). Role of HDL, ABCA1, and ABCG1 transporters in cholesterol efflux and immune responses. Arterioscler Thromb Vasc Biol *30*, 139-143. 10.1161/ATVBAHA.108.179283.

69. Wojcik, A.J., Skaflen, M.D., Srinivasan, S., and Hedrick, C.C. (2008). A critical role for ABCG1 in macrophage inflammation and lung homeostasis. J Immunol *180*, 4273-4282. 10.4049/jimmunol.180.6.4273.

70. Yvan-Charvet, L., Welch, C., Pagler, T.A., Ranalletta, M., Lamkanfi, M., Han, S., Ishibashi, M., Li, R., Wang, N., and Tall, A.R. (2008). Increased inflammatory gene expression in ABC transporter-deficient macrophages: free cholesterol accumulation, increased signaling via toll-like receptors, and neutrophil infiltration of atherosclerotic lesions. Circulation *118*, 1837-1847. 10.1161/CIRCULATIONAHA.108.793869.

71. Wang, N., Ranalletta, M., Matsuura, F., Peng, F., and Tall, A.R. (2006). LXR-induced redistribution of ABCG1 to plasma membrane in macrophages enhances cholesterol mass efflux to HDL. Arterioscler Thromb Vasc Biol *26*, 1310-1316. 10.1161/01.ATV.0000218998.75963.02.

72. Rasmussen, M.K., Mestre, H., and Nedergaard, M. (2018). The glymphatic pathway in neurological disorders. Lancet Neurol *17*, 1016-1024. 10.1016/S1474-4422(18)30318-1.

73. Nave, K.A. (2010). Myelination and support of axonal integrity by glia. Nature *468*, 244-252. 10.1038/nature09614.

74. Oesterle, A., Laufs, U., and Liao, J.K. (2017). Pleiotropic Effects of Statins on the Cardiovascular System. Circ Res *120*, 229-243. 10.1161/CIRCRESAHA.116.308537.

75. Beer, C., Blacker, D., Bynevelt, M., Hankey, G.J., and Puddey, I.B. (2012). A randomized placebo controlled trial of early treatment of acute ischemic stroke with atorvastatin and irbesartan. Int J Stroke *7*, 104-111. 10.1111/j.1747-4949.2011.00653.x.

76. Fracassi, A., Marangoni, M., Rosso, P., Pallottini, V., Fioramonti, M., Siteni, S., and Segatto, M. (2019). Statins and the Brain: More than Lipid Lowering Agents? Curr Neuropharmacol *17*, 59-83. 10.2174/1570159X15666170703101816.

77. Menge, T., Hartung, H.P., and Stuve, O. (2005). Statins--a cure-all for the brain? Nat Rev Neurosci *6*, 325-331. 10.1038/nrn1652.

78. Ni Chroinin, D., Callaly, E.L., Duggan, J., Merwick, A., Hannon, N., Sheehan, O., Marnane, M., Horgan, G., Williams, E.B., Harris, D., et al. (2011). Association between acute statin therapy, survival, and improved functional outcome after ischemic stroke: the North Dublin Population Stroke Study. Stroke *42*, 1021-1029. 10.1161/STROKEAHA.110.596734.

79. Kirchgessner, T.G., Sleph, P., Ostrowski, J., Lupisella, J., Ryan, C.S., Liu, X., Fernando, G., Grimm, D., Shipkova, P., Zhang, R., et al. (2016). Beneficial and Adverse Effects of an LXR Agonist on Human Lipid and Lipoprotein Metabolism and Circulating Neutrophils. Cell Metab *24*, 223-233. 10.1016/j.cmet.2016.07.016.

80. Zuchero, Y.J., Chen, X., Bien-Ly, N., Bumbaca, D., Tong, R.K., Gao, X., Zhang, S., Hoyte, K., Luk, W., Huntley, M.A., et al. (2016). Discovery of Novel Blood-Brain Barrier Targets to Enhance Brain Uptake of Therapeutic Antibodies. Neuron *89*, 70-82. 10.1016/j.neuron.2015.11.024.

SUPPLEMENTARY REFERENCES

1. Cramer, J.V., Gesierich, B., Roth, S., Dichgans, M., Düring, M., and Liesz, A. (2019). In vivo widefield calcium imaging of the mouse cortex for analysis of network connectivity in health and brain disease. Neuroimage *199*, 570-584. 10.1016/j.neuroimage.2019.06.014.
2. Llovera, G., Roth, S., Plesnila, N., Veltkamp, R., and Liesz, A. (2014). Modeling Stroke in Mice: Permanent Coagulation of the Distal Middle Cerebral Artery. JoVE, e51729. doi:10.3791/51729.
3. Llovera, G., Simats, A., and Liesz, A. (2021). Modeling Stroke in Mice: Transient Middle Cerebral Artery Occlusion via the External Carotid Artery. JoVE, e62573. doi:10.3791/62573.
4. Schlepckow, K., Monroe, K.M., Kleinberger, G., Cantuti-Castelvetri, L., Parhizkar, S., Xia, D., Willem, M., Werner, G., Pettkus, N., Brunner, B., et al. (2020). Enhancing protective microglial activities with a dual function TREM2 antibody to the stalk region. EMBO Mol Med *12*, e11227. 10.15252/emmm.201911227.
5. Cserép, C., Pósfai, B., Lénárt, N., Fekete, R., László, Z.I., Lele, Z., Orsolits, B., Molnár, G., Heindl, S., Schwarcz, A.D., et al. (2020). Microglia monitor and protect neuronal function through specialized somatic purinergic junctions. Science *367*, 528-537. 10.1126/science.aax6752.
6. Orsini, F., Villa, P., Parrella, S., Zangari, R., Zanier, E.R., Gesuete, R., Stravalaci, M., Fumagalli, S., Ottria, R., Reina, J.J., et al. (2012). Targeting mannose-binding lectin confers long-lasting protection with a surprisingly wide therapeutic window in cerebral ischemia. Circulation *126*, 1484-1494. 10.1161/circulationaha.112.103051.
7. Stefan Roth, J.Y., Julia V Cramer, Rainer Malik, Arthur Liesz (2021). Detection of cytokine-induced sickness behavior after ischemic stroke by an optimized behavioral assessment battery. Brain, Behavior, and Immunity *91*, 668-672. https://doi.org/10.1016/j.bbi.2020.11.016.
8. Ge, Y., Yang, J., Chen, J., Dai, M., Dou, X., Yao, S., Yao, C., and Lin, Y. (2024). Absence in CX3CR1 receptor signaling promotes post-ischemic stroke cognitive function recovery through suppressed microglial pyroptosis in mice. CNS Neurosci Ther *30*, e14551. 10.1111/cns.14551.
9. Zatcepin, A., Heindl, S., Schillinger, U., Kaiser, L., Lindner, S., Bartenstein, P., Kopczak, A., Liesz, A., Brendel, M., and Ziegler, S.I. (2022). Reduced Acquisition Time [(18)F]GE-180 PET Scanning Protocol Replaces Gold-Standard Dynamic Acquisition in a Mouse Ischemic Stroke Model. Front Med (Lausanne) *9*, 830020. 10.3389/fmed.2022.830020.
10. Ma, Y., Hof, P.R., Grant, S.C., Blackband, S.J., Bennett, R., Slatest, L., McGuigan, M.D., and Benveniste, H. (2005). A three-dimensional digital atlas database of the adult C57BL/6J mouse brain by magnetic resonance microscopy. Neuroscience *135*, 1203-1215. 10.1016/j.neuroscience.2005.07.014.
11. Mirrione, M.M., Schiffer, W.K., Fowler, J.S., Alexoff, D.L., Dewey, S.L., and Tsirka, S.E. (2007). A novel approach for imaging brain-behavior relationships in mice reveals unexpected metabolic patterns during seizures in the absence of tissue plasminogen activator. Neuroimage *38*, 34-42. 10.1016/j.neuroimage.2007.06.032.
12. Dana, H., Chen, T.W., Hu, A., Shields, B.C., Guo, C., Looger, L.L., Kim, D.S., and Svoboda, K. (2014). Thy1-GCaMP6 transgenic mice for neuronal population imaging in vivo. PLoS One *9*, e108697. 10.1371/journal.pone.0108697.
13. Chung, A.G., Frye, J.B., Zbesko, J.C., Constantopoulos, E., Hayes, M., Figueroa, A.G., Becktel, D.A., Antony Day, W., Konhilas, J.P., McKay, B.S., Nguyen, T.V., and Doyle, K.P. (2018). Liquefaction of the Brain following Stroke Shares a Similar Molecular and Morphological Profile with Atherosclerosis and Mediates Secondary Neurodegeneration in an Osteopontin-Dependent Mechanism. eNeuro *5*. 10.1523/eneuro.0076-18.2018.
14. Heindl, S., Gesierich, B., Benakis, C., Llovera, G., Duering, M., and Liesz, A. (2018). Automated Morphological Analysis of Microglia After Stroke. Front Cell Neurosci *12*, 106. 10.3389/fncel.2018.00106.
15. Kislinger, G., Niemann, C., Rodriguez, L., Jiang, H., Fard, M.K., Snaidero, N., Schumacher, A.-M., Kerschensteiner, M., Misgeld, T., and Schifferer, M. (2023). Neurons on tape: Automated Tape Collecting Ultramicrotomy-mediated volume EM for targeting neuropathology. In Methods in cell biology, (Academic Press). https://doi.org/10.1016/bs.mcb.2023.01.012.
16. Schindelin, J., Arganda-Carreras, I., Frise, E., Kaynig, V., Longair, M., Pietzsch, T., Preibisch, S., Rueden, C., Saalfeld, S., Schmid, B., et al. (2012). Fiji: an open-source platform for biological-image analysis. Nature Methods *9*, 676-682. 10.1038/nmeth.2019.
17. Yu, G., Wang, L.G., Han, Y., and He, Q.Y. (2012). clusterProfiler: an R package for comparing biological themes among gene clusters. Omics *16*, 284-287. 10.1089/omi.2011.0118.
18. Trapnell, C., Cacchiarelli, D., Grimsby, J., Pokharel, P., Li, S., Morse, M., Lennon, N.J., Livak, K.J., Mikkelsen, T.S., and Rinn, J.L. (2014). The dynamics and regulators of cell fate decisions are revealed by pseudotemporal ordering of single cells. Nat Biotechnol *32*, 381-386. 10.1038/nbt.2859.

19. Androvic, P., Schifferer, M., Perez Anderson, K., Cantuti-Castelvetri, L., Jiang, H., Ji, H., Liu, L., Gouna, G., Berghoff, S.A., Besson-Girard, S., et al. (2023). Spatial Transcriptomics-correlated Electron Microscopy maps transcriptional and ultrastructural responses to brain injury. Nature Communications *14*, 4115. 10.1038/s41467-023-39447-9.
20. Lopez, R., Regier, J., Cole, M.B., Jordan, M.I., and Yosef, N. (2018). Deep generative modeling for single-cell transcriptomics. Nat Methods *15*, 1053-1058. 10.1038/s41592-018-0229-2.
21. Lange, M., Bergen, V., Klein, M., Setty, M., Reuter, B., Bakhti, M., Lickert, H., Ansari, M., Schniering, J., Schiller, H.B., Pe'er, D., and Theis, F.J. (2022). CellRank for directed single-cell fate mapping. Nature Methods *19*, 159-170. 10.1038/s41592-021-01346-6.
22. Jin, S., Guerrero-Juarez, C.F., Zhang, L., Chang, I., Ramos, R., Kuan, C.-H., Myung, P., Plikus, M.V., and Nie, Q. (2021). Inference and analysis of cell-cell communication using CellChat. Nature Communications *12*, 1088. 10.1038/s41467-021-21246-9.
23. Dobin, A., Davis, C.A., Schlesinger, F., Drenkow, J., Zaleski, C., Jha, S., Batut, P., Chaisson, M., and Gingeras, T.R. (2013). STAR: ultrafast universal RNA-seq aligner. Bioinformatics *29*, 15-21. 10.1093/bioinformatics/bts635.
24. Holtmaat, A., Bonhoeffer, T., Chow, D.K., Chuckowree, J., De Paola, V., Hofer, S.B., Hübener, M., Keck, T., Knott, G., Lee, W.C., et al. (2009). Long-term, high-resolution imaging in the mouse neocortex through a chronic cranial window. Nat Protoc *4*, 1128-1144. 10.1038/nprot.2009.89.
25. Mazaheri, F., Snaidero, N., Kleinberger, G., Madore, C., Daria, A., Werner, G., Krasemann, S., Capell, A., Trümbach, D., Wurst, W., et al. (2017). TREM2 deficiency impairs chemotaxis and microglial responses to neuronal injury. EMBO reports *18*, 1186-1198-1198. https://doi.org/10.15252/embr.201743922.
26. Birngruber, T., Ghosh, A., Perez-Yarza, V., Kroath, T., Ratzer, M., Pieber, T.R., and Sinner, F. (2013). Cerebral open flow microperfusion: a new in vivo technique for continuous measurement of substance transport across the intact blood-brain barrier. Clinical and experimental pharmacology & physiology *40*, 864-871. 10.1111/1440-1681.12174.
27. Hughes, C.S., Moggridge, S., Muller, T., Sorensen, P.H., Morin, G.B., and Krijgsveld, J. (2019). Single-pot, solid-phase-enhanced sample preparation for proteomics experiments. Nature protocols *14*, 68-85. 10.1038/s41596-018-0082-x.
28. Chambers, M.C., Maclean, B., Burke, R., Amodei, D., Ruderman, D.L., Neumann, S., Gatto, L., Fischer, B., Pratt, B., Egertson, J., et al. (2012). A cross-platform toolkit for mass spectrometry and proteomics. Nature biotechnology *30*, 918-920. 10.1038/nbt.2377.
29. Cox, J., Hein, M.Y., Luber, C.A., Paron, I., Nagaraj, N., and Mann, M. (2014). Accurate proteome-wide label-free quantification by delayed normalization and maximal peptide ratio extraction, termed MaxLFQ. Molecular & cellular proteomics : MCP *13*, 2513-2526. 10.1074/mcp.M113.031591.
30. Tyanova, S., Temu, T., Sinitcyn, P., Carlson, A., Hein, M.Y., Geiger, T., Mann, M., and Cox, J. (2016). The Perseus computational platform for comprehensive analysis of (prote)omics data. Nature methods *13*, 731-740. 10.1038/nmeth.3901.
31. McDowell, I.C., Manandhar, D., Vockley, C.M., Schmid, A.K., Reddy, T.E., and Engelhardt, B.E. (2018). Clustering gene expression time series data using an infinite Gaussian process mixture model. PLoS Comput Biol *14*, e1005896. 10.1371/journal.pcbi.1005896.
32. Krämer, A., Green, J., Pollard, J., Jr., and Tugendreich, S. (2014). Causal analysis approaches in Ingenuity Pathway Analysis. Bioinformatics *30*, 523-530. 10.1093/bioinformatics/btt703.
33. Youssef, A., Paul, I., Crovella, M., and Emili, A. (2024). DESP demixes cell-state profiles from dynamic bulk molecular measurements. Cell Reports Methods *4*, 100729. https://doi.org/10.1016/j.crmeth.2024.100729.
34. Klein, D., Palla, G., Lange, M., Klein, M., Piran, Z., Gander, M., Meng-Papaxanthos, L., Sterr, M., Saber, L., Jing, C., et al. (2025). Mapping cells through time and space with moscot. Nature *638*, 1065-1075. 10.1038/s41586-024-08453-2.
35. Livesey, M.R., Magnani, D., Cleary, E.M., Vasistha, N.A., James, O.T., Selvaraj, B.T., Burr, K., Story, D., Shaw, C.E., Kind, P.C., et al. (2016). Maturation and electrophysiological properties of human pluripotent stem cell-derived oligodendrocytes. Stem Cells *34*, 1040-1053. 10.1002/stem.2273.
36. Reifschneider, A., Robinson, S., Van Lengerich, B., Gnörich, J., Logan, T., Heindl, S., Vogt, M.A., Weidinger, E., Riedl, L., Wind, K., et al. (2022). Loss of TREM2 rescues hyperactivation of microglia, but not lysosomal deficits and neurotoxicity in models of progranulin deficiency. The EMBO Journal *41*. 10.15252/embj.2021109108.
37. Jakobs, C., Bartok, E., Kubarenko, A., Bauernfeind, F., and Hornung, V. (2013). Immunoblotting for Active Caspase-1. In The Inflammasome: Methods and Protocols, C.M. De Nardo, and E. Latz, eds. (Humana Press), pp. 103-115. 10.1007/978-1-62703-523-1_9.
38. Rajamäki, K., Lappalainen, J., Öörni, K., Välimäki, E., Matikainen, S., Kovanen, P.T., and Eklund, K.K. (2010). Cholesterol Crystals Activate the NLRP3 Inflammasome in Human Macrophages: A Novel Link between Cholesterol Metabolism and Inflammation. PLoS ONE *5*, e11765. 10.1371/journal.pone.0011765.

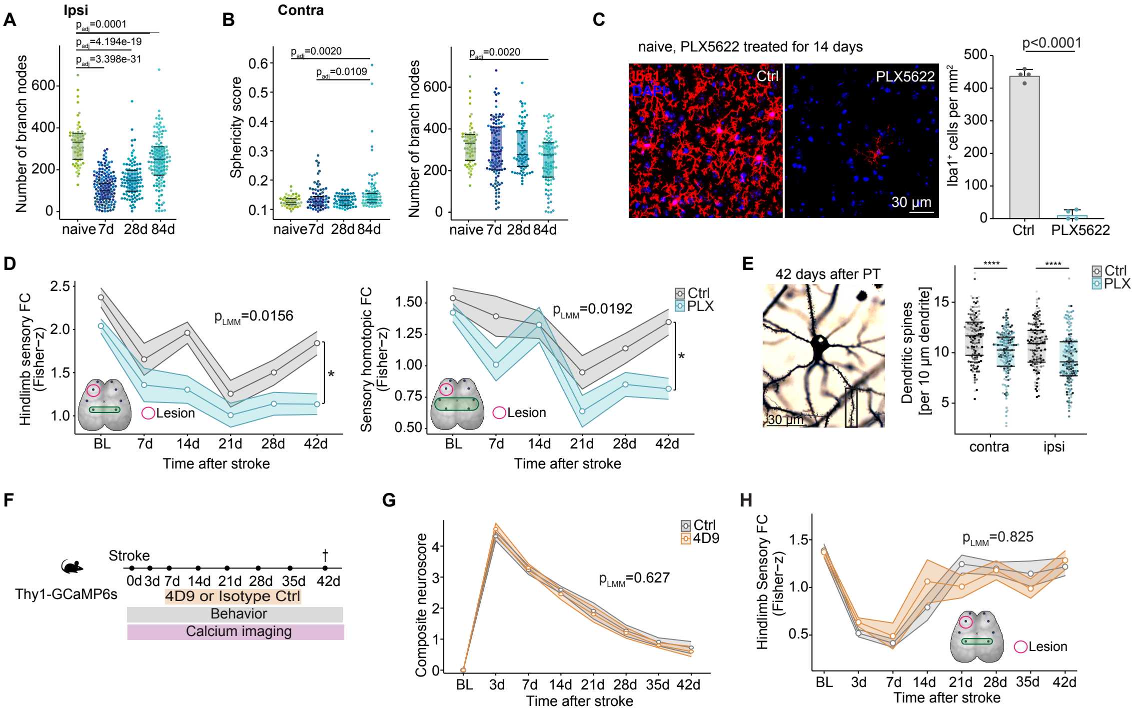

Figure S1. Microglia remain chronically reactive but are necessary for post-stroke recovery. (**A**) Numbers of branch nodes in perilesional microglia 300 µm away from lesion border until 84 days post stroke. Points represent individual cells, color coded for individual mice (Pairwise Wilcoxon test and Bonferroni correction, *n*=5-6 /group) (**B**) Sphericity score and numbers of branch nodes from microglia in the contralateral cortex until 84 days after stroke. Points represent individual cells, color coded for individual mice (Pairwise Wilcoxon test and Bonferroni correction, *n*=5-6 /group). (**C**) Representative confocal images and quantification of Iba1^{+} microglia in naïve mice after 14 days of treatment with PLX5622 for microglia depletion or control diet for evaluation of depletion efficacy in cortex (*n=4* /group, T test). (**D**) Time course of interhemispheric functional connectivity of sensory hind limb cortex and homotopic sensory areas in widefield calcium imaging. (Median ± SE, linear-mixed model, n= 11/13 group). (**E**) Representative image pyramidal neuron stained by Golgi-Cox staining (Scale bar=30 µm) and quantification of dendritic spine density 42 days after stroke within 500 µm from lesion border and contralateral cortex. (Kruskal-Wallis test, Bonferroni correction for multiple comparisons, n=6/7 /group). (**F**) Schematic of experimental outline for 4D9 or 4D5 isotype ctrl 0.05mg/g treatment. (**G**) Evaluation of composite neuroscore (Median ± SE, linear-mixed model, *n=6* /group). (**H**) Time course of interhemispheric functional connectivity of sensory hindlimb cortex in widefield calcium imaging (Median ± SE, linear-mixed model, post-hoc Kruskal-Wallis test, *n=8* /group).

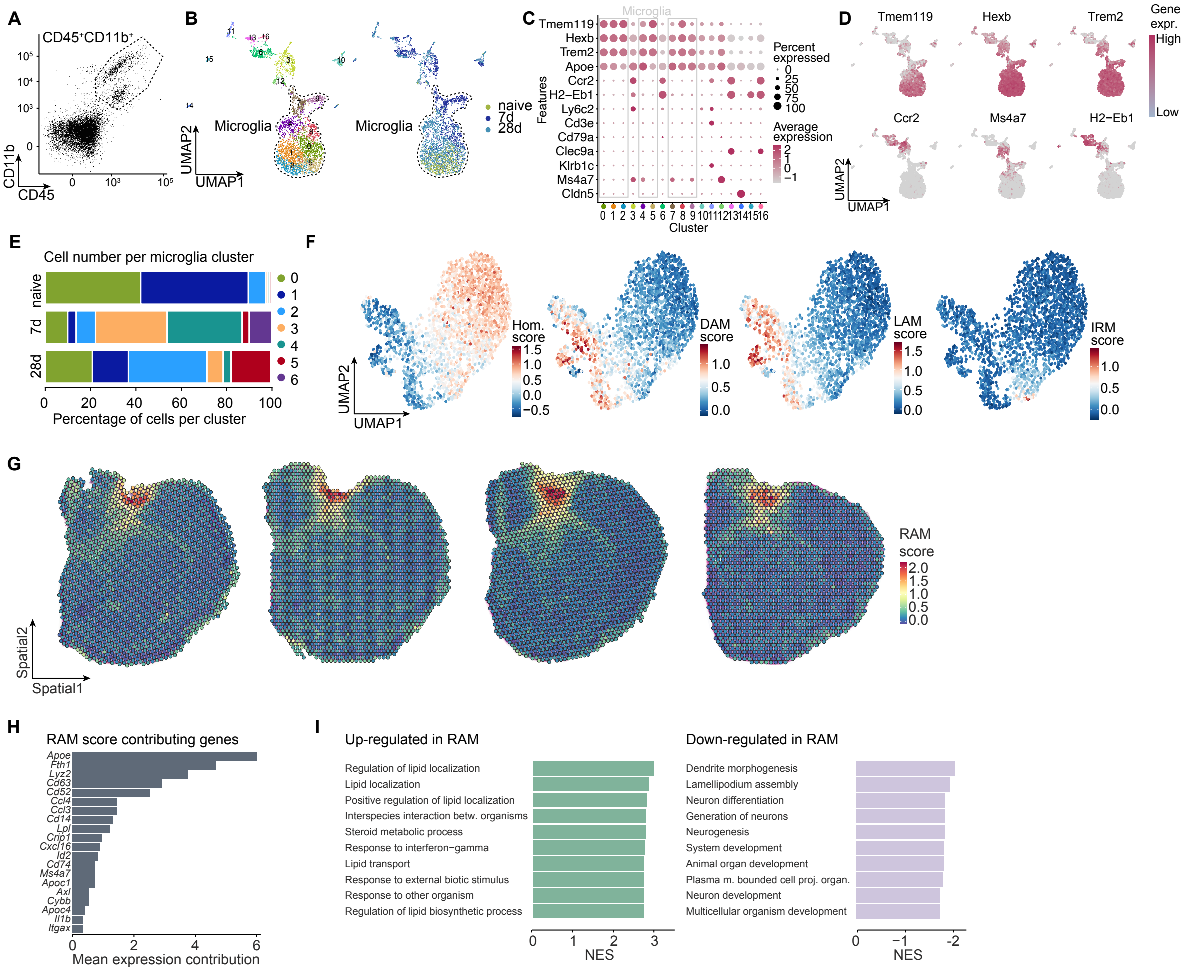

Figure S2. Repair-associated microglia (RAM) are a distinct microglial cell state that shape the chronic lesion microenvironment. **(A)** Sorted population of myeloid cells isolated from perilesional cortex for scRNA sequencing. (**B**) Dimensionality reduction using Uniform Manifold Approximation and Projection (UMAP), showing transcriptomic clusters of myeloid cells using a resolution of 1.2 (left) and pseudo-colored for timepoint (right). Microglia clusters are highlighted by dashed line. (**C**) Marker gene expression per cluster. Color code indicates average expression. Size of dots represents percentage of cells expressing the gene. (**D**) Marker gene expression of microglia and monocytes/macrophages illustrated in UMAP. (**E**) Illustration of cell number per microglia subcluster in scRNA sequencing data after creating microglia subset. (**F**) Expression of microglia subtype scores in UMAP of previously described microglia functional states: homeostatic microglia (Hom. score), Disease associated microglia (DAM score), Lipid associated microglia (LAM score), and Interferon responsive microglia (IRM score). (**G**) Expression of RAM score in spatial transcriptomics (10x Genomics Visium) 28 days after stroke in 4 individual animals. (**H**) Contribution of genes to RAM microglia score calculated by mean gene expression in top 25% of cells expressing the RAM module score. (**I**) Gene set enrichment analysis of up- and down regulated pathways in RAM cluster 5 compared to homeostatic clusters 0 and 1.

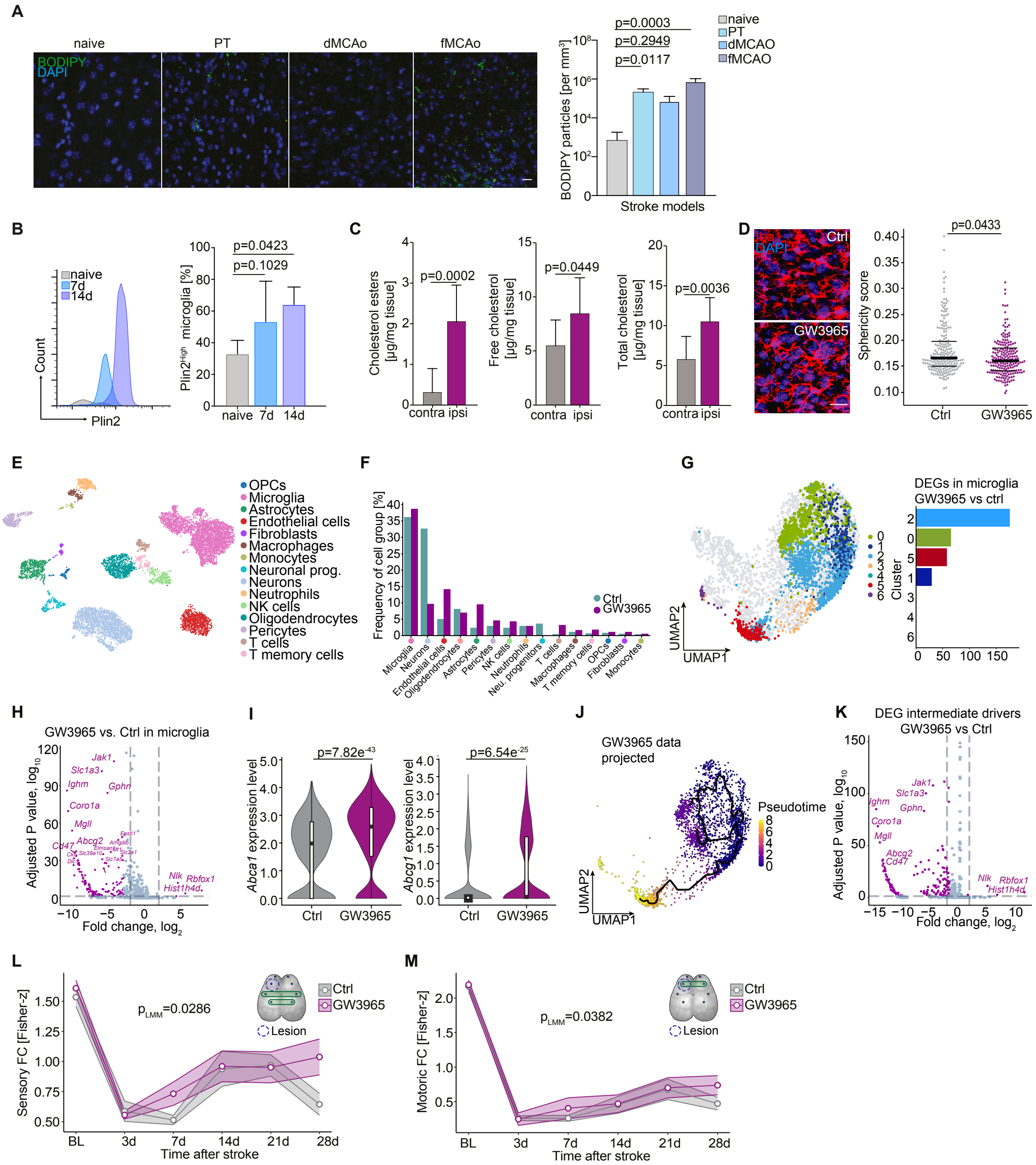

Figure S3. Microglial cholesterol crystallization impairs neuronal recovery after stroke. (A) Representative images and quantification of BODIPY (lipid particles) staining peri-infarct cortex across three experimental stroke models (dMCAo, fMCAo and photothrombosis) 28 days after stroke (scale bar 20 µm; Mann-Whitney U test, *n*=4/6 /group). **(B)** Microglia cells isolated from the brain of naïve, 7 and 14 days after stroke were analyzed by flow cytometry. Representative graph of Plin2 intensity in microglia (CD45^{int} CD11b^{+}) and quantification of Plin2^{High} (lipid droplets) microglia out of total microglia (T test, *n*=3-7 /group). **(C)** Cholesterol levels (esters, free and total) were measured and quantified from ipsilateral and contralateral cortical mouse tissue 28 days after stroke (T test, *n=9* /group). **(D)** Representative images of microglia (Iba1) in control and GW3965 in the peri-infarct cortex 28 days after stroke immunofluorescence (scale bar 20 µm). Quantification of microglia sphericity score. Points represent individual cells (Pairwise Wilcoxon test and Bonferroni correction *n*=7-10 /group). **(E)** UMAP and cell type annotation of scRNA sequencing of mixed cell types isolated from peri-lesional cortex 28 days after stroke, n=3 animals /group. **(F)** Number of cells per cell type in Ctrl and GW3965 treated groups. **(G)** UMAP of microglia subset from scRNA sequencing with projected microglia sub-clusters 0-6 from previous scRNA sequencing dataset (**Fig. 2**) and representation of cell number per sub-cluster. **(H)** Differentially expressed genes in microglia subset from GW3965 vs. Ctrl. Vertical dashed lines indicate log$_2$FC ³ |2|, horizontal line indicates adjusted log$_{10}$(p-value) ³ log$_{10}$(0.05). **(I)** Expression level of Abca1 and Abcg1 for Ctrl and GW3965 treated animals. Wilcoxon test. **(J)** Microglia from Ctrl and GW3965 treated groups projected in UMAP space of microglia subset UMAP (shown in **Fig. 2**) and trajectory representing microglia states along pseudotime. **(K)** Differential expression of detected driver genes for intermediate state in microglia from GW3965 vs. Ctrl. Vertical dashed lines (figure legend continued on next page) indicate log$_2$FC ³ |2|, horizontal line indicates adjusted log$_{10}$(p-value) ³ log$_{10}$(0.05). **(L)** Longitudinal in vivo widefield calcium imaging of Thy1-GCaMP6s animals assessing sensory FC (Median ± SE, linear-mixed models, group-by-time interaction, *n*= 10-15 /group). **(M)** Longitudinal in vivo widefield calcium imaging of Thy1-GCaMP6s animals assessing motoric FC (Median ± SE, linear-mixed models, group-by-time interaction, n= 10-15 /group).

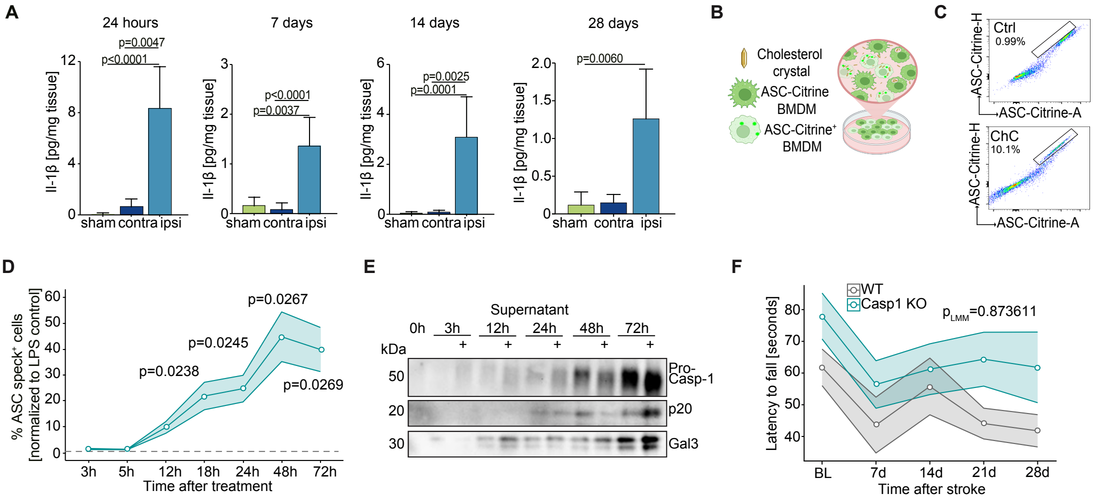

Figure S4. Cholesterol crystals induce chronic inflammation. (A) Brain tissue homogenate Il-1b levels in sham, contralateral and ipsilateral hemispheres 24 hours, 7 days, 14 days and 28 days after stroke (independent samples / time, Kruskal-Wallis test, Dunn's test, *n*=12-13 / group). (**B**) Schematic illustration of experimental set-up for flow cytometry analysis of inflammasome kinetics from ASC-Citrine bone marrow-derived macrophages treated with cholesterol crystals (ChC). (**C**) Representative gating strategy for ASC-Citrine bone marrow-derived macrophages treated with ChC. (**D**) Quantification of longitudinal ASC-speck formation in bone barrow derived macrophages treated with ChC (dashed line indicates LPS control levels) (Shapiro-Wilk test, Multiple T tests, post hoc Bonferroni correction, *n=3-10* /group). (**E**) Western blot time-course from supernatant of bone marrow-derived macrophages primed with LPS for 4h and treated with or without ChC. The (+) symbol indicates the samples treated with ChC. Dynamics of inflammasome activation with pro-caspase-1 and cleaved caspase-1 (p10) expression over time when cells were challenged with ChC. (**F**) Longitudinal assessment of motor coordination using the rotarod test in WT or Caspase-1 KO mice after stroke (Mean ± SEM, linear-mixed model, *n*= 7/15 /group).

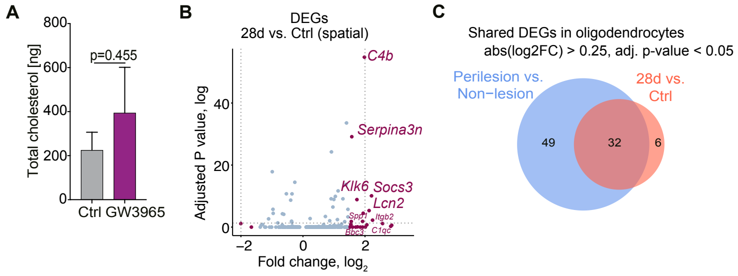

Figure S5. Enhancing cholesterol efflux improves chronic microglia function and post-stroke recovery. (A) Total cholesterol detected in CSF from GW3965 or Ctrl mice (Multiple Mann-Whitney U tests and Benjamini Hochberg correction, *n*= 5/4 /group). (**B**) Representative images and quantification of Ctrl and GW3965 peri-infarct cortex of Gal3 (lysosomal damage) and Iba1 (microglia) immunofluorescence 7 days after stroke (scale bar 20 µm; Mann-Whitney U test *n*= 8/9 /group). (**C**) Representative images and quantification of Ctrl and GW3965 peri-infarct cortex of Gal3 (lysosomal damage) and Iba1 (microglia) immunofluorescence 28 days after stroke (scale bar 20 µm; Mann-Whitney U test *n*= 9/11 /group).

4 DISCUSSION

4.1 T cell-mediated modulation of microglia after stroke

This study demonstrates that lymphocytes, specifically T cells, play a crucial role in influencing microglial morphology and transcriptional responses acutely after stroke. Using the distal model occlusion (dMCAO) experimental stroke mouse model and Rag1$^{-/-}$ mice, which lack B and T lymphocytes, we show that the absence of adaptive immune cells results in significantly altered microglial behavior. In particular, microglia in Rag1$^{-/-}$ mice exhibit a less reactive morphology, characterized by their extended ramifications and reduction in sphericity. This underscores the dependence microglia activation has on lymphocyte infiltration. Notably, microglial depletion in Rag1$^{-/-}$ mice also leads to an exacerbation of infarct size, which is not observed in wild-type animals, which suggests there is a compensatory or protective role of microglia when lymphocyte infiltration is lacking.

Single-cell RNA sequencing analysis brought to light that stroke alone is a strong driver of microglial transcriptional changes. However, in the context of lymphocyte deficiency, we found a distinct transcriptional signature in microglia, both before and after stroke. Rag1$^{-/-}$ after stroke also displayed enrichment of genes that are linked with disease-associated microglia (DAM), such as Apoe, Cd74, Lyz2 and Lgals3. These genes are typically associated with a reactive and neurodegenerative microglia phenotype, therefore implying that microglia reactivity is not abrogated but altered in the absence in the absence of lymphocytes. This dataset also revealed with trajectory analysis of microglia states that lymphocyte deficiency impacts microglia transitioning from a homeostatic to an active phenotype. This was characterized by a significant reduction of phagocytosis and activation markers along with an enhancement of chemokine and cytokine-related genes such as Ccl, Tnf and IL-1β. Overall, suggesting a push toward a dysfunctional, pro-inflammatory phenotype in microglia. Using flow cytometry, it became evident that T cells in comparison to other infiltrating cells, are likely the dominant modulators of microglia acutely after stroke given, they are about 14 times more abundant. Overall, even in relatively low numbers compared to resident cells, T cells seem to exert great influence by targeting microglia to amplify their signals to shape widespread neuroinflammation.

Overall, these findings indicate a cross-talk between T cells and microglia that is critical for dictating the neuroimmune response post-stroke. The absence of T cells results in microglia failure to transition into a reparative phenotype. Thus, potentially exacerbating brain injury when microglia are also depleted. Importantly, our study also gives further rational for immunomodulatory therapies that target T cell-microglia interaction.

4.2 Transcriptional reprogramming of microglia by T cells

As indicated by other studies, CD4 T cell subsets, such as Th1, Th17 and T_{REG} cells are known to elicit diverse effects on post-stroke neuroinflammation [6, 42]. We then wanted to understand how different CD4 T cell subsets with varying functions, effect the microglial response. We injected two opposing subpopulations, Th1 and T_{REG}, which have proinflammatory and anti-inflammatory features, respectively into the cisterna magna (CM) in Rag $^{-/-}$mice after stroke. Our findings show that T helper cells can reprogram microglia toward functionally different states.

Microglia injected with Th1 cells exhibited a unique transcriptional profile compared to vehicle or T_{REG} cells. They even show a significant increase in genes differentially expressed versus in response to Th1. When we performed gene ontology analysis, pathways related to antigen retrieval processing and presentation, cytokine signaling and type I interferon responses where upregulated. In addition, immunocompetent related and pro-inflammatory microglial phenotype related genes were upregulated, such as cd74, Lag3, Irf7 and Stat1. A transcriptional profile similar to reactive microglia seen in chronic neurodegeneration [105]. Overall, these findings suggest that Th1 cells may amplify inflammatory responses after stroke by influencing microglia toward an antigen-presenting and interferon-responsive state.

In contrast, microglia that were exposed to T_{REG} cells displayed a restrained transcriptional shift, with a limited number of differentially expressed genes versus control. The genes upregulated were associated with chemotaxis, with no indication of genes related to inflammatory or antigen presentation pathways. This modest transcriptional profile is also consistent with the known immunoregulatory role of T_{REG} cells and further supports that idea that they may be promoters of homeostatic or even a reparative microglial state after injury.

Collectively, this validates the strong influence of CD4 T cell polarization on microglia function and supports the hypothesis that adaptive immune cells are not just activating microglia but also compose the quality and functional outcome of this activation. Therefore, targeting specific T cell subpopulations to direct microglia function could be a promising strategy to promote a neuroprotective environment after stroke.

4.3 Therapeutic potential of engineered T cells

To explore the therapeutic potential of modulating T cell-microglia interactions, we sought to engineer T cells to overexpress the anti-inflammatory cytokine IL-10 (eTc-IL10). We designed this approach to leverage the clear immunoregulatory capacity of T_{REG} cells through IL-10 signaling with the goal to influence the inflammatory environment after stroke through targeting microglial activation. We injected these eTc-IL10 cells via the cisterna magna and observed no marked differences between eTc-IL10 animals or controls. This is also in alignment with the knowledge that the ischemic lesion size is dictated within the first hours after stroke onset and is found to be unaffected by delayed immune modulation [43]. However, more importantly, we saw a significant improvement in functional recovery, which was evident by reduced forelimb asymmetry. This observed improvement in neurological function indicates that T cell-derived IL-10 may play a role in the subacute phase after stroke by modifying neuroinflammatory processes or pathways that have an influence on synaptic function, plasticity and neuronal repair.

The transcriptional profile of the stroke affected hemisphere from mice with eTc-IL10 treatment, revealed a downregulation of genes associated with a DAM phenotype. These genes include cd68, Apoe, Trem2 and Cst7 and are linked to microglial phagocytic function and synaptic pruning. Further suggesting that t cell-derived IL-10 can regulate microglia from a reactive and potentially toxic phenotype toward a less inflammatory state. Further support of this anti-inflammatory shift is that sorted microglia showed an mRNA profile with a marked decrease in Trem2 levels after eTc-IL10 injections. Gene ontology analysis displayed that microglia show a decrease in effector functions such as complement activation and phagocytosis, meanwhile also increasing their chemokine response. These findings align with a previous transcriptional observations observed in lymphocyte deficient mice injected with T_{REG} cells. Thereby reinforcing the crucial role IL-10 plays in microglia reprogramming in a post-stroke environment [62, 98]

Our experiments included whole brain tissue for transcriptomic assessment, therefore this may include signals from other infiltrating immune cells, such as myeloid cells. However, we did sort microglia cells and confirm the microglia-specific effects of T cell-derived IL-10, which strongly supports that microglia are indeed key responders to this eTc-IL10 therapy. We also confirmed the microglia-specific downregulation of synaptic pruning and neuroimmune interaction, therefore highlighting the role of IL-10 in reducing neuroinflammation and potential to promote neural network recovery.

Our findings reveal that administration of engineered T cells secreting IL-10 acutely after stroke can reprogram microglia in a beneficial manner and ultimately enhance functional outcomes. This therapeutic approach supports immune modulation through cytokine delivery through T cells, as a potentially powerful tool to enhance recovery in human stroke patients who currently have a limited time window and treatment options.

4.4 A unique microglia transcriptomic profile chronically after stroke

Unresolved neuroinflammation after ischemic stroke has received increasing attention in neuroinflammation research involving both, brain infiltrating and resident immune cells [37, 40] Without inflammatory resolution, this puts the brain in a vulnerable position to be at an even greater risk of experiencing a secondary brain injury to further impair functional recover [84]. Microglia, the brain's first responders to injury after brain injuries, such as ischemic stroke, play a central role in the necessary acute immune process. Including peripheral immune cell recruitment and neuroprotection through cytokine and neurotrophin secretion, and maybe their most well described role, phagocytosis [65, 75].

However, microglia function in the chronic phase after stroke remains to be thoroughly explored. In this study, we describe a chronically altered microglial phenotype in an experimental ischemic stroke mouse model, which we refer to as "repair associated microglia" (RAM). Their unique transcriptional signature comprises of upregulation of Apoe, Lyz2, Spp1, Lgal3, Fabp5, Lpl, and Apoc1 as well as downregulation of homeostatic markers P2ry12, Selplg, Siglech, and Tmem119. Although many transcriptionally unique microglia phenotypes have been described such as, damage-associated microglia (DAMs) [51], white matter associated microglia (WAM) [88] interferon responsive microglia (IRM) (Sala Frigerio et al., 2019), lipid-associated microglia (LAM) [3], lipid droplet accumulating microglia (LDAM) [117]. RAM show a distinct transcriptional profile and only partially overlap with stroke associated myeloid cells (SAMC) [9]. RAM prove to play a significant role in regeneration and functional repair after stroke, which is seemingly hindered due to lipid dysregulation.

4.5 Chronic microglial activation is a central feature of post-stroke neuroinflammation

Our study shows evidence for chronic microglial activation until 3 months after experimental stroke in mice, shown by increased uptake of GE-180 tracer (TSPO-derivate) in the lesion and perilesional area, as well as increased microglia sphericity score, a morphological marker for microglial activation [36]. These findings are in line with the outputs of clinical PET-MRI studies showing TSPO uptake until 30 days post stroke, indicating chronic microglial activation and the clinical relevance of microglia during chronic neuroinflammation [30]. Given the capacity of microglia to remodel neuronal circuits through synaptic pruning in pathological conditions [94], their functional is essential for post-stroke recovery. However, our data demonstrate chronic impairment of microglial phagocytosis through an in vivo phagocytosis assay with zymosan and excessive stimulus response when microglia *in vivo* were challenged with a secondary stimulus (burn injury) after stroke and observed through 2-Photon imaging. In addition, we observed a reduction in pyramidal neuronal spine density chronically after stroke, possibly due to a dysfunction in microglial phagocytic capacity. Overall, our findings suggest microglia exhibit long lasting dysfunction after stroke.

Studies have shown that persistent or dysregulated microglial activation can worsen brain injury, promote secondary neurodegeneration and impair functional recovery. However, when microglia are depleted and allowed to repopulate the brain, these “newborn” microglia reduce secondary neurodegeneration and improve cognitive recovery following traumatic brain injury (TBI) [38]. Thus, we aimed to chronically deplete microglia using a common pharmacological CSF1-R inhibitor (PLX5622). We found that chronically depleting microglia exacerbated stroke outcome by increasing infarct size and worsening functional recovery in mice up to 42 days after stroke. Next instead of removing microglia from the equation, we attempted to further increase microglial activation by using 4D9 an anti-Trem2 antibody. Although we did not observe a worsened stroke outcome, we saw no improvement in terms of functionally recovery in mice. Together these findings show that microglia are required in the stroke recovery process, however, enhancing their activation state does not resolve chronic post-stroke recovery.

4.6 Lipid dysregulation in microglia drives chronic inflammation

Lipid metabolism is taking center stage as a central orchestrator of inflammation across demyelinating and neurodegenerative diseases [19]. Notably, the CNS harbors the highest concentration of cholesterol in the body and microglia play a critical role in maintaining the homeostasis of this cholesterol [71,113, 41]. During brain injury, microglia are tasked with the overwhelming burden of clearing myelin debris through phagocytosis. Aligning with this fact, others have reported microglia lipid metabolism becomes defective under these conditions, impairing their ability to convert cholesterol esters derived from myelin thereby driving the formation of intracellular cholesterol crystals [13, 7, 117].

Our findings corroborate that there is lipid dysregulation in microglia after brain injury, and it persists into the chronic phase [64]. Markedly, this phenotype extends beyond the initial site of injury into the perilesional cortex. We demonstrate that microglia in the perilesional cortex are laden with lipid droplets, as shown by BODIPY and Plin2 immunofluorescent staining, which was further validated by Plin2 flow cytometry and electron microscopy. The extend of this lipid overload seems to surpass the capacity of microglia processing, leading to the formation of intracellular crystals, which we detected using both reflection and electron microscopy. We then confirmed that these crystals were most likely composed of cholesterol, indicated by the strong cholesterol signal detected by MALDI-MSI in the ipsilateral hemisphere compared to the virtually absent signal in the contralateral hemisphere. Further evidence to support this was the significant increase in cholesterol esters in the effected tissue. This phenotype was also evident in human post-mortem stroke tissue, where we observed a significant increase in both Plin2 expression and crystal accumulation proximal to the infarct, further supporting the strong translational relevance of our findings.

Studies have revealed that the propagation of intracellular cholesterol crystals damages microglial lysosomes and trigger an inflammatory cascade [13]. Insights from the atherosclerosis field have further established that cholesterol crystals act as potent sterile inflammatory triggers by activating the NLRP3 inflammasome [97]. Building on these findings, we utilized a fluorescent reporter mouse line for inflammasome assembly (ASC-citrine) and observed a significant chronic increase in ASC-speck formation following stroke, indicating a correlation between lipid accumulation and chronic inflammasome activation in microglia. This was further supported by increased IL-1β expression from mouse and human post-mortem stroke tissue, as well as microperfusates longitudinally sampled from the cortex of mice. Interestingly, through integrating our protein and sc-seq data via a demixing algorithm, we were able to show the cell type most responsible for IL-1β production was microglia, both acutely and even more so one month after stroke. Thus, our findings further reinforce the role of lipid accumulation in microglia as a driving force in chronic inflammasome activation poststroke.

To directly test this mechanism, we used mouse bone marrow-derived macrophages and found cholesterol crystals alone were sufficient to longitudinally activate the inflammasome, as evidenced by increased ASC-speck formation. Notably, when we specifically targeted the inflammasome via a Caspase-1 knockout (KO) mouse line, this was insufficient to restore poststroke recovery. Overall, suggesting that cholesterol crystals and not inflammasome activation, are a direct mechanistic driver of chronic neuroinflammation.

4.7 Pharmacologically targeting cholesterol efflux enhances the microglial-oligodendrocyte axis, thereby promoting post-stroke regeneration

To investigate whether therapeutically targeting lipid dysregulation could mitigate chronic lipid accumulation and the observed neuroinflammatory features, we utilized synthetic LXR agonist GW3965. This compound specifically targets LXRα and LXRβ and in turn upregulates the expression of cholesterol transport genes such as ABCA1 and ABCG1, thereby enhancing cholesterol efflux. LXR agonists have been shown to successfully modulate lipid metabolism in vivo in the context of atherosclerosis, ageing, demyelinating and collectively demonstrate the therapeutic potential of targeting reverse cholesterol efflux has on improving outcomes in various disease models [119, 27, 11].

After chronic treatment with GW3965 there was a significant reduction in the lipid accumulation phenotype in post-stroke brain tissue, revealed by decreased lipid droplet and cholesterol crystal content. While much of our understanding of LXR agonists stems from studies on peripheral immune cells such as macrophages [47, 103], it is not surprising, that microglia are functionally influenced by this compound. Since phagocytosis is a core function of microglia, we challenged these cells with yeast particles and observed a significant enhancement in their phagocytic capacity following GW3965 treatment.

Interestingly, microglia emerged as the most responsive cell type to this intervention, exhibiting the highest differentially expressed genes based on sc-RNA sequencing analysis. Most notably, this intervention drove a transcriptional shift in microglia towards an intermediate, less inflammatory state, characterized by downregulation of genes associated with lysosomal dysfunction and inflammasome activation, alongside with upregulation of lipid transport pathways. These changes suggest enhancing reverse cholesterol transport may relieve microglia of the metabolic and inflammatory burden that seems to drive them into a chronically altered and self-protecting phenotype. A finding which aligns with current studies in the context of demyelination [94, 8]. Future studies to investigate cell-type specific LXR activation or deletion would be a great next step to further clarify the contribution of individual glial populations to functional outcomes.

This transcriptional reprogramming in microglia was also accompanied by improved poststroke functional recovery, as indicated by longitudinal wide-field calcium imaging of neuronal activity [17]. This improvement suggests a meaningful restoration of circuit-level communication. Importantly, enhancement in functional connectivity was not an attributable to differences in infarct size, as GW3965 treatment did not alter lesion volume between groups, underscoring that the effect was likely due to improved tissue and cellular function rather than neuroprotection alone.

In parallel, this treatment robustly expanded both oligodendrocyte progenitor cells (OPCs) and mature myelinating oligodendrocytes in the perilesional cortex. This was accompanied by upregulation of myelin at the protein level, consistent with a regenerative response. Oligodendrocytes in this region, which show based on MERFISH analysis, an upregulation of damage-associated markers such as C4b, Serpina3n and Klk6 following stroke, exhibited significantly reduced expression of these markers after GW3965 treatment. This suggests that in addition to promoting myelin repair, GW3965 mitigates oligodendrocyte stress responses.

We then hypothesized that this enhanced remyelination is likely due to improve lipid handling within the CNS. It is well described at basal level that astrocytes are the main suppliers of cholesterol to oligodendrocytes through ApoE containing lipoproteins [39, 1]. However, we suspect that in our model, microglial cholesterol efflux likely supports cholesterol transfer to OPCs to drive differentiation to mature remyelinating oligodendrocytes, which then require high lipid availability for membrane synthesis and myelin regeneration. Supporting this, our scRNA sequencing data shows oligodendrocytes express some of the highest levels of ApoE receptors, including Vldlr and Sort1, signifying a facilitation of efficient cholesterol uptake. Moreover, CSF analysis via mass spectrometry revealed that cholesterol and cholesterol derivatives were largely undetectable in GW3965 treated animals and none were significantly changed relative to controls, indicating that cholesterol is not excreted from the brain and most likely recycled.

To directly test our hypothesis that cholesterol is recycled locally within the brain and transferred to oligodendrocyte progenitor cells (OPCs), we performed a cholesterol uptake and transfer assay using a human iPSC-derived co-culture system. In this setup, iPSC-derived microglia were first loaded with fluorescently labeled cholesterol to stimulate lipid uptake, these cholesterol-loaded microglia were then cultured with human iPSC-derived oligodendrocytes in a transwell system that allowed for molecular exchange between cell types without direct cell-to-cell contact. Under basal conditions, oligodendrocytes in co-culture with cholesterol-loaded microglia showed minimal uptake of the fluorescent cholesterol, indicating limited passive transfer. However, when the co-cultures were treated with GW3965, oligodendrocytes exhibited a marked increase in cholesterol uptake, suggesting that pharmacologically enhancing microglial cholesterol efflux enabled efficient transfer to OPCs.

This experiment provides compelling evidence that oligodendrocytes, particularly in their progenitor state, are highly capable of taking up cholesterol that is actively effluxed by microglia. These findings support the hypothesis that cholesterol can be recycled between glial populations to support repair. Given the high metabolic demand of myelination and membrane synthesis, this mechanism likely plays a crucial role in promoting remyelination and structural recovery after brain injury. As the *in vitro* system used in this study only partially recapitulates the complexity of lipid exchange between heterogenous cell populations, further validation in an in vivo experimental model is warranted.

These results also reframe the role of microglia in the chronic post-stroke environment. While chronically activated microglia are often viewed as dysfunctional and pro-inflammatory, our data demonstrate that, when relieved of their intracellular lipid burden via LXR activation, these same microglia can re-engage in reparative functions. By enhancing cholesterol efflux, microglia indirectly support oligodendrocyte maturation and myelin regeneration through lipid transport, ultimately, promoting functional recovery after stroke. Thus, modulating microglial lipid handling not only restores their homeostatic function but also generates a proregenerative microenvironment, highlighting a previously underappreciated role for microglia as central orchestrators of post-stroke brain repair.

We also note that GW3965 is a systemically bioavailable compound with known off-target effects in the peripheral tissues, including the liver and immune system. The off-target effects may influence systemic lipid metabolism and immune responses and therefore complicating the interpretation of CNS-specific outcomes in our study. In addition, chronic activation of LXRs in the periphery have been associated with hepatic steatosis and hypertriglyceridemia in mice. Therefore, while our findings suggest the potential of modulating lipid metabolism in the brain, the development of CNS-specific LXR agonists, or alternative strategies that selectively target microglial lipid handling without peripheral activation, will be essential to advance this approach toward clinical translational for human stroke patients.

4.8 Conclusion

These studies reveal two central regulators of microglial function after stroke: adaptive immune modulation via T cells and metabolic reprogramming through lipid handling. We demonstrate that $CD4^+$ T cell subsets, particularly T_{H1} and T_{REG} cells, exert effects on microglial activation and transcriptional state in the acute phase. In the absence of T cells, microglia fail to adopt a reparative phenotype and instead develop a dysfunctional, pro-inflammatory profile that exacerbates tissue damage. This underscores how the quality, not just the presence, of immune engagement shapes microglial behavior and stroke outcomes.

Beyond acute immune interactions, we reveal that stroke induces chronic microglial dysfunction by lipid accumulation, including lipid droplets and cholesterol crystals. This metabolic burden triggers sustained inflammasome activation and impairs microglial phagocytosis, contributing to prolonged neuroinflammation. However, by pharmacologically enhancing cholesterol efflux using the LXR agonist GW3965, we were able to reprogram microglia towards a less inflammatory, more reparative state.

Importantly, this metabolic reprogramming extended to other glial populations. We show that improving microglial lipid handling promotes oligodendrocyte progenitor proliferation, maturation and remyelination- critical steps for functional recovery. These findings highlight a lipid recycling pathway from microglia to oligodendrocytes that supports regeneration.

In summary, our data position microglia as key orchestrators of both immune response and tissue repair after stroke. We show CD4$^+$ T cells direct microglial activation acutely, while chronic lipid dysregulation undermines their reparative potential. Targeting these axes- immune engagement and lipid metabolism- offers a promising therapeutic strategy to resolve neuroinflammation and promote brain regeneration after stroke.

5 REFERENCES

1. Abildayeva, K., et al. (2006). "24(S)-Hydroxycholesterol Participates in a Liver X Receptor-controlled Pathway in Astrocytes That Regulates Apolipoprotein E-mediated Cholesterol Efflux." Journal of Biological Chemistry 281(18): 12799-12808.
2. Andoh, M. and R. Koyama (2021). "Microglia regulate synaptic development and plasticity." Developmental Neurobiology 81(5): 568-590.
3. Androvic, P., et al. (2023). "Spatial Transcriptomics-correlated Electron Microscopy maps transcriptional and ultrastructural responses to brain injury." Nature Communications 14(1).
4. Antonio González-Pérez, M., David Gaist, MD, Mari-Ann Wallander, PhD, Gillian McFeat, PhD, and Luis A. García-Rodríguez, MD (2013). "Mortality after hemorrhagic stroke." Neurology 81(6): 559-565.
5. Armella Zadoorian, X. D., Hongyuan Yang (2023). "Lipid droplet biogenesis and functions in health and disease." Nature Reviews Endocrinology 19: 443-459.
6. Baaklini, C. S., et al. (2023). "Microglia promote remyelination independent of their role in clearing myelin debris." Cell Reports 42(12): 113574.
7. Berghoff, S. A., et al. (2022). "Local cholesterol metabolism orchestrates remyelination." Trends in Neurosciences 45(4): 272-283.
8. Berghoff SA, Spieth L, Sun T, Hosang L, Depp C, Sasmita AO, Vasileva MH, Scholz P, Zhao Y, Krueger-Burg D, Wichert S, Brown ER, Michail K, Nave KA, Bonn S, Odoardi F, Rossner M, Ischebeck T, Edgar JM, Saher G. Neuronal cholesterol synthesis is essential for repair of chronically demyelinated lesions in mice. Cell Rep. 2021 Oct 26;37(4):109889. doi: 10.1016/j.celrep.2021.109889. PMID: 34706227.
9. Beuker, C., et al. (2022). "Stroke induces disease-specific myeloid cells in the brain parenchyma and pia." Nature Communications 13(1).
10. Borucki, D. M., et al. (2020). "Complement-Mediated Microglial Phagocytosis and Pathological Changes in the Development and Degeneration of the Visual System." Frontiers in Immunology 11.
11. Bosch-Queralt, Mar L. C.-C., Alkmini Damkou, Martina Schifferer, Kai Schlepckow, Ioannis Alexopoulos, Dieter Lütjohann, Christian Klose, Lenka Vaculčiaková, Takahiro Masuda, Marco Prinz, Kathryn M Monroe, Gilbert Di Paolo, Joseph W Lewcock, Christian Haass, Mikael Simons (2021). "Diet-dependent regulation of TGFβ impairs reparative innate immune responses after demyelination." Nature metabolism 18(3).
12. Canton, J., et al. (2013). "Scavenger receptors in homeostasis and immunity." Nature Reviews Immunology 13(9): 621-634.
13. Cantuti-Castelvetri, L., et al. (2018). "Defective cholesterol clearance limits remyelination in the aged central nervous system." Science 359(6376): 684-688.
14. Cheng, Y.-J., et al. (2024). "Prolonged myelin deficits contribute to neuron loss and functional impairments after ischaemic stroke." Brain 147(4): 1294-1311.
15. Cohen, S. (2018). Lipid Droplets as Organelles, Elsevier: 83-110.
16. Colonna, M. (2023). "The biology of TREM receptors." Nature Reviews Immunology 23(9): 580-594.
17. Cramer, Julia, B. G., Stefan Roth, Martin Dichgans, Marco Düring, Arthur Liesz (2019). "In vivo widefield calcium imaging of the mouse cortex for analysis of network connectivity in health and brain disease." Neuroimage: 570-584.
18. Cserép, C., et al. (2020). "Microglia monitor and protect neuronal function through specialized somatic purinergic junctions." Science 367(6477): 528-537.

19. Cutler, C., & Kokiko-Cochran, O. N. (2022). Lipid metabolism: A central player in the immune response to CNS injury and disease. Frontiers in Immunology, 13, 927673.
20. Delong, J. H., et al. (2022). "Inflammatory Responses After Ischemic Stroke." Seminars in Immunopathology 44(5): 625-648.
21. Disabato, D. J., et al. (2016). "Neuroinflammation: the devil is in the details." Journal of Neurochemistry 139(S2): 136-153.
22. Donkor, E. S. (2018). "Stroke in the 21st Century: A Snapshot of the Burden, Epidemiology, and Quality of Life." Stroke Research and Treatment 2018: 1-10.
23. Duewell, P., et al. (2010). "NLRP3 inflammasomes are required for atherogenesis and activated by cholesterol crystals." Nature 464(7293): 1357-1361.
24. Endres, M., et al. (2022). "Immune Pathways in Etiology, Acute Phase, and Chronic Sequelae of Ischemic Stroke." Circulation Research 130(8): 1167-1186.
25. Farmer, B. C., et al. (2020). "Lipid Droplets in Neurodegenerative Disorders." Frontiers in Neuroscience 14.
26. Gao, C., et al. (2023). "Microglia in neurodegenerative diseases: mechanism and potential therapeutic targets." Signal Transduction and Targeted Therapy 8(1).
27. Gavini, C. K., et al. (2022). "LXR agonist improves peripheral neuropathy and modifies PNS immune cells in aged mice." Journal of Neuroinflammation 19(1).
28. Gelderblom, M., et al. (2009). "Temporal and Spatial Dynamics of Cerebral Immune Cell Accumulation in Stroke." Stroke 40(5): 1849-1857.
29. Geltinger, F., et al. (2020). "Friend or Foe: Lipid Droplets as Organelles for Protein and Lipid Storage in Cellular Stress Response, Aging and Disease." Molecules 25(21): 5053.
30. Gerhard, A. (2016). "TSPO imaging in parkinsonian disorders." Clinical and Translational Imaging 4(3): 183-190.
31. Goldmann, T. and M. Prinz (2013). "Role of Microglia in CNS Autoimmunity." Clinical and Developmental Immunology 2013: 1-8
32. Gouna, G., et al. (2021). "TREM2-dependent lipid droplet biogenesis in phagocytes is required for remyelination." Journal of Experimental Medicine 218(10).
33. Graham, D. K., et al. (2014). "The TAM family: phosphatidylserine-sensing receptor tyrosine kinases gone awry in cancer." Nature Reviews Cancer 14(12): 769-785.
34. Grebe, A. and E. Latz (2013). "Cholesterol Crystals and Inflammation." Current Rheumatology Reports 15(3).
35. Gu, Y., et al. (2022). "Cerebral edema after ischemic stroke: Pathophysiology and underlying mechanisms." Frontiers in Neuroscience 16.
36. Heindl, S., et al. (2018). "Automated Morphological Analysis of Microglia After Stroke." Frontiers in Cellular Neuroscience 12.
37. Heindl, S., et al. (2021). "Chronic T cell proliferation in brains after stroke could interfere with the efficacy of immunotherapies." Journal of Experimental Medicine 218(8).
38. Henry, R. J., et al. (2020). "Microglial Depletion with CSF1R Inhibitor During Chronic Phase of Experimental Traumatic Brain Injury Reduces Neurodegeneration and Neurological Deficits." The Journal of Neuroscience 40(14): 2960-2974.
39. Hornemann, T. (2021). "Mini review: Lipids in Peripheral Nerve Disorders." Neuroscience Letters 740.
40. Iadecola, C. and J. Anrather (2011). "The immunology of stroke: from mechanisms to translation." Nature Medicine 17(7): 796-808.
41. Ikonen, E. (2008). "Cellular cholesterol trafficking and compartmentalization." Nature Reviews Molecular Cell Biology 9(2): 125-138.
42. Iliff, J. J., et al. (2012). "A Paravascular Pathway Facilitates CSF Flow Through the Brain Parenchyma and the Clearance of Interstitial Solutes, Including Amyloid β." Science Translational Medicine 4(147): 147ra111-147ra141.

43. Jacob C. Zbeskoa, T.-V. V. N., b, Tao Yange, Jennifer Beischel Fryea, Omar Hussaina, Megan Hayesa, Amanda Chunga, W. Anthony Dayd, Kristina Stepanovica, Maj Krumbergera, Justine Monaa, Frank M. Longoe, Kristian P. Doyle (April 2018). "Glial scars are permeable to the neurotoxic environment of chronic stroke infarcts." Neurobiology of Disease Volume 112: 63-78.
44. Jayaraj, R. L., et al. (2019). "Neuroinflammation: friend and foe for ischemic stroke." Journal of Neuroinflammation 16(1).
45. Jeffrey D. Pressly, M. Z. G., Javier T. Varona Santos, Alessia Fornoni, Sandra Merscher, and Hassan Al-Ali (2022). "Adaptive and maladaptive roles of lipid droplets in health and disease." American Journal of Physiology Cell Physiology 322(3): C468-C481.
46. Jin, U., et al. (2019). "Cholesterol Metabolism in the Brain and Its Association with Parkinson’s Disease." Experimental Neurobiology 28(5): 554-567.
47. Joseph, S. B., et al. (2004). "LXR-Dependent Gene Expression Is Important for Macrophage Survival and the Innate Immune Response." Cell 119(2): 299-309.
48. Katherine Picard, M.-K. S.-P., Haley A. Vecchiarelli, Maude Bordeleau, Mari-Eve Tremblay (2021). "Neuroendocrine, neuroinflammatory and pathological outcomes of chronic stress: A story of microglial remodeling." Neurochemistry International 145.
49. Kawabori, M. and M. A. Yenari (2015). "The role of the microglia in acute CNS injury." Metabolic Brain Disease 30(2): 381-392.
50. Kedia, S. and M. Simons (2025). "Oligodendrocytes in Alzheimer’s disease pathophysiology." Nature Neuroscience 28(3): 446-456.
51. Keren-Shaul, H., et al. (2017). "A Unique Microglia Type Associated with Restricting Development of Alzheimer’s Disease." Cell 169(7): 1276-1290.e1217.
52. Koh, C.-H., et al. (2023). "CD8 T-cell subsets: heterogeneity, functions, and therapeutic potential." Experimental & Molecular Medicine 55(11): 2287-2299.
53. Lalive, P. H., et al. (2005). "TGF-β-treated microglia induce oligodendrocyte precursor cell chemotaxis through the HGF-c-Met pathway." European Journal of Immunology 35(3): 727-737.
54. Lampron A, Larochelle A, Laflamme N, Préfontaine P, Plante MM, Sánchez MG, Yong VW, Stys PK, Tremblay MÈ, Rivest S. Inefficient clearance of myelin debris by microglia impairs remyelinating processes. J Exp Med. 2015 Apr 6;212(4):481-95. doi: 10.1084/jem.20141656. Epub 2015 Mar 16. PMID: 25779633; PMCID: PMC4387282.
55. Lee, R. H. C. L., Michelle H. H. Wu, Celeste Y. C.1,2; Couto e Silva, Alexandre Possoit, Harlee E. Hsieh, Tsung-Han Minagar, Alireza Lin, Hung Wen (2018). "Cerebral ischemia and neuroregeneration." Neural Regeneration Reseach 13(3): 373-385.
56. Leishman, S., et al. (2024). "Fatty acid synthesis promotes inflammasome activation through NLRP3 palmitoylation." Cell Reports 43(8): 114516.
57. Li, S. (2023). "Stroke Recovery Is a Journey: Prediction and Potentials of Motor Recovery after a Stroke from a Practical Perspective." Life 13(10): 2061.
58. Liang, J. J., et al. (2021). "Lipid regulation of NLRP3 inflammasome activity through organelle stress." Trends in Immunology 42(9): 807-823.
59. Lier, J., et al. (2021). "Beyond Activation: Characterizing Microglial Functional Phenotypes." Cells 10(9): 2236.
60. Liesz, A., et al. (2009). "Regulatory T cells are key cerebroprotective immunomodulators in acute experimental stroke." Nature Medicine 15(2): 192-199.
61. Liu, X. and N. Quan (2018). "Microglia and CNS Interleukin-1: Beyond Immunological Concepts." Frontiers in Neurology 9.
62. Lively, S. and L. C. Schlichter (2018). "Microglia Responses to Pro-inflammatory Stimuli (LPS, IFNγ+TNFα) and Reprogramming by Resolving Cytokines (IL-4, IL-10)." Frontiers in Cellular Neuroscience 12.

63. Lloyd-Jones, D., et al. (2009). "Heart Disease and Stroke Statistics—2009 Update." Circulation 119(3): e21-e181.
64. Loving, B. A. and K. D. Bruce (2020). "Lipid and Lipoprotein Metabolism in Microglia." Frontiers in Physiology 11.
65. Makinodan, M., et al. (2023). Brain-derived neurotrophic factor from microglia regulates neuronal development in the medial prefrontal cortex and its associated social behavior, Research Square Platform LLC.
66. Masenga, S. K. and A. Kirabo (2024). "The NLRP3 inflammasome in ischemic stroke." Frontiers in Stroke 3.
67. Muhammad, S., et al. (2021). "Brain Immune Interactions—Novel Emerging Options to Treat Acute Ischemic Brain Injury." Cells 10(9): 2429.
68. Murray, K. N., et al. (2015). "Interleukin-1 and acute brain injury." Frontiers in Cellular Neuroscience 9.
69. Naik, S. U., et al. (2006). "Pharmacological Activation of Liver X Receptors Promotes Reverse Cholesterol Transport In Vivo." Circulation 113(1): 90-97.
70. Natrajan, M. S., et al. (2015). "Retinoid X receptor activation reverses age-related deficiencies in myelin debris phagocytosis and remyelination." Brain 138(12): 3581-3597.
71. Nugent, A. A., et al. (2020). "TREM2 Regulates Microglial Cholesterol Metabolism upon Chronic Phagocytic Challenge." Neuron 105(5): 837-854.e839.
72. Ooboshi H, Shichita T. [DAMPs (damage-associated molecular patterns) and inflammation]. Nihon Rinsho. 2016 Apr;74(4):573-8. Japanese. PMID: 27333742.
73. Orth, M. and S. Bellosta (2012). "Cholesterol: Its Regulation and Role in Central Nervous System Disorders." Cholesterol 2012: 1-19.
74. Paik, S., et al. (2025). "Updated insights into the molecular networks for NLRP3 inflammasome activation." Cellular & Molecular Immunology 22(6): 563-596.
75. Pallarés-Moratalla, C. and G. Bergers (2024). "The ins and outs of microglial cells in brain health and disease." Frontiers in Immunology 15.
76. Pereira, M., et al. (2024). "Arachidonic acid inhibition of the NLRP3 inflammasome is a mechanism to explain the anti-inflammatory effects of fasting." Cell Reports 43(2): 113700.
77. Philipp M. Lenzlinger, V. H. J. H., Helen I. Joller-Jemelka, Otmar Trentz, Maria Cristina Morganti-Kossmann, and Thomas Kossmann (2004). "Markers for Cell-Mediated Immune Response Are Elevated in Cerebrospinal Fluid and Serum After Severe Traumatic Brain Injury in Humans." Journal of Neurotrauma 18(5): 479-489.
78. Prinz, M. and J. Priller (2014). "Microglia and brain macrophages in the molecular age: from origin to neuropsychiatric disease." Nature Reviews Neuroscience 15(5): 300-312.
79. Puig, B., et al. (2018). "Molecular Communication of a Dying Neuron in Stroke." International Journal of Molecular Sciences 19(9): 2834.
80. Qian, L., et al. (2022). "Balancing cholesterol in the brain: from synthesis to disposal." Exploration of Neuroprotective Therapy: 1-27.
81. Qin, C., et al. (2022). "Signaling pathways involved in ischemic stroke: molecular mechanisms and therapeutic interventions." Signal Transduction and Targeted Therapy 7(1).
82. Raha, O., et al. (2023). "Advances in mechanical thrombectomy for acute ischaemic stroke." BMJ Medicine 2(1): e000407.
83. Ralhan, I., et al. (2021). "Lipid droplets in the nervous system." Journal of Cell Biology 220(7).
84. Ransohoff, R. M. (2016). "How neuroinflammation contributes to neurodegeneration." Science 353(6301): 777-783.

85. Ravichandran, K. A., Heneka, M.T. (2024). "Inflammasomes in neurological disorders — mechanisms and therapeutic potential." Nature Reviews Neurology: 67-83.
86. Reichert, F. and S. Rotshenker (2019). "Galectin-3 (MAC-2) Controls Microglia Phenotype Whether Amoeboid and Phagocytic or Branched and Non-phagocytic by Regulating the Cytoskeleton." Frontiers in Cellular Neuroscience 13
87. Rink, C. and S. Khanna (2011). "Significance of Brain Tissue Oxygenation and the Arachidonic Acid Cascade in Stroke." Antioxidants & Redox Signaling 14(10): 18891903.
88. Safaiyan, S., et al. (2021). "White matter aging drives microglial diversity." Neuron 109(7): 1100-1117.e1110.
89. Saher, G. S., Sina Kristin (2015). "Cholesterol in myelin biogenesis and hypomyelinating disorders." Biochimica et Biophysica Acta 1851(8): 1083-1094
90. Saher G, Quintes S, Nave KA. Cholesterol: a novel regulatory role in myelin formation. Neuroscientist. 2011 Feb;17(1):79-93. doi: 10.1177/1073858410373835. PMID: 21343408.
91. Sala Frigerio, C., et al. (2019). "The Major Risk Factors for Alzheimer's Disease: Age, Sex, and Genes Modulate the Microglia Response to Aβ Plaques." Cell Reports 27(4): 1293-1306.e1296.
92. Salaudeen, M. A., et al. (2024). "Understanding the Pathophysiology of Ischemic Stroke: The Basis of Current Therapies and Opportunity for New Ones." Biomolecules 14(3): 305.
93. Salvadori, E., et al. (2020). "Comparison between Ischemic and Hemorrhagic Strokes in Functional Outcome at Discharge from an Intensive Rehabilitation Hospital." Diagnostics 11(1): 38.
94. Schafer, D. P., et al. (2013). "The “quad-partite” synapse: Microglia-synapse interactions in the developing and mature CNS." Glia 61(1): 24-36.
95. Schetters, S. T. T., et al. (2018). "Neuroinflammation: Microglia and T Cells Get Ready to Tango." Frontiers in Immunology 8.
96. Shaheryar, Z. A., et al. (2021). "Neuroinflammatory Triangle Presenting Novel Pharmacological Targets for Ischemic Brain Injury." Frontiers in Immunology 12.
97. Sheedy, F. J., et al. (2013). "CD36 coordinates NLRP3 inflammasome activation by facilitating intracellular nucleation of soluble ligands into particulate ligands in sterile inflammation." Nature Immunology 14(8): 812-820.
98. Shemer, A., et al. (2020). "Interleukin-10 Prevents Pathological Microglia Hyperactivation following Peripheral Endotoxin Challenge." Immunity 53(5): 1033-1049.e1037.
99. Shi L, Sun Z, Su W, Xu F, Xie D, Zhang Q, Dai X, Iyer K, Hitchens TK, Foley LM, Li S, Stolz DB, Chen K, Ding Y, Thomson AW, Leak RK, Chen J, Hu X. Treg cell-derived osteopontin promotes microglia-mediated white matter repair after ischemic stroke. Immunity. 2021 Jul 13;54(7):1527-1542.e8. doi: 10.1016/j.immuni.2021.04.022. Epub 2021 May 19. PMID: 34015256; PMCID: PMC8282725.
100. Thiam, A. R., et al. (2013). "The biophysics and cell biology of lipid droplets." Nature Reviews Molecular Cell Biology 14(12): 775-786.
101. Tongtong Xu, C. L., Shiyu Deng, Lin Gan, Zhijun Zhang, Guo-Yuan Yang, Hengli Tian and Yaohui Tang (2022). "The roles of microglia and astrocytes in myelin phagocytosis in the central nervous system." Journal of Cerebral Blood Flow & Metabolissm 43: 325-340.
102. Tontonoz, P. and D. J. Mangelsdorf (2003). "Liver X Receptor Signaling Pathways in Cardiovascular Disease." Molecular Endocrinology 17(6): 985-993.
103. Traiffort, E., et al. (2020). "Astrocytes and Microglia as Major Players of Myelin Production in Normal and Pathological Conditions." Frontiers in Cellular Neuroscience 14.

104. Ulrich Dirnagl, C. I. a. M. A. M. (1990). "Pathobiology of ischaemic stroke: an integrated view." Stroke pathobiology 22(9): 391-397.
105. Vanherle, S., et al. (2025). "Lipid metabolism, remodelling and intercellular transfer in the CNS." Nature Reviews Neuroscience.
106. Wang, J., et al. (2024). "Th17 Cells and IL-17A in Ischemic Stroke." Molecular Neurobiology 61(4): 2411-2429.
107. Wang, Y., et al. (2022). "Microglia-mediated neuroinflammation and neuroplasticity after stroke." Frontiers in Cellular Neuroscience 16.
108. Wei Weia, Lin Zhangb,1, Wenqiang Xina, Yongli Pana, Lars Tatenhorsta, Zhongnan Haoa, Stefan T. Gernerc, Sabine Huberc, Martin Juenemannc, Marius Butzd, Hagen B. Huttnerc, Mathias Bahra, Dirk Fitznera, Feng Jiab, E, Thorsten R. Doeppner (2023). "TREM2 regulates microglial lipid droplet formation and represses post-ischemic brain injury." Biomedicine & Pharmacotherapy 170.
109. Xu, W., et al. (2025). "NLRP3 inflammasome in neuroinflammation and central nervous system diseases." Cellular & Molecular Immunology 22(4): 341-355.
110. Yang, D., et al. (2022). "Lipid metabolism and storage in neuroglia: role in brain development and neurodegenerative diseases." Cell & Bioscience 12(1).
111. Yoon, J. H., et al. (2022). "Brain lipidomics: From functional landscape to clinical significance." Science Advances 8(37)
112. Yoshio Yamauchi, S. A.-D., Noriyuki Iwamoto, Ryuichiro Sato, Shinji Yokoyama (2024). "ABCA1 deficiency causes tissue-specific dysregulation of the SREBP2 pathway in mice." BBA-Molecular and Cell Biology of Lipids 1869(8).
113. Zhang (2024). "Lipid droplets in the nervouse system: involvement in cell metabolic homeostasis." Neural Regeneration Research 20(3): 740-750.
114. Zhang, J. and Q. Liu (2015). "Cholesterol metabolism and homeostasis in the brain." Protein & Cell 6(4): 254-264.
115. Zhang, L., et al. (2024). "Role of NLRP3 inflammasome in central nervous system diseases." Cell & Bioscience 14(1).
116. Živančević, K., et al. (2021). Neuroinflammation in Post-Ischemic Brain. Cerebral Ischemia, Exon Publications: 87-110.
117. Marschallinger J, Iram T, Zardeneta M, Lee SE, Lehallier B, Haney MS, Pluvinage JV, Mathur V, Hahn O, Morgens DW, Kim J, Tevini J, Felder TK, Wolinski H, Bertozzi CR, Bassik MC, Aigner L, Wyss-Coray T. Lipid-droplet-accumulating microglia represent a dysfunctional and proinflammatory state in the aging brain. Nat Neurosci. 2020 Feb;23(2):194-208. doi: 10.1038/s41593-019-0566-1. Epub 2020 Jan 20. Erratum in: Nat Neurosci. 2020 Feb;23(2):294. doi: 10.1038/s41593-020-0595-9. Erratum in: Nat Neurosci. 2020 Oct;23(10):1308. doi: 10.1038/s41593-020-0682-y. PMID: 31959936; PMCID: PMC759513
118. Yvan-Charvet L, Ranalletta M, Wang N, Han S, Terasaka N, Li R, Welch C, Tall AR. Combined deficiency of ABCA1 and ABCG1 promotes foam cell accumulation and accelerates atherosclerosis in mice. J Clin Invest. 2007 Dec;117(12):3900-8. doi: 10.1172/JCI33372. PMID: 17992262; PMCID: PMC2066200.
119. Khandker L, Jeffries MA, Chang YJ, Mather ML, Evangelou AV, Bourne JN, Tafreshi AK, Ornelas IM, Bozdagi-Gunal O, Macklin WB, Wood TL. Cholesterol biosynthesis defines oligodendrocyte precursor heterogeneity between brain and spinal cord. Cell Rep. 2022 Mar 1;38(9):110423. doi: 10.1016/j.celrep.2022.110423. PMID: 35235799; PMCID: PMC8988216.
120. Ozgen, H., Baron, W., Hoekstra, D. *et al.* Oligodendroglial membrane dynamics in relation to myelin biogenesis. *Cell. Mol. Life Sci.* **73**, 3291–3310 (2016). https://doi.org/10.1007/s00018-016-2228-8.

121. Mikael Simons, E.-M. K., Christoph Thiele, Wilhelm Stoffel, Jacqueline Trotter (2000). "Assembly of Myelin by Association of Proteolipid Protein with Cholesterol- and Galactosylceramide-Rich Membrane Domains." Journal of Cell Biology 151(1): 143-154.

6 COPYRIGHT AND AI USE OF INFORMATION

Figure number	1
License number	5706351079191
License date	April 13, 2025
Licensed content publisher	Wolters Kluwer Health, Inc.
Licensed content publication	Stroke
Licensed content title	Temporal and Spatial Dynamics of Cerebral Immune Cell Accumulation in Stroke
Licensed content author	Mathias Gelderblom, Frank Leypoldt, Karin Steinbach, et al

Figure number	2
License number	6007191237999
License date	April 13, 2025
Licensed content publisher	Elsevier
Licensed content publication	Trends in Neurosciences
Licensed content title	Pathobiology of ischaemic stroke: an integrated view
Licensed content author	Ulrich Dirnagl, Costantino Iadecola,Michael A. Moskowitz

Figure number	3
License number	Creative Commons Attribution 4.0 International (CC BY 4.)
License date	Open access
Licensed content publisher	Frontiers Media S.A.
Licensed content publication	Frontiers in Immunology
Licensed content title	The ins and outs of microglial cells in brain health and disease
Licensed content author	Pallarés-Moratalla and Bergers

Figure number	4
License number	Creative Commons Attribution 4.0 International
(CC BY 4.)	
License date	Open access
Licensed content publisher	Nature Publishing Group UK
Licensed content publication	Experimental & Molecular Medicine
Licensed content title	CD8 T-cell subsets: heterogeneity, functions, and therapeutic potential
Licensed content author	Koh, CH., Lee, S., Kwak, M. et al.

Figure number	5
License number	6007201132653
License date	April 13, 2025
Licensed content publisher	Elsevier
Licensed content publication	Trends in Immunology
Licensed content title	Lipid regulation of NLRP3 inflammasome activity through organelle stress
Licensed content author	Jonathan J., Liang,Iain, D.C. Fraser, Clare E. Bryant

Figure number	6
License number	6007221419198
License date	April 13, 2025
Licensed content publisher	Springer Nature
Licensed content publication	Nature Reviews Neuroscience
Licensed content title	Lipid metabolism, remodelling and intercellular transfer in the CNS
Licensed content author	Sam Vanherle et al

Abstract and sections 1, 2 and 4 were corrected with the aid of ChatGPT.

7 LIST OF PUBLICATIONS

1. **Kelsey Pinkham***, Steffanie Heindl*, Daniel Varga, Alba Simats, Nicolas Snaidero, Yuxi Zhou, Sarantos Kostidis, Martina Schifferer, Gemma Llovera, Olga Carofiglio, Merle Bublitz, Elena Sanchez, Christoph Müller, Ludwig Huber, Natalija Ivljanin, Rainer Malik, Peter Androvic, Janos Groh, Stefan Berghoff, Christian Haass, Sarah Jäkel, Dominik Paquet, Rebeka Fekete, Thomas Misgeld, Martin Dichgans, Ozgün Gökce, Mikael Simons, Adam Denes, Hannah Spitzer, Peiying Li, Martin Giera, Arthur Liesz. Enhancing microglial cholesterol export promotes oligodendrocyte regeneration and functional recovery after stroke. *In progress.*
2. Gangqi Wang, Bernard M. van den Berg, Sarantos Kostidis, **Kelsey Pinkham**, Marleen E. Jacobs, Arthur Liesz, Martin Giera, Ton J. Rabelink. Spatial quantitative metabolomics enables identification of remote and sustained ipsilateral cortical metabolic reprogramming after stroke**.** *Accepted. Nature Metabolism.*
3. Corinne Benakis, Alba Simats, Sophie Tritschler, Steffanie Heindl, Simon Besson-Girard, Gemma Llovera, **Kelsey Pinkham**, Anna Kolz, Alessio Ricci, Fabian J Theis, Stefan Bittner, Özgüng Gökce, Anneli Peters, Arthur Liesz. T cells modulate the microglial response to brain ischemia. *eLife.* 2022 Dec. doi.org/10.7554/e.Life.82031
4. Gemma Llovera, **Kelsey Pinkham**, Arthur Liesz. Modeling Stroke in Mice: Focal Cortical Lesions by Photothrombosis**.** *J Vis Exp.* 2021 May. doi: 10.3791/62536
5. Jasper Che-Yung Chien, Elie Tabet, **Kelsey Pinkham**, Cintia Carla da Hora, Jason ChengYu Chang, Steven Lin, Christian E Badr, Charles Pin-Kuang Lai. A multiplexed bioluminescent reporter for sensitive and non-invasive tracking of DNA double strand break repair dynamics in vitro and in vivo. *Nucleic Acids Res.* 2020 September.
6. **Kelsey Pinkham***, David Jaehyun Park*, Arsalan Hashemiaghdam1, Aleksander Kirov, Isam Adam, Kamila Rosiak, Cintia Carla da Hora1, Jian Teng1, Pike See Cheah, Gitali Ganguli-Indra, Avalon Kelly, Arup K. Indra, and Christian E. Badr. Stearoyl CoA Desaturase is essential for regulation of ER homeostasis and tumor growth in glioma stemlike cells. *Stem Cell Reports*. 2019 Feb. doi.org/10.1016/j.stemcr.2019.02.012
7. Cintia Carla da Hora, **Kelsey Pinkham**, Litia Carvalho, Max Zinter, Elie Tabet, Bakhos A. Tannous*, Christian E. Badr* Sustained NF-kB-STAT3 signaling promotes resistance to Smac mimetics in Glioma stem-like cells but creates a vulnerability to EZH2 inhibition. *Cell Death Discovery* Feb 2019. doi:10.1038/s41420-019-0155-9.
8. Volak A, LeRoy SG, Natasan JS, Park DJ, Cheah PS, Maus A, Fitzpatrick Z1, Hudry E, **Pinkham K**, Gandhi S, Hyman BT, Mu D1, GuhaSarkar D, Stemmer-Rachamimov AO, Sena-Esteves M, Badr CE, Maguire CA**.** Virus vector-mediated genetic modification of brain tumor stromal cells after intravenous delivery. *J Neurooncol*. 2018 May. doi:10.1007/s11060-018-2889-2.

8 CURRICULUM VITAE

EDUCATION

LUDWIG-MAXIMILIANS-UNIVERSITÄT MÜNCHEN PhD Candidate, GSN Neuroscience (Fast-Track) Neuro-Immunology/ Neuroinflammation Supervisor: Prof. Dr. Arthur Liesz	Munich, DE October 2019 – Present
BRIDGEWATER STATE UNIVERSITY Bachelor of Science in Biology Concentration: Molecular Biology	Bridgewater, MA, USA August 2013

PROFESSIONAL/ RESEARCH EXPERIENCE

INSTITUTE FOR STROKE AND DEMENTIA RESEARCH PhD candidate, Stroke-Immunology Supervisor: Prof. Dr. Arthur Liesz Project: Targeting microglial function in post-stroke regeneration	Munich, DE September 2020 – Present
MASSACHUSETTS GENERAL HOSPITAL/ HARVARD UNIVERSITY Research Technician II/ Lab Manager, Neurology Supervisor: Prof. Dr. Christian E. Badr Project: Stearoyl CoA Desaturase is essential for regulation of ER homeostasis and tumor growth in glioma stem-like cells	Boston, MA, USA January 2016 – July 2018
EPIGENDX Hopkinton, MA, USA Research Associate Pyrosequencing and NGS company	Hopkinton, MA, USA December 2014 – December 2015

9 DECLARATION OF AUTHOR CONTRIBUTION

Publication 1: (Benakis, Pinkham et al. 2022) “T Cells Modulate the Microglial Response to Brain Ischemia”

Corinne Benakis, Alba Simats, Sophie Tritschler, Steffanie Heindl, Simon Besson-Girard, Gemma Llovera, **Kelsey Pinkham**, Anna Kolz, Alessio Ricci, Fabian J Theis, Stefan Bittner, Özgün Gökce, Anneli Peters, Arthur Liesz

Author contributions: Corinne Benakis: Conceptualization, Formal analysis, Supervision, Funding acquisition, Investigation, Visualization, Methodology, Writing - original draft, Writing - review and editing. Alba Simats: Supervision, Validation, Investigation, Methodology. Sophie Tritschler: Data curation, Formal analysis, Visualization. Steffanie Heindl: Data curation, Formal analysis, Visualization. Simon Besson-Girard: Data curation, Formal analysis, Visualization. Gemma Llovera: Formal analysis, Investigation, Methodology. Kelsey Pinkham: Formal analysis, Investigation, Methodology. Anna Kolz: Investigation, Methodology. Alessio Ricci: Investigation, Methodology. Fabian J Theis: Data curation, Supervision. Stefan Bittner: Writing - review and editing. Özgün Gökce: Data curation, Formal analysis, Writing - review and editing. Anneli Peters: Investigation, Methodology, Writing - review and editing. Arthur Liesz: Conceptualization, Supervision, Funding acquisition, Writing - original draft, Project administration, Writing - review and editing.

My contribution to Publication 1 in detail:

I engineered CD4$^+$ T cells overexpressing IL-10 that were injected into the cisterna magna of mice post-stroke. I also performed and analyzed the cylinder behavior test of mice injected with control aCSF or IL-10 overexpressing CD4$^+$ T cells.

Publication 2: (Pinkham, Heindl. et al., 2025) “Enhancing Microglial Cholesterol Export Promotes Oligodendrocyte Regeneration and Functional Recovery After Stroke”

Kelsey Pinkham*, Steffanie Heindl*, Daniel Varga, Alba Simats, Nicolas Snaidero, Yuxi Zhou, Sarantos Kostidis, Martina Schifferer, Gemma Llovera, Olga Carofiglio, Merle Bublitz, Elena Sanchez, Christoph Müller, Ludwig Huber, Natalija Ivljanin, Rainer Malik, Peter Androvic, Janos Groh, Stefan Berghoff, Christian Haass, Sarah Jäkel, Dominik Paquet, Rebeka Fekete, Thomas Misgeld, Martin Dichgans, Ozgün Gökce, Mikael Simons, Adam Denes, Hannah Spitzer, Peiying Li, Martin Giera, Arthur Liesz

*Contributed equally

Author contributions:
Conceptualization, K.P., S.H., A.L.; Investigation, K.P., S.H., D.V., N.S., Y.Z, S.K., M.S., G.L., S.R., O.C., E.S., C.M., L.H., N.I., P.A., J.G., R.F., N.L., B.H.; Formal Analysis, K.P., S.H., D.V., N.S., Y.Z, S.K., M.S., G.L., E.S., C.M., L.H., N.I., P.A., J.G., R.F., O.G., P.L. H.S., B.H., M.G.; Resources,S.B., C.H., S.J., D.P., T.M., O.G., M.S., A.D., P.L., M.G; Writing – Original Draft, K.P., S.H., A.L.; Writing – Review & Editing, K.P., S.H., A.L.; Visualization, K.P., S.H., P.L., B.H., M.G, A.L.; Supervision: C.H., S.J., D.P., T.M., O.G., M.S., A.D., H.S., P.L., M.G., A.L.; Funding Acquisition: C.H., S.J., D.P., T.M., O.G., M.S., A.D., P.L., B.H., M.G., A.L.

My contribution to Publication 2 in detail:

For this publication I performed the surgeries, antibody treatments and widefield calcium imaging and analysis for the in vivo 4D9 experiment. I also performed the surgeries for all the following experiments described. I conducted staining, confocal images and quantification for the microglia morphology analysis of the PLX5622 experiment. I established and performed the staining, imaging and quantification of BODIPY, Plin2 and crystals experiments on human and mouse tissue. I established Plin2 and FIlica660 co-staining for flow cytometry analysis and quantification. I prepared tissue sections for MALDI-MSI and electron microscopy analysis. I established, performed and analyzed the cholesterol assay in stroke and control mice. I was also responsible for all GW3965 in vivo cohort surgeries and treatments. I performed widefield calcium imaging in addition to the analysis, microglia morphology staining, imaging and analysis for the GW3965 experiment. I also performed and sacrificed all GW3965 and Ctrl mice used for the sc-sequencing, in addition to proving gene target lists for the analysis. I performed the staining, imaging and analysis of caspase-1 in the GW3965 experiment. In addition, I performed the longitudinal IL-1β ELISA and quantification from mouse brain tissue post-stroke and after GW3965 treatment and analyzed the behavior tests performed on the Caspase-1 KO mice. I established an in vitro assay to test the effect of cholesterol crystal treatment and inflammasome activation on ASC-Citrine BMDMs and performed and analyzed the flow cytometry aspect of the experiment. In addition, I made the cholesterol crystals. I established, performed and analyzed the western blot of the supernatants from BMDMs treated with cholesterol crystals over time. I performed the staining, imaging and analysis of the CAII/Olig2 and NG2 immuno after GW3965 treatment. For the lipid GC-MS experiment from CSF samples from GW3965 and Ctrl mice, I performed the final analysis. I also established, performed and analyzed the iPSC co-culture experiment to test cholesterol uptake and transfer experiment using GW3965 in collaboration with Sarah Jäkel (design), Merle Bublitz and Natalija. I contributed to conceiving the project, designing experiments and writing and reviewing manuscript.

Herewith, I confirm the contributions of Kelsey Pinkham to the articles.

Munich, 06.06.25

______________ ______________

Kelsey Pinkham Dr. Corinne Benakis

(First author publication 1)

______________ ______________

Dr. Steffanie Heindl Dr. Prof. med. Arthur Liesz

(Co-first author publication 2) (Supervisor)

10 AFFADAVIT

Eigenständigkeitserklärung

Hiermit versichere ich an Eides statt, dass die vorliegende schriftliche Dissertation / Masterarbeit / Bachelorarbeit / Zulassungsarbeit mit dem Titel

Targeting Microglial Function in Post-Stroke Regeneration

von mir selbstständig verfasst wurde und dass keine anderen als die angegebenen Quellen und Hilfsmittel benutzt wurden. Die Stellen der Arbeit, die anderen Werken dem Wortlaut oder dem Sinne nach entnommen sind, wurden in jedem Fall unter Angabe der Quellen (einschließlich des World Wide Web und anderer elektronischer Text- und Datensammlungen) kenntlich gemacht. Weiterhin wurden alle Teile der Arbeit, die mit Hilfe von Werkzeugen der künstlichen Intelligenz de novo generiert wurden, durch Fußnote/Anmerkung an den entsprechenden Stellen kenntlich gemacht und die verwendeten Werkzeuge der künstlichen Intelligenz gelistet. Die genutzten Prompts befinden sich im Anhang. Diese Erklärung gilt für alle in der Arbeit enthaltenen Texte, Graphiken, Zeichnungen, Kartenskizzen und bildliche Darstellungen.

München, 12.June.2025

(Ort / Datum)

Kelsey Pinkham	Kelsey Pinkham
(Vor und Nachname in Druckbuchstaben)	(Unterschrift)

Affidavit

Herewith I certify under oath that I wrote the accompanying Dissertation / MSc thesis / BSc thesis / Admission thesis myself.

Title: Targeting Microglial Function in Post-Stroke Regeneration

In the thesis no other sources and aids have been used than those indicated. The passages of the thesis that are taken in wording or meaning from other sources have been marked with an indication of the sources (including the World Wide Web and other electronic text and data collections). Furthermore, all parts of the thesis that were de novo generated with the help of artificial intelligence tools were identified by footnotes/annotations at the appropriate places and the artificial intelligence tools used were listed. The prompts used were listed in the appendix. This statement applies to all text, graphics, drawings, sketch maps, and pictorial representations contained in the Work.

München, 12.June.2025

(Location/date)

Kelsey Pinkham	Kelsey Pinkham
(First and last name in block letters)	(Signature)